The Growth and Characterization of 2D Van Der Waals Crystals by Molecular Beam Epitaxy

A Dissertation Presented to the Faculty of the School of
Engineering and Applied Science,
University of Virginia

In Partial Fulfillment of the Requirements for the
Degree of Doctor of Philosophy in Materials Science and Engineering

Peter Matthew Litwin

May 2023

APPROVAL SHEET

This
Dissertation
is submitted in partial fulfillment of the requirements for the degree of
Doctor of Philosophy

Author: Peter Litwin

This Dissertation has been read and approved by
the examing committee:

Advisor: Stephen McDonnell
Committee Member: Jerrold Floro
Committee Member: Petra Reinke
Committee Member: Kyusang Lee
Committee Member: Joshua Choi

Accepted for the School of Engineering and Applied Science:

Jennifer L. West, School of Engineering and Applied Science
May 2023

Abstract

As metal–oxide–semiconductor field-effect transistor (MOSFET) scaling pushes to the limits of Moore's Law, future improvements in transistor performance will require new materials or novel device structures. Low-dimensional materials, such as two-dimensional (2D) materials, offer new pathways in device scaling and design. 2D materials are atomically thin, self-terminating planar sheets of atoms that represent the limit in material thinning. For this reason, 2D materials are of interest for the continued scaling of transistors. They also show promise for use in new device technologies such as the tunnel field effect transistor and various spintronic devices.

A significant hurdle to the widespread integration of 2D materials into commercial technologies is achieving controlled and scalable synthesis methods. Despite the intense research focus on layered van der Waals crystals over the last two decades, challenges in controlling nucleation density, stoichiometry, and effective doping of 2D materials remain. In this thesis, we use molecular beam epitaxy (MBE) to investigate the growth of various 2D materials, including semiconducting WSe_2, metallic $Nb_{1+x}Se_2$, and the topological insulator Bi_2Se_3. Despite their similar layered structures, the growth of each of these materials pose their own unique engineering challenges. We use a combination of in-situ and ex-situ characterization techniques to explore the *processing-structure-properties* relationship as it applies to the synthesis of these 2D systems.

Acknowledgements

The work presented in this thesis would not have been possible without considerable contributions from those around me. One of the most important lessons I have learned through this journey is that the scientific process is one best pursued in collaboration with others. Taking advantage of the knowledge and skills of those around you greatly enhances the capacity of any scientific pursuit. As we have often said in the McDonnell Lab, *teamwork makes the dream work*.

I would first like to thank my research advisor, Stephen McDonnell. During my time in graduate school, I have progressed significantly as a researcher under his guidance. As I enter the next phase of my career, I feel confident that I have all the necessary tools to succeed and much of that is to his credit. As a founding member of his team, I can only hope to have made as significant a contribution to his career endeavors as he has to mine. I would also like to thank my committee members, professors Jerrold Floro, Petra Reinke, Kyusang Lee, and Joshua Choi for each of their time and effort in helping me navigate these early stages of my career.

Numerous additional researchers have aided in the work reported in this thesis. Professor Costel Constantin and Dr. Harry Hu of James Madison University guided and assisted with AFM measurements. The Reinke Lab members (including Nathaniel Kabat, William Blades, and Devin Jessup) provided useful STM/STS contributions. Samantha Jaszewski collected and assisted in analysis of XRD and XRR contributions to this work. Wendy Sarney and Asher Leff from the Army Research Laboratory (ARL) collected and helped interpret TEM data. Albert Davydov and Sergiy Krylyuk from NIST provided synthetic $NbSe_2$ reference crystals and contributed to the interpretation of the studies of $NbSe_2$ reported here. Patrick Taylor (ARL) synthesized the Bi_2Se_3 crystals studied in this thesis and Brandi Wooten (The Ohio State University) performed

complimentary electrical and thermal transport measurements. I would also like to thank Patrick, Brandi, Harry Hier, and Sina Najmaei for making me feel welcome during my time at ARL and for the informative discussions which aided not only to this work, but also influenced my career decisions going forward.

It would be wrong to not also acknowledge Kim Fitzhugh and Bryana Amador. The two of them helped me navigate the logistical side of graduate school. Their enthusiastic willingness to provide assistance (and candy) makes the lives of the graduate students easier and the MSE department a more welcoming community.

I was also blessed to have been part of an amazing lab group (Keren, Meg, Gaby, Lee, Vicker, and Clayton). As mentioned above, progressing through graduate school requires support from those around you and no one provided as much direct support, both scientific and emotional, as my labmates. Other members of the B-floor team, including Eli, Will, Adrian, and Jonathan, also aided to this work through plenty of scientific (and otherwise) discussions. Professor Fitz-Gerald was also critical to the mission through the continuous supply of liquid energy.

Lastly, I would also like to thank my family (Mom, Dad, Maggie, Nick, Matt, Lukey, Josh, Ben and Em) for all their continued encouragement.

I am grateful for everyone’s support throughout this journey. I couldn’t have done it without you.

Table of Contents

1. Introduction

1.1.Purpose

The purpose of this thesis is to present experimental investigations focused on understanding the *processing-structure-properties* relationships at play in the growth of layered two-dimensional (2D) compounds by molecular beam epitaxy (MBE). We investigate the growth of a variety of 2D material systems including semiconductors, metals, and topological insulators (TIs) with the goal of controlling the grown materials' surface/grain morphology, chemistry, phase (polytype), and electronic character. This work also constitutes the first of such studies in the McDonnell Lab at the University of Virginia, and thus, we set the ground work for future investigations focused on the growth of 2D materials using MBE.

1.2. 2D Materials

2D materials have been heavily studied since the Nobel Prize was awarded for the isolation and characterization of single-layer graphene [1]. Broadly characterized as materials with strong in-plane bonding and a basal plane absent of dangling bonds, in their bulk form, 2D materials are composed of stacked planar sheets held together by van der Waals forces. The relationship between bulk graphite and monolayer graphene is presented in *Figure 1.1*.

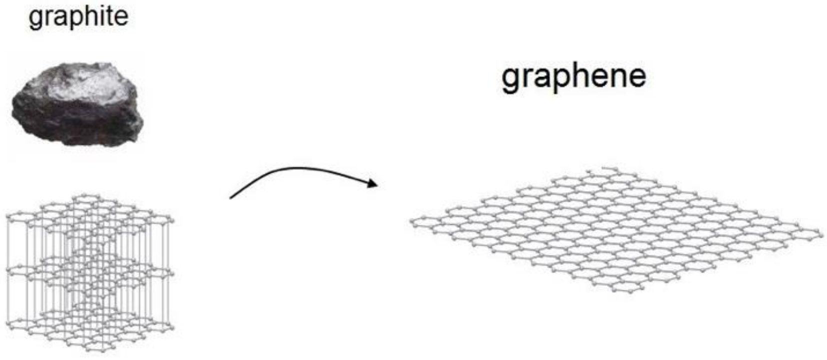

Figure 1.1: The structure and relationship of graphite and graphene. Image adapted from N. Barrial [2].

Beyond graphene, there exists a variety of 2D van der Waals compounds including hexagonal boron nitride, transition metal dichalcogenides (TMDCs), and V-VI sesquichalcogenides, such as Bi_2Se_3 and Bi_2Te_3. In total, 2D van der Waals crystals are believed to encompass in excess of 600 structurally stable monolayer materials [3]. 2D compounds span the range in electronic character from metals to insulators; the diversity in the electronic character of 2D materials is represented in *Figure 1.2* [4]. These materials are the subject of intense research for a range of applications in next generation electronic devices, showing promise for use in tunneling field effect transistors (TFETs), photonics, thermoelectric and thermomagnetic energy harvesting, and flexible electronics [5-10].

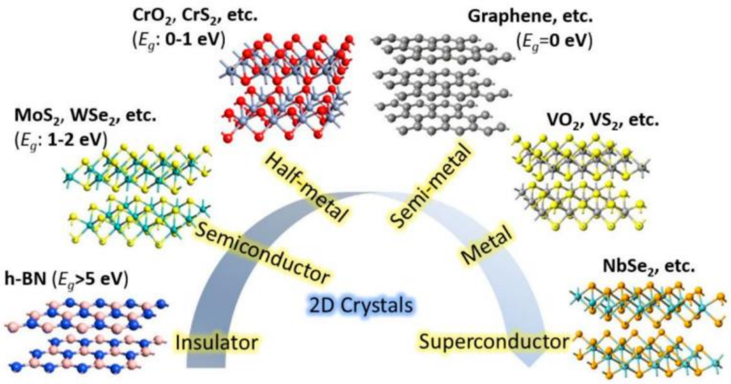

Figure 1.2: Examples of 2D materials along with their respective electronic character. Image adapted from [4] .

A principal interest in 2D materials relates to their scalability. In 1965, Gordon Moore predicted that the maximum number of transistors in an integrated circuit will double every year [11]. Later termed *Moore's Law*, this prediction prophesied that transistors and related components of integrated circuits would continue to get smaller with time. The scaling of integrated circuits has the benefit of increasing transistor packing density, increasing device speed, and reducing power dissipation [12]. However, challenges arise with the scaling of integrated circuits. As the length of the semiconducting channel in a transistor shrinks, its thickness must also shrink to maintain electrostatic control by the gate. Thinning of semiconducting channels in field effect transistors (FETs) allows for superior gate control of the channel and a reduction of short-channel effects [5, 13]. 2D materials show promise for the continued scaling of transistors beyond 3D semiconductors as they represent the atomic limit of material thinning. When 3D materials are thinned, defects associated with the semiconductor/gate dielectric interface begin to dominate the properties of the channel resulting in a decrease in carrier mobility. Due to the self-passivating nature and absence of dangling surface bonds in 2D materials, they can be thinned down to monolayer thicknesses without degradation of their electronic properties. Challenges also exist in the scaling of 3D metallic interconnects which experience a large increase in resistivity due to diffuse surface scattering of charge carriers as a result of atomic scale surface roughness [14]. 2D materials do not suffer from this increase in resistivity due to their atomically smooth surfaces. For these reasons, 2D materials are of interest for numerous integrated circuit components in ultra-scaled devices.

Beyond the advantages 2D materials have in scaled devices, these materials also facilitate new device designs that decrease the energy requirement for computing such as the TFET and spintronic devices [15-21]. For example, the TFET operates on the concept of band-to-band tunneling (BTBT) which requires precise band alignment across a heterointerface [15-17]. Interfacial defects associated with 3D heterostructures can limit the performance of TFETs. In contrast, the atomically sharp interface across the van der Waals gap of adjacent 2D materials, even in the presence of a large degree of lattice mismatch, are an ideal platform to engineer BTBT [15, 17]. 2D materials have also been considered for numerous applications in energy harvesting technologies. A particularly large focus has been in the area of wearable/flexible electronics due to the high fracture strain tolerances of 2D materials which are on the order of 10% [22-24].

1.2.1. Transition Metal Dichalcogenides (TMDCs)

Graphene is the most heavily researched 2D material. However, graphene is intrinsically limited in the roles it can serve in electronic devices due to its lack of a band gap. This fundamental limitation has motivated the study of additional 2D material systems. One of the more extensively studied 2D systems is the family of TMDCs [25-29]. TMDCs are written as MCh_2 where M represents a transition metal and Ch represents a chalcogen (S, Se, or Te). TMDC monolayers are three atoms thick and consist of a layer of transition metal atoms sandwiched between layers of chalcogen atoms; these *Ch-M-Ch* stacks are depicted in *Figure 1.3*. A large focus of TMDC research has been on semiconductors with band gaps similar to Si; two examples of which are MoS_2 and WSe_2. Other TMDCs, such as $NbSe_2$, are metallic and exhibit superconductivity and charge density wave states at low temperatures. TMDCs can be alloyed to further tune their electronic properties, giving this material class a large range of flexibility in electronic character.

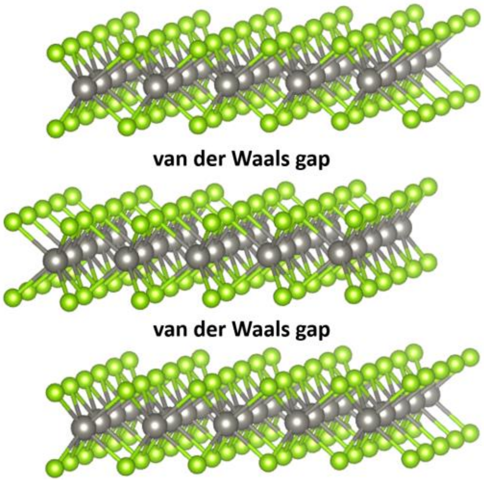

Figure 1.3: Ball-and-stick model of TMDC structure (2H polytype). Green spheres represent chalcogen atoms and grey spheres represent transition metal atoms. Model in figure was created using Vesta [30].

1.2.2. Layered Sesquichalcogenides and Topological Insulators

The layered V-VI sesquichalcogenides, such as Bi_2Se_3 and Bi_2Te_3, have historically been of interest to both the research and commercial sectors due to their thermoelectric performance [31-33]. More recently, a subset of the sesquichalcogenides have been identified as topological insulators (TIs) which has caused them to garner a lot of recent theoretical and experimental attention [34]. The 2016 Nobel Prize in physics was awarded "for theoretical discoveries of topological phase transitions and topological phases of matter," which has only brought a greater focus to these materials. TIs are materials that possess a bulk band gap, typically on the order of a few hundred meV, and topologically protected boundary (surface or edge) states (*Figure 1.4a*). These boundary states exhibit spin-momentum locking and are thus immune to backscattering from non-magnetic impurities [35]. This resistance to scattering results from the fact that in order for an electron to scatter 180° to its initial direction, its spin must also flip, which is forbidden in the absence of a magnetic field [35]. The structure of these materials is slightly more complex than the TMDCs previously discussed. In the case of the sesquichalcogenides, a *monolayer* of the material is five atoms thick and is referred to as a quintuple layer (QL); the structure is a *Ch-M-Ch-M-Ch* stack and is depicted in *Figure 1.4b*.

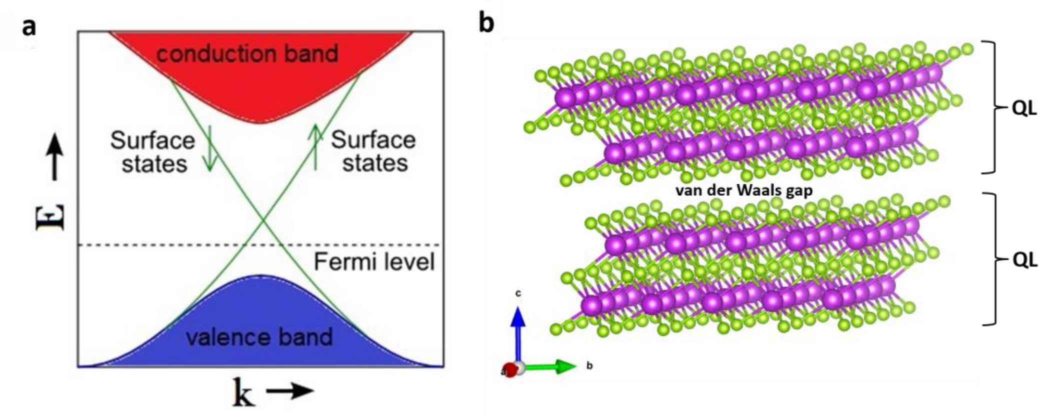

Figure 1.4: a) Cartoon representing the band structure of Bi_2Se_3. Cartoon used with permission of © IOP Publishing, from M. Autore et al., Terahertz plasmonic excitations in Bi_2Se_3 topological insulator, Journal of Physics: Condensed Matter, vol. 29, no. 18, p. 183002, 2023; permission conveyed through Copyright Clearance Center, Inc. [36]. b) Ball and stick model of Bi_2Se_3 with Bi and Se atoms depicted in purple and green, respectively. Model created in VESTA [30].

1.3.Synthesis of 2D Materials

The growth of bulk 2D van der Waals compounds has been an established technique since the 1950’s [33]. However, to make working devices from bulk crystals requires layers to be removed and isolated, which is a low yield process and not commercially scalable. This has driven an effort to develop routes of wafer scale, thin film synthesis of 2D compounds. This challenge has proven to be one barrier towards the realization of large-scale device fabrication based on 2D materials. Some major steps towards this goal have been achieved over the previous two decades. Chemical vapor deposition (CVD) techniques are now routinely used to synthesize large area TMDC thin films [37-40]. The metal-organic chemical vapor deposition (MOCVD) method has shown promise for device-ready, large area WSe_2 thin films showing highly uniform growth and field effect transistor performance on a scale of 1 cm^2 [41, 42]. However, both CVD and MOCVD typically utilize growth conditions beyond the thermal budgets required for back end of line (BEOL) integration. Molecular beam epitaxy (MBE) shows promise for the scalable synthesis of TMDCs and sesquichalcogenide compounds at temperatures compatible with BEOL integration [26, 43-46]. The ultra-high vacuum (UHV) environment inherent to the MBE technique helps limit contamination in the grown thin films and facilitates heterostructure synthesis with atomically clean and abrupt interfaces. The UHV environment also permits in-situ studies of grown 2D compounds using techniques such as x-ray photoelectron spectroscopy, angle resolved photoemission spectroscopy, and scanning tunneling microscopy/spectroscopy. These reasons make MBE a useful growth technique for both the scientific and industrial sectors.

Though significant progress has been made in the MBE synthesis of 2D compounds, challenges remain which prohibit the industrial application of this technique. The lower growth temperatures common to MBE, compared to typical growth conditions for other deposition methods such as CVD and MOCVD, result in high nucleation densities, poor adatom migration, and difficulties in promoting layer-by-layer growth. While the resultant characteristics can be beneficial or detrimental depending on the intended application, efforts to improve control of these growth characteristics are necessary to increase the range of potential applications for these materials [47-49]. Thin film V-VI sesquichalcogenides such as Bi_2Se_3 and Bi_2Te_3 are intrinsically doped materials due to native defects such as chalcogen vacancies and anti-site defects [50-53]. Though successful counter-doping measures have been shown effective in bulk samples, the successful doping of thin film materials remains a significant challenge [54].

1.4. Dissertation Overview

This thesis investigates the *processing-structure-properties* relationships at play in the growth of 2D compounds by MBE. We start with an introduction to the experimental methods and techniques used to carry out investigations of the various 2D compounds. The first experimental chapter reports on investigations into the growth of semiconducting WSe_2. The W-Se system only contains a single known equilibrium phase, i.e., WSe_2, which makes it an ideal system to study the fundamentals of thin film growth. In this chapter, we investigate how processing parameters such as growth temperature and elemental/molecular flux ratio affect the morphology and chemistry of the synthesized WSe_2 films. The second experimental chapter focuses on the growth of metallic $NbSe_2$. Though the structure of $NbSe_2$ is isomorphic to WSe_2, the Nb-Se system is more complex, hosting numerous stable equilibrium compounds. We investigate how the flux ratio used during growth affects the stoichiometry and electrical conductivity of the grown thin films. In the final experimental chapter, we investigate Sn counter-doping of Bi_2Se_3 in an effort to move the Fermi level into the bulk band gap facilitating its use in spin-logic devices.

2. Experimental Methods

2.1.Synthesis Methods

2.1.1. Molecular Beam Epitaxy

Molecular beam epitaxy (MBE) is a thin film growth technique in which a surface (substrate) is supplied with constituent species by atomic or molecular beams [55]. *Figure 2.1* is a diagram of a generic MBE system. Molecular beams are generated by heated solid source materials directed at the substrate. The substrate is held at an elevated temperature to provide adsorbed species with sufficient thermal energy to migrate across the substrate to preferred lattice sites. The deposition of a thin film is the result of this continued process of adsorption and surface diffusion. The MBE method was originally developed studying the semiconductor GaAs and has since become a routine method for the synthesis of many 3D elemental and compound semiconductors [55]. The word epitaxy is derived from the Greek roots *epi* meaning “upon” or “above” and *taxis* meaning “arrangement” or “an ordered manner.” In the context of crystal growth, epitaxy refers to the growth of a material whose order or arrangement is dictated by the substrate. Due to the van der Waals nature of the 2D systems, the growth of these materials proceeds differently than 3D systems. For this reason, the next few sections will be dedicated to discussing these differences and defining relevant terminology.

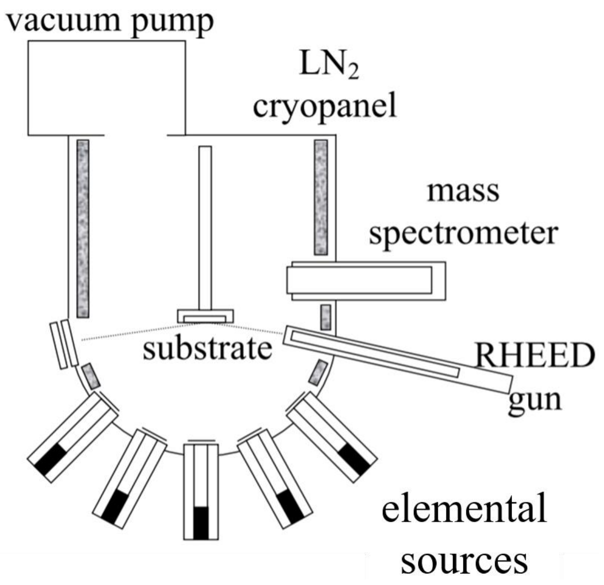

Figure 2.1: Diagram of a generic MBE system. Image adapted from Savchuk et al. [56].

2.1.1.1. Traditional Epitaxy

Traditional epitaxy refers to the epitaxial growth of 3D materials on a 3D substrate. In traditional epitaxy, the grown epilayer will adopt the interatomic spacing of the substrate in the monolayer limit. If the epilayer and substrate are not latticed matched, i.e., they do not intrinsically possess the same lattice constants, the epilayer will be strained, this is referred to as pseudomorphic growth. This strain is a consequence of the primary bonding which takes place between the epilayer and substrate. As the epilayer growths thicker, the increased strain energy will be released through the generation of defects such as misfit dislocations [55]. These defects originating from lattice mismatch can have detrimental effects on the performance of devices produced from these heterostructures. Thus, lattice matching is often a constraint when engineering material systems for a specific application. Methods to reduce interfacial strain in 3D heterostructures exist, such as the use of buffer layers with intermediate lattice constants.

2.1.1.2. Van Der Waals Epitaxy (VDWE)

VDWE refers to the growth of a 2D material on a van der Waals surface; this surface can be either a 2D material or a sufficiently passivated 3D crystal. Due to the van der Waals interlayer bonding of 2D systems, no primary bonds form between the substrate and epilayer. Thus, even in the monolayer limit, the lattice constant of 2D materials grown by VDWE are dictated by in-plane primary bonds of the epilayer and not by the substrate. For this reason, the lattice matching constraint of traditional epitaxy is highly relaxed in VDWE [57]. The differences between traditional epitaxy and VDWE are highlighted in *Figure 2.2*.

Despite the lack of primary bonds between the substrate and epilayer, substrate-epilayer interactions often dictate the rotational alignment of the epilayer [58, 59]. This *rotational order* communicated to the growing 2D material by the substrate fits the previously mentioned definition of epitaxy. The first demonstration of VDWE was reported in 1984 by Atsushi Koma et al. where monolayer 2H-$NbSe_2$ was synthesized on the basal plane of cleaved 2H-MoS_2 [57]. Reflection high-energy electron diffraction (RHEED) was used to show that the $NbSe_2$ monolayer grew with a lattice constant indistinguishable from bulk $NbSe_2$ despite being only ~0.6 nm thick and possessing a ~10% lattice mismatch with MoS_2. VDWE has proven to be a versatile technique which can be used in conjunction with 3D systems. In the previously described example, the substrate (MoS_2) and epilayer ($NbSe_2$) were both 2D crystals; however, passivating the surface dangling bonds of 3D crystals opens the door to integrating 2D materials into traditional 3D structures through VDWE. For example, high-quality 2D $MoSe_2$ has been grown on F-terminated CaF_2, S- and Se-terminated GaAs (111), and GaSe-terminated Si (111) [60-63]. In these reports, high-quality $MoSe_2$ films were confirmed by streaky RHEED patterns on each surface post growth providing evidence for crystalline $MoSe_2$ epitaxially aligned to the substrate.

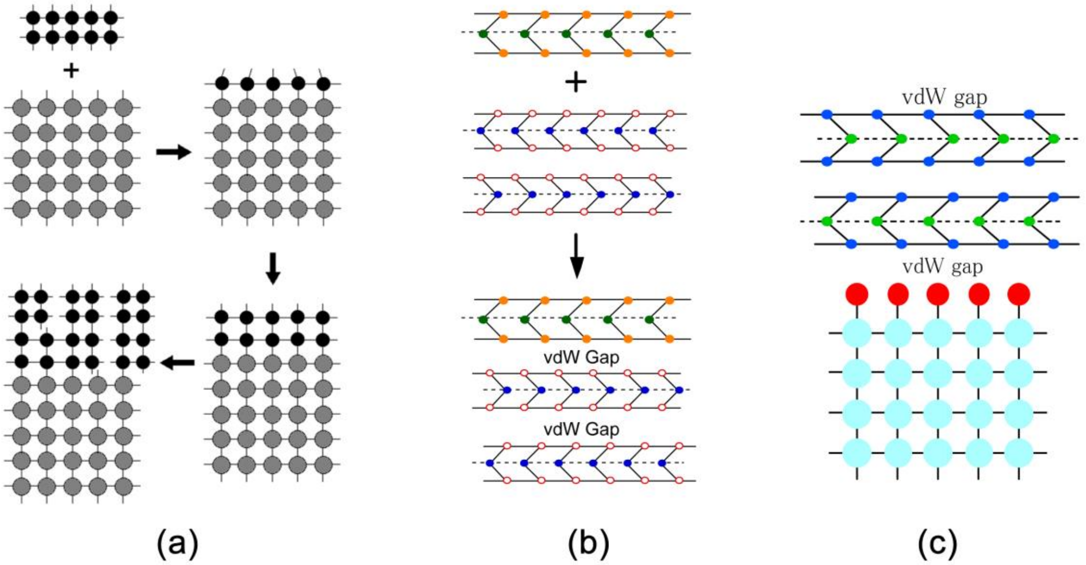

Figure 2.2: Cartoons representing a) heteroepitaxy of 3D crystals showing lattice mismatch and associated misfit dislocations, b) VDWE of 2D materials, and c) VDWE of 2D material on passivated 3D crystal. Image adopted from K. Ueno [64].

2.1.1.3. Physical Vapor Deposition (PVD)

In some instances, the in-plane orientation of grown 2D materials will not be dictated by the substrate which is sometimes referred to as PVD or molecular beam deposition. This is true for the growth of WS_2, WSe_2, and $NbSe_2$ on amorphous SiO_2 presented in this document. In these cases, the lack of in-plane rotational alignment is a consequence of a lack of in-plane order in the substrate. Despite this lack of in-plane rotational alignment in the grown 2D materials on SiO_2, the TMDCs still grow with a uniform c-axis orientation normal to the substrate surface [65]. In this way, the growth of TMDCs still fits the definition of epitaxy as a *degree of order* in the grown material exists, albeit to a lesser extent in PVD than traditional epitaxy or VDWE of 2D materials. For simplicity's sake, the term MBE in this work will be used to describe all three growth mechanisms (traditional epitaxy, VDWE, and PVD).

2.1.1.4. MBE Experimental Details

MBE is carried out under UHV conditions which has multiple benefits. First, the UHV environment provides an ultra-clean environment which minimizes the incorporation of contaminants into the grown thin film. Second, the UHV environment provides a nearly unobstructed path for molecular beams directed at the substrate surface. Each elemental source is equipped with a shutter allowing for the produced molecular beams to be effectively shut off over short time windows (~1 second). The MBE tool used in this work can be seen in *Figure 2.3* and is equipped with two Focus EFM-4 evaporators for the deposition of transition metals and two standard effusion cells for the deposition of chalcogens [66]. The substrate can be heated from room temperature up to 1130 K. Growth rates demonstrated for TMDCs on this system range from ~0.1 to 4 nm/hour and are controlled by the elemental fluxes and substrate temperature used during material synthesis. To generate stable fluxes of the transition metals used in this work (e.g., W, Mo, and Nb), the EFM-4 evaporators are typically operated in constant power mode (emission current × accelerating voltage). An integrated flux monitor on each source allows the elemental fluxes to be monitored in real time. During extended periods of metal deposition, the elemental rod’s position can be adjusted to compensate for the shortening of source material over time. The standard effusion cells are operated via a PID controller and are maintained at a constant temperature during growth. The temperature ramp rate for the standard effusion cells is typically set to 10 °C/min. Once the cell is at the set temperature, it takes ~1 hour to achieve a constant elemental/molecular flux. The elemental fluxes and effect on chamber background pressure are monitored using a beam flux monitor (BFM) and residual gas analyzer (RGA). The BFM is a movable ion gauge that can be placed in the path of the elemental/molecular beams generated by either style of evaporator to measure a beam equivalence pressure (BEP); the BEP is proportional to the atomic/molecular flux of a given source. The BFM is routinely used to measure BEPs of the elemental/molecular sources prior to (and typically upon conclusion) of sample growth. We report BEPs in this work, opposed to atomic fluxes (represented in number of atoms/area/time), to keep consistent with relevant literature. However, the measured BEPs can be theoretically or experimentally calibrated to atomic fluxes; this is discussed in *section 7.4*. The RGA is a 200 AMU model mass spectrometer from Stanford Research Systems (SRS) and used to monitor the background pressure of specific elemental and molecular species in the UHV chamber. The RGA is particularly useful in monitoring the chalcogen sources during material synthesis as the standard effusion cells are not equipped with integrated flux monitors but contribute significantly to the background pressure of the UHV system. The system is equipped with a liquid nitrogen shroud to lower the background pressure during TMDC synthesis. An integrated RHEED system allows for real-time characterization of synthesized films and is used to estimate growth rates and identify material growth modes (see *section 2.2.5*).

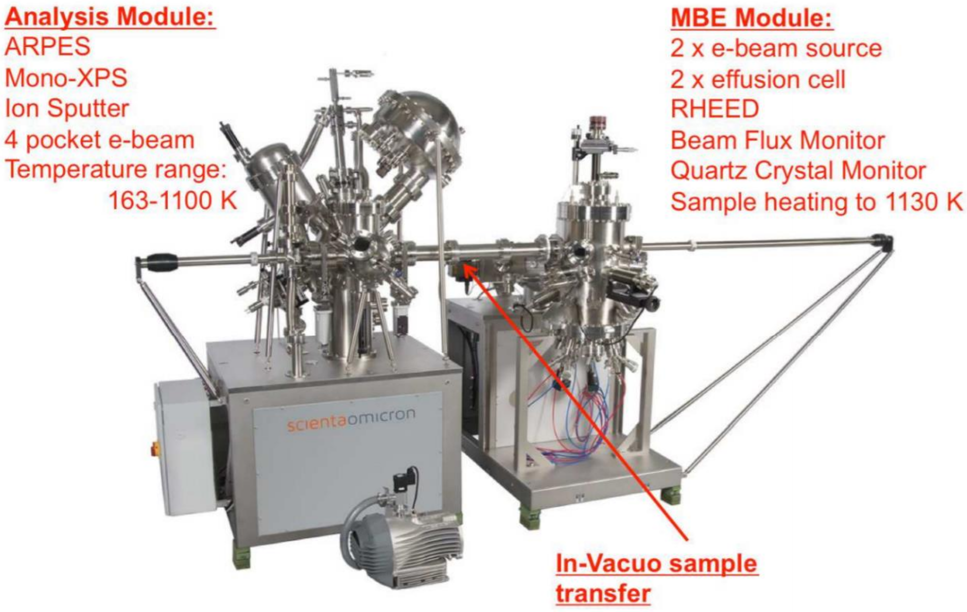

Figure 2.3: ARPES-MBE UHV system from Scienta Omicron [66].

2.2. Characterization Methods

2.2.1. Photoelectron Spectroscopy

2.2.1.1. Photoemission Physics

Photoelectron spectroscopy (PES) describes any technique in which the kinetic energies of photoelectrons are measured. Photoelectrons are electrons emitted from a material upon adsorption of a photon. All PES techniques are a direct example of the photoelectric effect originally observed by Hertz and later explained by Einstein [67, 68]. The kinetic energy of electrons after being removed from a material's surface can be described by the following equation:

$$E_{K(true)} = h\nu - (E_B + \varphi_s).$$

In this equation, $E_{K(true)}$ represents the kinetic energy of the ejected photoelectron, E_B is the binding energy of the ejected photoelectron, φ_s is the work function of the sample, and $h\nu$ represents the product of Plank's constant and photon frequency (this product is equal to the energy of the photon). The binding energy of an electron is defined as the energetic difference between the initial and final states of the atom involved in the photoemission process. The work function is the energy difference between the Fermi level of the sample and the vacuum level. During PES data acquisition the sample is grounded and in contact with the electron energy analyzer, thus the measured kinetic energies of photoelectrons are affected by the difference in work function between the sample and analyzer. Ultimately, the kinetic energy equation for measured electrons can be calculated with the following equation:

$$E_{K(measured)} = h\nu - (E_B + \varphi_{sp}).$$

$E_{K(measured)}$ is the measured kinetic energy of the ejected photoelectron, and φ_{sp} is the work function of the spectrometer. This is significant from an experimental point of view because it allows for the determination of spectral feature positions relative to a material's Fermi level and thus also allows for the determination of a material's work function. The described relationships can be seen in *Figure 2.4*.

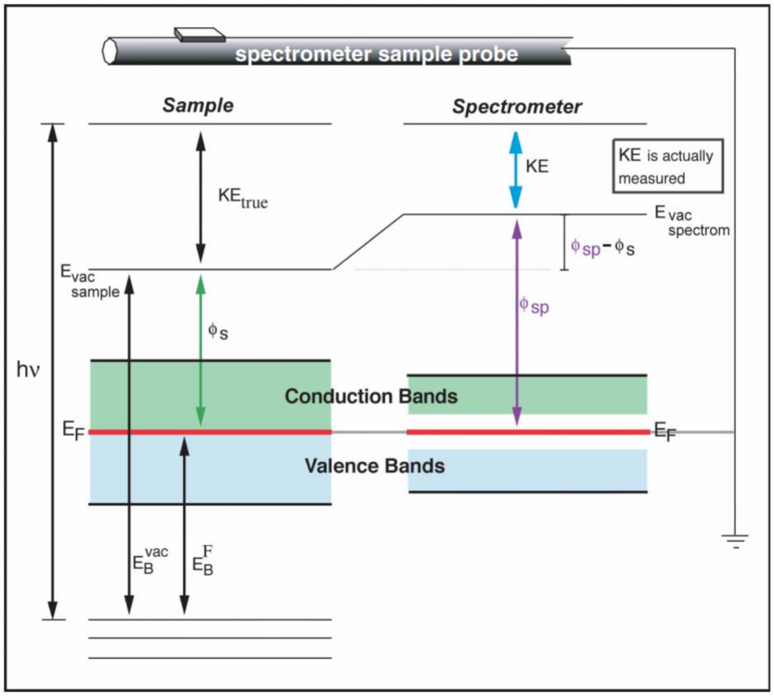

Figure 2.4: Energy band diagram for a sample in electric contact with the spectrometer. Figure reused with permission from Copyright © 2009, John Wiley and Sons [69].

Fundamentally, the binding energy is the difference in energy between the final (E_f (n-1)) and initial (E_i (n)) states of the atom involved in the photoemission process:

$$E_B = E_f\,(n-1) - E_i\,(n).$$

E_i (n) is the energy associated with the ground state of the atom and E_f (n-1) is the is the energy associated with the atom after the photoemission process taking into account additional energetic considerations such as relaxation processes, i.e., rearrangement of electrons in response to the creation of a vacant electron energy level. Due to these relaxation processes, the magnitude of E_B is less than the orbital energy.

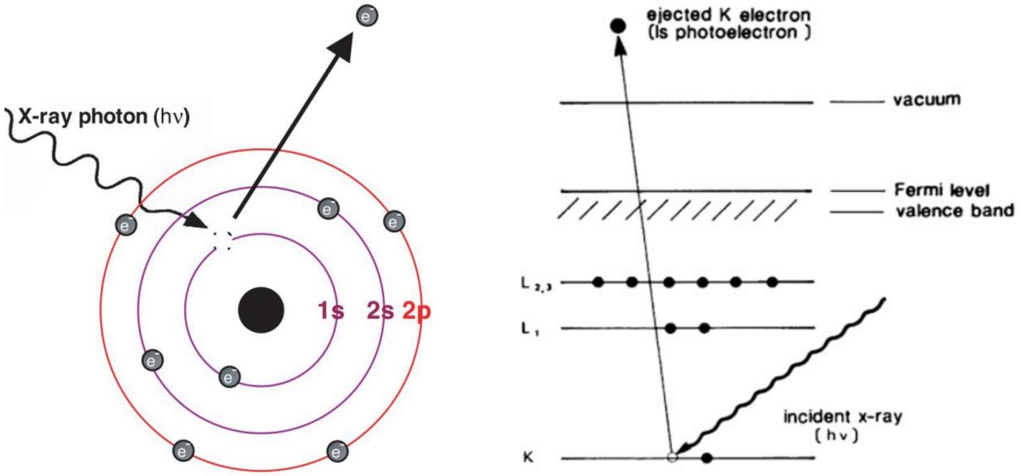

Figure 2.5: Diagrams showing the photoemission process. Left-hand image adapted from Vickerman and Gilmore and reused with permission from Copyright © 2009, John Wiley and Sons [69]. Right-hand image adapted from Watts and reused with permission from Copyright © 1994, John Wiley and Sons [70].

The most commonly employed PES technique in this work is x-ray photoelectron spectroscopy (XPS). XPS is a versatile tool allowing for elemental identification, determination of sample composition, and chemical analysis. Due to its chemical sensitivity, XPS was originally referred to as electron spectroscopy for chemical analysis (ESCA) [71]. Typically, an XPS spectrum is represented in a two-dimensional plot in which intensity (number of electrons detected) vs binding energy is plotted as shown in *Figure 2.6*. The convention is to plot XPS spectra with binding energy in descending order from left to right. This convention comes from the fact that XPS in reality measures the kinetic energy of photoelectrons from which the binding energy is inferred. An XPS spectrum is really a plot of intensity vs kinetic energy in ascending order. However, the binding energy is used in plotting XPS data as it is characteristic of a given core level while the kinetic energy of the measured electron is dependent on the photon energy used. *Figure 2.6* is a low-resolution survey spectrum of Au deposited on MoS_2. Each element has a unique set of core level binding energies associated with the elements electronic structure which allows XPS to be used as a “fingerprint” elemental analysis technique. In addition to Au, Mo, and S in the spectrum below, O 1s and C 1s signals are also detected and are a result of atmospheric contaminates on the surface.

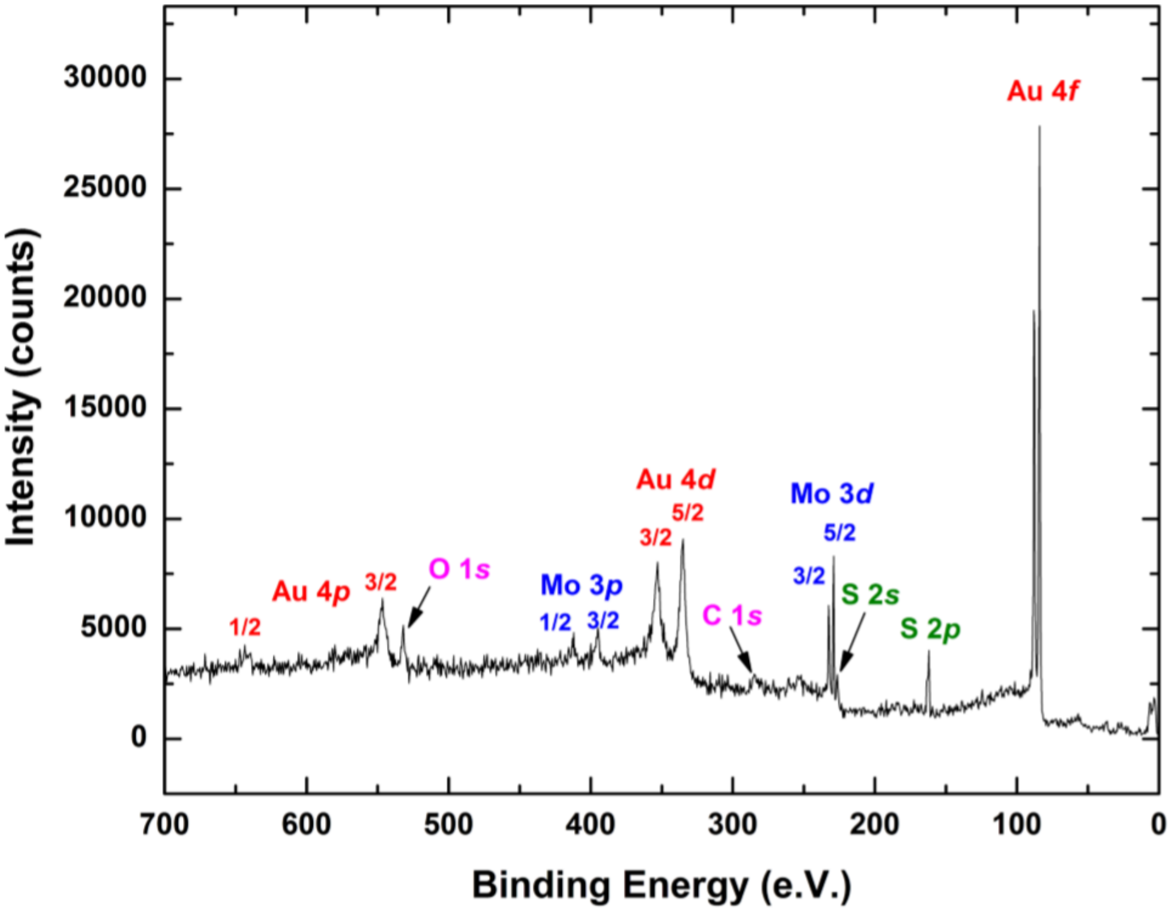

Figure 2.6: XPS survey spectrum of Au deposited on MoS_2. Figure courtesy of K. Freedy.

When an atom is bonded to another element, a redistribution of charge will occur due to the formation of chemical bonds. This will have effects on both E_f (n-1) and E_i (n); however, this will typically have a larger effect on E_i (n) than on E_f (n-1) [69]. When this occurs, E_B associated with a given core level will alter due to the change in the chemical environment of the atom; this is called a chemical shift. *Figure 2.7* shows high-resolution spectra of the Se 3*d* core level. These spectra are of elemental Se and Se in Bi_2Se_3. A chemical shift of ~1.8 eV allows for the two chemical environments of Se to be distinguished.

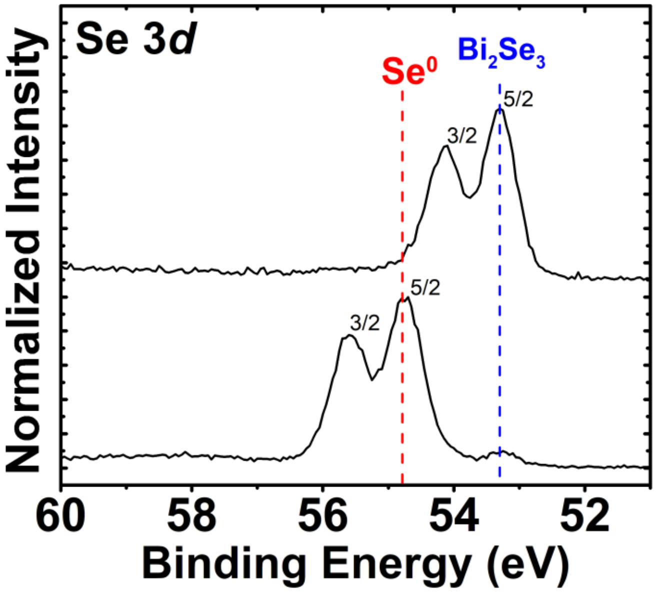

Figure 2.7: The XPS spectra of the Se 3*d* core level in Se^0 and Bi_2Se_3 demonstrating a chemical shift between Se in the two different environments.

The degree of a chemical shift is often related to the degree of the charge transfer between bonded atoms; that is, chemical shifts typically scale with the oxidation state of an atom. However, this correlation doesn't always hold true due to final state effects. Other phenomena can also have effects on the measured E_B of a given core level. One example is the presence of a charge density wave (CDW) in which periodic changes in electron densities throughout a material will results in apparent chemical shifts despite no change in chemistry. CDWs are low temperature states which occur in some group VB TMDCs and can be confused with changes in chemistry.

The two peaks in each Se 3*d* spectra in *Figure 2.7* arise from spin-orbit coupling (SOC). SOC occurs due to the interaction of an electron's spin, *s*, with its orbital angular momentum, *l*. The result of this interaction is that the total angular momentum, *j*, associated with an electron is the sum of these two components, i.e., $j = |l + s|$. Electrons, being fermions, will carry ± ½ spin while *l* will have the values of 0, 1, 2, or 3 for *s*, *p*, *d*, and *f* orbitals, respectively. Since no angular momentum is associated with *s*-orbitals, no SOC is observed. In the above example of the Se 3*d* core level, *j* will take values of 5/2 and 3/2. The 3/2 peak corresponds with electrons of lower (more negative) orbital energy and is therefore seen as the feature with the higher binding energy. The intensity ratio of the Se $3d_{5/2}$ to the Se $3d_{3/2}$ peaks approximate 3:2. This ratio is due to the relative degeneracy among the two energy levels ($2j + 1$); 6 for $J = 5/2$ and 4 for $J = 3/2$ which have a relative ratio of 3:2 [69]. *P*-orbitals will have SOC intensity ratios of ~2:1 and *f*-orbitals will have intensity ratios of ~4:3 for the same reason.

2.2.1.2. Experimental Set Up for Lab-Based PES

The experimental set up of a lab-based XPS system can be seen in *Figure 2.8* [69]. XPS uses x-rays generated in UHV as an excitation source and are generated by the bombardment of a metal anode (Al for the system used in this work) with high energy electrons (15 keV). This process produces a spectrum of x-rays characteristic of Al. Al kα x-rays ($hv = 1486.7\ eV$) are isolated with the use of a monochromator. The sample to be analyzed is placed in the path of the monochromated x-ray beam. Photoelectrons ejected from the sample are collected by an electronic lens system before entering the hemispherical analyzer which separates electrons based on kinetic energy. Pass energies (E_p) of 50 and 100 eV are used for core level and survey XPS spectral acquisitions in this work, respectively. The x-ray spot size on the sample is ~1 mm^2. The XPS system is calibrated using the Au $4f_{7/2}$ peak and its known binding energy of 83.94 eV [72]. The majority of the presented XPS data was collected utilizing a Scienta Omicron XM1200 x-ray source and a Scienta Omicron R3000 hemispherical analyzer paired with a 2D low noise digital charge-coupled device microchannel plate (CCD-MCP) detector; this tool is paired to the MBE module previously discussed in *section 2.1.1.4* through an in-vacuo sample transfer tube allowing for in-situ characterization of MBE grown TMDCs. A Phi 5000 VersaProbe III tool at the Army Research Laboratory in Adelphi, MD was also used for ex-situ characterization.

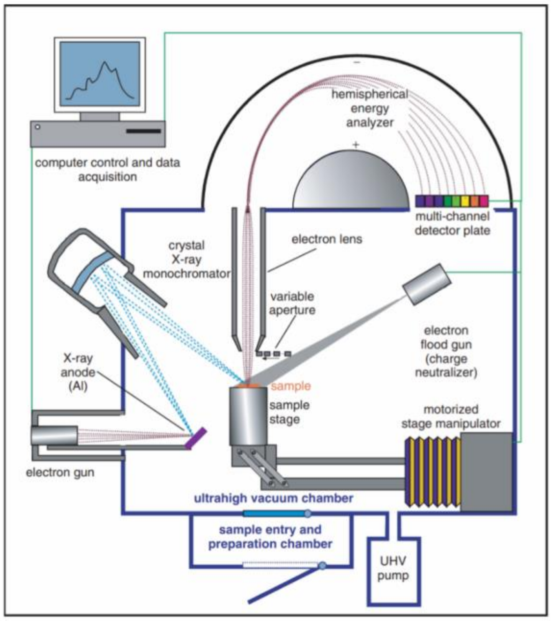

Figure 2.8: Diagram detailing major components of a typical lab-based XPS system. Figure reused with permission from Copyright © 2009, John Wiley and Sons [69].

Lab-based PES techniques are highly surface sensitive due to the small inelastic mean free path of electrons in solids. PES data collected is largely sampled from the top ~10 nm of the sample surface with the detected signal decaying exponentially as a function of depth in the sample. The surface sensitivity of any PES technique is dependent on the energy of the photoelectron, the material the photoelectron is traveling through, and the geometry of the experimental setup. The attenuation of an electron source due to inelastic scattering can be described using Beer's law as follows:

$$I_k = I_0 e^{(-d/\lambda\cos\Theta)}.$$

In this equation I_k is the measured photoelectron intensity, I_0 is the intensity of the photoelectron source, d is the thickness of the attenuating material, λ is the inelastic mean free path (IMFP) of photoelectrons in the attenuating layer, and Θ is the angle of the detector relative to the sample normal. The IMFP of electrons is based on several factors including electron energy and overlayer material with atomic number and density being critical factors. This equation can be used to calculate the thickness of a thin film on a substrate if the intensity of the bare substrate is known. Alternatively, if the intensity of an infinitely thick film is known, the thickness of an overlayer can also be determined by the following equation:

$$I_{ko} = I_{\infty o}[1-e^{(-d/\lambda\cos\Theta)}].$$

This modified equation uses intensities of the overlayer (opposed to substrate) to calculate film thickness; I_{ko} and $I_{\infty o}$ represents the intensities of a thin film and infinitely thick film, respectively.

XPS spectra in this work are analyzed with the software kolXPD and OriginPro. KolXPD is used for spectral deconvolution of core level spectra. Core-level spectra are often fitted with Voigt line shapes, allowing for independent control of the Lorentzian and Gaussian widths, and a Shirley background is used. In some cases, Doniach-Sunjic line shapes are used to more accurately represent the core-level spectra of metallic materials [73].

Ultraviolet photoelectron spectroscopy (UPS) and angle-resolved photoelectron spectroscopy (ARPES) share many underlying principles with XPS. Lab-based UPS/ARPES systems typically use ultraviolet light produced by a cold cathode capillary discharge lamp as an excitation source. The photon source used for UPS/ARPES in this work is a Focus HIS14 HD VUV (vacuum ultraviolet) source. The source typically uses He gas allowing for photon energies of 21.22 (He Iα) and 40.81 eV (He IIα), associated with the resonant lines of neutral and singly ionized He atoms, to be accessed. The ratio of He Iα and He IIα emission can be controlled by adjusting the source operating discharge current and gas pressure. The UV spot size focused on the sample is ~300 microns across but varies slightly with photon energy. A three-stage differential pumping system is utilized to retain UHV pressure during data acquisition. The low energy excitation source means most core levels are not accessible using this technique. UPS and ARPES are primarily used to study the valence band spectra of materials; though not utilized in this thesis, UPS is also used to measure the work function of a surface through analysis of the secondary electron cutoff. UPS spectra are represented, similarly to XPS data, in a two-dimensional plot in which intensity (number of electrons detected) vs binding energy are plotted. ARPES also measures valence band spectra of materials, but adds an emission angle dependence, allowing for mapping of the electronic structure of materials in a 3-dimensional plot. For ARPES data collection the energy analyzer operates in an angular mode with a 20° acceptance angle of emission. E_p of 2 and 5 eV are used for He Iα and He IIα emission lines, respectively. For UPS/ARPES, the system is calibrated using the Fermi edge of a clean metal (pure Ag or Ni). ARPES data is plotted and analyzed using Igor Pro software. Additional UPS/ARPES measurements were carried out in the Taylor Laboratory at the Army Research Laboratory in Adelphi, MD. This second UPS/ARPES system utilizes a Scienta Omicron VUV5000 monochromated UV source, which produces UV photons from a He plasma generated with the electron cyclotron resonance technique, and a Scienta Omicron DA30-L hemispherical analyzer.

ARPES allows for the electronic structure of crystalline materials to be observed by measuring the intensity of photoelectrons as a function of both kinetic energy and angle of emission relative to the sample surface, θ. To a good approximation, the in-plane (parallel to surface) crystal momentum of electrons in a solid, $p_{||}$, will be retained through the photoemission process and therefore characterize the photoelectron emitted into vacuum (*see Figure 2.9b*); this approximation is valid in part due to the negligible momentum transferred to the photoelectron by the UV-photon [74]. Because the in-plane momentum of electrons in a solid is conserved through the photoemission process, the crystal momentum will impact the emission angle of photoelectron leaving the sample surface. Measuring the angular dependence of the photoelectrons emitted from a solid thus provides information regarding the crystal momentum of the electron in the solid. ARPES measurements are typically represented as plots of intensity vs energy and wave vector, k. The wave vector and momentum of an emitted photoelectron are related by Plank's constant, $\hbar$:

$$p_{\parallel} = \hbar k_{\parallel}.$$

The angular deflection of the photoelectrons is a function of the electron kinetic energy and in-plane wave vector, $k_{||}$, and can mathematically be described with the following equation:

$$k_{\parallel} = \sqrt{\frac{2mE_k}{\hbar^2}} sin\theta.$$

While $k_{||}$, will be conserved during the photoemission process, the momentum component perpendicular to the surface ($k_{\perp}$) will not be conserved. This is due to the photoelectron passing through the sample surface and needing to overcome the sample work function, a process which alters the momentum of the electron normal to the sample's surface. To measure $k_{\perp}$ it is common to collect data at varying photon energies. This allows the crystal's inner potential to be determined. The inner potential is material specific and describes the effect a photoelectron passing through the materials surface has on $k_{\perp}$. This allows for the three-dimensional band structure of materials to be measured and is typically carried out at synchrotron light sources where continuous changes of the photon energy can be made. However, low-dimensional systems, such as layered TMDCs and other 2D materials, can typically be characterized as having a negligible level of dispersion normal to the basal plane and are therefore fully described by the in-plane dispersion. This type of measurement is facilitated by the lens system of the hemispherical analyzer which focuses electrons entering the hemispherical energy analyzer with their emission angles relative to the sample surface intact (see *Figure 2.9c*). In contrast, the lens mode for XPS and UPS measurements in this work focus photoelectrons entering the hemispherical analyzer as a function of position (termed transmission mode) rather than emission angle.

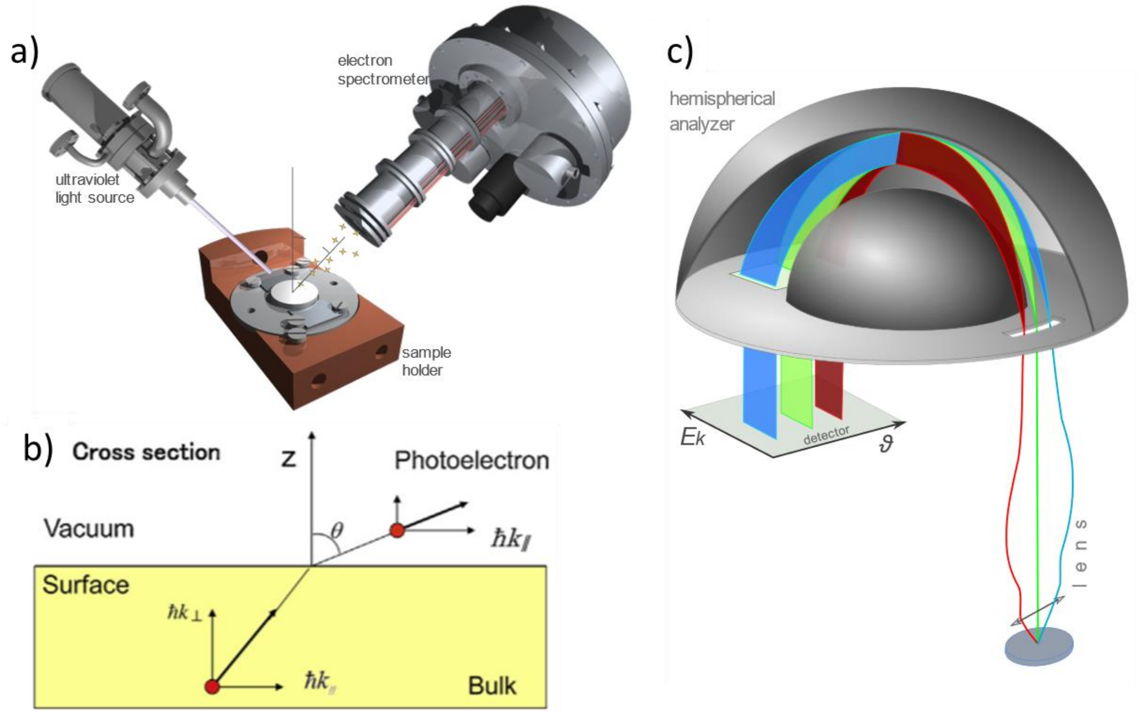

Figure 2.9: a) Diagram depicting a UPS/ARPES experimental set up. b) Figure showing in-plane momentum is conserved through the photoemission process. c) Hemispherical energy analyzer operating in angular mode. Frames *a* and *c* adapted under Creative Commons CC BY-SA 4.0 from Ponor - Own work, https://commons.wikimedia.org/w/index.php?curid=90324755). Frame *b* adapted from Suga and Tusche [75].

2.2.2. X-ray Diffraction

X-ray diffraction (XRD) is a technique used to probe the crystalline structure of materials. X-rays of a known wavelength impinge on a sample and the intensity of x-rays leaving the sample are detected as a function of angle. When x-rays probe a material, there is a probability that they will scatter off atoms, primarily by electrons, in that material. Many of these x-rays will scatter with their energy (or wavelength) unperturbed, a process known as Thompson scattering. The atomic planes in a crystal act as a series of scattering planes for impinging x-rays. At certain angles, the x-rays scattering off atomic planes in a crystal will be in phase with one another; this angle is dependent on the wavelength of the x-rays, λ, and the plane spacing, d. When the scattered x-rays from a series of atomic planes is in phase, the signal will be enhanced due to constructive interference; at most angles, however, there will be significant destructive interference. The relationship describing the geometrical constrains of constructive interference is known as Bragg's Law and is written as:

$$n\lambda = 2d_{hkl}sin\theta,$$

where d_{hkl} is equal to the lattice spacing of *hkl* planes, θ is the angle satisfying the diffraction condition, and n is any integer greater or equal to 1. XRD data is typically plotted as intensity vs 2θ angle. A pictorial representation of Bragg's law can be seen in *Figure 2.10* which shows the line segments mapped out by x-rays scattering off adjacent crystal planes which remain in phase. The x-rays remain in phase at an angle θ relative to the crystal planes because the excess distance traveled is equaled to an integer number of wavelengths ($SQ + QT = n\lambda$).

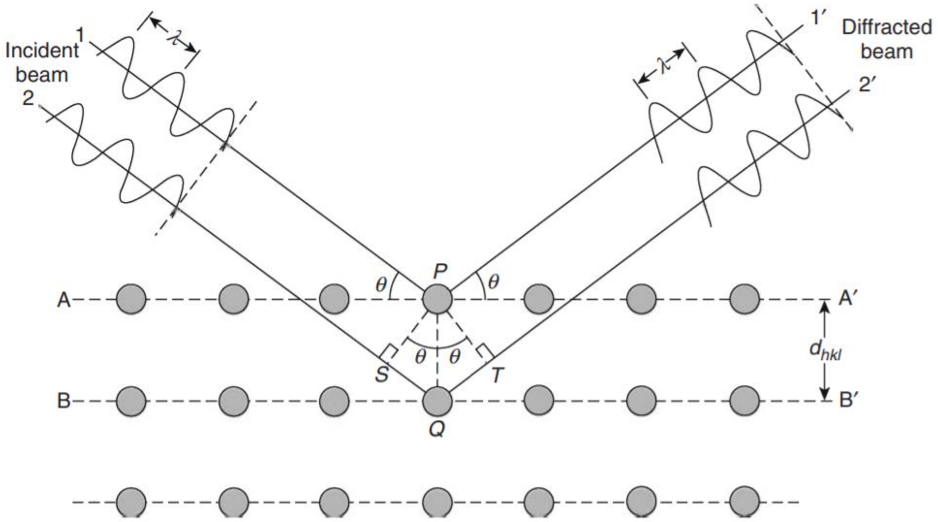

Figure 2.10: Pictorial demonstration of Bragg's Law. The diffracted beams 1' and 2' will be in phase when the line segment SQT is equal to $2d_{hkl}sin\theta$. Figure reused with permission from Copyright © 2013, John Wiley and Sons [76].

The vector bisecting the incident and diffracted x-ray beams is known as the scattering vector. The *hkl* planes probed by an XRD measurement are those normal to the scattering vector which is dictated by the experimental geometry of the XRD measurement. Three experimental XRD geometries can be seen in *Figure 2.11*. The most common XRD geometry used is known as a symmetrical out-of-plane measurement. In a symmetrical out-of-plane measurement, the incident x-rays and x-ray detector are maintained at angles of equal magnitude relative to the sample surface. A consequence of this geometry is that the scattering vector of measured x-rays is fixed normal to the sample surface through the entire measurement and thus only *hkl* planes parallel to the sample surface will be detected. This is the typical geometry for powder XRD. The layered structure of deposited TMDC thin films, which typically grow with their c-axis directed normal to the substrate surface, allow symmetrical out-of-plane XRD measurements to probe the *00l* planes. This geometry is used in this work for probing the *00l* family of planes in TMDCs deposited by MBE.

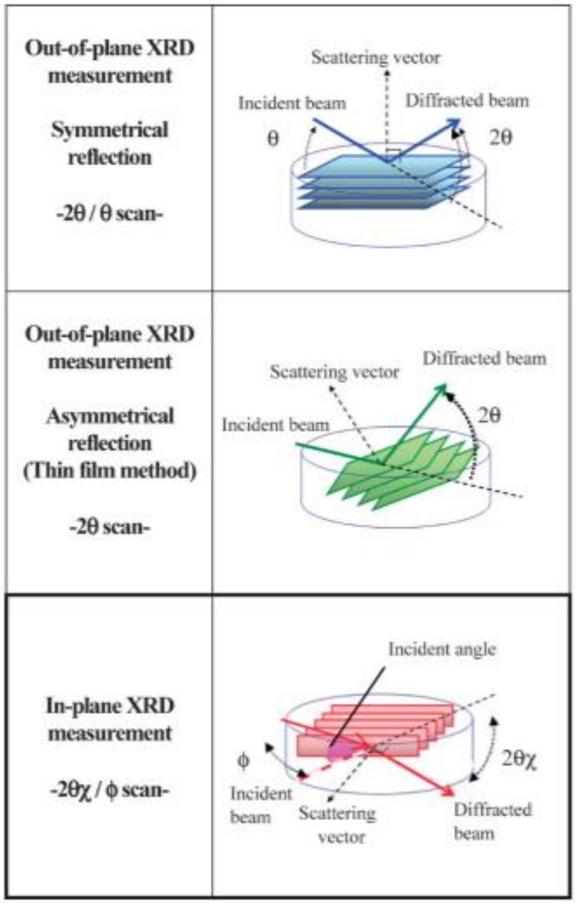

Figure 2.11: The three XRD geometries used for this work. Image adapted from S. Kobayashi [77].

Two additional XRD geometries are often used to study thin film materials and are discussed below. The first of these is an asymmetrical out-of-plane measurement, also referred to as grazing incidence XRD (GIXRD) or thin-film XRD. This geometry fixes the x-ray beam incident on the sample at glancing angle of ~1° and moves the detector with respect to the fixed sample. GIXRD is used to study polycrystalline thin film samples which are too thin for symmetrical out-of-plane XRD measurements, i.e., there are not enough atomic planes parallel to the surface to generate sufficient constructive/destructive interference. The glancing incidence of the incident x-ray beam in GIXRD results in a larger amount of material being probed compared to symmetrical out-of-plane measurements. A final XRD geometry used in this work is in-plane XRD. In this geometry the incident x-ray beam is held at a glancing angle to the substrate (<1°) and the detector is moved around the sample in the plane of the sample surface. This geometry detects diffraction corresponding to a scattering vector in the plane of the sample surface and is therefore able to detect crystal planes with a surface normal rotated 90° with respect to the sample surface's normal. In-plane XRD allows for diffraction patterns to be collected of TMDC thin film samples on the order of monolayer thicknesses [78].

XRD data in this work was collected using two x-ray diffractometers, a SmartLab diffractometer from Rigaku and an Empyrean diffractometer from Malvern-Panalytical, using Cu Kα radiation (1.5406 Å) in a parallel beam configuration. A 2θ range of 10–60° was used for most symmetrical out-of-plane measurements.

2.2.3. X-ray Reflectivity

X-ray reflectivity (XRR) is a non-destructive analysis technique used in this work to measure the thickness of thin film samples; XRR can also be used to quantify the density of thin films and the roughness of interfaces. XRR uses a glancing x-ray beam which probes the sample surface. A percentage of the x-rays will undergo specular reflection from each interface. In the example of a thin film on an arbitrary substrate, x-rays will reflect from the thin film surface (the thin film-air interface) and the thin film-substrate interface (*Figure 2.12a*). These reflected x-ray signals will interfere with one another and thus the measured intensity of the total reflected signal will change with angle of reflection (equal to angle of incidence). This periodic oscillation in measured intensity due to interference between the reflected signals from each interface are referred to as Kiessig fringes [79, 80].

Figure 2.13b shows a typical XRR pattern taken of a thin film material on a substrate which has *normalized intensity* and *2θ* angle plotted along the y- and x-axis, respectively [81]. Each of the labeled features in *Figure 2.12b* provide qualitative information about the thin film. At very small angles of incident relative to the surface (*θ*), none of the x-ray beam will penetrate the sample surface; this is known as total external reflection and can be seen in *Figure 2.12b* as a normalized intensity of ~1 in the low angle regime of the plot. As the angle of incidence increases, x-rays will start to penetrate the surface of the thin film and the normalized intensity drops, the angle at which this happens is known as the critical angle. The critical angle is dependent on the index of refraction which itself is highly dependent on electron density [81]. Therefore, the critical angle can provide information as to the density of the thin film being measured. The angular periodicity of the Kiessig fringes is related to the separation of the scattering interfaces and is used to determine the thin film thickness. Lastly, the roughness of the interfaces can qualitatively be observed from the decay of the measured intensity as a function of *2θ* angle [79]. The decay in average intensity is due to diffuse scattering from the thin film surface. The decay in the amplitude of the observed Kiessig fringes comes as a result of diffuse scattering from the thin film-substrate interface. Quantitative analysis is less straightforward and is accomplished through a least square fitting routine to extract each property's contribution to the total reflected x-ray signal. XRR measurements in this work are performed on a Panalytical Empyrean with Cu Kα radiation. XRR patterns were fit using GSAS-II software [82]. XRR is primarily used in this work to extract the thickness of $NbSe_2$ thin films grown on SiO_2; knowledge of the materials thickness is critical for extracting the material's electrical conductivity.

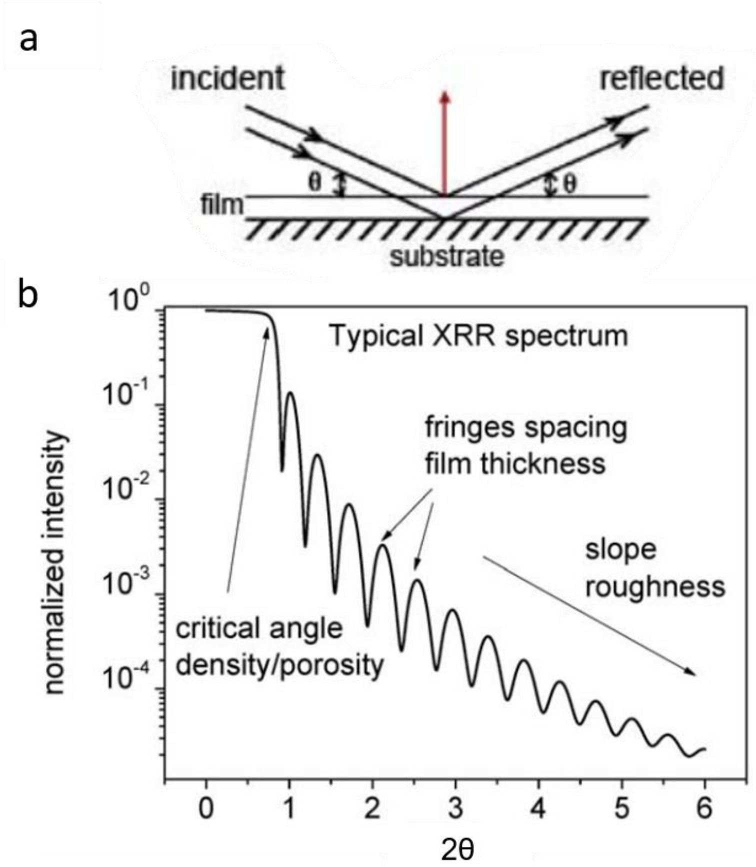

Figure 2.12: a) Cartoon depicting the specular reflection of x-rays from the thin film surface and the thin film-substrate interface. b) Typical XRR spectra highlighting spectral features to the properties they provide information of. Figure adapted from Saw et al. [81].

2.2.4. Low Energy Electron Diffraction

Low energy electron diffraction (LEED) is a UHV surface characterization tool allowing the surface structure of a crystalline surface to be characterized. LEED takes advantage of the wave-like nature of electrons. In fact, experiments by Davisson and Germer in the 1920's, considered to be the first LEED experiments, were the first experimental evidence for the wave-like nature of electrons [83, 84]. If sufficient ordering of a surface exists, elastically scattered electrons will interfere, producing a pattern of varying intensity on a phosphor screen. The electron source and phosphor screen are positioned normal to the sample surface as depicted in *Figure 2.13*.

In contrast to XRD, LEED is highly surface sensitive due to the small IMFP of electrons in solids as previously discussed in the context of XPS. LEED uses electrons of ~100 eV to probe the surface resulting in an IMFP of ~1 nm meaning only the top few atomic layers will be probed LEED is often used to study the epitaxial relationships of thin films deposited on a substrate. LEED is also used to optimize sample orientation for ARPES measurements, which are highly dependent on sample geometry. The LEED system used in this work is a BDL800IR-LMX-ISH by OCI Vacuum Microengineering and is installed on the characterization chamber in the McDonnell Lab.

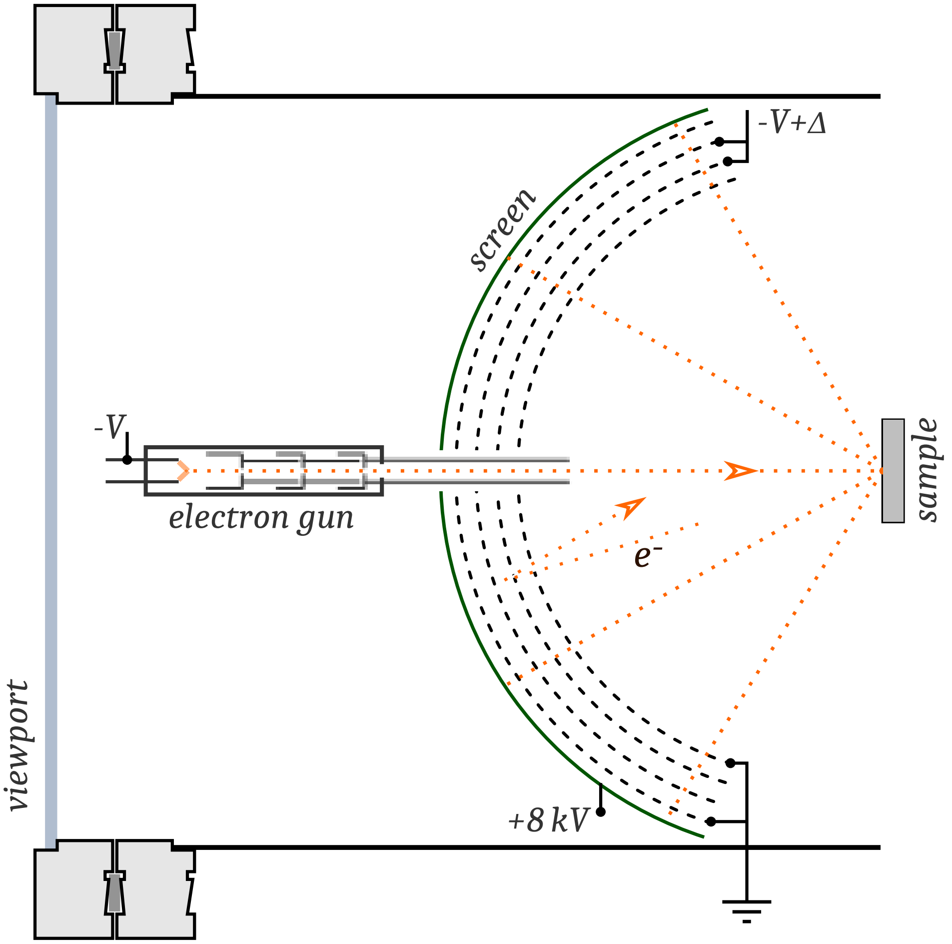

Figure 2.13: Geometry of the LEED system used in the McDonnell Lab. The electron gun and screen are arranged normal to the sample surface. The diffraction pattern cast on the phosphor screen is visible through the viewport. Image from: https://en.wikipedia.org/wiki/Low-energy_electron_diffraction#/media/File:Low-energy_electron_diffraction_(LEED)_instrument_-_schematic_diagram.svg

2.2.5. Refection High-Energy Electron Diffraction

Reflection high-energy electron diffraction (RHEED) is an electron diffraction technique common to MBE systems [55]. It is similar in principle to LEED; however, the geometry of this diffraction technique allows for real-time diffraction analysis to take place during MBE growth as depicted in *Figure 2.14*. LEED systems need to be situated normal to a sample's surface for operation, which would get in the way of systems necessary for MBE growth. RHEED uses a focused beam of high-energy electrons (~10 to 15 keV) which impinge on a substrate or grown thin film at a glancing angle (typically 1-3°). The diffracted beam of electrons then impinges upon a phosphor-coated window opposite the electron gun revealing a diffraction pattern characteristic of the exposed surface (see *Figure 2.15* for examples).

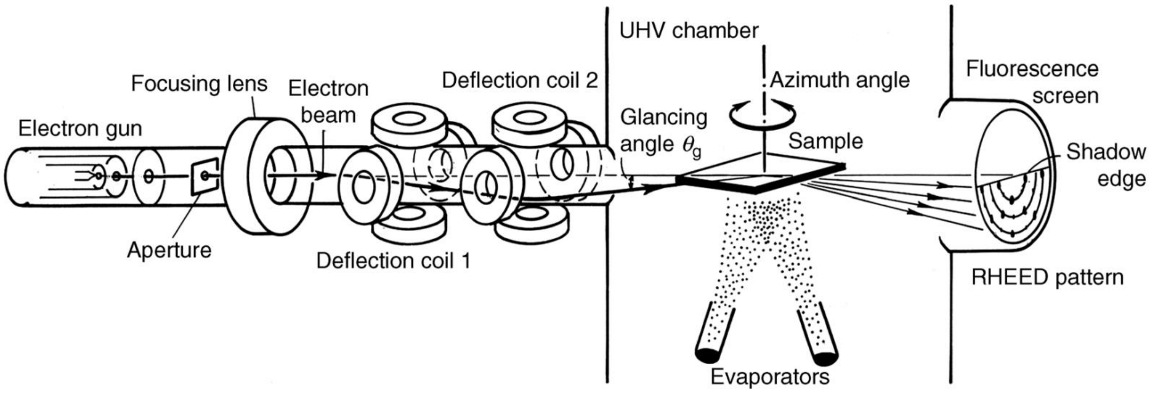

Figure 2.14: Configuration of a typical RHEED system. The geometry facilitates is implementation during MBE growth. Image adapted from S. Hasegawa [85].

RHEED is a highly surface sensitive technique that allows real-time characterization of a surface, observation changes in surface structure, determination of growth rates, and identification of growth modes [55]. The grown material's lattice constant and its rotational alignment relative to the substrate can also be determined. The RHEED system used in this work is a RHEED 15 S by Staib Instruments and operating using 15 keV electrons. RHEED imaging is acquired using a kSA 400 RHEED System.

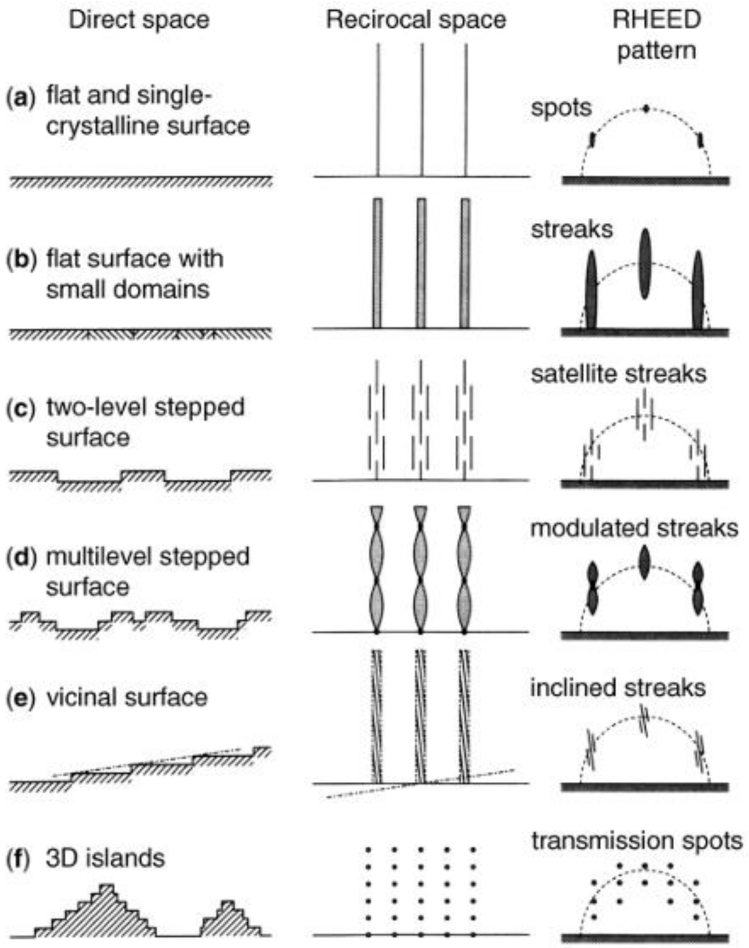

Figure 2.15: Image showing the relationship between real (direct) space surfaces and associated reciprocal space and produced RHEED patterns. Image adapted from S. Hasegawa [85].

RHEED is used for real-time estimations of a material's growth rate. This is done through analysis of intensity line profiles across the collected RHEED images as a function of time. A monolayer is estimated at the point which the intensity of the substrate peak reaches a minimum. This is depicted in *Figure 2.16b* for WSe_2 growth on HOPG in which a monolayer is grown over approximately 36 minutes. A more accurate analysis of the sample growth rate can be estimated after material synthesis using the calculated sample thicknesses obtained from XPS or XRR analyses. Intensity oscillations of the RHEED signal during the growth of 2D TMDCs in these studies were not observed and therefore are not suitable for growth rate estimations.

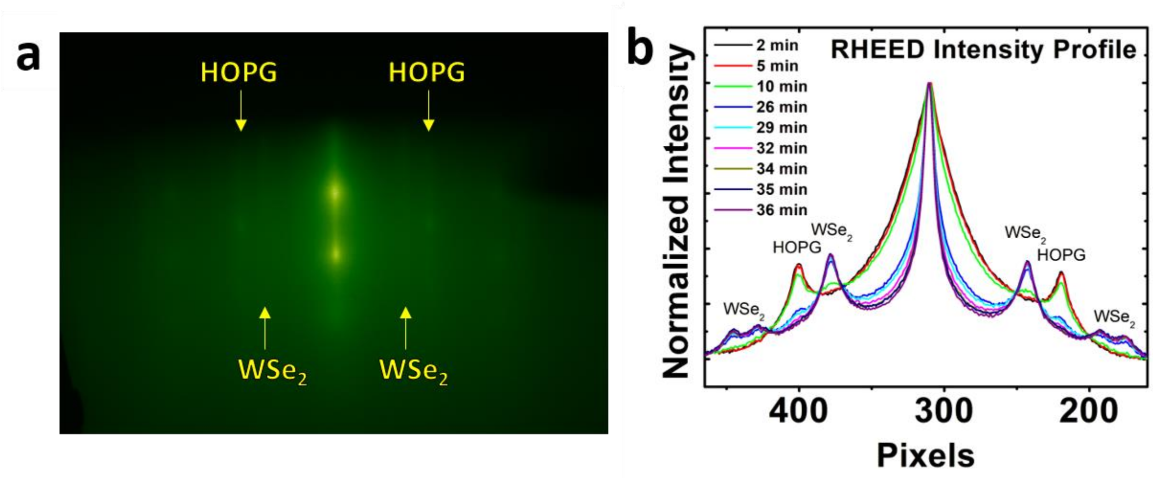

Figure 2.16: a) RHEED of partial monolayer growth of WSe_2 on HOPG and b) extracted intensity line profiles for RHEED images taken at different points during the growth.

2.2.6. Atomic Force Microscopy

Atomic force microscopy (AFM) is a scanning probe technique used for topographic imaging. AFM generates topographic images from forces that arise when an AFM tip is brought in proximity of a sample. The measurement probe is a sharp tip attached to a cantilever. When the tip comes in proximity of the sample to be measured, forces felt by the tip are transmitted to the cantilever. A laser is used to measure deflections in the cantilever by reflecting off the back of the cantilever and hitting a photodiode array. As the cantilever deflects, the laser position on the photodiode array will alter converting this physical deflection into an electrical signal. A cartoon depicting the experimental setup can be seen in *Figure 2.17*. Topographic images can be produced under a variety of imaging modes including contact, tapping (non-contact or intermittent contact), and PeakForce tapping (PFT) modes. The AFM used in this work is located in the Department of Physics and Astronomy at James Madison University. The AFM tool is a Bruker Dimension Icon AFM and is typically operated in PFT mode. In PFT mode, the AFM tip approaches the sample until a setpoint force (the maximum or peak force) is reached, and the tip is then retracted. The peak force setpoint is maintained as the tip and cantilever raster over the sample surface allowing the topography to be imaged [86]. AFM is commonly carried out in air and does not require the added complications of a UHV environment to operate allowing for quick data acquisition. AFM can routinely measure atomic steps in graphite (~3 Å) making it useful in understanding growth modes and topography of 2D material systems. Gwyddion is the software used to produce and analyze the AFM images in this work [87]. Typical image processing steps include leveling, row alignment, and correcting horizontal scars. Leveling is a plane subtraction such that the corners of a given image all sit at the same height. Row alignment is used to correct imaging artifacts in the form of discontinuities between adjacent rows (perpendicular to the raster direction). Scars are an imaging artifact that occurs along the raster direction.

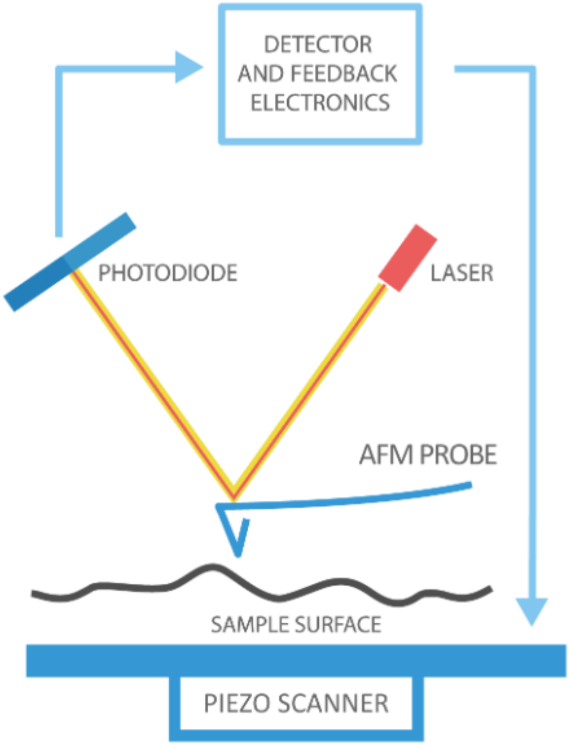

Figure 2.17: Cartoon depicting experimental setup of AFM. Image adapted from https://www.nanoandmore.com/what-is-atomic-force-microscopy.

2.2.7. Measurement of Electrical and Thermal Properties of MBE Grown TMDCs

2.2.7.1. Electrical Resistivity Measurements of MBE-grown $NbSe_2$

Resistivity measurements were carried out using a *multiheight prob*e by Jandel Engineering Limited. This tool utilizes a 4-point probe set up in a linear array to penetrate and contact the sample. The probes are spring loaded to 60 g and are precision ground and polished tungsten carbide with 45° angled tips. The tips are 40 microns thick and equally spaced 1.00 mm apart. The tool provides a setpoint current through the thin film and measures the required voltage to achieve the current setpoint. From this a sheet resistance is calculated in ohms/square. Dividing this value by the sample thickness yields a resistivity value in Ω-cm. Conductivity measurements in this work were carried out on $NbSe_2$ thin films grown on 285 nm-SiO_2/Si substrates. Blank SiO_2 substrates were tested prior to thin film deposition and no sheet resistance value could be obtained due to their electrically insulating nature. This ensured that the probe tips were not capable of penetrating the SiO_2 layer and making contact of the doped Si substrate.

2.2.7.2. Electrical and Thermal Transport of MBE-Grown Bi_2Se_3

Electrical and thermal measurements were collected at The Ohio State University. To collect electrical and thermal measurements, samples were mounted as shown in *Figure 2.18. Figure 2.18a* represents a cartoon of the experimental setup and *Figure 2.18b* shows a sample ready for measurement. The thin film sample was epoxied to a copper platform that was epoxied to an Alumina wafer using silver epoxy (Epo-Tek H20E). Two thermocouples type T (copper/Constantan 25 um in diameter) were epoxied to the edge of the sample and two copper wires were epoxied adjacent to the thermocouples on the opposite side. Current wires were epoxied to the ends of the sample and a resistive heater (Omega, 120 Ohms strain gauge) was attached to the sample along with a brass plate to ensure proper heat distribution. The sample was placed in the cryostat using rubber cement (Elmer's).

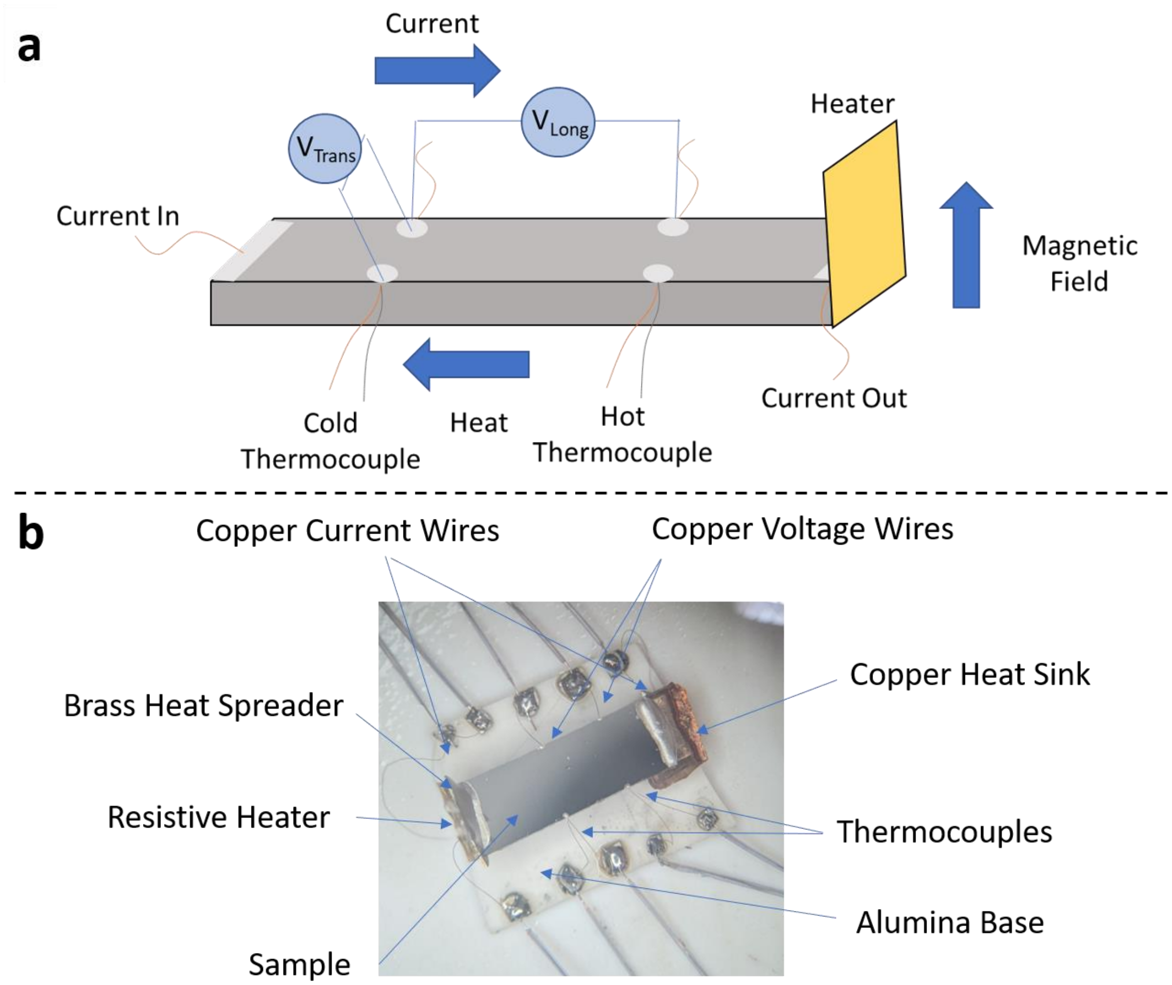

Figure 2.18: a) cartoon of the experimental setup and b) a sample ready for measurement.

Measurements were taken using a nitrogen-cooled LakeShore Janis Cryostat. Temperatures were stabilized for a minimum of 20 minutes. DC current and heat was applied using a Keithley 6220 for ~5 minutes before measurements were taken to ensure stability. Voltage readings were taken with a Keithley Nanovoltmeter 2182A to minimize noise. During a measurement, the transverse and longitudinal voltages are measured directly which allows electrical resistivity (as described previously), Hall resistivity, and thermopower (Seebeck coefficient) to be measured directly given known sample dimensions. Other transport data, such as carrier concentration and mobility are calculated from these directly measured values.

2.2.8. Transmission Electron Microscopy

Transmission electron microscopy (TEM) is an electron imaging technique that utilizes the transmission of high energy electrons through thin samples to image the micro and atomic structure. In this work, we use TEM to look at the cross-section of $Nb_{1+x}Se_2$ thin films on SiO_2 substrates. TEM allows for the magnification of up to 10^6 times [76]. This is made possible due to the short wavelength of electrons at the energies used for TEM (~50 to 200 keV). For TEM analysis, samples need to be transparent to the electron beam; this requires thin samples, on the order of 100 nm thin. The limits of sample thickness will scale inversely with the atomic number of the elements composing a sample as heavier elements are more likely to scatter electrons. Due to the need for thin samples, TEM often requires extensive sample processing prior to imaging. The electron beam used in TEM is generated using a field emission gun (FEG) electron source and an accelerating voltage applied to an anode. The electron beam is then controlled and focused using a series of electromagnetic lenses, condenser lenses, and physical apertures. The resolution of the tool is limited by the accelerating voltage used as the wavelength of the electrons are directly related to their kinetic energy. A typical accelerating voltage of 200 kV will allow for a resolution of ~0.24 nm, though the actual resolution may be limited due to additional aspects of instrument setup (e.g., lens aberrations).

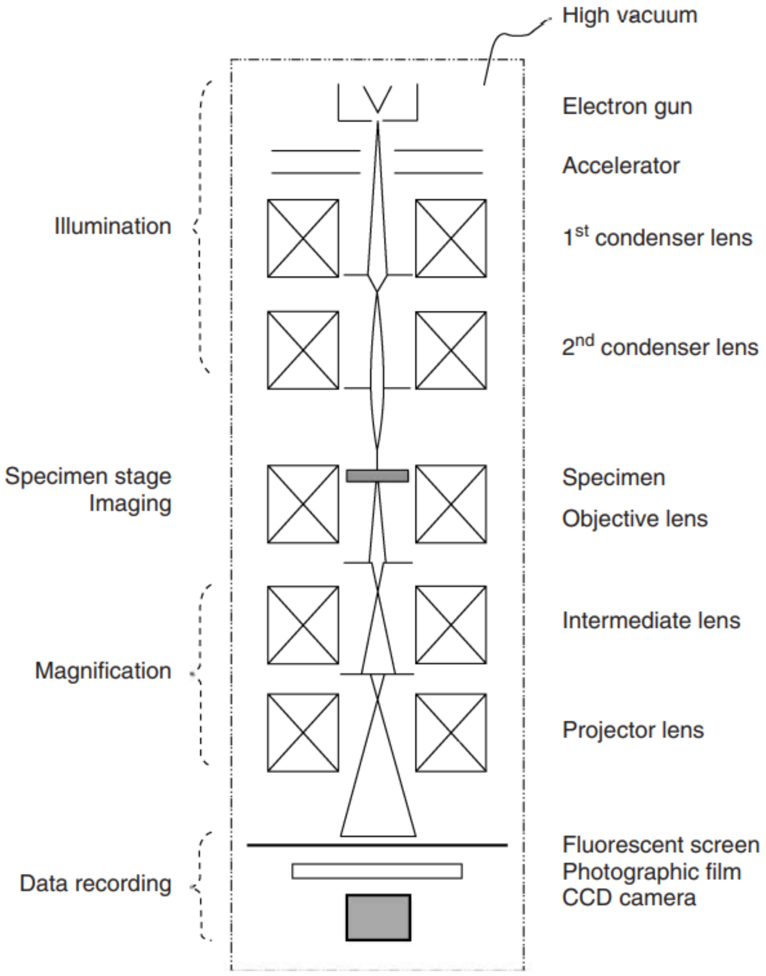

Figure 2.19: Diagram of TEM set up. Figure reused with permission from Copyright © 2013, John Wiley and Sons [76].

Contrast in TEM micrographs is attributed to a few specific mechanisms referred to mass-density contrast, diffraction contrast, and phase contrast [76]. Contrast, in all cases, is produced by varying amounts of electrons reaching the spatially resolved detector which produces an image. Mass-density contrast is a consequence of a varying number of electrons scattering at different locations on a sample. The probability of electron scattering, and thus not reaching the detector, scales with atomic number and sample thickness. Therefore mass-density contrast is related to the probability of electron scattering as it passes through the sample either due to increase atomic number of atoms in the sample or sample thickness. Diffraction contrast is due to collective scatting off of parallel atomic planes in crystalline samples. If the Bragg condition is satisfied for a given crystal grain, electrons passing through that crystal will be deflected and not reach the detector. Because diffraction contrast is due to constructive interference of electrons, the orientation of grains has a large impact on the image contrast and tilting the sample can greatly impact the contrast of various grains in a sample. Adjacent grains in a polycrystalline solid may not simultaneously satisfy the Bragg condition and more of the electron beam will transmit the one grain than another. For this reason, diffraction contrast is useful for identifying individual grains in polycrystalline samples. Phase contrast comes from the interference of the transmissive and diffracted electron beams that pass through a sample, i.e., the electron paths that are responsible for mass-density and diffraction contrasts. The interpretation of phase contrast is complex as it involves the interaction of multiple electron sources (the transmissive and diffracted electron beams). Often computer simulations are required to fully interpret the data. Though complex, phase contrast offers superior resolution compared to mass-density and diffraction contrast; for this reason, phase contrast imaging is frequently referred to as high-resolution TEM (HRTEM).

2.3. Additional Experimental Methodologies

2.3.1. In-Situ Sample Cleaving Using Kapton Tape

Bulk 2D crystals will adsorb contaminates in atmosphere and most will also oxidize. To achieve the cleanest sample possible, bulk samples are cleaved in-situ which ensures the surface is never exposed to atmosphere. The first step is to secure a bulk 2D flake to a sample plate with conductive C-tape. This ensures the sample is electrically grounded to the plate. Kapton tape, which is compatible with UHV pressures is then secured to the top of the bulk 2D flake in a loop as shown in *Figure 2.20a*. The wobble stick can then be rotated to remove the tape from the sample

(*Figure 2.20b*). If successful, removed material will be visible on the Kapton tape which now resides on the wobble stick (*Figure 2.20c*). XPS can be used to confirm an oxide free surface.

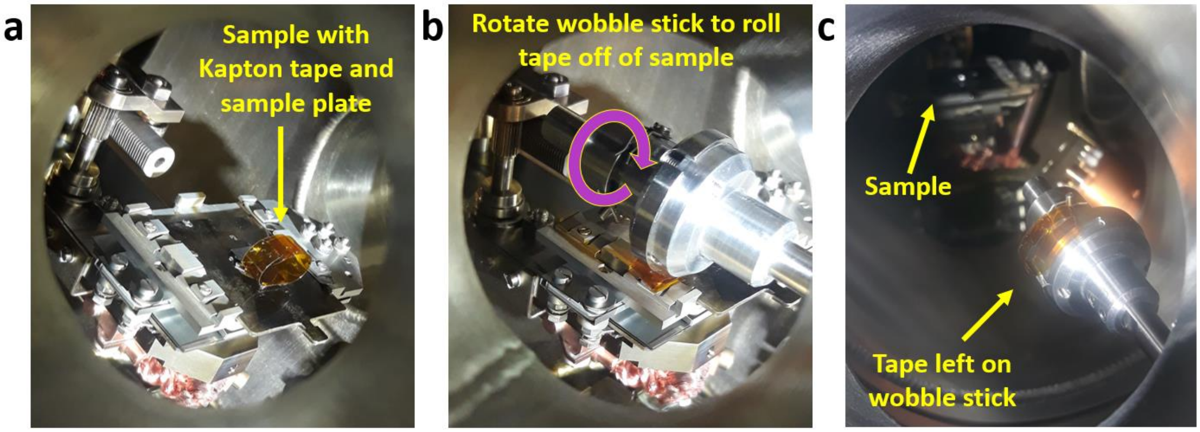

Figure 2.20: Pictures of process for in-situ cleaving of samples using Kapton tape. Written procedure in main text.

2.3.2. In-Situ Sample Cleaving Using Torr Seal

Unlike bulk 2D crystals, which can be easily cleaved using adhesive tapes, MBE-grown films require a stronger adhesive to successfully cleave. Torr Seal is a UHV compatible adhesive which showed success in cleaving MBE-grown 2D materials. The process is depicted in *Figure 2.21*. First, Torr Seal is used to secure the MBE-grown sample to a sample plate and then a bolt was mounted to the sample with Torr Seal (*Figure 2.21a*). It is important to ground a corner of the wafer to the sample plate with C-tape as the Torr Seal is insulating. After letting the Torr Seal cure for ~24 hours at room temperature, the sample with the attached bolt was loaded into the fast entry load lock (FELL). Once the sample is in the FELL, a 2nd bolt can be secured to the sample/bolt on the sample plate using a nut (*Figure 2.21b*). The FELL is then pumped down to high vacuum over the course of ~1 hour. The sample is then rotated in the FELL causing the bolt to hit against the chamber wall. This will cause the paired bolts to break away from the sample (*Figure 2.21b* and *c*). The sample is then immediately introduced into UHV. Successful cleaving can be checked by looking at the sample (*Figure 2.21d*) and the bolt, which will retain any removed material (*Figure 2.21e*). An oxide free surface can be confirmed with XPS.

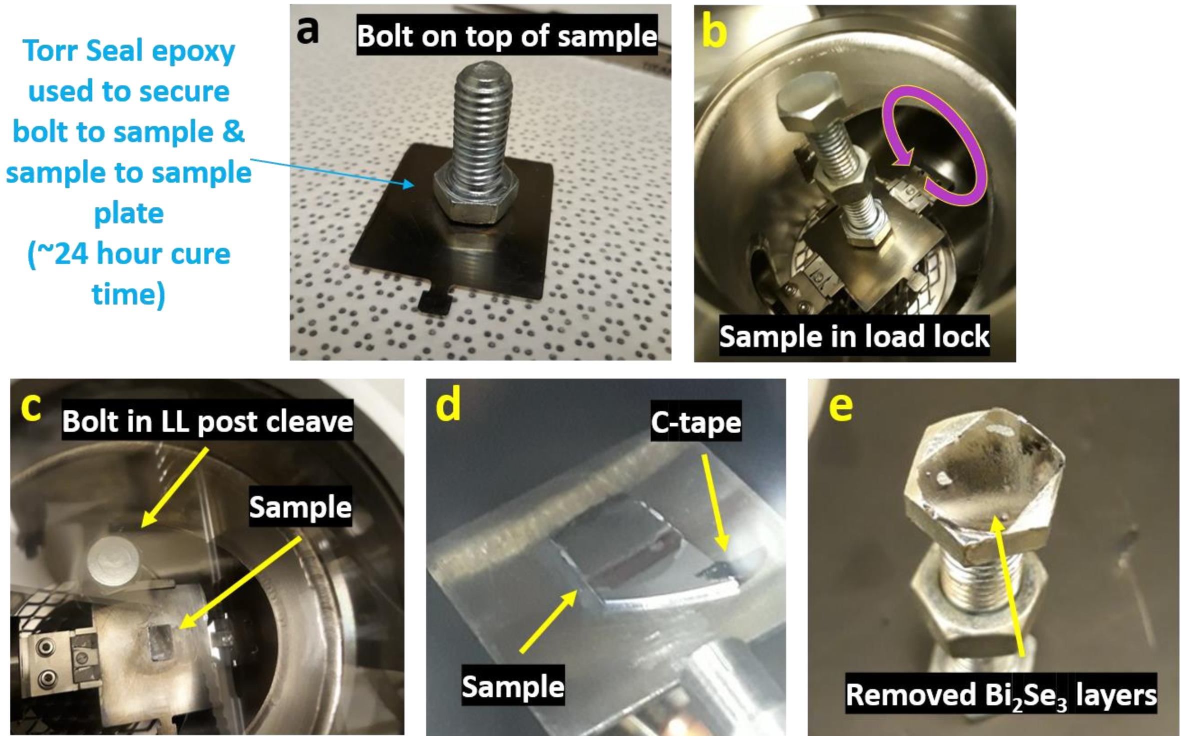

Figure 2.21: Pictures of process for in-situ cleaving of samples using Torr Seal. Written procedure in main text.

3. The Growth of Semiconducting Transition Metal Dichalcogenides by Molecular Beam Epitaxy

3.1.Purpose

The purpose of this chapter is to report on investigations into the growth of WSe_2 and other semiconducting, group-VIB transition metal dichalcogenides (TMDCs) by molecular beam epitaxy (MBE). This thesis reports on the first investigations into TMDC growth with the MBE tool in the McDonnell Lab at the University of Virginia. For these initial investigations, we choose to study the growth of WSe_2 on highly ordered pyrolytic graphite (HOPG). The W-Se system only has one known equilibrium compound, i.e., WSe_2, and HOPG is chemically inert. These properties make the WSe_2/HOPG heterostructure an ideal platform to study how processing parameters, such as growth temperature and elemental/molecular beam equivalence pressure ratio (BEPR), impact the growth of TMDCs. We first establish a baseline for this study by identifying the expected chemical, morphological, and electronic characteristics of MBE-grown WSe_2. We then report on investigations into the dependency of the material's chemistry and surface morphology on the substrate temperature and elemental/molecular BEPRs used during growth. Lastly, we show that the growth conditions used for synthesis of WSe_2 can be extended to the growth of WS_2. While many similarities exist, the generation of sulfur fluxes in UHV poses unique challenges when growing sulfides such as WS_2 by MBE.

3.2.Introduction to Semiconducting Group VIB TMDCs

The group VIB TMDCs are the most heavily studied of the TMDCs to date. This is represented in *Figure 3.1* which shows the number of published articles in the ScienceDirect database for select TMDCs. In fact, the number of scientific articles published on MoS_2 alone is on par with all other TMDCs combined. The reason for the comparatively greater interest in the group VIB TMDCs are fewfold. First, the sulfides and selenides of Mo and W are semiconducting in their equilibrium phases. With band gaps similar to that of Si, it is believed that materials such as MoS_2 and WSe_2 can be used in ultra-scaled field effect transistors. The first examples of working transistors based on semiconducting TMDCs were demonstrated in 2004 [88]. Transistors utilizing monolayer TMDCs were demonstrated in 2011 [89]. Secondly, well studied members of this group such as MoS_2, WS_2, and WSe_2 exhibit an indirect to direct bang gap transition when thinned to monolayers; their direct band gap nature in the monolayer greatly enhances their ability to both adsorb and emit photons making them attractive for photonic applications. Lastly, the interest in this group of TMDCs was further enhanced by the ease of access to geological MoS_2, which is the only naturally occurring TMDC in appreciable quantities. The availability of MoS_2 coupled with exfoliation strategies than can yield monolayer and few layer flakes facilitated many studies and prototype devices using semiconducting MoS_2 as the development of synthesis techniques in the case of MoS_2 was not required. However, for any scaled application, the controlled synthesis of these materials is desired. Thus, a large scientific effort has been dedicated to study the growth of these materials.

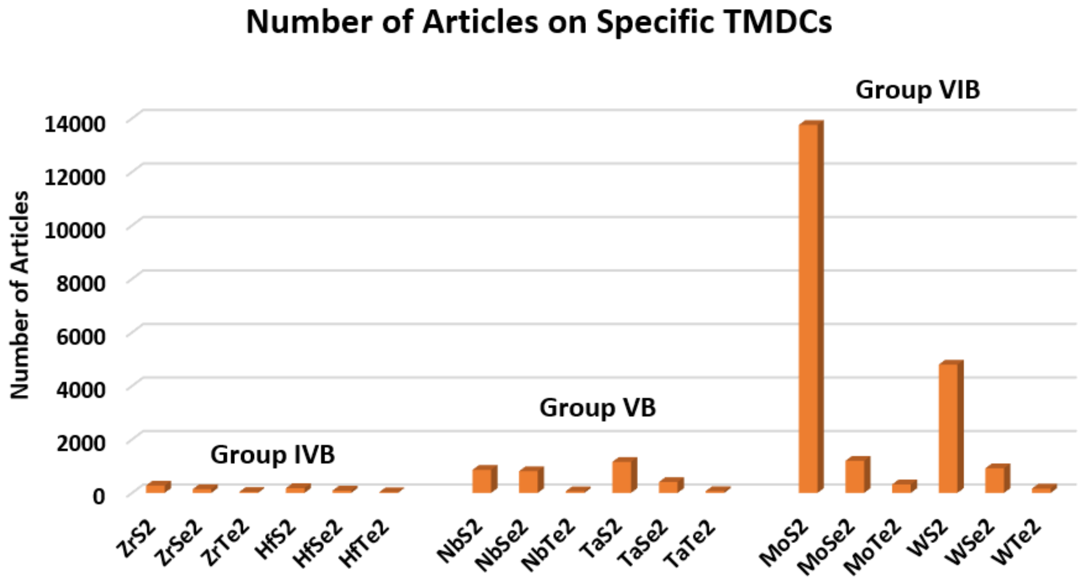

Figure 3.1: Number of articles returned under the ScienceDirect search engine for given TMDCs. The group VIB TMDCs are the most well studied of the TMDCs with MoS_2 accounting for more articles than all other listed TMDCs combined. *Data taken from ScienceDirect search function on October 9th 2022.*

3.3. Synthesis of WSe_2 Thin Films

The synthesis of TMDCs by MBE is carried out by simultaneous exposure of a heated substrate to chalcogen and transition metal fluxes. Chalcogen and transition metal elemental fluxes are generated by thermal evaporation and electron beam deposition, respectively. The growth of TMDCs is typically achieved by creating an overpressure of the chalcogen during growth; the chalcogen to metal beam equivalence pressure ratios (BEPRs) are regularly reported in excess of 10:1 [90-95]. Substrate temperatures of 300 to 600 °C during MBE synthesis of TMDCs are common [26]. As a prelude to the follow-up studies on WSe_2, we start by establishing a baseline of the expected spectroscopic and morphological characteristics of MBE-grown WSe_2. We then investigate how these properties change as we alter the Se to W BEPR and substrate temperature for WSe_2 growth in sections 3.4 and 3.5, respectively.

Under suitable processing conditions, MBE can be used to grow crystalline WSe_2. In-situ x-ray photoelectron spectroscopy (XPS), angle resolved photoelectron spectroscopy (ARPES), and ex-situ scanning tunneling microscopy/spectroscopy (STM/STS) have been used to characterize MBE-grown WSe_2. *Figure 3.2* presents the core level XPS spectra of bilayer WSe_2 grown on a HOPG substrate. The positions of the Se $3d_{5/2}$ and W $4f_{7/2}$ in the grown material are 54.68 eV and 32.44 eV; the peak separation of 22.24 eV is consistent with bulk 2H-WSe_2 [96]. The symmetric peaks in each spectrum are characteristic of a chemically homogeneous semiconductor. In this work, chemically homogeneity refers to samples with no detectable chemical variability over the ~1 x 1 mm scanned area of the sample; the detection limit of any potential chemical variability with XPS is on the order of 1%. The O 1*s* spectrum shows no evidence of oxygen contamination. The C 1*s* spectrum shows a single prominent C feature from the HOPG substrate which overlaps with a Se Auger feature originating from the grown WSe_2 film.

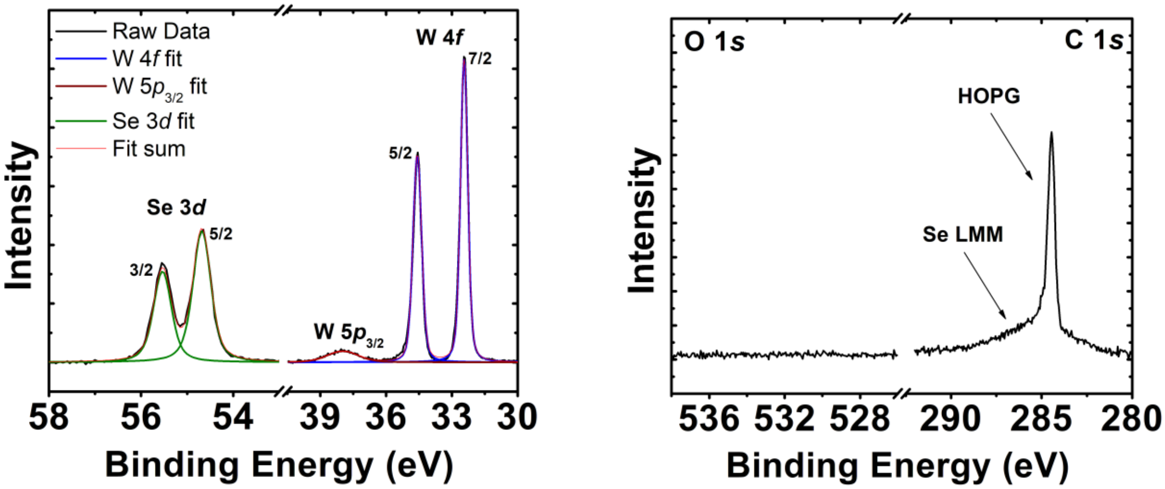

Figure 3.2: XPS spectra of Se 3*d* and W 4*f* core levels of WSe_2 thin films grown at 480 °C on an HOPG substrate. The Se to W BEPR was ~5000:1.

Ex-situ STM/STS was carried out on partial monolayer WSe_2 and is presented in *Figure 3.3*; STM/STS data was collected by W. Blades in the Reinke Lab at UVA on a sample grown in the McDonnell Lab by MBE. The topographic image in *Figure 3.3A* shows areas of single layer and bilayer WSe_2 along with areas of the exposed HOPG substrate. This indicates that growth of WSe_2 under the conditions used here adopts a Volmer-Weber growth mechanism, i.e., 2nd and 3rd layer nucleation occur prior to the coalescence of the first monolayer. Inset into *Figure 3.3A* is an atomically resolved image revealing the expected hexagonal atomic structure of the WSe_2 surface. A moiré pattern is observed due to the superposition of the WSe_2 and HOPG lattices and exhibits a periodicity of 1.15 nm, indicative of rotational alignment between the WSe_2 monolayer and HOPG substrate. *Figure 3.3B* shows a line profile taken across the topographic image in *Figure 3.3A*; the measured height of the WSe_2 layers agree well with the expected value at ~0.72 nm [38, 97]. The STS spectra in *Figure 3.3C* shows the variation in the band gap with thickness. The decrease in the band gap from 1.6 eV in the monolayer to 1.5 eV in for bilayer WSe_2 follows the expected trend [98]. The STS plot also indicates that the Fermi level is near the center of the band gap and that the grown material does not show any tendency towards n- or p-type character. Additional STM/STS analysis of the WSe_2 grown here, along with a controlled study on the evolution of defects in the material, is available in the work carried out and published by Blades et al. [99].

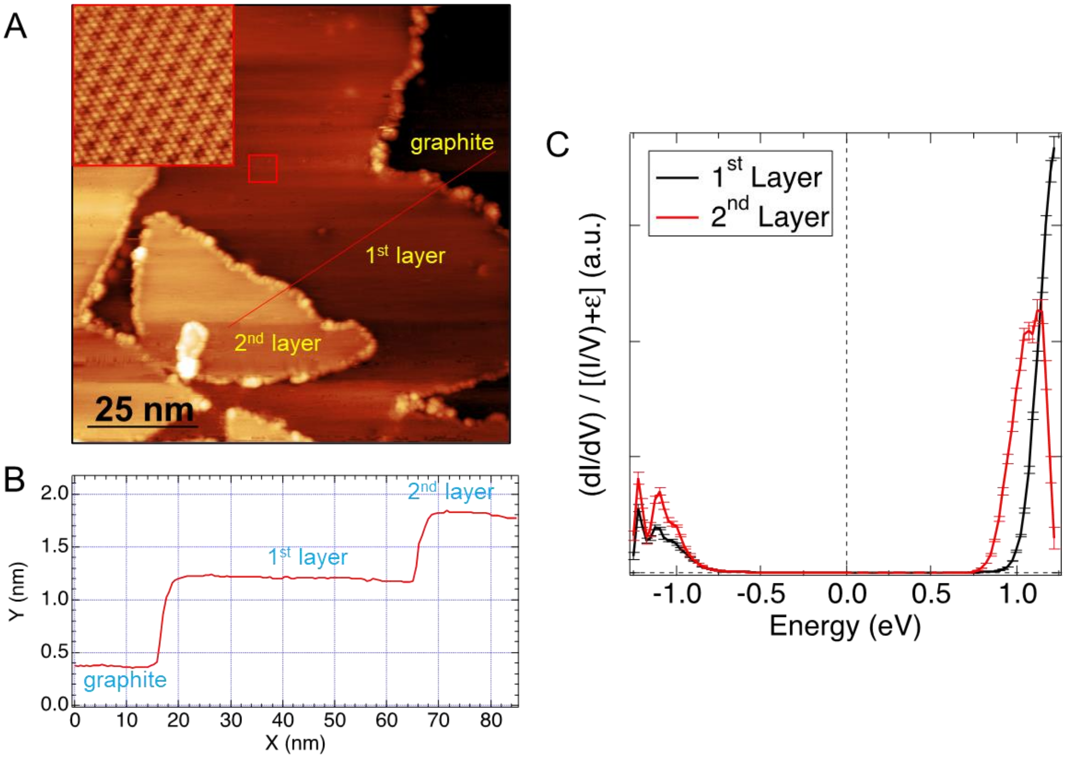

Figure 3.3: A) Topographic STM image of WSe_2/HOPG sample. Inset shows atomically resolved surface). B) Extracted height profile from *a*. C) STS spectra of monolayer and bilayer WSe_2. WSe_2 synthesized in McDonnell Lab and characterized in Reinke Lab. Figure adapted with permission from W. H. Blades et al., "Thermally Induced Defects on WSe_2," The Journal of Physical Chemistry C, vol. 124, no. 28, pp. 15337-15346. Copyright 2023 American Chemical Society. [99].

WSe_2 grown on single crystal graphene allows for the electronic structure to be measured using in-situ ARPES. Previously discussed samples grown on HOPG are polycrystalline, i.e., grains are randomly orientated in-plane despite having a high degree of order along the c-axis; this is due to the polycrystallinity of the HOPG substrate. In contrast to HOPG, graphene grown epitaxially on SiC has a single in-plane orientation over an entire wafer. Therefore, the epitaxial growth of WSe_2 on graphene by MBE is also single crystal, a prerequisite for studying the electronic structure with ARPES. *Figure 3.4* shows acquired ARPES spectra of the K-point of graphene on SiC prior to WSe_2 growth and the K- and M-points of monolayer WSe_2 grown on the graphene substrate. The white dashed line in each spectrum represents the position of the Fermi level. The electronic structure calculated by density functional theory (DFT) overlaid in the figure was taken from Liu et al. and demonstrates good agreement with the experimentally determined electronic structure [100]. The measured electronic structure presented here is evidence that the MBE-grown WSe_2 is of the expected trigonal prismatic coordination.

The data presented in this section all confirm the synthesized material shares the expected chemical, physical, and electronic structures consistent with crystalline and chemically homogenous 2H-WSe_2. In the following sections, we detail studies investigating how the morphology and chemistry of WSe_2 thin films alter as a function of BEPR (Section 3.4) and substrate temperature (Section 3.5). Both the morphology and chemistry of the synthesized material are important as they will affect how WSe_2 performs in a given application. While a similar study has previously been carried out on MBE-grown WSe_2 by Yue et al., we expand on the previously demonstrated work by exploring a wider range of growth conditions [95]. Uniquely, we explore higher growth temperatures, increased BEPRs, and identify the formation of metastable phases not considered in the work by Yue et al.

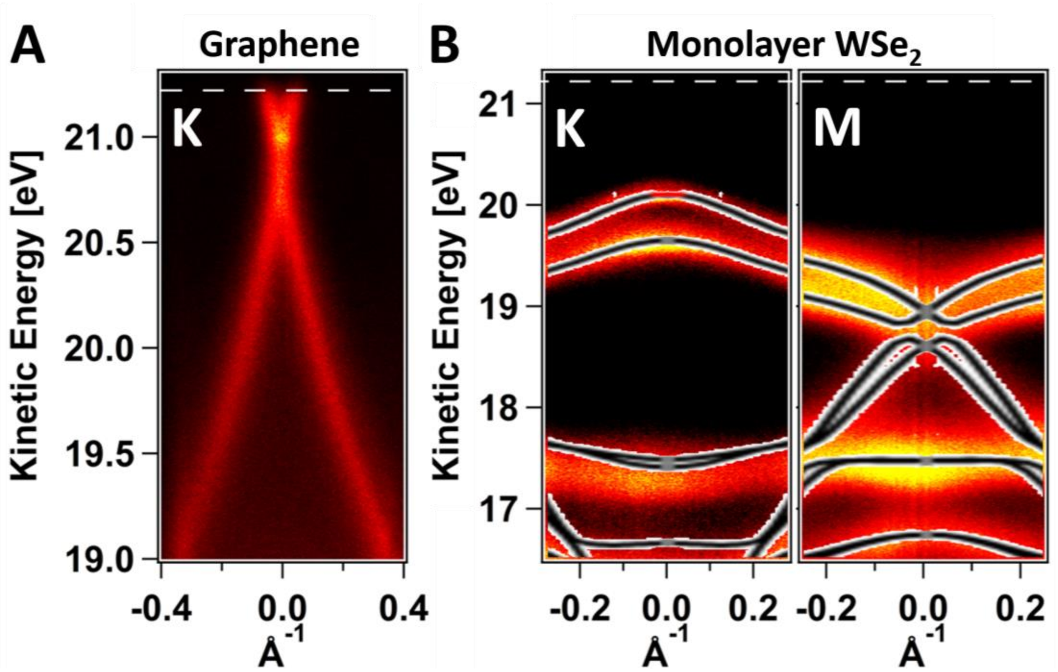

Figure 3.4: ARPES spectra of A) graphene K-point on SiC and B) the K- and M-points of monolayer WSe_2 grown on the graphene substrate. The white dashed line in each spectrum represents the position of the Fermi level. WSe_2 synthesis and data collection in McDonnell Lab. Overlaid DFT from Liu et al. [100].

3.4.Effect of Chalcogen to Metal BEPR on the Growth of WSe_2 on HOPG

To study the effect of the chalcogen-to-metal BEPR on the growth of WSe_2 by MBE, sub-monolayer films were grown on HOPG substrates at 565 °C. The grown thin films were studied with in-situ XPS/RHEED and ex-situ AFM. The BEPs of the Se and W sources were measured prior to the start of growth using a beam flux monitor. The Se to W BEPRs used varied from 28:1 to 20250:1. This was achieved by holding the W BEP at ~4 x 10^{-10} mbar and varying the Se BEP for each growth. The effect of varying the Se to W BEPR on the chemical makeup of the grown WSe_2 can be seen in *Figure 3.5*. All Se 3*d* and W 4*f* spectra contain peaks characteristic of 2H-WSe_2 as described in the previous section. Films grown using high BEPRs, 3250:1 and greater, produced the most chemically homogeneous films. In contrast, the least chemically homogeneous films were produced using the lowest BEPR (28:1 and 65:1); under these conditions W^0 forms, evidenced by the presence of a feature at ~31.3 eV in the W $4f_{7/2}$ spectra. The intermediate BEPRs, 100-1,067:1 are sufficient in suppressing the formation of W^0, but contain subtle contributions from sub-stoichiometric WSe_{2-x} which manifest as an asymmetry to the low-binding energy side of the W 4*f* peaks.

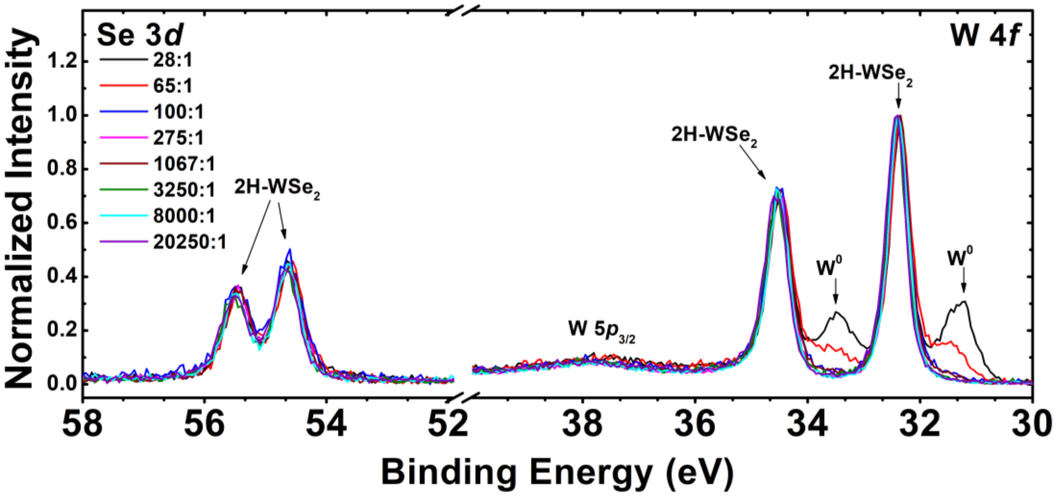

Figure 3.5: XPS spectra of Se 3*d* and W 4*f* core levels of WSe_2 thin films grown at 565 °C utilizing different BEPR ratios. Se to W BEPRs used for each growth are inset into image legends. Figure adapted from previously published work [101].

The same sub-monolayer WSe_2 thin films were characterized with AFM to reveal details of the grain morphology and nucleation density which can be seen in *Figure 3.6*. We used the relative RHEED intensities from the substrate and thin film to monitor the growth and targeted similar coverages for each BEPR. In the AFM images it is observed that Se to W BEPRs of 28:1 and 65:1 produced tall structures that are attributed to the W^0 previously discussed; similar features are not seen in the AFM images of the six higher BEPRs which agrees with the lack of an W^0 signature in the XPS spectra of these films. These results are qualitatively in agreement with Yue et al. who used AFM to observe tall structures at the center of their grains produced at BEPRs of

20:1; these features were not present in their films at BEPRs of 140:1 [95]. The lowest nucleation density (and largest grain size) in our work was seen at a BEPR of 8000:1; the nucleation density is plotted as a function of BEPR in *Figure 3.6b* and was calculated by counting the number of nuclei present per area in the respective AFM images. A BEPR of 3250:1 was optimal in terms of suppressing second layer nucleation resulting in only ~2% bilayer coverage which was determined by analyzing the fractional surface coverage of first WSe_2 layer. *Table 3.1* presents surface coverage analysis of the AFM images presented in *Figure 3.6a*. Surface coverage was determined using a thresholding and masking function in the software Gwyddion used to generate the images. The coverage of the HOPG substrates varied from 25 to 43%.

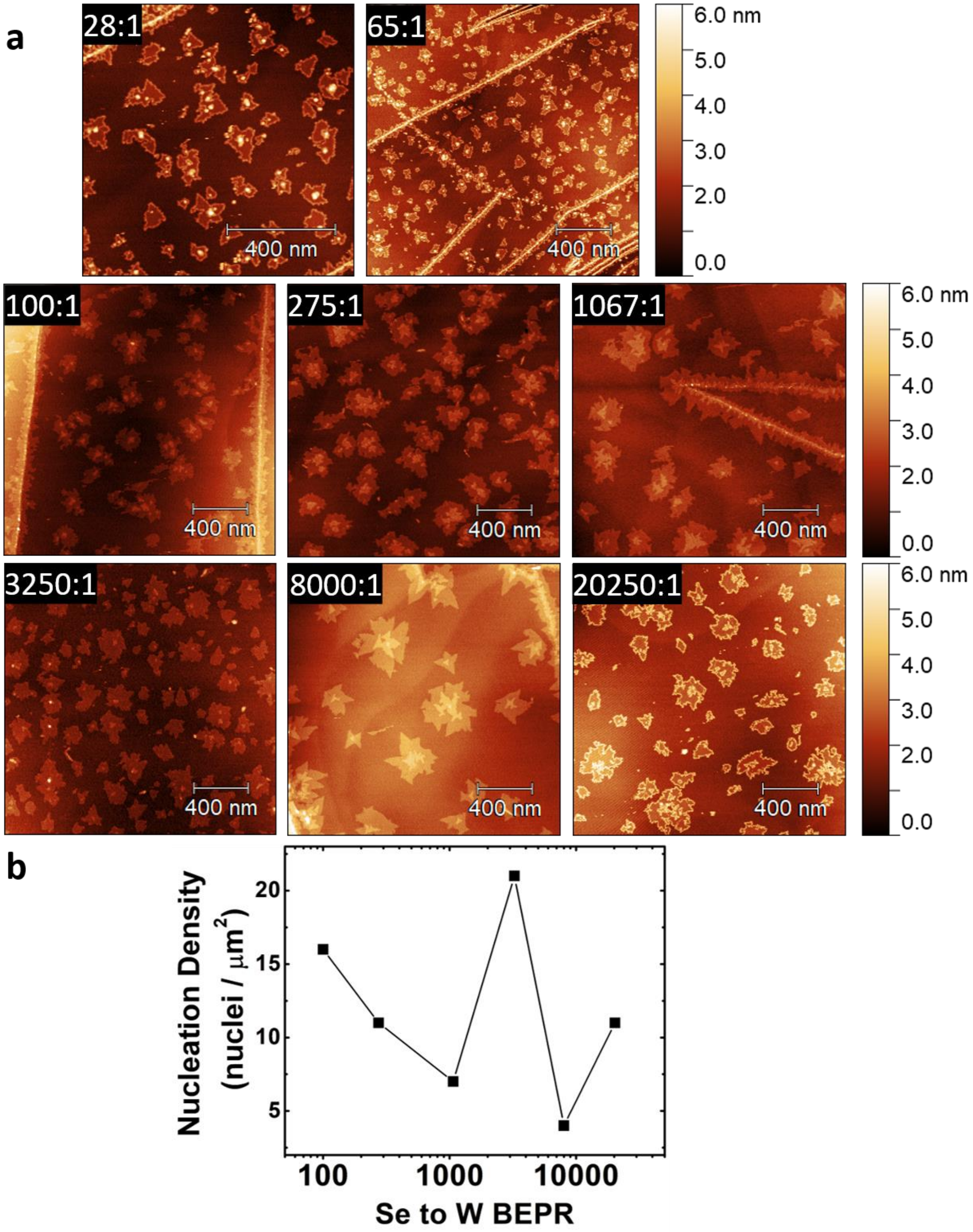

Figure 3.6: a) AFM images of WSe_2 partial monolayers grown at 565 °C utilizing different BEPR. Se to W BEPR is inset into each image. Note the smaller field of view for the 28:1 BEPR image (1 x 1 μm); images of higher BEPRs are 2 x 2 μm. Figure adapted from previously published work [101]. b) Nucleation density as a function BEPR extracted from respective AFM images.

Table 3.1: *Monolayer coverage* (% of HOPG surface covered in WSe_2), *bilayer coverage* (% of HOPG surface covered in 2L-WSe_2), and *monolayer covered* (% of 1L-WSe_2 covered in 2L-WSe_2) with varying BEPR used during MBE growth.

BEPR (Se:W)	**% Monolayer Coverage**	**% Bilayer Coverage**	**% Monolayer Covered**
100:1	32	5	15.6
275:1	42.7	9.5	22.2
1067:1	31.6	6.1	19.3
3250:1	42.9	2	4.7
8000:1	25.7	4.7	18.3
20250:1	25.2	2.5	9.9

The formation of W^0 clusters under low Se to W BEPRs (28:1 and 65:1) is apparent from both the XPS spectra and AFM images of these films. The reason for the formation of W^0 under these growth conditions, despite an overpressure of Se, is likely twofold (and will be discussed in detail below): 1) the residence time of Se atoms on the surface is significantly lower than that of W and 2) the variety of Se molecules (Se_x) produced by the effusion cell means not all Se on the substrate surface has equal probability of being incorporated into the growing thin film.

The difference in residence times between Se and W atoms on the surface of graphene have previously been studied by Nie et al.; these results are meaningful in the context of our work due to the chemically analogous surfaces of graphene and HOPG [102]. Monte Carlo simulations carried out by Nie et al. calculated that the residence time of Se atoms were 4 to 5 orders of magnitude lower than that of W atoms at a range of MBE growth temperatures. This result suggests that many Se atoms desorb from the substrate surface before being incorporated into the growing thin film. The second reason W^0 cluster formed during growth with low Se to W BEPRs is that the Se flux is not composed of atomic Se, but instead a distribution of molecular clusters, Se_x ($x = 1$-8) [103]. Larger clusters tend to be more stable and are thus less likely to contribute to WSe_2 growth before being desorbed back into vacuum [104]. The combined effect is that there is not enough Se incorporated into the growing thin film to prevent W-W bond formation resulting in three-dimensional clustering. At BEPRs greater than 65:1, the formation of W^0 is suppressed, but the presence of WSe_{2-x} persists. The degree of WSe_{2-x} in the films reached a minimum at a BEPR of 3250:1; changes beyond this BEPR had no further effect on the observed chemistry.

The nucleation density of WSe_2 has an impact on properties important for use in devices. For example, the nucleation density is directly tied to the number of grain boundaries that exist in coalesced WSe_2 thin films. A high nucleation density during growth results in grain boundaries that form where WSe_2 islands merge and is expected to degrade charge carrier mobilities [47, 95]. The nucleation density and the degree of bilayer growth are related to adatom mobility/diffusion length and critical size of stable nuclei. Nuclei will continue to develop until the average nuclei separation decreases below the diffusion length of adatoms. The highest nucleation density was observed at Se:W BEPRs of 28 and 65:1 as observed in *Figure 3.6a* (note the smaller lateral scale of the AFM image of a BEPR of 28:1, this was done to better observe the smaller, more densely packed nuclei). At these BEPRs W^0 forms in addition to WSe_2; more specifically W-rich protrusions sit at the center of WSe_2 islands. This is evidence that W-rich nuclei seed the growth of WSe_2; that is, W^0 promotes heterogeneous nucleation of WSe_2. The high nucleation density at these BEPRs is a result of the smaller critical radii of W^0 compared to WSe_2 [95]. Yue et al. calculated the critical nucleus size of W^0 to be ~0.31 nm, roughly an order of magnitude smaller than that of the critical nucleus for WSe_2, at 500 °C. At higher BEPRs (100:1 and greater) W^0 no longer forms. This is due to the greater presence of Se which subdues the formation of W-W bonds; in this case the nucleation density of WSe_2, rather than W^0, dictates the overall nucleation density. The larger critical nucleus size of WSe_2 compared to W^0 explains the presence of fewer nuclei at BEPRs above 65:1. Beyond a BEPR of 100:1 there is no clear trend in the dependence of the nucleation density with BEPR (*Figure 3.6b*); this lack of an observed trend is further discussed in the following paragraphs.

The ability to control the degree of 2nd layer nucleation of WSe_2 is of interest for numerous applications as the nature of the material's band gap is highly sensitive to the number of WSe_2 layers [98, 99]. For example, monolayer WSe_2 is characterized as having a larger, direct band gap compared to the smaller, indirect band gap of the bilayer; the change in the magnitude of the band gap between monolayer and bilayer WSe_2 was observed in the STS presented earlier in this chapter (*Figure 3.3*) [98]. Thus, control over the growth of 2nd layer nucleation is desired as it directly dictates the nature of the material's band gap. Under all synthesis conditions used in this work, 2nd layer nucleation occurs prior to coalescence of the 1st monolayer, that is, in all cases a Volmer-Weber growth mechanism is observed. At BEPRs of 100:1 and greater, no clear trend exists relating the BEPR used and the degree of 2nd layer coverage. Whether or not 2nd layer nucleation occurs prior to the completion of a monolayer is a consequence of adatom diffusion. Adatoms on the 1st layer of WSe_2 must be able to diffuse down to the graphite surface in order to contribute to growth of the 1st layer. The work here shows that any dependence of adatom diffusion length on the Se to W BEPR is small as no obvious trend between nucleation density or 2nd layer nucleation exist with varying BEPR. Yue et al. demonstrated small changes in nucleation density once Se pressures were high enough to subdue W^0 formation [95]. Work by Rajan et al. demonstrated a ~2x increase in grain size of $TiSe_2$ and $NbSe_2$ through an increase of the BEPR from 60:1 to 600:1 [105]. This relatively large dependence on BEPR observed by Rajan et al. is not mimicked in our work presented here.

During MBE growth there are numerous parameters of the growth that can impact nucleation density and 2nd layer nucleation in the context of this work; these parameters include

Se to W BEPR, growth rate, and growth temperature. While speculative, the variability in (and lack of a BEPR dependence of) nucleation density and 2nd layer nucleation likely relate to imperfect control of growth rate and growth temperature. *Table 3.1* details the chamber pressure, Se BEP, and growth time for each sample. Apparent in this table is the high degree of variation in growth time. It is known that during MBE growth of TMDC compounds, the growth rate is largely dictated by the flux of the transition metal source [95]. Therefore, the variation we see in growth time points to a variability in our W flux during growth. The growth rate has been shown to impact nucleation density of TMDC thin films previously; high growth rates result in greater nucleation densities [105]. While growth rate likely impacts the variation in nucleation density we see in our material, there is not a clear trend between the two suggesting other factors, such as unintentional variation in growth temperature, exist in this work. As will be observed in the next section, growth temperature has a high impact on nucleation density. The work in this section was carried out prior to the installation of a pyrometer on the MBE tool in the McDonnell Lab. The temperature for this study was measured using the thermocouple in contact with the sample holder (substrates are held in contact with a sample plate which sits in the sample holder). Errors in our measured growth temperature likely exist due to the indirect temperature measurement using the thermocouple (i.e., thermocouple is not in direct contact with the substrate) and therefore can have an impact on the nucleation density and degree of 2nd layer nucleation. It is likely that the combined errors associated with growth rate and growth temperature obscure the subtle impacts of BEPR on the nucleation density and degree of 2nd layer nucleation in this study. Through analysis of the sample heater electrical currents used during growth, the sample-to-sample variance in temperature can be up to 25 °C. However, this does not account for additional error in sample temperature which may arise due to differences in sample mounting, i.e., sample holder-to-sample holder variation, sample holder deformation over time from spot welding/annealing, and variability in sample mounting (samples were held to sample holders with spot-welded Ta foil). The analysis of this work has been published [101].

Table 3.1: Growth parameters used during WSe_2 synthesis.

Sample/BEPR (Se:W)	Chamber pressure	Se BEP	Growth time
1) 28:1	7.3E-10 mBar	1.1E-8 mBar	232 minutes
2) 65:1	2.3E-9 mBar	2.6E-8 mBar	132 minutes
3) 100:1	2.5E-9 mBar	4.0E-8 mBar	156 minutes
4) 275:1	1.2E-9 mBar	1.1E-7 mBar	156 minutes
5) 1067:1	3.3E-9 mBar	3.2E-7 mBar	266 minutes
6) 3250:1	3.0E-9 mBar	1.3E-6 mBar	124 minutes
7) 8000:1	8.0E-9 mBar	3.2E-6 mBar	190 minutes
8) 20250:1	1.1E-8 mBar	8.1E-6 mBar	58 minutes

3.5.Effect of Substrate Temperature on the Growth of WSe_2 on HOPG

The effect of substrate temperature on the growth of WSe_2 on HOPG was also studied. The substrate temperatures investigated were 375, 565, and 750 °C. The XPS results can be seen in *Figure 3.7*. The growth of six samples was carried out using two Se to W BEPRs; a moderate BEPR of ~3500:1 and a high BEPR ~20,000:1. As seen in the XPS spectra, both growths carried out at 565 °C showed nearly symmetric peaks in the Se 3*d* and W 4*f* spectra that are assigned to 2H-WSe_2 with only small contributions from a WSe_{2-x} component. The effect of increasing the Se:W BEPR from 3250:1 to 20250:1 at a growth temperature of 565 °C had negligible effects on the observed chemistry, as discussed in the previous section.

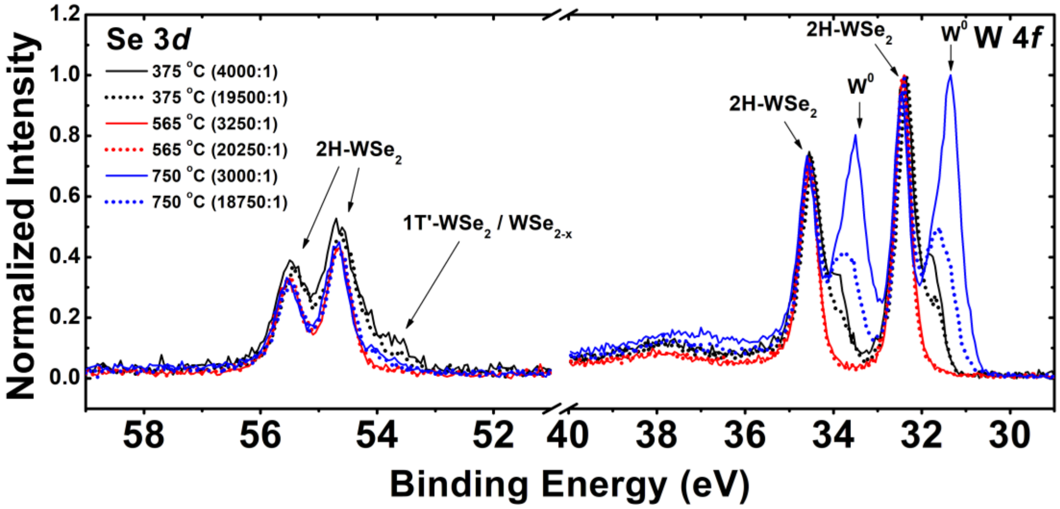

Figure 3.7: XPS spectra of Se 3*d* and W 4*f* core levels of WSe_2 thin films grown at 375, 565, and 750 °C. Se to W BEPRs for each growth are inset into image legends.

Growing at 375 and 750 °C resulted in the formation of low binding energy features in both the Se 3*d* and W 4*f* XPS spectra. The low binding energy features in the films grown at 375 °C are likely due to the presence of metastable 1T'-WSe_2; evidence for the existence of this phase can be seen in the observed RHEED pattern for WSe_2 grown at this temperature (*Figure 3.8a*). Ugeda at al. previously measured the in-plane lattice constant of 1T'-WSe_2 to be 75% greater than the equilibrium 2H phase and thus the difference in the reciprocal lattice spacing for the two phases is apparent in RHEED [106]. The difference in the 2H and 1T' structures can be seen in *Figure 3.8b*.

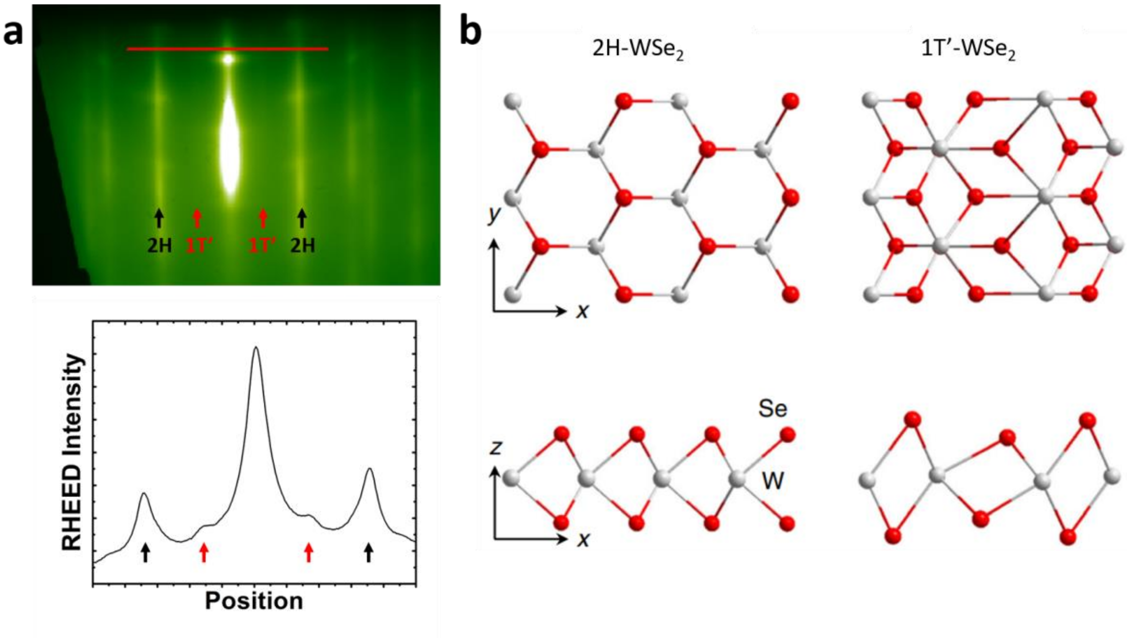

Figure 3.8: a) RHEED pattern and corresponding line profile of WSe_2 synthesized at 375 °C providing evidence of 1T'-WSe_2. Figure adapted from previously published work [101]. b) Structural models of the 2H- and 1T'-WSe_2 polytypes. Apparent in the 1T' structure is 2 nonequivalent Se environments. Image adapted from Chen at al. [107].

Evidence of 1T'-WSe_2 in the thin films grown at 375 °C is further supported by the deconvoluted XPS spectra (*Figures 3.9*). Previous reports have revealed that the presence of 1T'-WSe_2 manifests itself as chemical states to the low binding energy side of 2H-WSe_2 as observed here [106-108]. The origin of two peaks making up the 1T'-WSe_2 component of the Se 3*d* core level is hypothesized to come from the variance in Se bonding environments in the 1T' structure; this variance is expected to result in a difference in charge density associated with each Se atom and thus result in two chemical features (*Figure 3.8b*). In contrast, the bonding environment of all Se atoms is identical in the 2H structure and thus is fit with a single chemical state. In the work presented here, the 1T' structure is found to result in a 0.67 eV chemical shift of the W 4*f* peak to lower binding energy compared to the equilibrium 2H phase; this chemical shift of the W 4*f* core level was found to be the same for both samples produced at 375 °C. Stoichiometry estimates of the synthesized 1T’-WSe_2 were estimated to be 1.87:1 and 1.95:1 for the growths carried out at 375 °C with Se to W BEPRs of 4000:1 and 19500:1, respectively. All Se 3*d* spectra further contain an elemental Se component as a result of sample cooling in the growth chamber with a high background pressure of Se. AFM images for growths carried out at 375 °C are presented in *Figure 3.9* and can be characterized by the absence of large 2D grains (in contrast to films grown at 565 °C) and a high nucleation density. The unique morphology and high nucleation density are likely due to a lack of thermal energy which would suppress adatom diffusion.

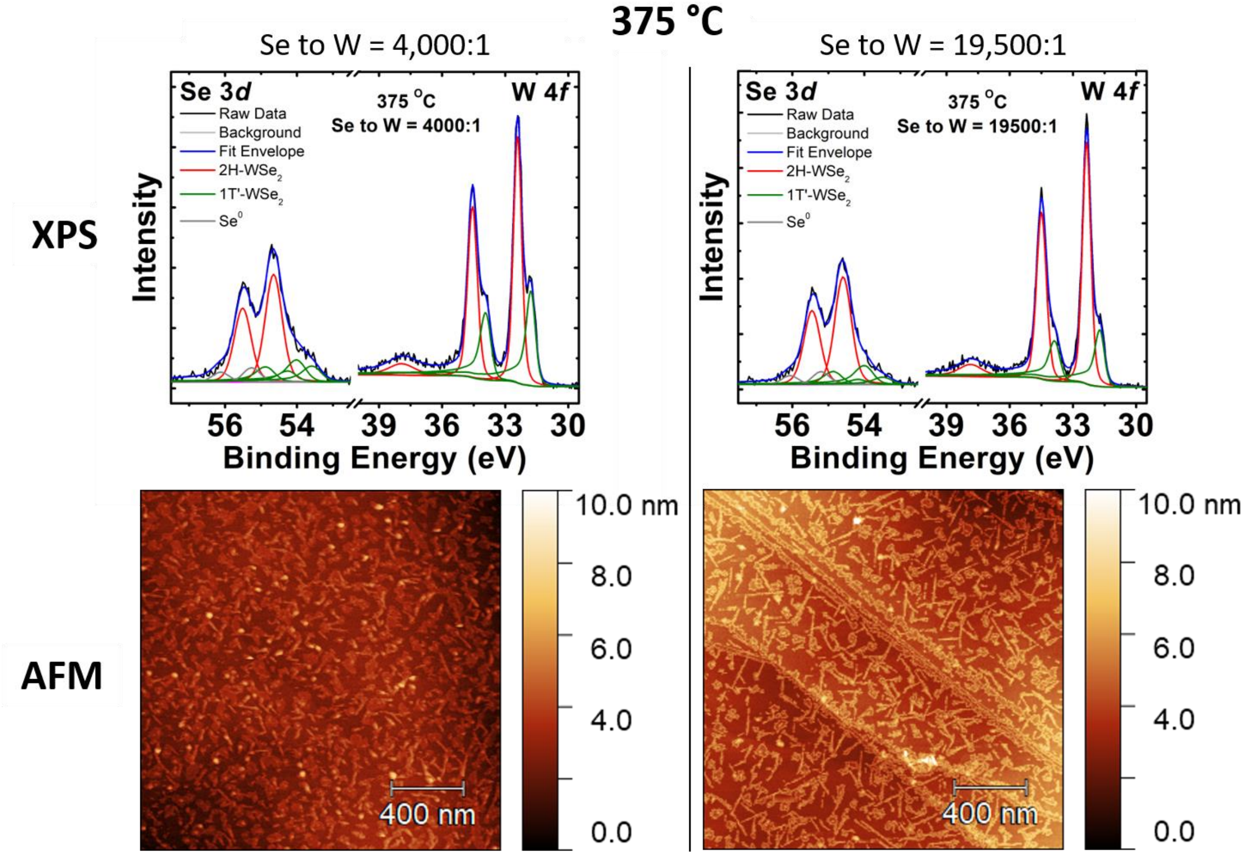

Figure 3.9: Deconvoluted XPS spectra and AFM images of thin films grown at 375 °C under varying Se to W BEPRs. Figure adapted from previously published work [101].

XPS spectra for thin films grown at 750 °C provide evidence for the existence of three chemical states of W: 2H-WSe_2, WSe_{2-x}, and W^0, as shown in the deconvoluted spectra in *Figure 3.10*. A significant decrease in the W^0 peak is seen with increasing the Se to W BEPR, while there was no significant change in the WSe_{2-x} peak. The relatively small changes in the Se 3*d* spectra are consistent with the subtle changes in the WSe_{2-x} features of the W 4*f* spectra. However, the stoichiometry of the WSe_{2-x} component varied with BEPR. Stoichiometry estimates were found to be 1.17: and 0.53:1 (Se to W) for thin films grown at 3000:1 and 20,500:1, respectively. The reason for this stoichiometric variation is not understood, but it does suggest a large composition space exists for the synthesized WSe_{2-x} phase. The AFM images at 750 °C (*Figure 3.10*) reveal a large decrease in the density of metal clusters is observed at an increased BEPR, which agrees with the XPS results in (*Figure 3.10*) which show a decrease in the W^0 component. A closer look at the AFM under high temperature/high BEPR conditions (750 °C, Se/W = 18750:1) reveal that all WSe_2 grains possess W^0 clusters at their center. This suggests that W^0 clusters act as nucleation cites for WSe_2 synthesis at this temperature. This observation is a reasonable assumption if the critical radius of W^0 nuclei is smaller compared to WSe_2 nuclei at 750 °C; this is likely given the tendency for WSe_2 to decompose at temperatures near 750 °C and the extremely high melting point of elemental W [109]. Additionally, Yue et al. calculated the critical nucleus size of W^0 to be ~0.31 nm, roughly an order of magnitude smaller than that of WSe_2, at 500 °C [95]. The reason W^0 formation is not observed at 375 or 565 °C, despite the smaller critical nucleus of W^0 compared to WSe_2, is likely a consequence of greater residence times of Se on the HOPG surface at these temperatures compared to 750 °C. This kinetic limitation prevents W-W bond formation as all available W atoms are in incorporated in to WSe_2 nuclei before stable W^0 are able to form.

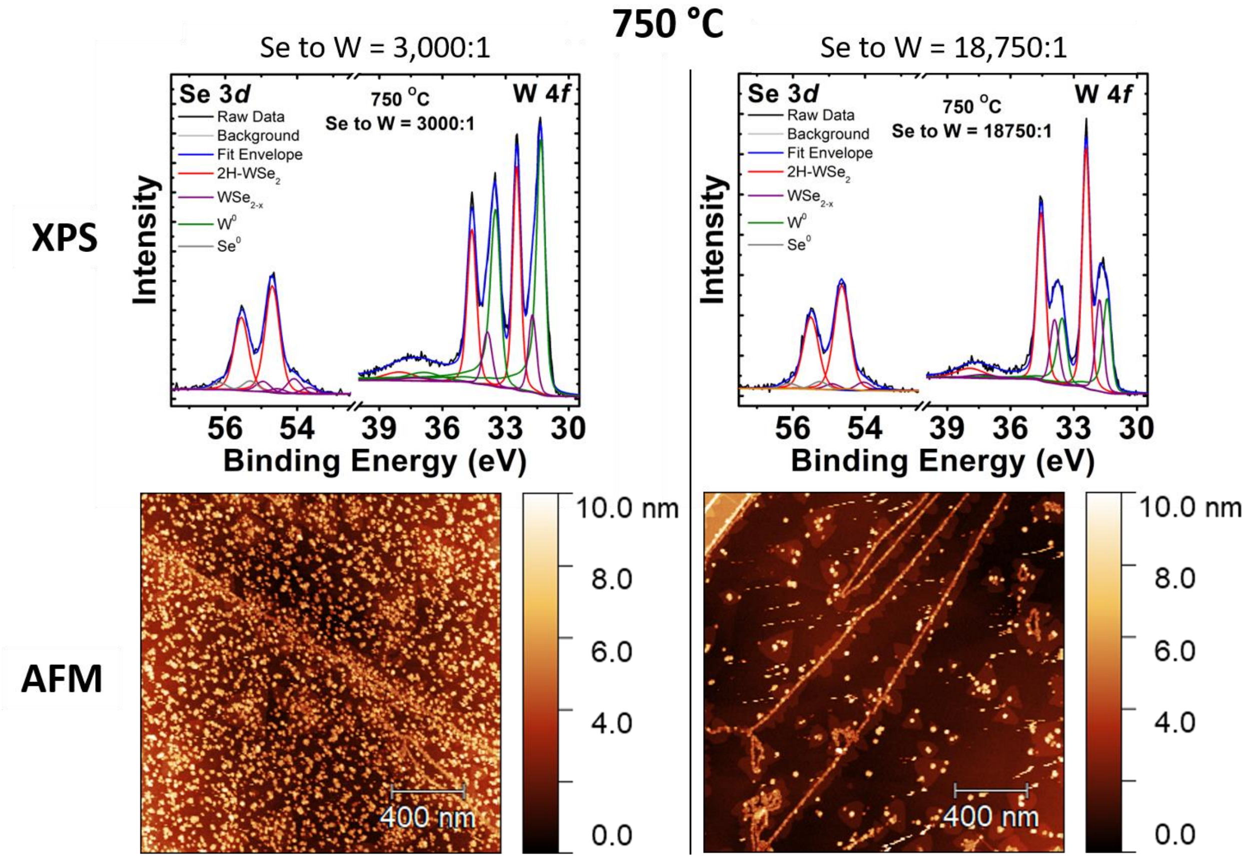

Figure 3.10: Deconvoluted XPS spectra and AFM images of thin films grown at 750 °C under varying Se to W BEPRs. Figure adopted from previously published work [101].

While the XPS of 1T'-WSe_2 and WSe_{2-x} share common XPS features, i.e., additional chemical signatures to the low binding energy side of 2H-WSe_2 in the Se 3*d* and W 4*f* core levels, they are unique in terms of structure and chemistry. First, the growth of 1T'-WSe_2 is limited to temperatures at or below 400 °C and therefore cannot be confused with WSe_{2-x} grown at 750 °C [109]. Due to its metastable character, 1T'-WSe_2 readily coverts to the equilibrium 2H phase above 400 °C [109]. Secondly, RHEED diffraction patterns show convincing evidence for 1T'-WSe_2 in the grown material at 375 °C (*Figure 3.8*). Lastly, the estimated stoichiometries of WSe_{2-x} were found to be Se deficient compared to 1T'- and 2H-WSe_2. Thus, we conclude that the high temperature WSe_{2-x} phase and low temperature 1T'-WSe_2 phase are unique materials. 1T'-WSe_2

is the focus of multiple reports that discuss its synthesis, structure, and stability [106, 107, 109, 110]. In contrast, the structure of WSe_{2-x} is not well understood.

To help elucidate the structure of the WSe_{2-x} phase, density function theory (DFT) was carried out by V. Nilsson and P. Balachandran to compliment the XPS data presented here. Three possible WSe_{2-x} structures were investigated: W_2Se_3 (isotypic to the equilibrium Mo_2S_3 phase), the presence of a high degree of isolated Se vacancies, and the presence of Se vacancy clustering. The W_2Se_3 phase was explored as it is Se deficient with respect to WSe_2 and would place Se in two unique bonding environments explaining the multiple Se chemical features associated with the WSe_{2-x} compound in XPS. However, DFT convex hull analysis predicted that the W_2Se_3 structure is +262.67 meV/atom above the convex hull indicating this phase is unlikely to form and therefore is not the origin of the WSe_{2-x} detected in our material. It should be noted that in contrast to the group VB TMDCs, no chalcogen deficient (metal-rich), self-intercalated phase of WSe_2 (i.e. $W_{1+x}Se_2$) is known to exist and thus is not considered here [111]. Self-intercalated group VB TMDCs will be discussed in the following chapter in the context of $Nb_{1+x}Se_2$. DFT was also used to explore the effect of isolated Se vacancies and Se vacancy clusters on the bonding in WSe_2 (see structures in *Figure 3.11*). From this work, it is revealed that a distribution of W-Se bond lengths arises in the presence of both isolated Se vacancies and Se vacancy clustering. More importantly, it is revealed that that Se vacancy clustering can result in multiple atomic coordinations for Se (*Figure 3.11c*); changes in the atomic coordination of Se will alter the local charge distribution around these atoms and should be detected as unique chemical shifts in XPS if they are present in sufficient quantities. This could explain the two peaks assigned to the WSe_{2-x} state in the Se 3*d* core level as Se atoms will experience atomic coordinations of both two and three W atoms. We know WSe_{2-x} is not simply a high degree of isolated Se vacancies (though Se vacancies in WSe_2

necessarily exist) as isolated Se vacancies would not result in multiple Se atomic coordinations and therefore would not produce additional features in the Se 3*d* spectra as observed here. This DFT work further calculated that the formation energy difference between isolated Se vacancies and Se vacancy clusters were similar (~3.12 meV/atom greater for clustered Se vacancies) and thus both are likely to exist in the grown material. This suggests clusters of Se vacancies in WSe_2 is a plausible origin of WSe_{2-x} detected here; however, while this DFT work supports this hypothesis, there is no experimental confirmation at this time. Lastly, it is possible that, due to the high degree of elemental W clusters that form at 750 °C, the WSe_{2-x} signal observed in XPS originates from the high density of W^0-WSe_2 interface regions which may possess unique chemical character. This work, along with the DFT work carried out by V. Nilsson and P. Balachandran, can be found in our collaborative published work [101].

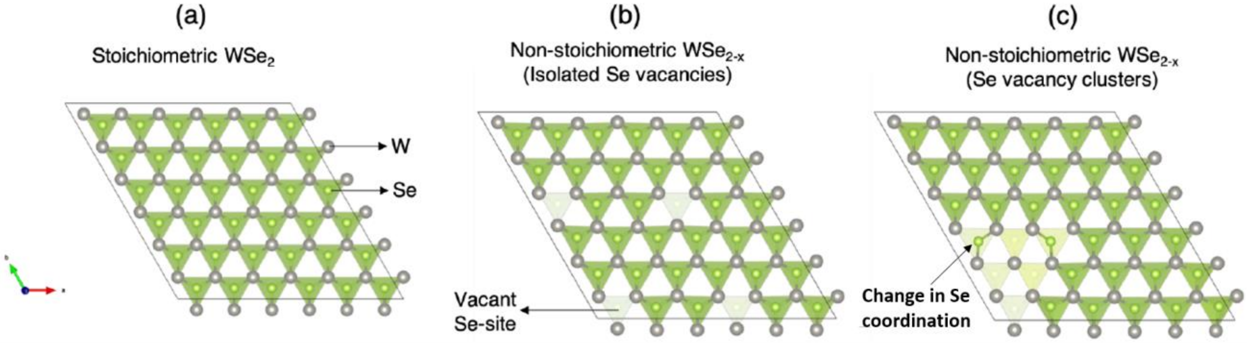

Figure 3.11: The structure of a) stoichiometric WSe_2, b) non-stoichiometric WSe_{2-x} through isolated Se vacancies, and c) non-stoichiometric WSe_{2-x} through Se vacancy clustering. Structures are viewed along the c-axis (normal to WSe_2 basal plane). Structure in *c* uniquely places Se in a 2nd atomic coordination.

3.6. Growth of Transition Metal Disulfides

The growth of transition metal disulfides (MS_2) such as WS_2 and MoS_2 by MBE are less common than the growth of their diselenide counterparts. This is due to the difficulty associated with the high vapor pressure of S in UHV. Elemental S powders evaporate at temperatures near or below typical bakeout temperatures of UHV systems and thus reaching UHV pressures without simultaneously evaporating the S source requires additional considerations. One way of depositing MS_2 by MBE is the use of a valved cracker cell [112]. This type of evaporator has a valve that closes off the cell containing the high vapor pressure element (in this case S) from the rest of the UHV chamber. This type of cell allows for the bake out procedures and fine control of elemental fluxes that cannot be achieved for high vapor pressure materials using the standard effusion cells installed on the MBE system used in this work. A second way to generate a S flux in UHV is the decomposition of S based compounds such as iron pyrite (FeS_2) [113, 114]. In this process, the S based compound is heated to decompose the disulfide into the monosulfide and produce a S flux in the process. Iron pyrite was used as the S source for MBE growth in the McDonnell Lab.

~3-layer WS_2 was grown on 50 nm SiO_2/Si substrates by MBE. It was observed that the conditions required for the successful synthesis of WSe_2 can also be applied to the growth of WS_2. *Figure 3.12* shows a deconvoluted XPS spectra of the S 2*p* and W 4*f* core levels in MBE-grown WS_2. The S to W BEPR was ~5000:1 and the substrate growth temperature was 480 °C. The S 2*p* core level shows the presence of two overlapping core levels: the S 2*p*, which represents a single chemical state attributed to WS_2, and the Se 3*p* core level. The presence of Se in the synthesized WS_2 films is due to contamination associated with depositing WS_2 in a UHV chamber routinely used for the growth of transition metal diselenides as previously discussed. The W 4*f* core level shows the presence of the W 4*f* core level and the W $5p_{3/2}$ which are fit well with a single chemical state attributed to WS_2. The semiconducting nature of the WS_2 film is confirmed by analysis of the valence band spectrum which shows the density of states reduces to a minimum below the Fermi level (0 eV binding energy). The valence band maximum of ~0.9 eV also confirms the Fermi level falls within the known band gap of WS_2 (1.35 eV) [115].

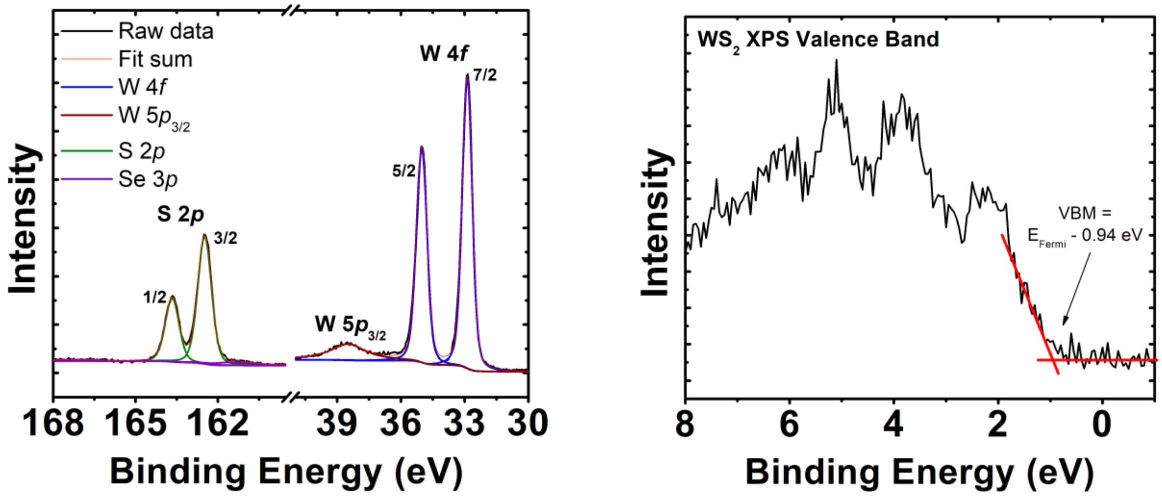

Figure 3.12 XPS spectra of synthesized WS_2 on SiO_2. Fit S 2*p* and W 4*f* core levels indicate a chemically homogeneous film with small levels of Se contamination. The valence band spectrum confirms the semiconducting nature of the grown WS_2 thin film.

The decomposition of FeS_2 as a S source poses unique challenges not experienced with the growth of selenides using an elemental Se source. The elemental Se source produces a constant Se flux for a given temperature of the Knudsen cell and does not show significant growth-to-growth variation. In contrast, the S flux produced through the decomposition of FeS_2 decays over the timescales common to sample synthesis; this is represented in *Figure 3.13* for four different growths using the FeS_2 S-source. *Figure 3.13* shows that the S flux generated can decay to ~50% the starting value over the course of ~120 minutes (typically produces 2-4 layers of WS_2). Additionally, the source temperature to reach a given S flux must be increased from growth to growth which results in an increase of the background pressure during growth. The growth-to-growth increase in required source temperature can be counteracted through replacement of the FeS_2 source, as was done between *Growth 2* and *Growth 3* represented in *Figure 3.13*. However, the decay of the FeS_2 source over time results in a significantly shorter lifetime than an elemental Se source. The decay of the S flux using a FeS_2 source also results in a limit to the amount of WS_2 which can be deposited in a single experiment.

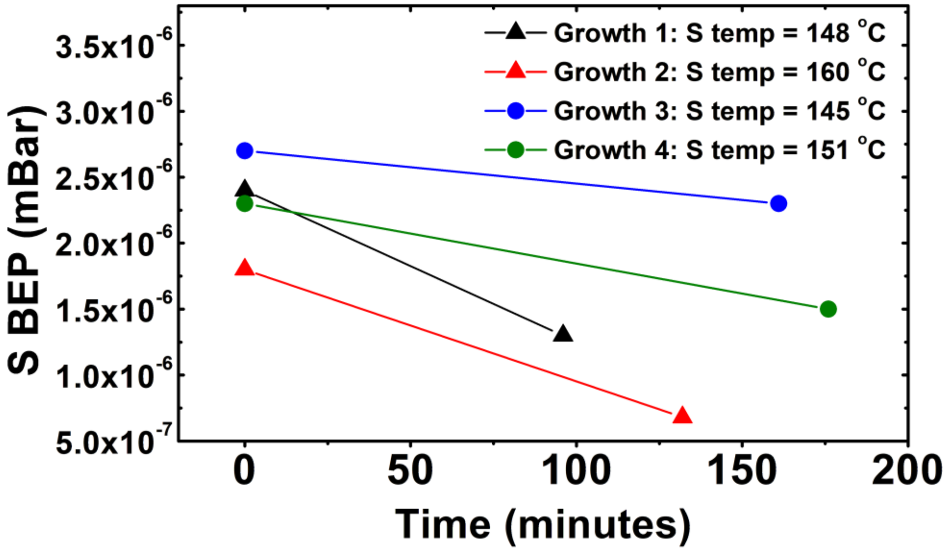

Figure 3.13: S BEP vs time for four WS_2 growths. S source replaced after *Growth 2*.

3.7. Conclusions

To conclude, the work here developed the ability to synthesize high-quality TMDCs by MBE in the McDonnell Lab. This work includes parametric studies that establish the effect of Se to W BEPR and temperature on the growth of WSe_2 by MBE. It was found that BEPRs of ~100:1 are necessary to subdue W^0 formation during growth and that BEPRs an order of magnitude higher are necessary to reduce the amount of WSe_{2-x} to a minimum. We further demonstrate a “Goldilocks zone” for growth temperature to produce 2H-WSe_2. Low temperatures growth results in the formation of metastable 1T’-WSe_2 to form coexistent with the 2H phase and result in poor grain morphology. High temperature growth results in the formation of W^0 and WSe_{2-x}, even in the presence of BEPRs as high as 20,000:1. While this work does not constitute the first published works investigating the growth of WSe_2, it expands on previously reported works investigating greater BEPR and temperature regimes. Growing at elevated temperatures (>600 °C) is commonly employed in WSe_2 synthesis by other methods, e.g., chemical vapor transport and chemical vapor deposition, as high temperature improves adatom mobility resulting in improved grain structure. This result highlights how processing parameters for a given material are dependent on the growth method. Given the decreased processing temperatures for MBE compared to other growth techniques means it may be suitable for back-end-of-line (BEOL) processes; however, a focused effort around the compatible temperatures for BEOL synthesis needs to be carried out. Lastly, we show that the efforts made here can be extended to WS_2.

3.8.Future Work

3.8.1. Exploring Temperature Boundaries of the WSe_2 Growth Window

A limitation in the studies reported in this chapter was precise control over substrate growth temperature. Substrate temperature measurements for this work was carried out using a thermocouple secured to the sample stage. As stated earlier in the chapter, sample to sample variations in growth temperature may have been the reason that variability (but no clear trend) in average grain size and degree of 2nd layer nucleation were observed with changing Se to W BEPR. In works since (such as the growth of $NbSe_2$ discussed in the next chapter), we have adopted the practice of using an optical pyrometer resulting in a more precise reading of substrate temperature.

Figure 3.15 shows the effect of substrate temperature on the chemistry of grown WSe_2; most of this data was previously discussed, but now includes data corresponding to the growth of WSe_2 at 650 °C which demonstrates nearly identical chemistry to the film produced at 565 °C. We know the lower temperature limit for growth of uniform 2H-WSe_2 is ~400 °C; below this temperature 1T'-WSe_2 starts to form. These data points suggest a temperature processing window of ~250 °C exists. With the high precision temperature control of the pyrometer, this temperature window of 2H-WSe_2 synthesis can be further investigated. Two questions worth investigating are: 1) What is the upper temperature limit beyond which WSe_{2-x}/W^0 starts to be observed in detectable quantities? 2) How does the grain size/morphology and degree of 2nd layer nucleation vary in this processing space. This study will help define limits of the surface/grain morphologies that can be expected from MBE-grown 2H-WSe_2. The results will define the suitability of this technique for application in both the research and industrial sectors.

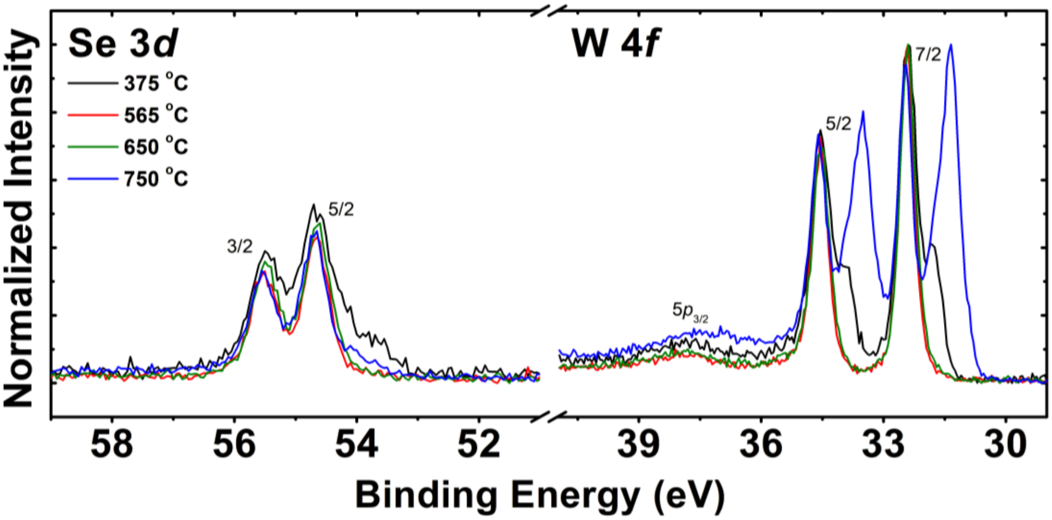

Figure 3.15: XPS of the W 4*f* core level in WSe_2 as a function of growth temperature.

3.8.2. Growth of Ternary and Quaternary Alloys with Controlled Stoichiometries

In this work, we have demonstrated the growth of WSe_2 and WS_2. The MBE tool in the McDonnell Laboratory is equipped with two electron beam evaporators and two effusion cells. This allows for both the co-deposition of transition metals and chalcogen (S and Se) sources which allows for the alloying or doping of grown TMDCs. Alloying/doping of TMDCs is one route to tuning the material's properties. This has been shown recently for Nb-doped WSe_2 grown by CVT in which the carrier density was altered by more than three orders of magnitude [116]. One aspect of TMDC alloy growth that is not understood is the relative degrees of incorporation between different chalcogen species during co-deposition, i.e., the growth of $MSe_{2-x}S_x$. The generation of Se and S fluxes in this work are carried out through unique processes. Se flux are produced through the sublimation of elemental Se and S fluxes are generated through the decomposition of FeS_2. The Se flux is known to exist in Se_x molecules of varying size (x = 1-8) which have different probabilities of being incorporated into the growing film [103]. The exact nature of the S flux is not known (though both S_1 and S_2 are detected with the RGA during MS_2 synthesis). The relative sticking coefficient of each chalcogen source will be impacted by the other as a limited number of chalcogen lattice sites are available during growth (which is limited by the metal source flux). Therefore, controlling the stoichiometry in $MSe_{2-x}S_x$ films is likely not trivial. Investigating the competing propensities of each chalcogen source to be incorporated during $MSe_{2-x}S_x$ growth will facilitate the growth of alloys with predictable stoichiometries.

4. The Growth of Niobium Selenide by Molecular Beam Epitaxy

4.1.Purpose

The purpose of this chapter is to report on studies of the growth of $NbSe_2$ by MBE. This chapter was motivated by the prospect of using $NbSe_2$ for thermomagnetic energy harvesting. However, the synthesized $NbSe_2$ was found to deviate from the expected chemistry and structure which resulted in a rigorous study of the material's growth. In contrast to the W-Se system discussed in the previous chapter, the Nb-Se system is known to support a large number of equilibrium compounds [117, 118]. Furthermore, $NbSe_2$ is known to exist over a greater composition range compared to WSe_2 (discussed further below) [111]. These differences make the growth of $NbSe_2$ less trivial than the growth of WSe_2. Utilizing techniques such as XPS, XRD, and TEM, we conclude that our MBE-grown $NbSe_2$, grows in a Nb-rich, self-intercalated (SI) variety where excess Nb atoms populate the vdW gap between adjacent $NbSe_2$ layers. This Nb-rich phase, written $Nb_{1+x}Se_2$, was found to form under a large processing space and under no synthesis conditions was stoichiometric $NbSe_2$ (in the absence of SI) obtained.

We begin this chapter by discussing initial chemical and morphological studies into $NbSe_2$ grown on HOPG by MBE. We identify a chemical variability that exists across a wide range of processing conditions and a correlation between growth temperature and surface morphology. Next, we discuss a more detailed study of $NbSe_2$ grown on SiO_2 in which we investigate changes in the physical structure with XRD and identify the correlation between the physical structure and electrical conductivity. We observe that Nb SI is detrimental to the material's in-plane electrical conductivity. Lastly, we also comment on the scaling of the electrical conductivity in the sub-15 nm regime.

4.2. The Growth of $NbSe_2$ on HOPG

To study the effect of Se to Nb BEPR and substrate temperature on the MBE growth of $NbSe_2$, ~2-layer $NbSe_2$ was grown on HOPG and the resulting chemistry and surface morphology was studied with XPS and RHEED/AFM, respectively. *Figure 4.1* shows the XPS and RHEED taken of $NbSe_2$ thin films as a function of BEPR at a growth temperature of 470 °C; the XPS spectra of each sample are normalized to the maximum intensity of the Nb 3*d* core level. This temperature and BEPR regime were chosen as they resulted in chemically uniform WSe_2 and WS_2 growth as discussed in the previous chapter. However, in contrast to the growth of WSe_2 and WS_2, the $NbSe_2$ thin films are found to result in broad XPS features, indicative of chemical inhomogeneity, and spotty RHEED patterns, indicative of 3D growth, i.e., rough surfaces. Also apparent is the lack of change in the XPS and RHEED with altering the BEPR.

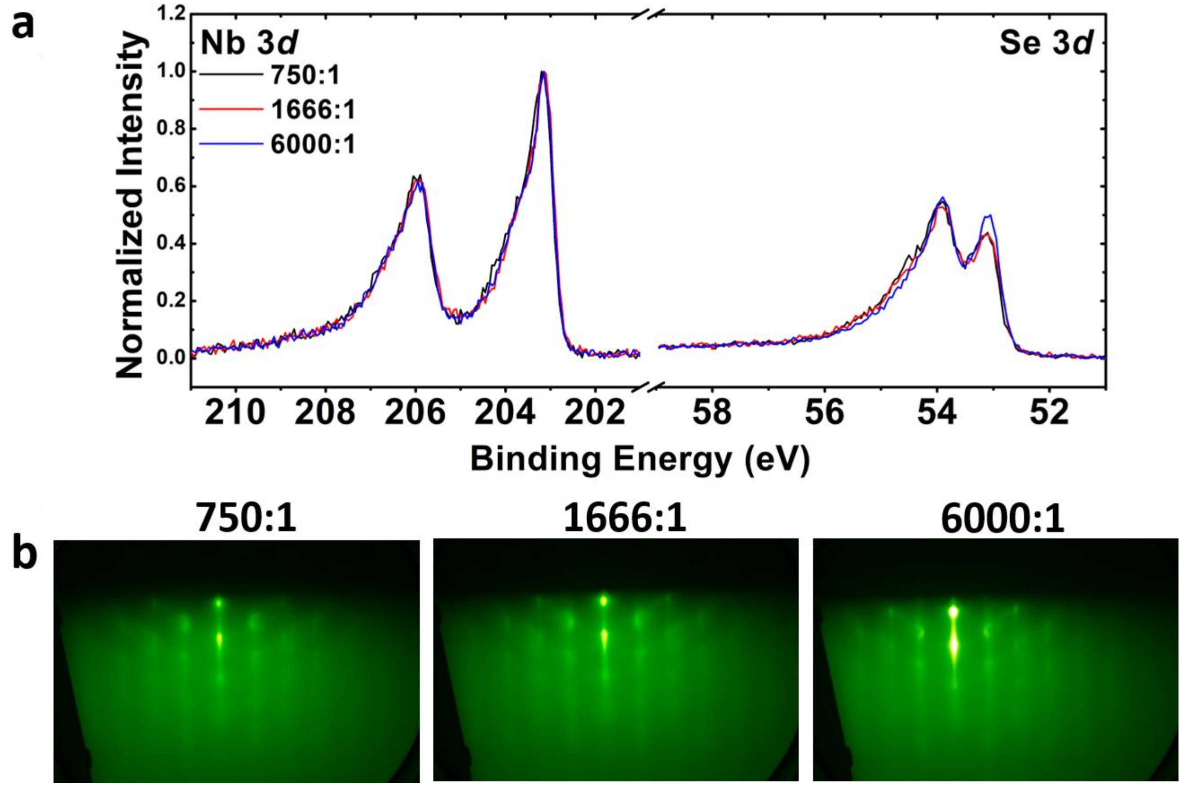

Figure 4.1: a) XPS spectra of $NbSe_2$ bilayers produced at three different BEPRs (BEPRs inset in figure legend). b) RHEED patterns of the same three $NbSe_2$ samples. Growth temperature of 470 °C was used for all samples.

$NbSe_2$ films were also grown and studied as a function of growth temperature in the range of 370 to 770 °C; for this set of samples, the Se to Nb BEPR was held at ~1600:1. The XPS spectra are presented in *Figure 4.2*. Regardless of the temperature used, no Nb^0 was found to form. The intensity of the Se 3*d* core level decreases at higher growth temperatures indicating these films were more Se deficient (Nb rich). In contrast to the WSe_2 films discussed in the previous chapter, we find that similar chemistries exist over a larger temperature range (though the overall stoichiometry varies). At no point do we observe XPS spectra indicitive of a chemically homogeneous sample.

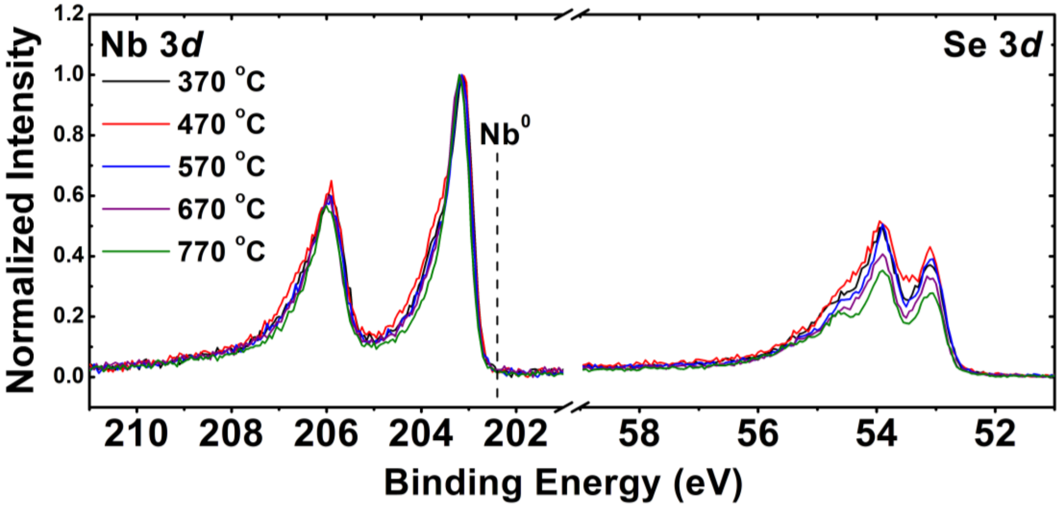

Figure 4.2: XPS spectra of ~2-layer $NbSe_2$ films grown as a function of temperature on HOPG. Se to Nb BEPR of ~1600:1 used for all samples.

The ~2-layer $NbSe_2$ films were also studied with RHEED and AFM and are presented in *Figure 4.3* for films grown at 370, 570, and 770 °C. The change of the RHEED pattern from spotty at 370 °C to streaky at 770 °C implies a change in the surface morphology. A transition between the two patterns is visible at 570 °C, where subtle spots are apparent (marked with yellow arrows). The streaky RHEED pattern observed at 770 °C is typical of layered TMDCs. The AFM of the same three samples supports the conclusions drawn from RHEED analysis. With increasing temperature, we see a decrease in surface roughness with RMS values of 1062, 899, and 675 pm for temperatures 370, 570 and 770 °C, respectively. Also, apparent is a large dependence of the grain size with temperature. Grains measure 10's of nanometers across at 370 °C and hundreds of nanometers across at 770 °C, roughly an order of magnitude increase. As discussed in context of RHEED, 570 °C shows a transition in the growth morphology; the AFM reveals large flat areas as observed at 770 °C, but also the tall needle/rod like structures observed at 370 °C. For the film grown at 770 °C, there are additional conclusions which can be drawn from the AFM image. First, significant growth of the 2nd $NbSe_2$ layer is observed prior to the completion of the first monolayer.

The 2nd layer of $NbSe_2$ often extends to the boundary of the 1st layer which, in many cases, end up sharing the same perimeter (that is, there is no traditional wedding cake structure). The second observation is a lack of screw dislocations. In similar samples grown on SiO_2/Si substrates numerous screw dislocations were observed by scanning tunneling microscopy (STM). This suggests that the substrate will have an impact on the growth normal to the substrate and, in part, dictate whether it is initiated through second layer nucleation and growth or through the propagation of screw dislocations. The former looks most likely for films grown at 770 °C on HOPG while the latter seems more likely for films grown on SiO_2.

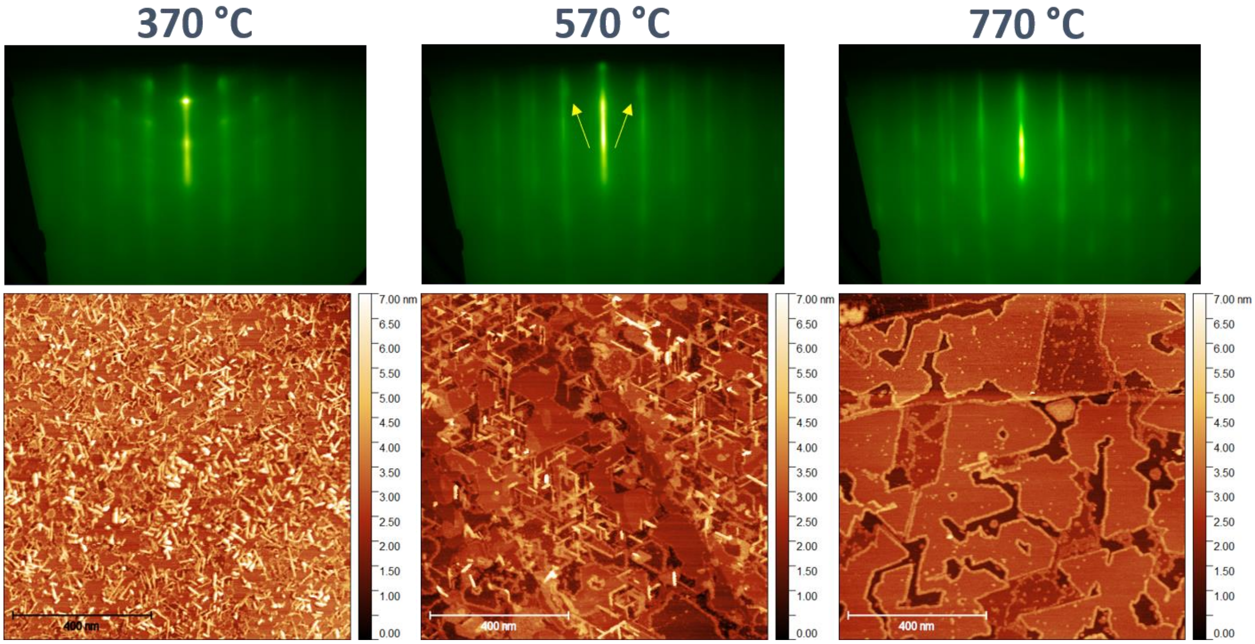

Figure 4.3: Top) RHEED and bottom) AFM of ~2-layer $NbSe_2$ films grown on HOPG at 370, 570, and 770 °C (from left to right). All inset scale bars read 400 μm. Se to Nb BEPR of ~1600:1 used for all samples.

The progression of RHEED in films grown at 370 °C is presented in *Figure 4.4 (top)* and shows that the film growth is initially flat and adopts the island growth nature as the film progresses beyond the monolayer (ML); the hazy appearance of the RHEED in the *<ML* and *~ML* frames is

due to the data being collected at growth temperature rather than room temperature as in the final frame. This progressions shows that the pattern associated with $NbSe_2$ starts out predominately consisting of streaks and adopts spots as the growth continues. This result shows that the growth at 370 °C is best described as *layer + island growth*, i.e., *Stranski–Krastanov* growth. In contrast, RHEED of the growth at 770 °C remains streaky at ~20-layer thicknesses (*Figure 4.4 (bottom)*). Early work by Yamamoto et al. showed that multilayer $NbSe_2$ films resulted in a spotty RHEED pattern [119]. This was likely a consequence of the relatively low substrate temperature (500 °C) employed in their work. Here we show that the increased growth temperature of 770 °C retains a smooth film in 20-layer films.

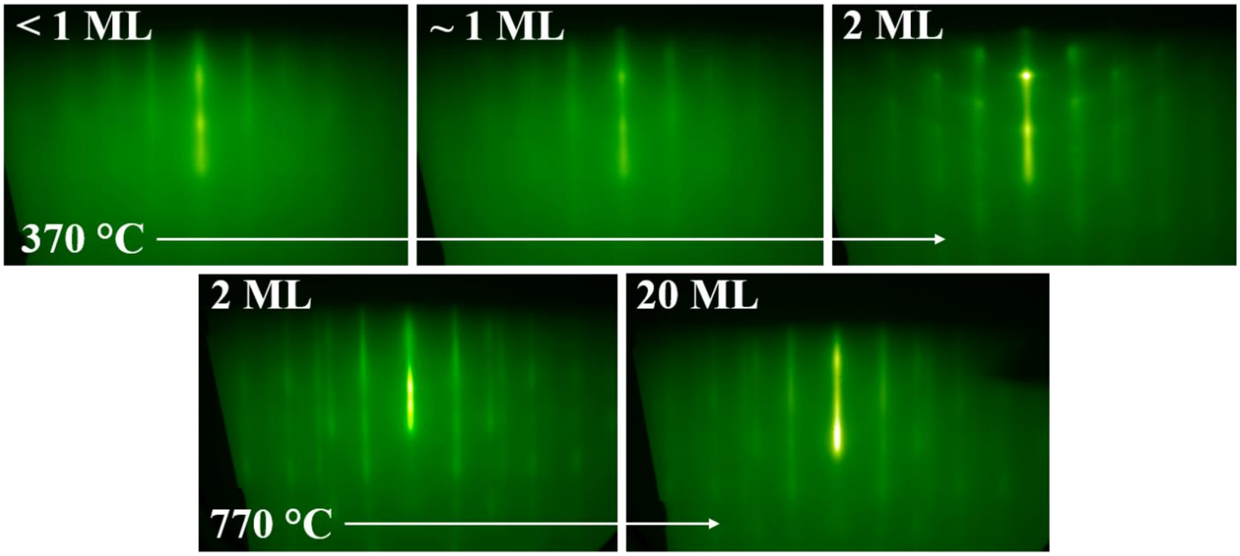

Figure 4.4: Top: Progression of the RHEED during the initial stages of growth at 370 °C. Spotty pattern dominates as growth continues past initial monolayer. Bottom: RHEED pattern of $NbSe_2$ after 2 and 20 monolayers (ML). Two samples produced under identical conditions with the exception of growth time. The streaky RHEED pattern at 20 ML indicates the continued 2D growth mode when growing at 770 °C. Se to Nb BEPR was held at ~1600:1 for all samples.

Lastly, RHEED is further employed to extract the in-plane lattice constant of the grown material. This is acomplished through analysis of the RHEED pattern of a partial monolayer $NbSe_2$

on HOPG. Due to the growth of $NbSe_2$ on HOPG proceeding by van der Waals epitaxy, each material, to a good approximation, will retain their bulk lattice constant values, even at monolayer $NbSe_2$ thicknesses. By fitting the RHEED intensity profile (*Figure 4.5*) and knowledge of the lattice constant of HOPG at 2.46 Å, the lattice constant of $NbSe_2$ is estimated to be 3.46 Å. This is in good agreement with the bulk 2H-$NbSe_2$ lattice constant of 3.445-3.446 Å [120, 121]. This result suggests our grown $NbSe_2$ is structurally consistent with the bulk $NbSe_2$ despite the chemical variability observed in the XPS spectra discussed previously.

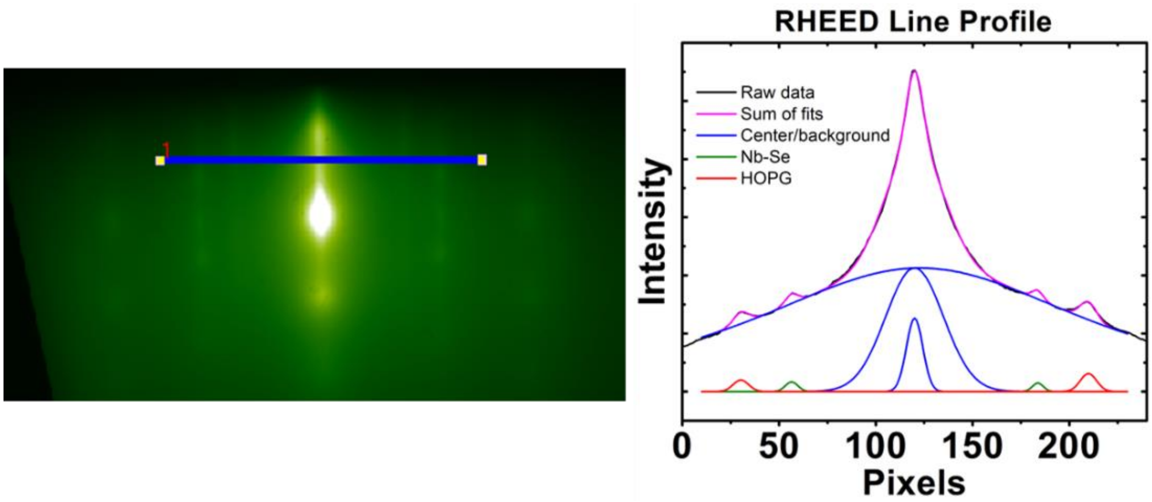

Figure 4.5: Partial monolayer growth of $NbSe_2$ on HOPG. Line profile of RHEED intensity shows signatures from both the epilayer and substrate allowing the in-plane $NbSe_2$ lattice constant to be estimated. Sample grown with substrate at 470 °C and Se to Nb BEPR of 1600:1

The work discussed in this section highlights the consistentcy in the observed chemistry in the $NbSe_2$ films through a wide range of BEPRs and substrate temperatures. However, the work reveals a significant dependence of the films' morphology on substrate temperature. $NbSe_2$ synthesized at high temperature (770 °C) showed a large decrease in surface roughness and substantial increase in grain size (*Figure 4.3*). Additionally, growing at 770 °C resulted in the uniform 2D growth of $NbSe_2$ (opposed to 3D growth observed at lower temperatures) for ~20 ML thick films (*Figure 4.4*). For these reasons, the studies in the following sections, which investigate the structure and cooresponding effects on the electrical resistivity, utalize a synthesis temperature of 770 °C.

4.3. The Growth of $NbSe_2$ on SiO_2 and Identification of the $Nb_{1+x}Se_2$ Phase

In this section, we report on studies investigating the growth of $NbSe_2$ on insulating 285 nm SiO_2/Si substrates which allows for the measurement of the material's electrical resistivity. The films are grown to thicknesses of ~10 nm over the course of 5 hours; this increased thickness over the ~2-layer films grown on HOPG in the previous section allows for collection of the out-of-plane XRD reflections facilitating the structural characterization of the films.

The XPS spectrum of a ~10 nm $NbSe_2$ thin film is presented in *Figure 4.6*. Also in *Figure 4.6* is the XPS spectrum of a bulk 2H-$NbSe_2$ sample which we use as a reference; this reference sample was grown by chemical vapor transport (CVT) at the National Institute of Standards and Technology (NIST) and is assumed to be a 2:1 stoichiometry. Comparing the two spectra, additional features are present in the spectrum of the MBE-grown $NbSe_2$ thin film; this difference is more pronounced in the Se 3*d* core level. Additionally, the MBE-grown $NbSe_2$ film is Nb-rich compared to the CVT reference sample having an estimated stoichiometry of $Nb_{1.18}Se_2$; this estimation was calculated using the total Nb 3*d* and Se 3*d* peak areas with RSF values established using the CVT reference sample. For details regarding core level fitting and stoichiometry calculations, refer to *Section 7.1-7.2*.

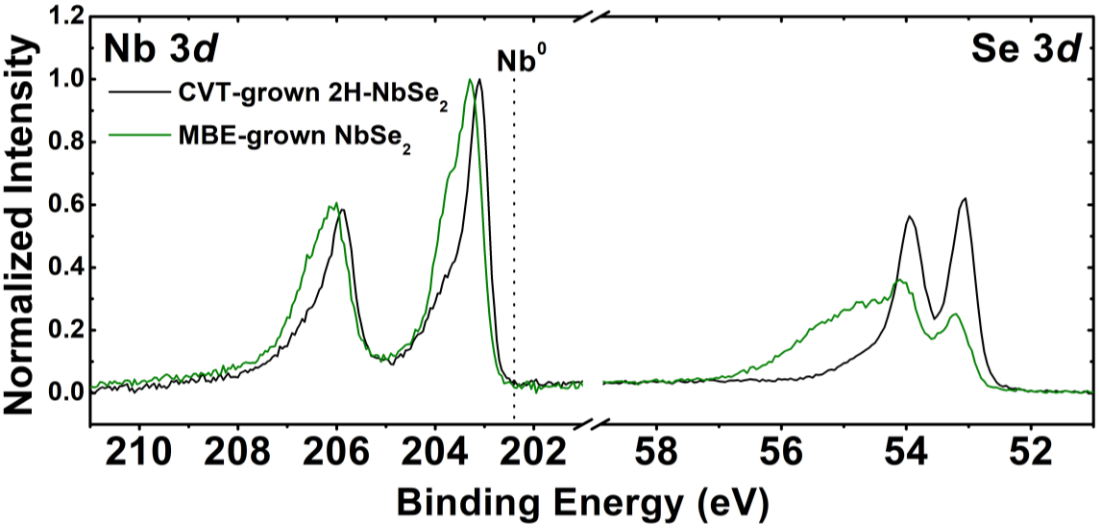

Figure 4.6: XPS spectra of CVT 2H-$NbSe_2$ (black) and MBE-grown $NbSe_2$ (green). MBE-$NbSe_2$ thin film grown with a Se to Nb BEPR of 1600:1.

Figure 4.7 shows symmetrical, out-of-plane XRD collected from the same ~10 nm $NbSe_2$ film and CVT grown reference sample presented in *Figure 4.6*. For both samples, only the out-of-plane, i.e., *00l*, peaks are present indicative of highly ordered samples in which the c-axis is parallel to the sample surface normal. Compared to the CVT pattern, the measured reflections of the MBE-grown $NbSe_2$ pattern are significantly broader. This is attributed to Scherrer broadening which is consistent with a ~10 nm thick sample. It is also apparent that the *00l* reflections of the MBE-grown materials are to lower 2θ angles than the CVT sample. This implies an expanded c-lattice parameter in the MBE-grown $NbSe_2$ compared to the CVT sample. Estimates for the lattice constants of the two materials are 12.54 Å and 13.06 Å for the CVT and MBE-grown materials, respectively. These estimates were made through analysis of the *00l* reflections using the Nelson-Riley extrapolation method [122]. The lattice constant estimate of the CVT samples is in good agreement with the lattice constant of stoichiometric 2H-$NbSe_2$ reported to be 12.54-12.55 Å [117, 121, 123]. Additional features, labeled *substrate/stage*, are present in the analysis of bare SiO_2/Si substrates and are therefore not due to our MBE-grown $NbSe_2$. XRD of the bare SiO_2/Si substrate is presented in *Section 7.3*.

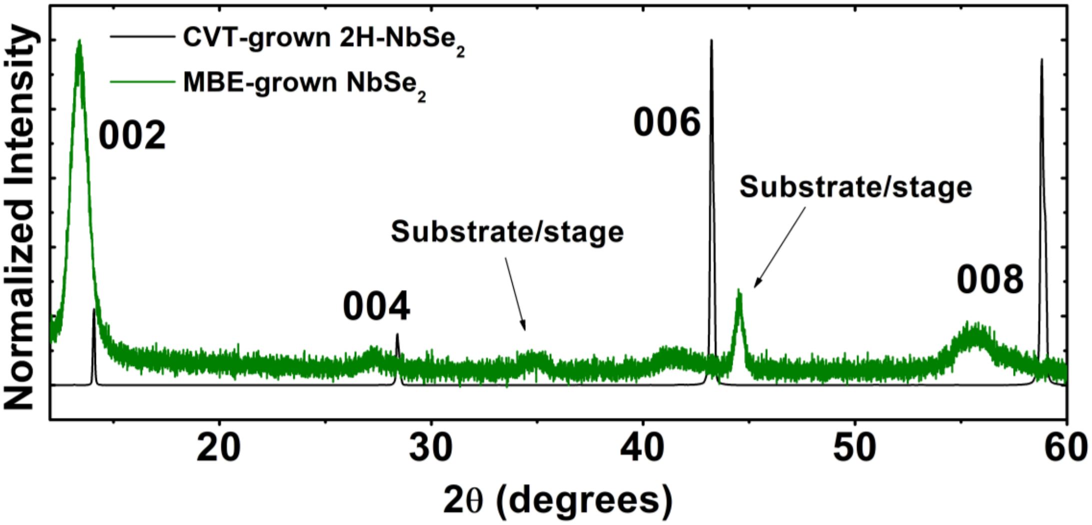

Figure 4.7: XRD of CVT-grown 2H-$NbSe_2$ (black) and ~10 nm MBE-grown $NbSe_2$ on SiO_2 (green). MBE-$NbSe_2$ thin film grown with a Se to Nb BEPR of 1600:1.

The MBE-grown $NbSe_2$ was imaged by HRTEM and is presented in *Figure 4.8* at two different magnifications; the images were taken along the Si $[\bar{1}10]$ zone axis of the SiO_2/Si substrate. Observed in the lower magnification image (*Figure 4.8a*) are the SiO_2 substrate, the NbO_x layer due to atmospheric exposure, and Ir and Pt layers intentionally deposited as part of sample preparation prior to HRTEM imaging. HRTEM reveals a layered film which is consistent with the XRD patterns which showed only *00l* reflections. The film is also uniform and no unexpected structures are observed; the rightmost part of the film in *Figure 4.8a* is consistent with the presence of a screw dislocation known to exist in our $NbSe_2$/SiO_2 films. *Figure 4.8b* is a higher resolution images taken of the same sample after application of an average background subtraction filter (ABSF). Appearent in this image is a periodicity of 4 atoms along the c-axis. In stoichiometric 2H-$NbSe_2$ the expected periodicity along the c-axis is expected to be 3 atoms. This image highlights a structural deviation in our MBE-grown $NbSe_2$ from the expected structure.

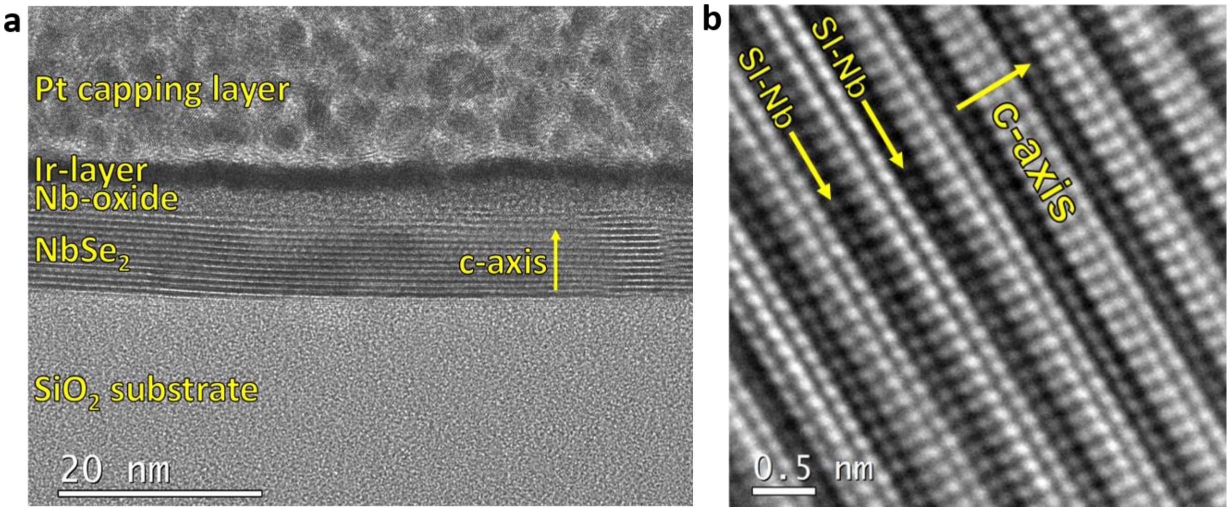

Figure 4.8: HRTEM images of ~10 nm MBE-grown $NbSe_2$ grown on SiO_2. MBE-$NbSe_2$ thin film grown at BEPR of 1600:1. Images were taken along the Si $[\bar{1}10]$ zone axis of the SiO_2/Si substrate.

STEM was used to further investigate the atomic structure of the MBE-grown $NbSe_2$; STEM analysis was carried out on a $NbSe_2$ thin film grown with a BEPR of 5:1 (BEPRs of 5:1 and greater showed qualitatively similar XPS and RHEED patterns as will be discussed in *section 4.4*). The high angle annular dark field (HAADF) and bright field (BF) STEM images employing a ABSF are presented in *Figure 4.9a* and *4.9b*, respectively. Both the HAADF and BF images are presented for clarity; the HADDF imaging provides superior resolution while BF provides a superior depth of field. To guide the eye, a pair of adjacent $NbSe_2$ layers are highlighted with red boxes in the images. The stacking of the $NbSe_2$ layers along the c-axis is consistent with 2H-$NbSe_2$. Also observed in the images is a weak periodic signal originating in the vdW gap of the material (labeled SI-Nb in the images) implying a periodic array of atoms in the gap. The presence of additional atoms in the vdW gap is consistent with the observed HRTEM imaging which revealed a periodicity of 4 atoms along the c-direction, i.e., normal to the $NbSe_2$ layers.

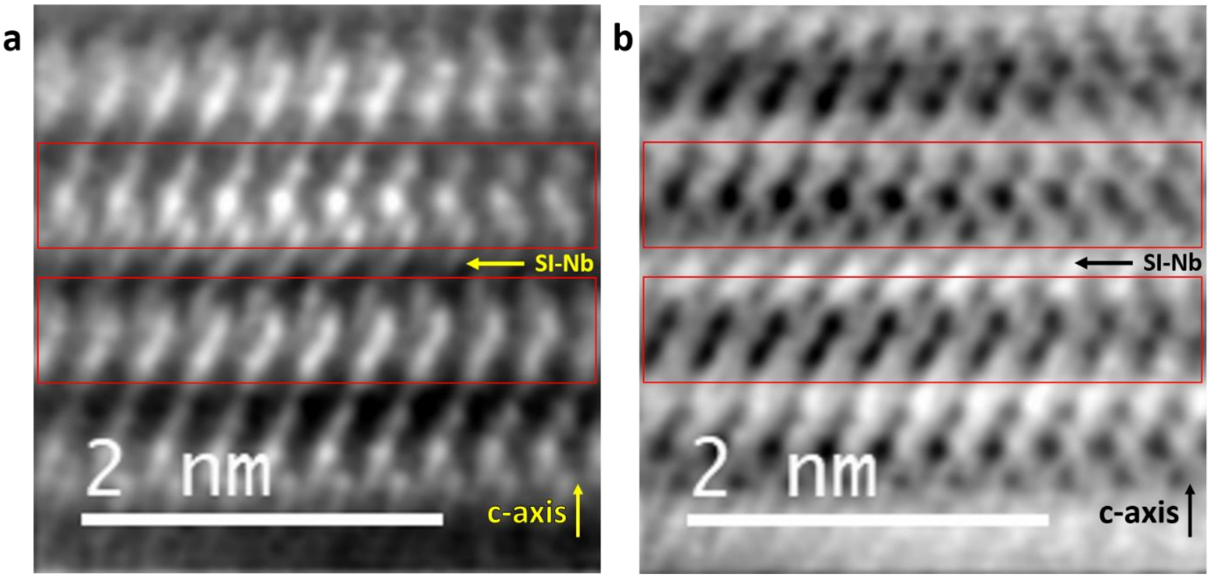

Figure 4.9: a) HAADF and b) BF STEM images of ~10 nm MBE-grown $NbSe_2$ grown on SiO_2. Red boxes highlight individual $NbSe_2$ layers which are separated by additional atoms, marked SI-Nb. MBE-$NbSe_2$ thin films grown at Se to Nb BEPR of 5:1 for STEM imaging.

XPS and XRD analysis together suggest the MBE-grown $NbSe_2$ is Nb-rich and has an expanded c-lattice parameter compared to stoichiometric, 2H-$NbSe_2$. Furthermore, HRTEM and STEM imaging reveal a periodicity of 4 atoms along the c-direction instead of 3 atoms as expected in stoichiometric $NbSe_2$. These observations are consistent with the synthesis of self-intercalated (SI) $Nb_{1+x}Se_2$. The estimated stoichiometry of our MBE-grown $NbSe_2$ falls within the known stoichiometry range for the bulk $Nb_{1+x}Se_2$ phase ($0 < x < 0.29$) [121]. In the $Nb_{1+x}Se_2$ phase, excess Nb atoms are known to sit at octahedral sites in the vdW gap between adjacent $NbSe_2$ layers [123, 124]. This structure is presented as a ball and stick model in *Figure 4.10*. In this model, the blue and grey spheres represent Nb and Se atoms of a given $NbSe_2$ slab, respectively. The orange spheres represent SI Nb atoms; the partially orange filling of these spheres represent partial occupancy.

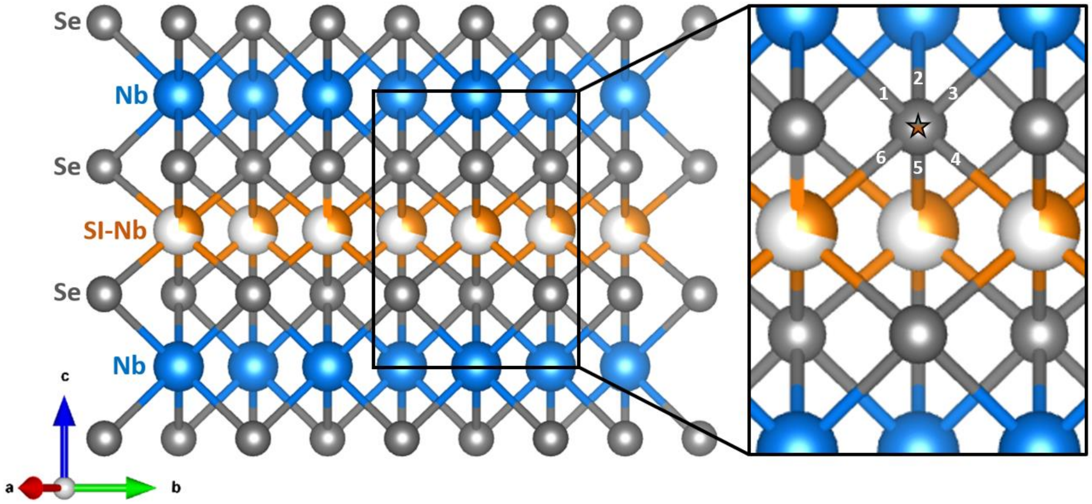

Figure 4.10: Ball and stick structural model of $Nb_{1+x}Se_2$ phase viewed along the [210] axis. Se atoms are grey in color. Nb atoms originating from the $NbSe_2$ slab are blue. SI Nb atoms are white with a partially shaded in orange area to represent partial occupancy. Right-side of the image highlights how the coordination of a given Se atom (marked with star) changes in the presence of 1, 2 or 3 SI-Nb atoms. Grey/blue lines represent bonds between Se and Nb of a given layer. Grey/orange lines represent bonds between Se and SI-Nb atoms. Ball and stick model created in VESTA [30]. Model adapted from Sidoumou et al. [125].

The chemical variability observed in XPS (*Figure 4.6*) can be understood through knowledge of how the local chemical environment changes in the presence of Nb intercalants; Selte and Kjekshus previously investigated the effect of SI on the coordination of atoms in metal-rich TMDCs; it will be further discussed here in the context of $Nb_{1+x}Se_2$ and aided by the inset in *Figure 4.10* [121]. In stoichiometric $NbSe_2$, the coordination of all Se atoms is 3. However, the coordination of Se atoms changes from 3 to 4, 5, or 6 in the presence of 1, 2, or 3 adjacent Nb intercalants, respectively. In contrast, the coordination of all Nb atoms is 6, regardless of whether a Nb atom is an intercalant or part of a $NbSe_2$ layer. A change in the atomic coordination of Se atoms will alter the atom's oxidation state and therefore manifest itself as a unique chemical shift in XPS. An XPS spectra will include the superposition of all detected oxidation states in a sample and thus, in the presence of partial SI, multiple unique chemical shifts are expected to be present in the XPS spectra. From the XPS spectra is apparent that the Se 3*d* feature associated with stoichiometric $NbSe_2$ is at ~53.1 eV with additional features at higher binding energies associated with SI. Variation in the Nb 3*d* spectra is more subtle and likely a consequence of 2nd neighbor interactions. The interpretation of the XPS data presented here is similar to that of Bonilla et al., who observed a high binding energy component of the Se 3*d* core level in SI-$V_{1+x}Se_2$; this observation was attributed to a change in atomic coordination of the Se atoms in the presence of SI [126].

XPS of $Nb_{1.27}Se_2$ was previous reported by O. Khyzhun [127]. In contrast to the work here, no significant broadening of the Se or Nb core levels were observed compared to the stoichiometric $NbSe_2$ compound. The reasoning for the discrepancy in this work and data presented from our MBE-grown samples is not fully understood. However, it may be due to the difference in XPS resolution between the two studies. The work by O. Khyzhun was carried out using a conventional Mg kα x-ray source. In contrast, the work here is collected using a monochromated Al kα x-ray source which results in a significantly higher resolution for our XPS data. Additionally, the work by O. Khyzhun was carried out on bulk crystal in contrast to the thin films studied here. This highlight two significant differences between the two works which may account for the different observations.

4.4. The Effect of BEPR on the Chemistry and Electrical Conductivity of $Nb_{1+x}Se_2$

In the previous section, we identified the presence of Nb SI in the MBE-grown $Nb_{1+x}Se_2$ thin films. In this section, we explore the degree of control over SI through modulation of the BEPR; this is done by maintaining a constant Nb BEP and varying the Se BEP for each sample. We investigate the effects of varying the BEPR on the chemistry and physical structure with XPS and XRD, respectively. Lastly, we also investigate the effect of Nb SI on the electrical resistivity of the grown $NbSe_2$ films.

The dependence of the chemistry on the Se to Nb BEPR was studied with XPS (*Figure 4.11* (*Top*)). The BEPR was varied from 0:1 to 45,000:1. Though the 0:1 growth was carried out without an intentional Se flux, i.e., the Se source was left unheated, a background pressure of Se species remain in the chamber due to the high vapor pressure of Se and large Se pressures typically used to deposit TMDCs in this MBE system. This background pressure of Se species can be detected with a residual gas analyzer and suggests an effective BEPR of ~0.001:1. The XPS spectra reveal 3 distinct spectra shapes with varying BEPR. Using a BEPR of 0:1 the majority of the film is Nb^0 with some contribution from a $NbSe_x$ compound. At a BEPR of 2:1 a material with a roughly 1:1 stoichiometry is produced. The XPS spectra of this sample can be fit with a single chemical state. However, the RHEED pattern is diffuse and show no evidence of a crystalline nature. BEPRs of 5:1 and greater all share common XPS spectral line shapes and RHEED patterns; the change in observed RHEED patterns between growths carried out at BEPRs of 2:1 and 5:1 is presented in *Figure 4.11* (*bottom*). At BEPRs of 5:1 and higher the variability in the films is subtle with compositions ranging from $Nb_{1.15}Se_2$ to $Nb_{1.23}Se_2$.

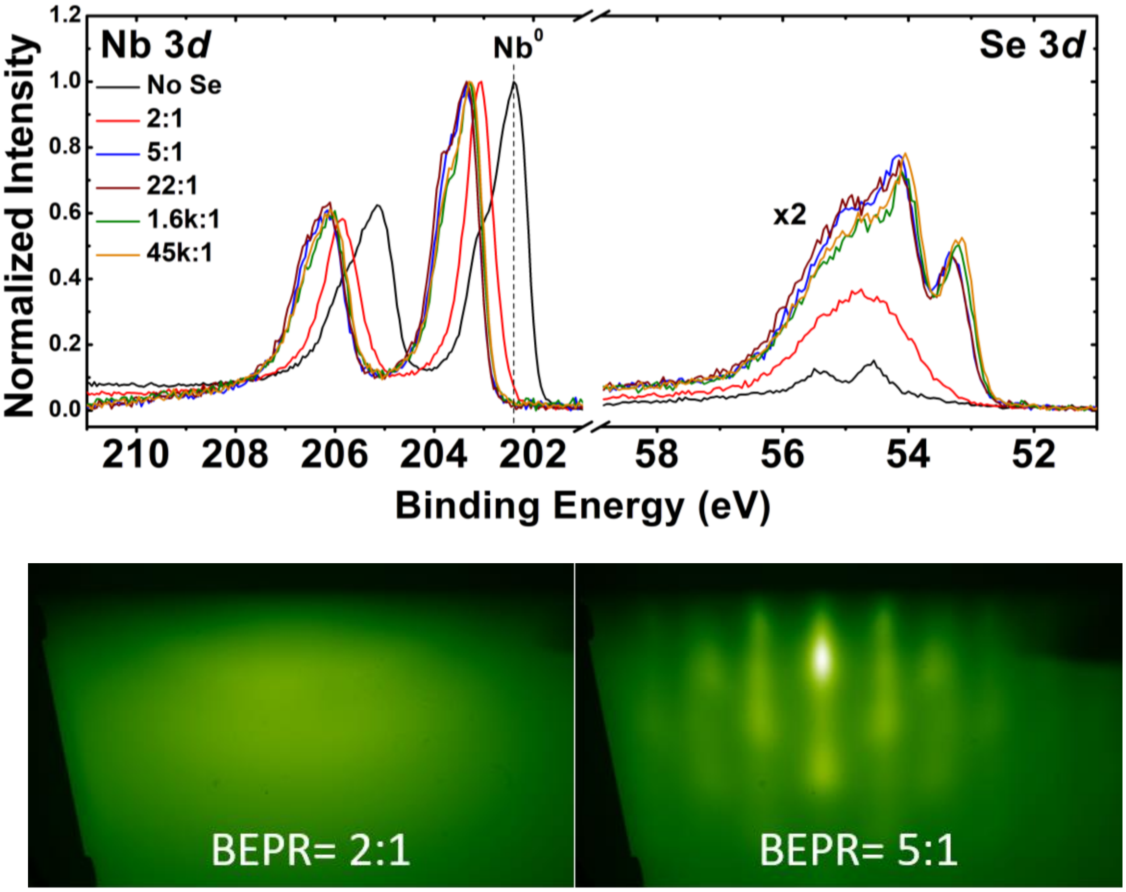

Figure 4.11: Top: XPS spectra as a function of Se to Nb BEPR used during growth. Se 3*d* amplitude doubled for clarity. Bottom: RHEED patterns of films grown with BEPRs of 2:1 and 5:1. All samples grown on SiO_2/Si substrates at 770 °C.

XRD was used to study the structure of $NbSe_2$ thin films as a function of BEPR. The *002* reflections are presented in *Figure 4.12a*. The position of the *002* reflection of bulk, stoichiometric $NbSe_2$ is also included on the plot. As previously discussed, the *002* reflections of the MBE grown materials are to lower 2θ angles indicating that the c-lattice parameter is greater in the MBE-grown material than in bulk, stoichiometric $NbSe_2$. Also apparent is the BEPR dependence of the *002* reflection, i.e., lattice constant. Here we observed an inverse relationship between the BEPR and lattice parameter where high BEPRs result in a smaller lattice constant. However, even under the highest BEPR used, the lattice constant is still greater than that of the bulk, stoichiometric compound. *Figure 4.12b* shows the extracted lattice constant as a function of BEPR. Included on the plot are reported literature values for stoichiometric 2H NbSe$_2$ and Nb-rich Nb$_{1.27}$Se$_2$ and Nb$_{1.29}$Se$_2$. The extracted lattice constants of our films were estimated using the Nelson-Riley extrapolation method and found to be 13.03, 13.06, and 13.18 Å for BEPRs of 45,000:1, 1,600:1, and 22:1, respectively [122]. The smallest lattice constant values for out MBE NbSe$_2$ films are similar in magnitude to the works by Khyzhun and Selte and Kjekshus [121, 127].

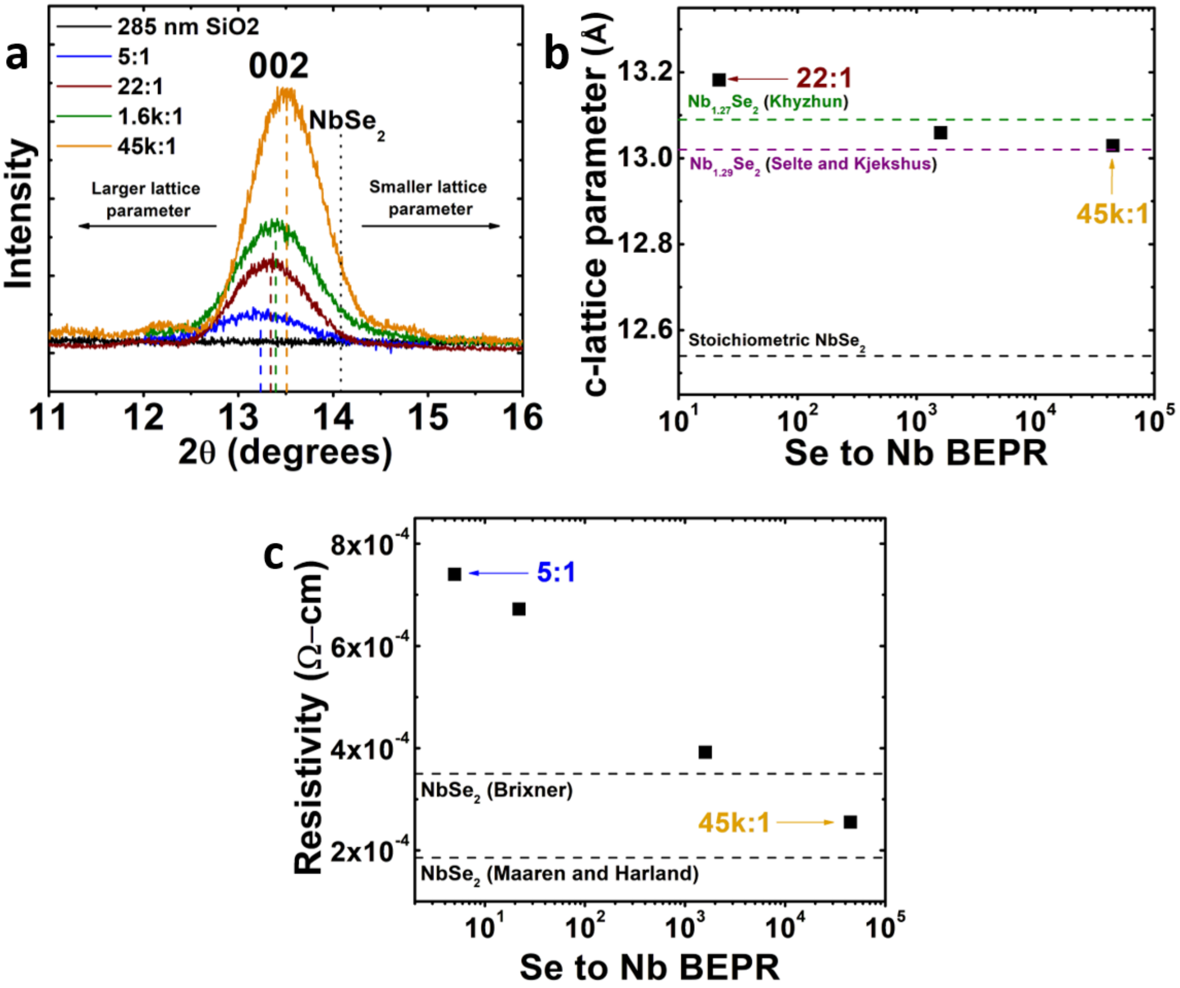

Figure 4.12: a) XRD of the *002* reflection of MBE-grown NbSe$_2$, b) extrapolated lattice constants compared to literature values, and c) in-plane electrical resistivity as a function of Se to Nb BEPR used during growth. Lattice constants inset into *b* taken from [121] and [127]. Resistivity value inset onto *c* taken from [128].

To study how SI of $NbSe_2$ effects the functional properties of the material, we studied the effect of varying the BEPR on the electrical conductivity of the MBE-grown $NbSe_2$ thin films. *Figure 4.12c* shows the measured electrical resistivity as a function of BEPR used during growth. Also included on the plot is the electrical resistivity of bulk $NbSe_2$ by Brixner and Maaren and Harland [128, 129]. As observed in the plot, the measured electrical resistivity is inversely related to the BEPR used during growth and ranges from 2.55 x 10^{-4} to 7.40 x 10^{-4} Ω-cm.

Table 4.1: Effect of processing conditions on estimated stoichiometry, c-lattice parameter, sample thickness, and in-plane electrical conductivity.

Se to Nb BEPR	**Estimated Stoichiometry**	**c-lattice parameter (Å)**	**XRR Sample Thickness (nm)**	**In-plane Electrical Resistivity (x 10^{-4} Ω-cm)**
2:1	$Nb_{2.14}Se_2$	(non-layered)	-	-
5:1	$Nb_{1.15}Se_2$	-	9.95	7.40
22:1	$Nb_{1.20}Se_2$	13.18	9.87	6.72
1,600:1	$Nb_{1.18}Se_2$	13.06	10.3	3.92
45,000:1	$Nb_{1.23}Se_2$	13.03	7.22	2.55

The XPS and XRD results show that at BEPRs of 5:1 and greater the $Nb_{1+x}Se_2$ phase is produced. XPS of the films show similar spectra line shapes in this processing space. Additionally, the estimated stoichiometries for the films produced under these conditions are all within the bulk composition range for the $Nb_{1+x}Se_2$ phase (x = 0 to 0.29) [121]. However, there is no conclusive trend in the stoichiometry of the films as a function of BEPR. This is due to the error associated with stoichiometry estimates using XPS; this error has been established at $x \approx 5\%$ through the analysis of nominally identical samples as presented in *Section 7.1-7.2*. XRD spectra of the thin films grown at BEPRs of 5:1 and greater all share the same 00*l* reflections. RHEED patterns for these 4 films suggest these films are all structurally similar in terms of their in-plane lattice constant and surface morphology. Both the XRD and RHEED are distinct from that of $NbSe_x$ grown with a 2:1 BEPR which both showed no evidence of crystallinity. The c-lattice parameter is found to be inversely related to the Se to Nb BEPR at BEPRs of 5:1 and greater. This is the expected trend in the presence of Nb SI where more Se supplied during growth is expected to limit the degree of SI; less SI is known to result in a smaller c-lattice parameter in bulk $Nb_{1+x}Se_2$ [121]. Generally, the c-lattice parameters of the $NbSe_2$ films produced here are larger than the expected values based on previous literature reports. Selte and Kjekshus measured a maximum out-of-plane lattice constant of 13.02 Å at the uppermost solubility limit of the $Nb_{1+x}Se_2$ phase [121]. However, O. Khyzhun measured an out-of-plane lattice constant of 13.09 Å for $Nb_{1.27}Se_2$ which puts a degree of uncertainty in the maximum expected value [127].

The inverse relationship between BEPR and lattice constant suggests that there is less SI when greater BEPRs are used (*Figure 4.12b*). The in-plane electrical resistivity is also observed to be inversely related to the BEPR (*Figure 4.12c*). From these trends it is reasonable then to conclude that SI increases the in-plane electrical resistivity. This conclusion mechanistically makes sense when the atomic structures of $NbSe_2$ with and without SI are compared. In the absence of SI, $NbSe_2$ is composed of atomically smooth $NbSe_2$ layers separated by a vdW gap. In the presence of SI, there are periodic disruptions to these otherwise atomically smooth $NbSe_2$ layers as the SI Nb atoms are covalently bonded to adjacent Se atoms. For this reason, it would be expected for SI Nb atoms to act as scattering sites which increases the in-plane electrical resistivity.

4.5. Ruling Out Alternative Interpretations

The collection of XPS, XRD and HRTEM/STEM all provide strong evidence that the MBE-grown $NbSe_2$ is of the SI, Nb-rich variety. However, it is important to consider other possible explanations for the collected data, especially the chemical heterogeneity observed with XPS. To help support our conclusions we investigate numerous alternative explanations for some of the data discussed above in the following sections.

4.5.1. ARPES Studies of Monolayer $NbSe_2$ to Investigate Possible 1T-$NbSe_2$ Synthesis

The 1T phase of $NbSe_2$ is a metastable phase which has been shown to preferentially form over the equilibrium 2H phase in the monolayer under high temperature MBE synthesis (>600 °C) [130, 131]. The in-plane lattice constant of the 1T phase is very similar to that of the equilibrium 2H phase which makes its identification using diffraction techniques, such as RHEED and LEED, challenging. However, the electronic structure of the 1T phase is unique from that of the 2H phase and as such its presence can be confirmed with ARPES [130]. *Figure 4.13a* shows the ARPES spectra (centered at Γ, M-Γ-M direction) of MBE-grown partial monolayer $NbSe_2$ on a single crystal graphene/SiC substrate. The expected electronic structure is visible in the reference ARPES data of 1T-$NbSe_2$ and possess both a flat band at ~20.8 eV and a hole-like band in the energy range of 19.9 to 20.8 eV. Neither of these characteristic features of 1T-$NbSe_2$ are observed in the ARPES data collected here and thus no evidence for the existence of 1T-$NbSe_2$ in this sample is found. To the contrary, the ARPES data agrees well with the previously reported literature results for 2H-$NbSe_2$. Previous work on bulk $NbSe_2$ has demonstrated that the 1T phase is not expected to be stable in multilayer films. Though 1T-$NbSe_2$ has been observed at ~900 °C in bulk samples, it has not been retained at room temperature, even upon quenching [132]. 1T-$NbSe_2$ has only been observed in the monolayer and given that the $NbSe_2$ films in this work are ~10 nm thick, it is highly unlikely that 1T-$NbSe_2$ would be stable. The ARPES data reported here, along with the known instability of 1T-$NbSe_2$ in the bulk, put a high level of doubt that it exists in the MBE-grown material presented here.

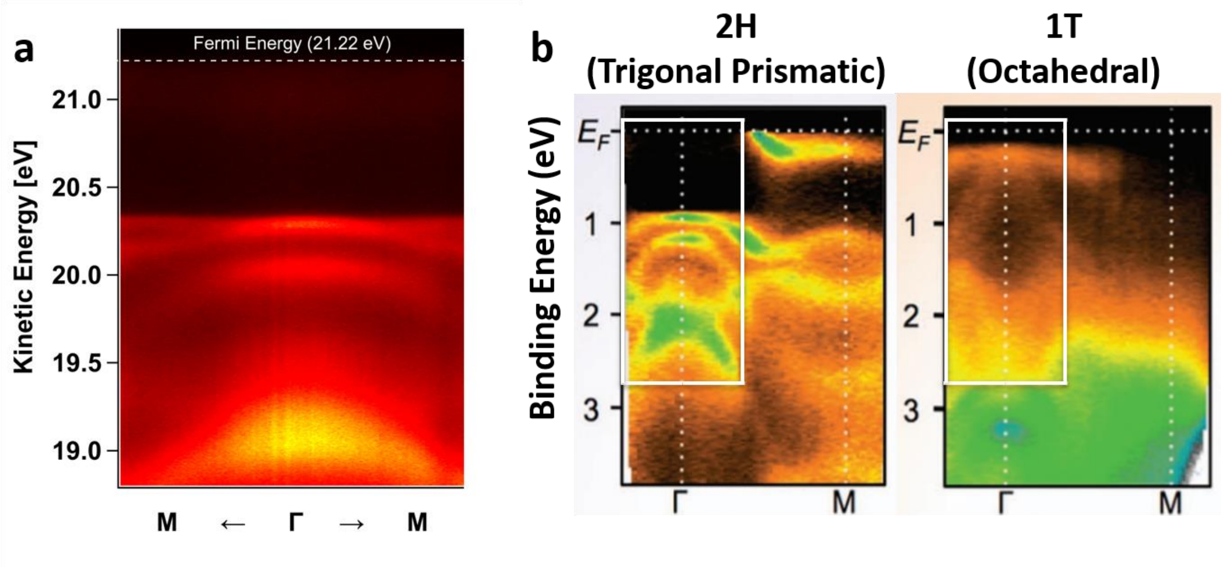

Figure 4.13: a) ARPES data showing the electronic structure of partial monolayer $NbSe_2$ showing no contributions from 1T-$NbSe_2$. b) Reference electronic structure data adapted from Nakata, et al. under Creative Commons CC BY license (Copyright © 2016, Springer Nature) [130]. White boxes in *b* identify energy-momentum space captured in ARPES spectrum in *a*.

4.5.2. Investigating the Possibility of Interfacial Reactions and Chemical Impurities

Here we consider the possibility of chemical impurities or interfacial reactions with the SiO_2 substrate as the cause of the chemical diversity we observe in XPS. A wide energy range survey spectrum of the MBE-grown material in *Figure 4.14* shows only signatures from Nb and Se. This is evidence that there are no impurities of appreciable quantity in the grown material. High resolution scans of the Si 2*p* and O 1*s* show no evidence of Si or O. This suggests the SiO_2 substrate is effectively buried beyond the sampling depth of XPS due to the ~10 nm $NbSe_2$ film thickness and thus the chemistry of the interface is not contributing to the measured spectra. The lack of a Si or O signature also reveal that no Si or O is diffusing into the grown material which would result in unexpected chemical variability in the analyzed sample.

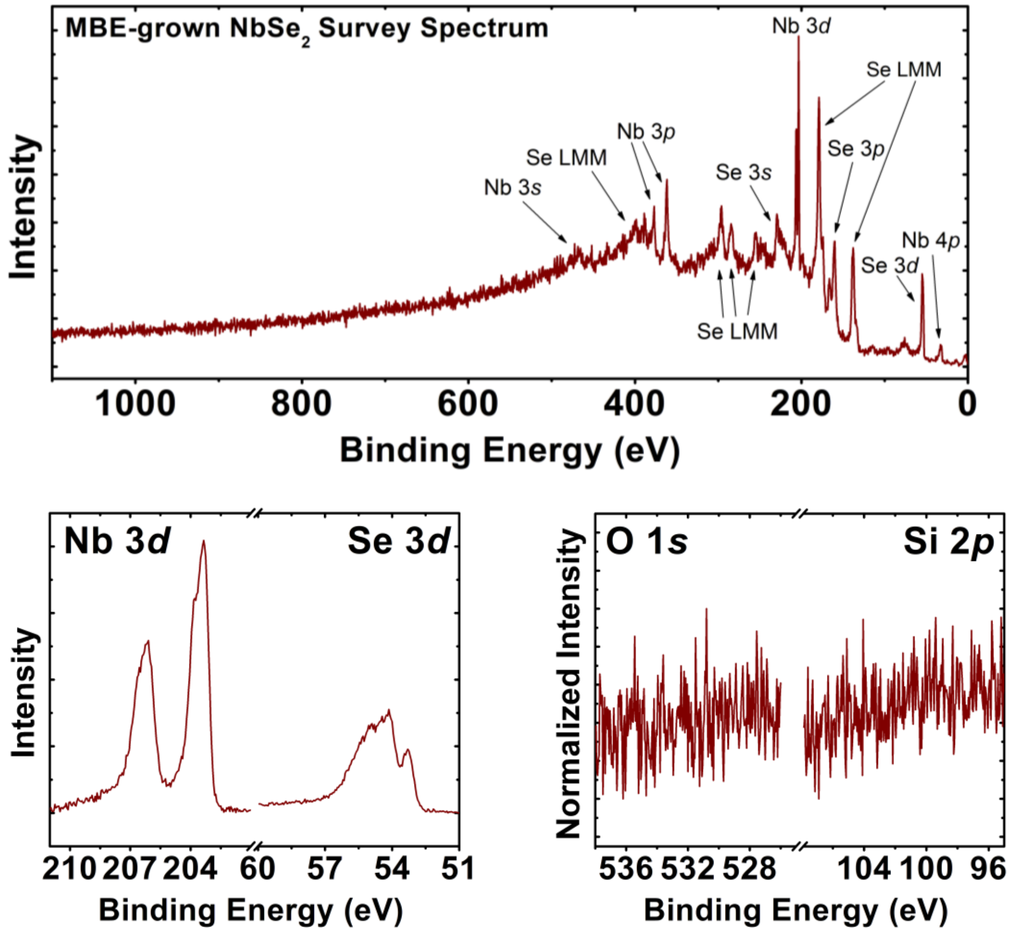

Figure 4.14: XPS spectra of a ~10 nm $NbSe_2$ thin film grown on SiO_2 by MBE. Spectra reveal only signatures from Nb and Se with no contributions from the substrate or foreign atomic species. Film grown with a BEPR of 22:1.

4.5.3. Investigating the Presence of Charge Density Waves

Charge density waves (CDWs) are a low temperature state that occur in many of the group V TMDCs. The presence of CDWs have been observed in the XPS of TaS_2 which manifests as a splitting of the Ta 4*f* core level [133-136]. This is due to local changes in electron densities associated with the CDW state [133]. While CDW states are a low temperature state, they can exist at or above room temperature for some group V TMDCs, such as 1T-TaS_2 and 1T-$NbSe_2$ [133, 135-137]. However, metastable 1T-$NbSe_2$ (octahedral coordination) is not believed to be stable in multilayer $NbSe_2$ and there is no evidence for its existence in the work presented here [132]. *Figure 4.15* shows XPS collected at room temperature and 565 °C of MBE-grown ~2-layer $NbSe_2$ grown on HOPG. The latter temperature is understood to be well in excess of the thermal limitations of CDW states in 2H-$NbSe_2$, the equilibrium trigonal prismatic phase, which have been found to be most stable in monolayer $NbSe_2$ up to 145 K; the stability of the CDW state decreases at greater $NbSe_2$ thicknesses [138]. The lack of a change in the peak line shape of either core level at 565 °C is evidence that the additional features are not due to room temperature CDW states.

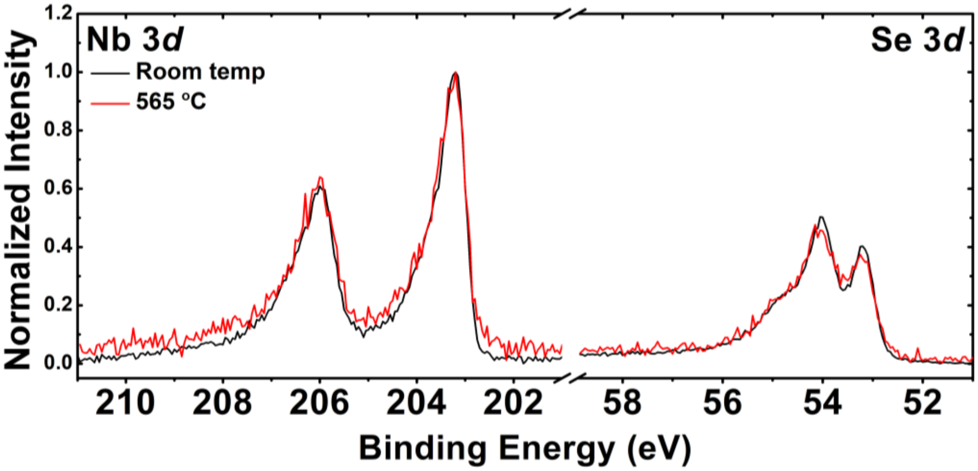

Figure 4.15: XPS spectra of a ~2-layer $NbSe_2$ film grown on HOPG. XPS data collected at room temperature and 565 °C.

To further rule out the possibility that CDWs could impact the spectra of the grown $NbSe_2$ films, ~4-layer MBE-grown $NbSe_2$ was cooled to see if a CDW could be induced. The XPS and UPS spectra in *Figure 4.16* remain unchanged upon cooling to ~100 K which suggests no CDW state is present at this decreased temperature; this is consistent with the reported CDW transition temperature of few layer samples which is expected to be <100 K [138]. These data, along with the XPS collected at elevated temperature (*Figure 4.15*), puts a high degree of confidence in the absence of CDW states in the MBE-grown $NbSe_2$ thin films and therefore not impacting the observed XPS spectra.

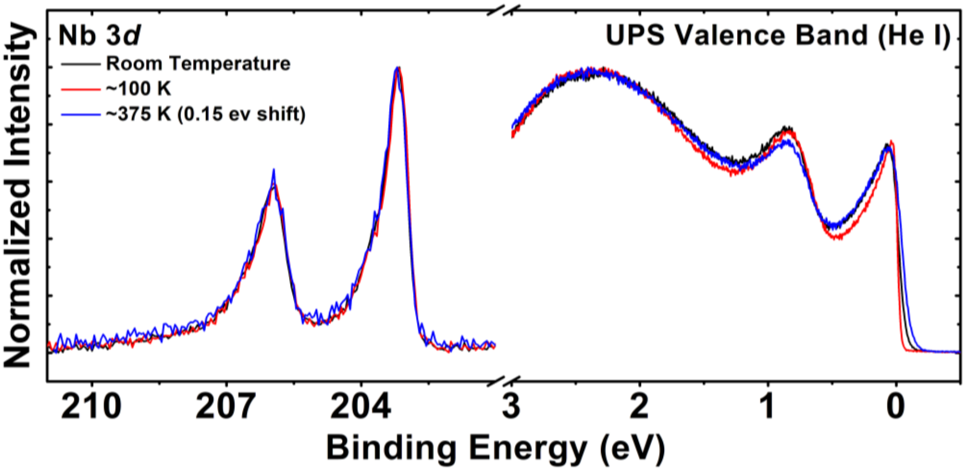

Figure 4.16: XPS and UPS spectra of a ~4-layer $NbSe_2$ film grown on SiO_2/Si. XPS/UPS data collected at room temperature and 100 and 375 K.

4.5.4. Effect of High Temperature Annealing

To further demonstrate that the chemical diversity observed by XPS is due to an excess of Nb in the film, we annealed a sample post growth under a Se BEP of ~3 x 10^{-6} mBar for ~3 hours at 900 °C. *Figure 4.17* shows the XPS spectra collected of the grown film before and after an anneal in Se. While both core levels show the same result, the changes are more pronounced in the Se 3*d* core level where a clear increase in the signal from stoichiometric $NbSe_2$ is observed alongside a decrease in states associated with intercalated Nb. The estimated stoichiometries of this film was $Nb_{1.13}Se_2$ and $Nb_{1.08}Se_2$ in the as-grown state and post annealing in Se, respectively.

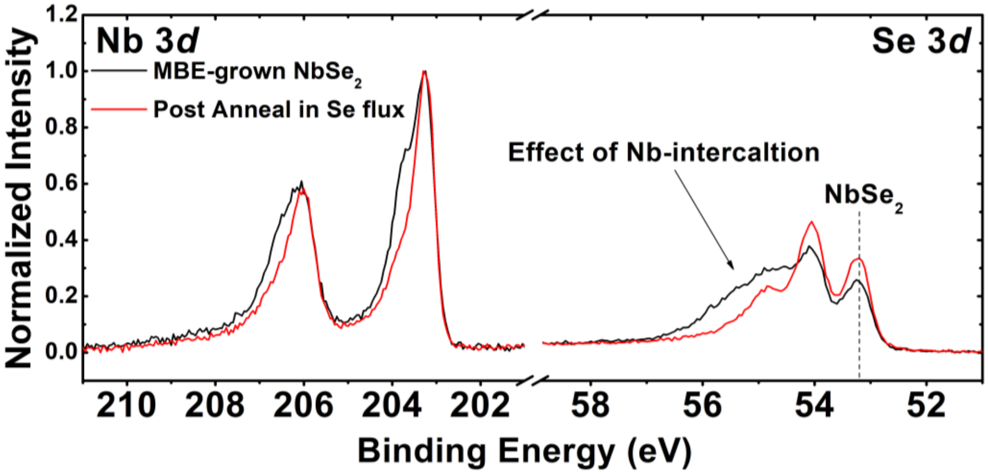

Figure 4.17: The XPS spectra of MBE-grown $NbSe_2$ in the as grown state (black) and post annealing in a Se flux at 900 °C (red). Annealing the sample reduces the signal associated with Nb-intercalated and enhances the signal associated with intercalant-free $NbSe_2$.

4.6. Concluding Remarks on the Effect of BEPR and the State of the Literature on MBE-grown $NbSe_2$

The growth of SI group-VB TMDCs has been studied in the bulk since the 1960's. These early works largely focused on understanding the compositional space of the stable SI phases and the effect of stoichiometry of the polymorphism of the respective systems [117, 121, 123, 124, 129, 139-144]. Over the past few years, it has been theoretically and experimentally determined that controlling the degree of SI in these materials can be a useful way of tuning the materials' properties. For example, DFT by Zhao et al. highlights the emergence of ferromagnetism in SI Nb- and Ta-based TMDCs in contrast to their non-ferromagnetic, stoichiometric counterparts [145]. Additionally, Yang et al. showed experimental evidence of improved catalytic performance of CVD grown $Nb_{1.35}S_2$ over NbS_2 due to increased current densities in the former; the increased current densities were attributed to a partial elimination of the van der Waals gap in the SI compound [146]. These finding have helped motivated recent investigations into the thin film growth of SI compounds. This experimental focus on SI group-VB compounds only goes back about five years with examples of $Ta_{1+x}S_2$, $Ta_{1+x}Se_2$, $Nb_{1+x}S_2$, and $V_{1+x}S_2$ produced as thin films [126, 145, 146].

An intriguing result from this work is how insensitive the system is to alteration of the BEPR. While clear trends in lattice constant were observed, none of the processing parameters employed here resulted in stoichiometric $NbSe_2$. This is concluded from the XPS measurements which always show chemical features associated with SI (*Figure 4.11*) and the lattice constant measured with XRD which under no conditions measures the expected lattice constant of stoichiometric $NbSe_2$ (*Figure 4.12a* and *4.12b*). In comparison, Zhao et al. demonstrated better control in the Ta-S system and was able to demonstrate complete elimination of SI during MBE synthesis of TaS_2 [145]. DFT work by Sidoumou et al. suggest that the free energy of $Nb_{1+x}Se_2$ is comparable for $x = 0$ and $x = 0.1$ at the growth temperature used in this work [125]. Since both structures show a similar theoretical stability, it is likely that kinetic factors play a role in the formation of SI $Nb_{1+x}Se_2$. Zhao et al. performed additional DFT work suggesting the formation energy of $Nb_{1.17}Se_2$ was below that of $NbSe_2$, again suggesting the formation of SI, multilayer $Nb_{1+x}Se_2$ is preferred [145].

$NbSe_2$ has been synthesized by MBE since the 1980's [57]. However, many of these studies were limited in analytical capabilities. Some of these early works relied exclusively on RHEED which, as we discussed, is not useful in distinguishing different polytypes of $NbSe_2$ nor the nature of SI, as the changes to the in-plane lattice constant are minimal. Recently, there have been numerous studies published on synthesis of metastable 1T-$NbSe_2$ [130, 131, 137, 147-149]. However, these studies exclusively involve monolayers as 1T-$NbSe_2$ isn't believe to be stable in multilayer films.

Notably, two other publications have recently discussed the growth of multilayer $NbSe_2$ by MBE [150, 151]. The first, by Calavalle et al., reported on 1-2 layer $NbSe_2$ grown HOPG and graphene substrates. The XPS of their $NbSe_2$ films look to share common features with the data reported in our work, i.e., high binding energy features present in the Se 3*d* spectra. Calavalle et al. assigned this additional Se chemical feature to elemental Se on the surface of their films. In the context of our work, we know elemental Se does not reside on the surface of our films which was concluded via high temperature XPS (see *Figure 4.15*) which is beyond the desorption temperature of Se (<200 °C). The fact that the $NbSe_2$ thin films in the work of Calavalle et al. contain bilayer regions, SI in their material is a possible alternate interpretation of their data. Additionally, the high binding energy component of their Se 3*d* spectra (which we point to as evidence of SI) is of greater intensity in the film with greater 2nd layer coverage which supports the theory of SI in their $NbSe_2$ films. A 2nd publication, by Chen et al., reports on the growth of multilayer $NbSe_2$ on Al_2O_3 substrates. The films were characterized with XRD and TEM with selected area diffraction (SAD). They reported on substrate induced strain that resulted in an expanded c-lattice parameter and a compressed in-plane lattice constant. While the expanded c-lattice parameter is similar to what we observe in our work, the compressed in-plane lattice parameter is not an expected consequence of SI. For that reason, we acknowledge that the origin of the expanded c-lattice parameter in the work by Chen et al. is likely of a different origin than in our work presented here.

4.7.Future Work

This section reports on the current state of investigations into MBE-grown $NbSe_2$ and discusses potential future work.

4.7.1. The Effect of $NbSe_2$ Scaling

This section reports on current work investigating how scaling effects the chemistry and electrical conductivity of MBE-grown $NbSe_2$; $NbSe_2$ is a candidate for ultra-scaled metallic interconnects which motivates investigations into how the thickness effects the material properties.

4.7.1.1. Impacts of $NbSe_2$ Scaling on Thin Film Chemistry

Unexpectantly, the XPS spectra of $NbSe_2$ was highly dependent on the sample thickness. *Figure 4.18a* shows a collection of XPS spectra of eight MBE-grown $NbSe_2$ thin films at two different thicknesses. The ~3 nm $NbSe_2$ films are all grown to the same thickness under nominally identical conditions and are all represented in black. The spectra of the ~10 nm thick films are grown under varying Se to Nb BEPRs and are colored according to the figure caption. As we previously discussed in *section 4.4*, altering the BEPR beyond 5:1 has only subtle effects on the chemistry of the grown films. In comparison, altering the thickness of the film has a much higher impact on the observed chemistry. These spectra also show that the dependence of the XPS spectra on sample thickness is highly repeatable and therefore not a consequence of sample-to-sample variability. *Figure 4.18b* shows the XPS spectra of a greater range of sample thicknesses; the observed spectra do not change beyond ~6.5 nm. To allow for the comparison of the spectra more clearly, the spectra of the ~0.6 nm $NbSe_2$ film was artificially shifted to lower binding energy by 1.3 eV. Despite the observed changes in the spectral shape, the estimated stoichiometry of each sample fall within the known stoichiometry range for $Nb_{1+x}Se_2$.

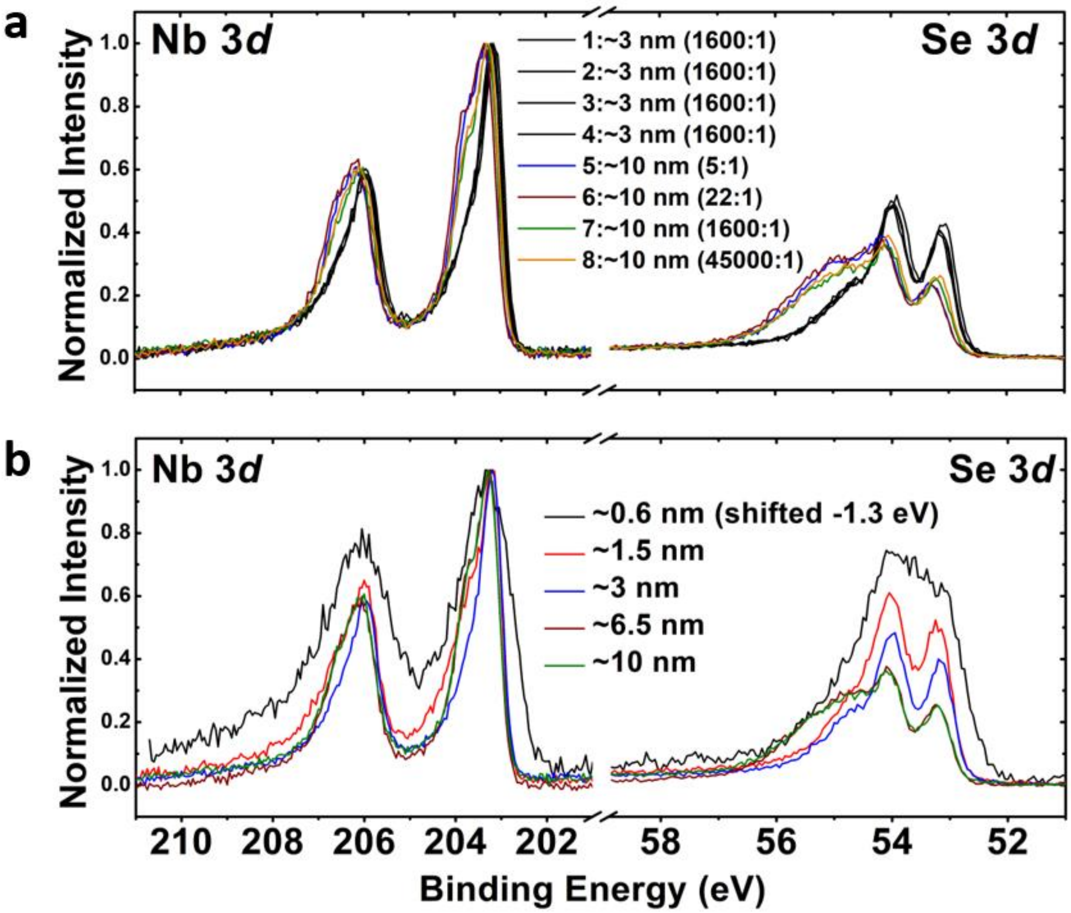

Figure 4.18: a) The XPS of 8 MBE-grown $NbSe_2$ thin films at 2 thicknesses. The ~3 nm $NbSe_2$ spectra are in black with the ~10 nm films colored according to BEPR which are inset into figure legend. b) XPS of $NbSe_2$ thin films on SiO_2/Si substrates. Films varied in growth time to adjust sample thickness and were otherwise carried out under identical conditions. All samples grown at 770 °C.

A simple explanation of the observed trend for the varying XPS spectra, i.e., chemistry, at $NbSe_2$ thicknesses below ~6.5 nm is that there are interfacial reactions with the substrate and that these reactions are being represented to varying degrees due to attenuation of the interface by the grown $NbSe_2$ thin film. *Figure 4.19* show the XPS spectra of the O 1*s* and Si 2*p* spectra pre and post growth of ~0.6 nm of $NbSe_2$. In the presence of interfacial reactions, either a broadening of the substrate peaks or the addition of distinct new features would be expected. A small shoulder on the O 1*s* core level at ~532 eV could represent the formation of small amounts of NbO_x. Unexpectantly, the peak width of both substrate core levels narrows slightly upon deposition of the partial monolayer $NbSe_2$ film. The reason for this is not clear, but it could relate to adsorbed species from the atmosphere being desorbed when the substrate was exposed to the high temperatures necessary for growth.

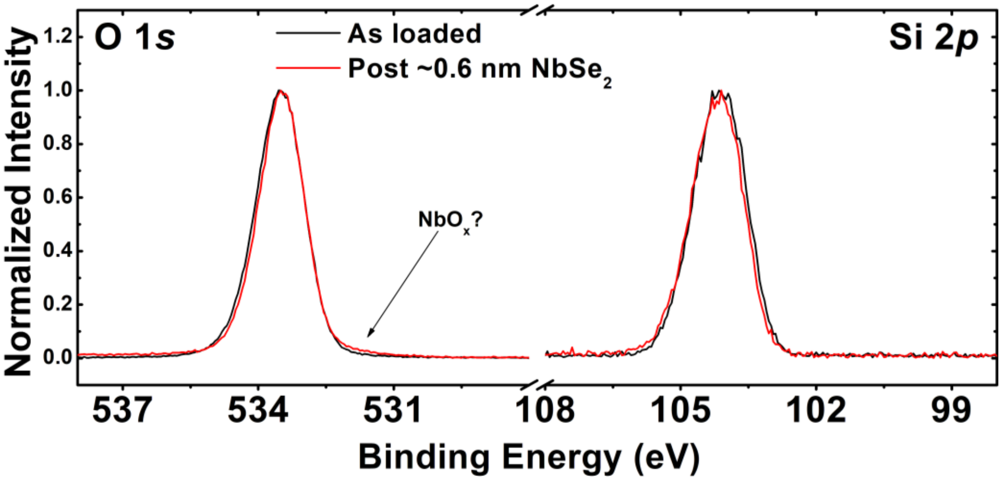

Figure 4.19: The XPS spectra of the O 1*s* and Si 2*p* core levels before and after deposition of a ~0.6 nm $NbSe_2$ thin film.

The XPS data in *Figure 4.19* is evidence that interfacial reactions at $NbSe_2/SiO_2$ interface exist. However, the presence of NbO_x alone does not fully explain the XPS thickness dependence of $NbSe_2$ presented in *Figure 4.18* for two reasons. First, the presence of NbO_x would only be expected to induce changes to the Nb 3*d* core level. Instead, changes in the Nb 3*d* core level are always associated with changes in the Se 3*d* core level which retain a $Nb_{1+x}Se_2$ stoichiometry. Second, similar thickness dependent XPS trends are observed for $NbSe_2$ grown on chemically inert HOPG; these results are presented in *Figure 4.20*. These results suggest that the formation of NbO_x at the $NbSe_2/SiO_2$ interface cannot completely explain the XPS thickness dependence of $NbSe_2$. The thickness dependence of the chemical nature of $NbSe_2$ thin films is a focus of current research.

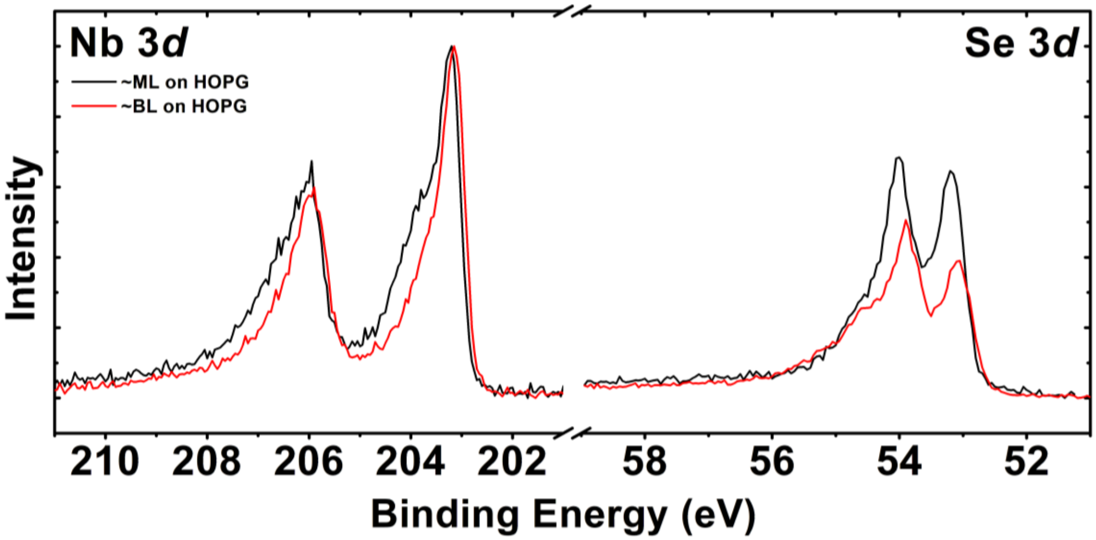

Figure 4.20: XPS spectra of monolayer (ML) and bilayer (BL) $NbSe_2$ on HOPG. Films grown at a substrate temperature of 570 °C and Se to Nb BEPR of ~1600:1.

4.7.1.2. The Effect of $NbSe_2$ Scaling on Electrical Conductivity

The in-plane electrical resistivity of the MBE-grown thin films was also recorded as a function of sample thickness. The results can be seen in *Figure 4.21* for $NbSe_2$ at four different thicknesses. These results are normalized to the bulk resistivity of $NbSe_2$. A line at a value of 1 shows where the data would fall if no change in the resistivity from the bulk was observed. Also included in the figure are the simulated results for Cu metal in the same thickness range. This plot shows that thinning $NbSe_2$ down to thicknesses of ~5 nm results in roughly a 2x to 3x increase in the electrical resistivity over the bulk value. Cu on the other hand is expected to be about 12x the bulk resistivity at 5 nm thicknesses.

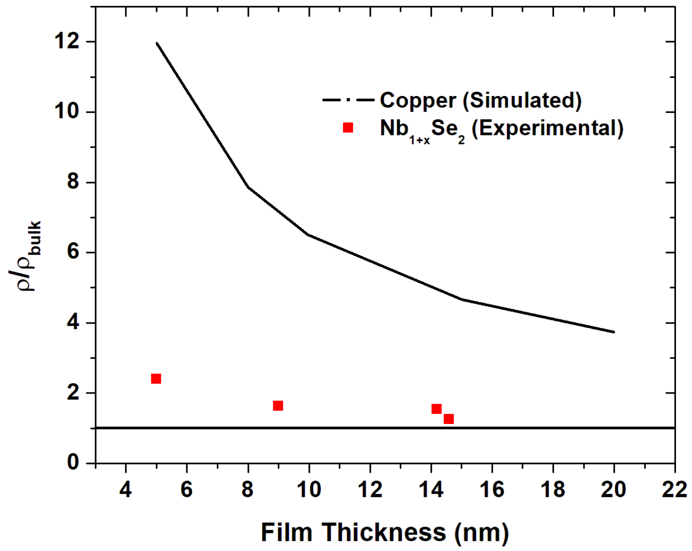

Figure 4.21: A plot of electrical resistivity normalized to the bulk value. Data in red are experimentally determined and data for Cu are simulated.

The results described in this section reveal that the MBE-grown $NbSe_2$ shows varying chemistry with sample thickness and superior scaling of the electrical resistivity in comparison with Cu. The fact that the XPS spectra vary with thickness marks a stark contrast with other TMDCs produced in the McDonnell Lab, such as WS_2 and WSe_2, which show no dependence of chemistry on sample thickness. The reasons for this difference are likely related to the greater complexity in the Nb-Se system compared to that of the W-S/Se systems which vary in several ways. First, $NbSe_2$ is known to host SI while WS_2 and WSe_2 do not, i.e., there are no W-rich $W_{1+x}Ch_2$ phases [111]. This allows for a greater range of $NbSe_2$ compositions compared to WS_2 and WSe_2. Additionally, the Nb-Se system shows a greater diversity in stable chemical compounds compared to that of the W-S/Se systems. The Nb-Se equilibrium phase diagram is known to host at least 7 equilibrium phases compared to the W-S/Se systems in which WS_2/WSe_2 is the only known stable compound. Lastly, at monolayer thicknesses, additional non-equilibrium compounds, such as Nb_9Se_8, have been found to be stable; this report highlights how the chemistry in ultra-thin $NbSe_x$ thins have previously shown to vary in chemistry from multilayer films [152]. Ultimately, understanding the chemistry of ultra-thin $NbSe_2$ and how it varies is beyond the scope of this thesis. That said, it leaves a new frontier to be explored in the context of engineering $NbSe_2$ thin films.

The electrical resistivity of the $NbSe_2$ thin films in this work showed superior scaling of the electrical resistivity compared to ultra-thin Cu. This is expected for scaled 2D materials compared to their 3D counterparts. The reason the electrical resistivity typically increases in scaled 3D materials is diffuse charge scattering from the material's surface. This is due to intrinsic atomic scale surface roughness at the surface of 3D metals [14]. As a material is thinned, surface scattering becomes the dominate scattering mechanism and increases the material's resistivity beyond that of the bulk value; this effect becomes more pronounced with continued thinning. This is true for bulk metals, such as Cu which have atomic scale surface roughness. 2D materials, such as $NbSe_2$, are ideally atomically smooth and don't suffer from diffuse surface scattering. For this reason, 2D materials can, in theory, be scaled to single monolayers without a change in their electrical resistivity. In practice this is not always the case due to extrinsic factors. The $NbSe_2$ thin films in this work do increase in their electrical resistivity at lower thicknesses. The exact reason for this has not been identified but there are a few reasons why this might occur. First, there is evidence for subtle reactions at the $NbSe_2/SiO_2$ interface. Due to reactions at this interface, there is likely a deviation from the atomically smooth interface resulting in diffuse scattering that will result in an increase in the material's resistivity. A 2^{nd} reason the resistivity might increase in 2D materials is atomic scale surface roughening due to oxidation at the material's surface. The electrical resistivity measurements of $NbSe_2$ thin films in this work were taken ex-situ. While the data was collected upon removal from UHV, the early stages of oxidation likely disrupt the atomically smooth nature of the materials surface. Lastly, on the macroscale the surfaces our of $NbSe_2$ will deviate from atomically smooth films. AFM and STM images (*Figure 4.22*) of the surfaces reveal that step edges as a consequence of islanding and/or screw dislocations exist. These features will result in scattering reducing the electrical resistivity of the film and their effect will be enhanced in thinner samples. For these reasons, the increase in the electrical resistivity of the $NbSe_2$ films characterized here with decreasing dimensions is expected. However, the superior scaling properties of $NbSe_2$ compared to Cu highlight the potential for 2D materials in applications of scaled interconnects.

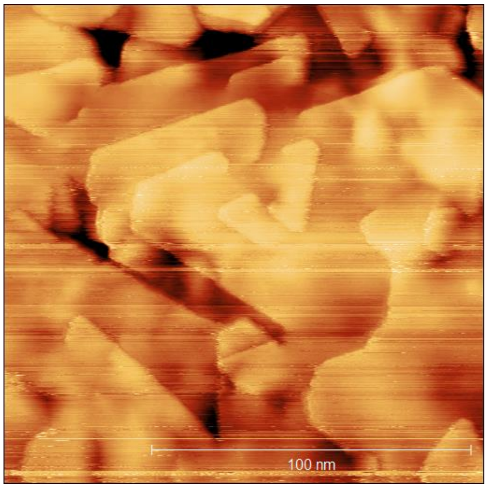

Figure 4.22: STM image of ~4-layer $NbSe_2/SiO_2$. Image collected by Devin Jessup in the Reinke Lab at UVA. Scale bar = 100 nm.

4.8.$NbSe_2$ Conclusions

In summary, $NbSe_2$ thin films grown by MBE were characterized under a range of growth conditions. It was found that to obtain smooth, 2D growth, high temperature synthesis is required. Further growth studies on SiO_2 revealed that $NbSe_2$ is synthesized in a Nb-rich, SI nature where additional Nb atoms populate the vdW gap of the material. The degree of SI could be controlled through modulation of the BEPR. However, under no conditions could stoichiometric $NbSe_2$ be synthesized in the absence of SI. Lastly, we identified that the scaling properties of the electrical conductivity are superior to Cu metal which highlights applications for 2D metals in the area of scaled metallic interconnects.

5. The Study of MBE-Grown Topological Insulators

5.1.Purpose

The purpose of this chapter is to report on studies of the topological insulator (TI) Bi_2Se_3. A common hurdle in the analysis of TIs is their poor atmospheric stability making ex-situ analysis of MBE-grown TIs an experimental challenge. To address this problem and facilitate our own study of ex-situ grown Bi_2Se_3, we explore different methods to prepare ex-situ grown Bi_2Se_3 for characterization and present our results in *Section 5.4*. In *Section 5.5* we use the established methods to analyze the effects of Sn doping on the electronic structure, chemistry, and electrical/thermal transport properties of Bi_2Se_3. In the final sections of this chapter, we further explore the effects of EuS doped Bi_2Se_3.

5.2.Introduction

TIs are materials which are insulating in the bulk, i.e., they possess a bulk band gap, but have conductive topological surface states (TSS). Though TIs have a bulk band gap, it is typically only on the order of a few tenths of an eV. Bi_2Se_3 is known to have a relatively large bulk band gap compared to other TIs at ~0.3 eV [34, 153]. Though many materials can possess electronic surface states, the TSS of a TI like Bi_2Se_3 are non-trivial and topologically protected by time-reversal symmetry [52, 53, 154, 155]. Furthermore, the TSS of Bi_2Se_3 exhibit spin-momentum locking where the electrons momentum and spin are fixed at right angles to one another [51]. The spin-momentum locking of the TSS mean that scattering of these electronic states is highly suppressed as U-turn scattering requires a flip of the electrons spin state. However, the TSS can be perturbed by magnetic fields which break time reversal symmetry. A cartoon and ARPES spectra of the band structure of Bi_2Se_3 are presented in *Figure 5.1a* and *Figure 5.1b,* respectively. Both the cartoon and ARPES spectra identify the surface states that cross the bulk band gap. An additional observation in *Figure 5.1b* is that the Fermi level of Bi_2Se_3 is in the bulk conduction band (CB). This observation is typical for MBE grown Bi_2Se_3 and is typically cited as a consequence of Se vacancies in the as-grown material [50-53].

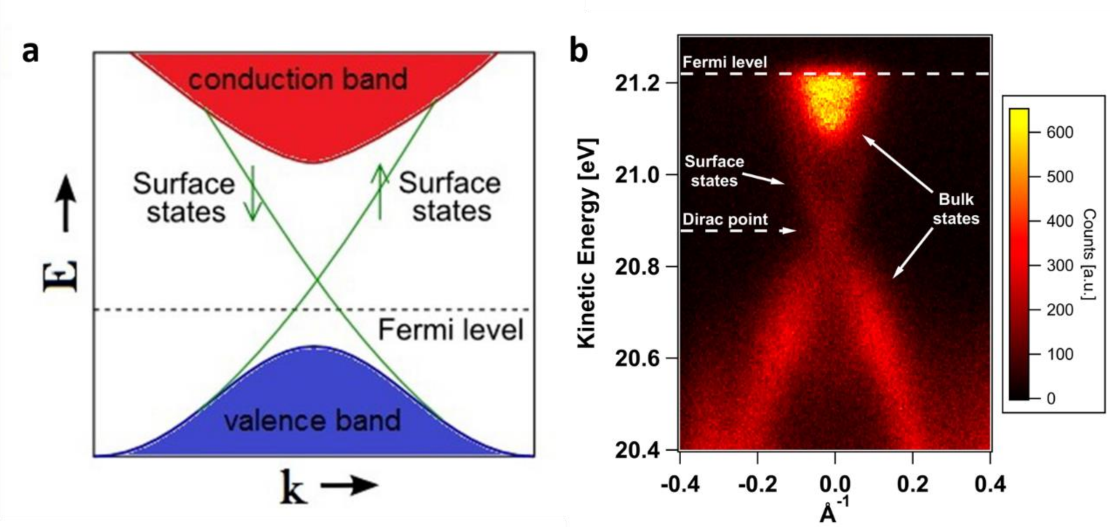

Figure 5.1: a) Cartoon and b) ARPES spectra representing the band structure of Bi_2Se_3. Cartoon used with permission of © IOP Publishing, from M. Autore et al., *Terahertz plasmonic excitations in Bi_2Se_3 topological insulator*, Journal of Physics: Condensed Matter, vol. 29, no. 18, p. 183002, 2023; permission conveyed through Copyright Clearance Center, Inc.[36]. APRES data collected in the McDonnell Lab at UVA.

The n-type nature of as-grown Bi_2Se_3 means that the material's properties will be dominated by the bulk CB rather than the TSS. This limits the material's potential role in future devices. One such device is presented in *Figure 5.2*. Such a device takes advantage of the exchange interaction at the interface of a ferromagnetic insulator (FMI) and a TI [21]. By gating, and thus changing the position of the Fermi level in the TI, the magnetic polarization of the FMI can be switched between the easy and hard axes. Ultimately, the FMI can be used to spin filter charges in a graphene channel and in turn be used in spin-logic devices. Devices such as this are investigated for ultra-low power computing.

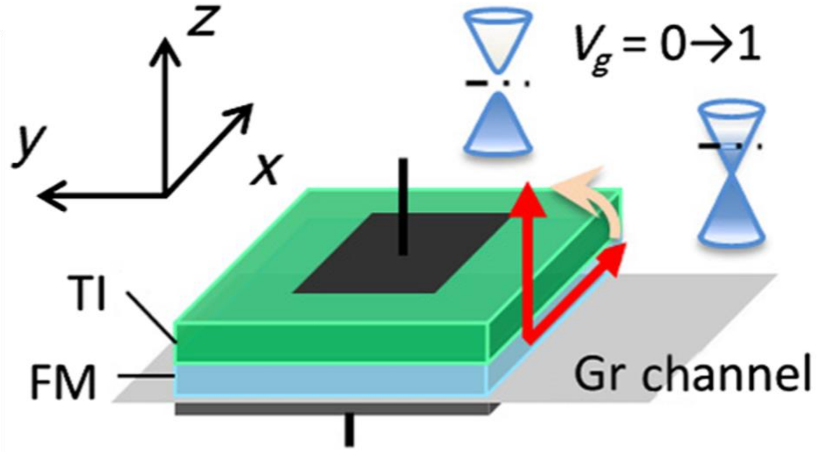

Figure 5.2: Proposed spin logic device consisting of a TI, FMI, and graphene channel. Reprinted figure with permission from Duan et al., *Physical Review Applied*, vol. 2, no. 4, p. 044003, 2014. Copyright (2023) by the American Physical Society [21].

Control of the Fermi level in Bi_2Se_3 is needed for the abovementioned device to function efficiently. With this aim we explore the use of p-type counter dopants, such as Sn and Eu, to move the position of the Fermi level into the bulk band gap. Sn is a hypothesized resonant dopant in Bi_2Se_3 [156]. A resonant dopant state sits in the bulk valence or conduction bands of an insulator/semiconductor. Due to the dopant state being in an electronic band of the host material, as opposed to the band gap, the resonant state perturbs the density of states (DOS) of the band, as seen in *Figure 5.3a*. Resonant states have previously been demonstrated to increase the thermopower of thermoelectric materials due to this modulation of the DOS [157]. Eu is of interest as an alternative p-type dopant in Bi_2Se_3 due to its magnetic properties. Magnetic TIs are of interest to study additional phenomena such as the quantum anomalous Hall effect (QAHE) [158, 159]. In this work, we dope Bi_2Se_3 with EuS which is ferromagnetic with a Curie temperature of 16 K. Though we choose to study the dopants Sn and Eu in this work, other techniques for controlling of the Fermi level exist. These include other substitutional dopants, such as Ca and Sb, and electrostatic gating [160, 161].

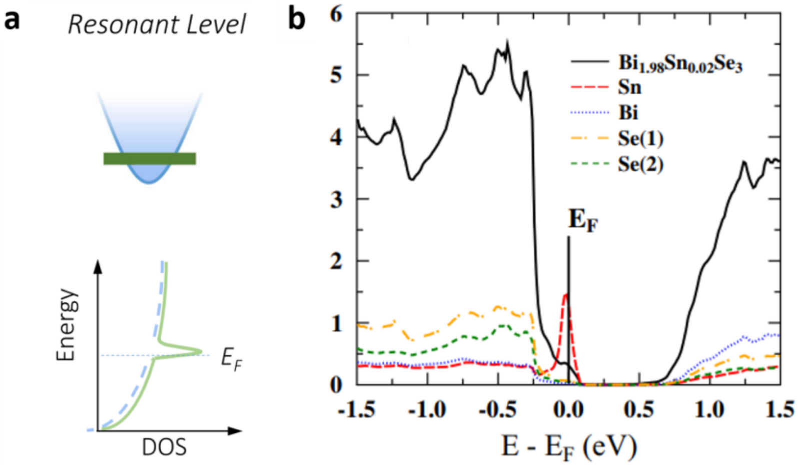

Figure 5.3: a) Cartoon depicting the effect of a resonant doping level on the DOS. Figure adapted from Li et al. under Creative Commons CC BY license [162]. b) calculated DOS of $B_{1.98}Sn_{0.02}Se_3$ including Sn resonant doping level. Frame *b* reused from B. Wiendlocha under Creative Commons CC BY license (Copyright © 2016, Springer Nature) [156].

5.3. $Bi_{2-x}Sn_xSe_3$ Growth and Characterization Experimental Details

Sn-doped Bi_2Se_3 samples were grown by Patrick Taylor by MBE at the Army Research Laboratory (ARL) in Adelphi, MD. Film growth was carried out on GaAs substrates after the thermal desorption of GaO_x revealing an atomically clean GaAs surface prior to growth. The Se to Bi BEPR was held at 10:1 for each growth and the substrate temperature was maintained at 260 °C during synthesis. Sn was co-deposited during growth and the estimated stoichiometries were made from comparison of the Bi/Sn BEPR. Electrical and thermal transport measurements were collected by Brandi Wooten at The Ohio State University. Some additional/complimentary transport measurements were collected at ARL by Greg Meissner, Patrick Taylor, and myself. Surface analysis (ARPES, XPS, LEED, AFM) of the $Bi_{2-x}Sn_xSe_3$ were all performed by myself at the University of Virginia (AFM collected using tool at James Madison University).

5.4. The Study of Ex-situ Grown Bi_2Se_3: Methods of Sample Transfer

This section reports on work carried out to establish methods for ex-situ analysis of Bi_2Se_3 films grown by colleagues at ARL and studied at UVA. Bi_2Se_3 readily oxidizes in air meaning ex-situ analysis is complicated by this change in surface chemistry, particularly in the case of photoemission spectroscopy analysis which are surface sensitive techniques. Due to this experimental challenge of sample degradation, we explore various techniques for surface protection or recovery: an ion-bombardment + anneal (IBA) process, the thermal desorption of protective Se capping layers, and mechanical cleavage. All three methods have been previously reported in the literature; however, preparation methods are typically carried out as part of isolated studies. What lacks in the literature is a comparison of the three methods in a single study such that the results can be directly compared.

Figure 5.3 shows a cartoon representation of all three methods used. The IBA process utilizes an Ar^+ sputter to remove oxide layers present on the surface and is followed by an anneal in a Se flux to compensate for any preferential sputtering of Se over Bi. The Se decap is performed by annealing the sample which thermally desorbs the protective Se capping layers. Lastly, the mechanical cleave is carried out through securing a metal post to the surface and mechanically fracturing the sample revealing an atomically clean surface. Though not depicted, the use of adhesive tapes was also investigated as an additional method to cleave Bi_2Se_3.

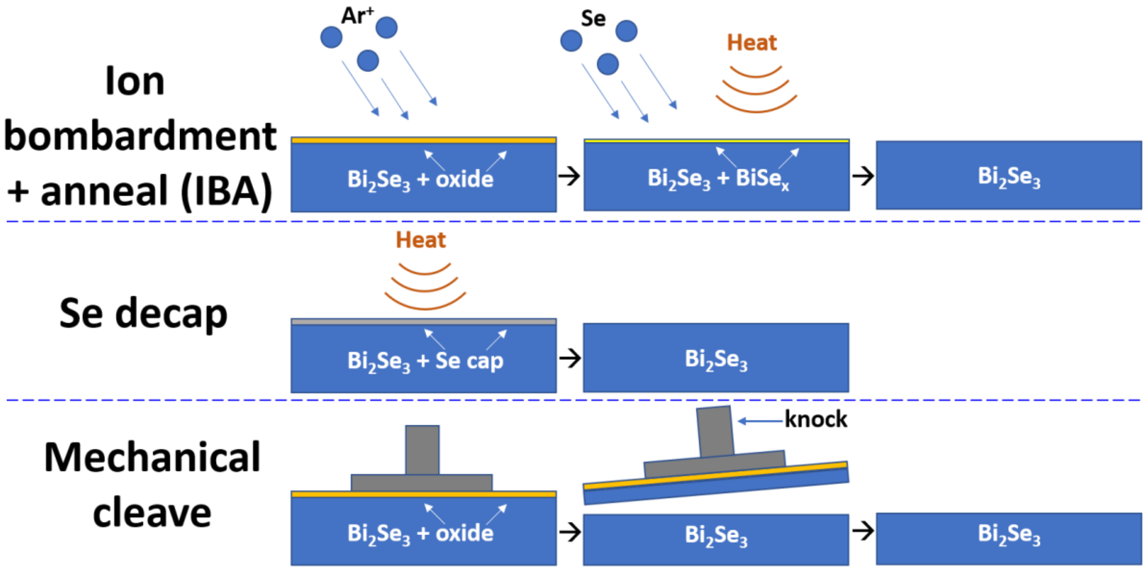

Figure 5.3: Three sample preparation methods used to study ex-situ grown Bi_2Se_3.

Due to this work being part of a larger study investigating the effects of Sn doping on Bi_2Se_3, some of the samples are doped with Sn. While the effects of the dopants on the overall conclusions of this section are believed to be negligible, we will specify when doped samples are employed to maintain full transparency.

5.4.1. Ion-Bombardment + Annealing

IBA in this work was carried out as a 2-step process. The first step is a low energy Ar^+ sputter; this work used 0.5 keV Ar^+ ions at a current of 10 mA for 30 minutes. The second step is an anneal at 400 °C in a Se flux (BEP = 1×10^{-6} mBar); 400 °C was chosen as it sits below the decomposition temperature of Bi_2Se_3 (450 °C) as reported elsewhere and a Se flux was provided to counteract the expected preferential removal of Se over Bi during the Ar^+ sputter [163]. Our process is unique compared to IBA processes previously reported as we provide a Se flux during the annealing step. This study was carried out on a Sn-doped Bi_2Se_3 sample grown on GaAs (100). The estimated composition of the film was $Bi_{1.99}Sn_{0.01}Se_3$.

XPS spectra and LEED patterns of the MBE-grown $Bi_{1.99}Sn_{0.01}Se_3$ sample surface are presented in *Figure 5.4* for the as loaded surface (black), the surface after the Ar^+ sputter step (red), and the surface after the anneal in Se (blue). For the as loaded sample, the O 1*s*, Se 3*d*, and Bi 5*d* signals at ~531 eV, ~59 eV, and ~26 eV, respectively, all indicate the surface has an oxide layer present. This is consistent with the diffuse LEED pattern indicating an amorphous surface. After Ar^+ sputtering, the oxide is removed, as indicated by the lack of a peak in the O 1*s* spectrum. Despite the absence of a surface oxide, a broad Bi 5*d* core level (red spectra) is observed. A weak, hexagonal LEED pattern can be detected. Post completion of the IBA process, XPS spectra show sharp Se 3*d* and Bi 5*d* core levels characteristic of Bi_2Se_3 and a sharp LEED pattern is visible indicating a crystalline surface.

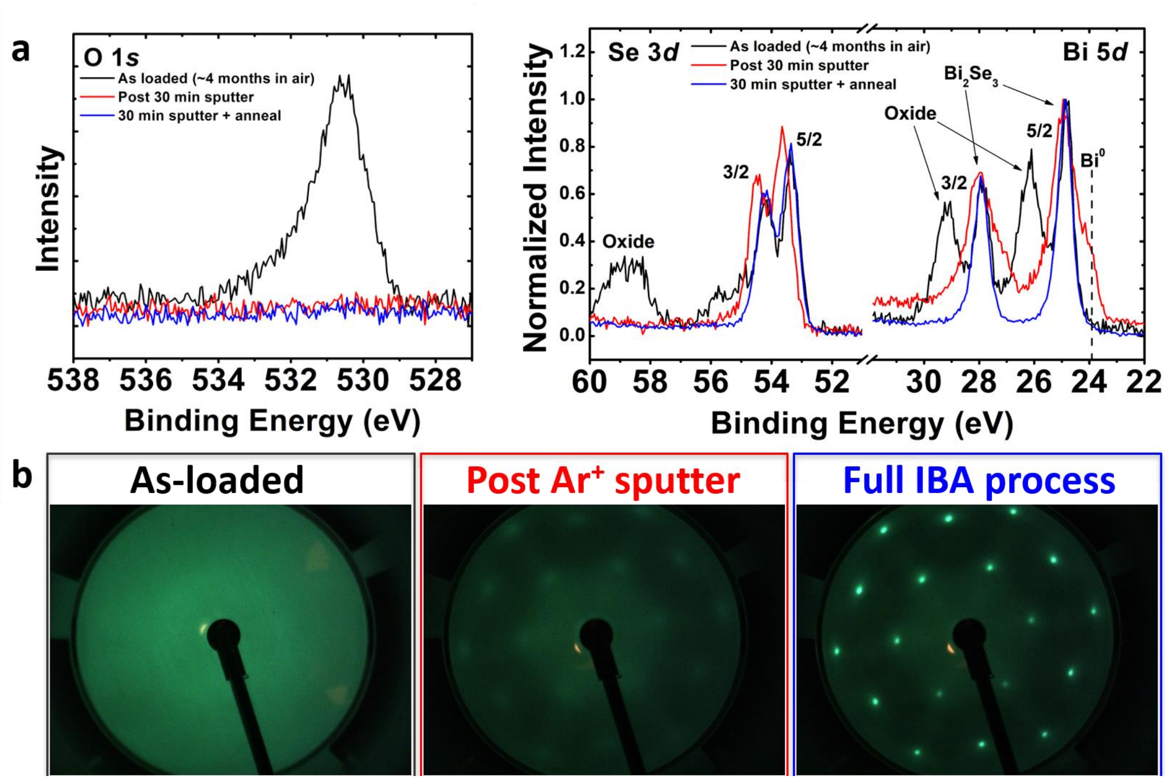

Figure 5.4: a) XPS spectra of air exposed $Bi_{1.99}Sn_{0.01}Se_3$ in the as loaded state, post Ar^+ sputter, and post the complete IBA treatment. b) LEED patterns of air exposed $Bi_{1.99}Sn_{0.01}Se_3$ in the as loaded state, post Ar^+ sputter, and post the complete IBA treatment.

The XPS and LEED data in this section reveal that the surface of the air exposed Bi_2Se_3 material is covered in an amorphous oxide layer which can be removed by Ar^+ sputtering. However, the diffuse hexagonal LEED pattern after the Ar^+ sputtering step suggests that the surface was partially amorphized. This conclusion is consistent with the broad Bi 5*d* spectra indicative of chemical heterogeneity which is likely a consequence of a preferential sputtering of Se atoms over Bi atoms due to differences in atomic mass. A low binding energy component of the Bi 5*d* core level after the Ar^+ sputter step is evidence for reduced Bi_2Se_3, i.e., Bi_2Se_x where $x < 3$. After the complete IBA process, a sharp diffraction pattern is observed with LEED which is evidence for a recrystallization of the material surface; furthermore, there is no evidence for polycrystallinity which would manifest as diffraction rings rather than spots. A sharpening of the Bi 5*d* and Se 3*d* core levels indicate the annealing step in Se improves the chemical homogeneity of the surface by replacing Se lost in the Ar^+ sputter process. The recovery of the electronic structure, as measured with ARPES (*Figure 5.5*), provides additional evidence for both the crystallization of the surface and restoration of the Bi_2Se_3 stoichiometry.

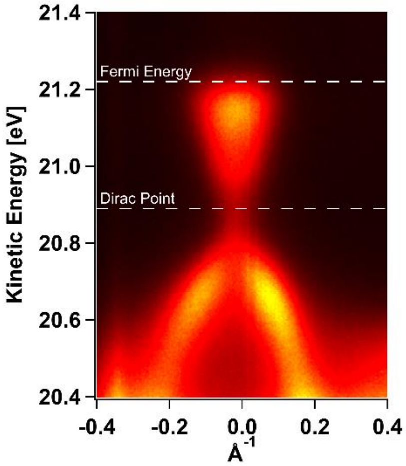

Figure 5.5: ARPES spectrum of $Bi_{1.99}Sn_{0.01}Se_3$ upon completion of the IBA process. Image centered at Γ in the K-Γ-K direction.

5.4.2. Thermal Desorption of Protective Se Capping Layers

Protective amorphous Se capping layers were deposited in-situ onto grown Bi_2Se_3 thin films at room temperature upon completion of sample growth and prior to removal from UHV. The Se layer acts as a protective barrier in air preventing sample degradation. After the sample is transferred through air and introduced to the UHV analysis chamber, the Se capping layer is removed through mild heating (~150 °C) [164]. This process can be monitored in real time using XPS, as demonstrated in *Figure 5.6a*, which ensures high control of the process reducing the likelihood of accidental damage to the Bi_2Se_3 material. The reduction in detectable Se-Se bonds and a plateau of the Se-Bi peak intensity signifies the complete removal of the Se cap. Upon removal of the cap, Bi and Se core levels consistent with Bi$_2$Se$_3$ are observed (*Figure 5.6b*). *Figure 6c* shows the recovered ARPES spectra after the thermal removal of Se capping layers further indicating the Se cap sufficiently protected the Bi$_2$Se$_3$ surface in air.

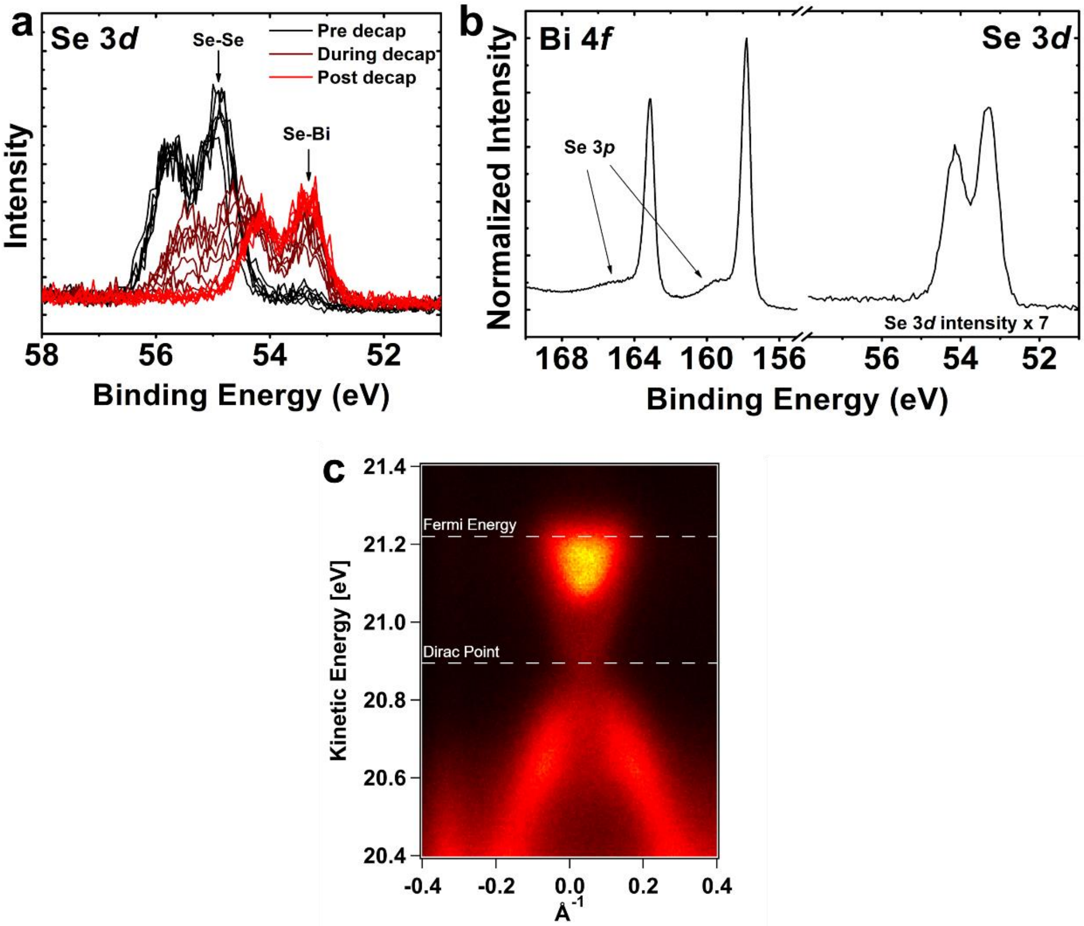

Figure 5.6: a) Real-time XPS of the Se 3*d* core level during the thermal Se decap process. b) XPS core level and c) ARPES spectra of Bi$_2$Se$_3$ after the thermal Se decap process. The bulk and TSS are clearly resolved in the ARPES image. Image centered at Γ in the K-Γ-K direction.

A pitfall of using Se capping layers to preserve the Bi$_2$Se$_3$ surface is that the Se layers are volatile. *Figure 5.7* shows the XPS spectra of a Se capped Bi$_2$Se$_3$ sample in the as received state (*black spectra*) and after sitting in air for 11 days (*blue spectra*). The increase in intensity of the Bi$_2$Se$_3$ spectral features relative to that of the Se^0 features indicate a thinning Se capping layer.

Additionally, the large increase in the Bi 4*f* feature at ~159 eV indicates that BiO_x is forming and thus the thinned cap is no longer protecting the sample surface; this result is mirrored in the O 1*s* spectra which is consistent with BiO_x. This result suggests that the use of amorphous Se capping layers is not ideal for long term sample storage. These observations are consistent with the work by Li et al. who also observed the thinning of Se capping layers on similar timescales [165].

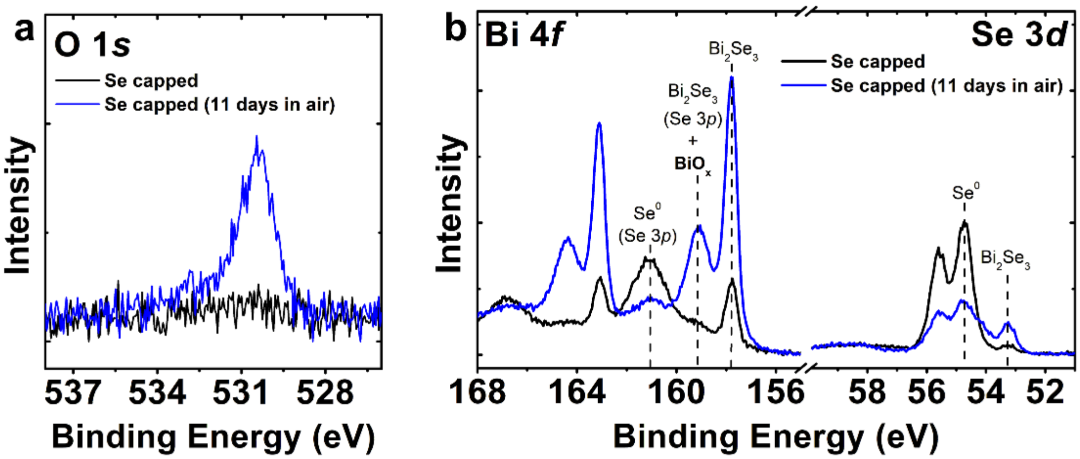

Figure 5.7: XPS spectra of the a) O 1*s*, b) Bi 4*f* and Se 3*d* core levels of a Se capped Bi_2Se_3 sample in the as-received state and after 11 days in air. XPS data indicates a thinning of the Se cap over time leading to oxidation of Bi_2Se_3.

5.4.3. In-Situ Mechanical Cleave

In this section we explore cleaving MBE-grown Bi_2Se_3 with adhesive tapes and UHV compatible resins/epoxies. Refer to *Section 2.3* for step-by-step details of each procedure.

5.4.3.1. In-Situ Cleave with Adhesive Tapes

Adhesive tapes such as Scotch or Kapton tapes are commonly used to exfoliate bulk van der Waals crystals either grown by chemical vapor transport or of geological origin. Cleaving of bulk crystals reveals pristine, atomically clean surfaces and thus, cleaving is a potential candidate for preparation of ex-situ grown Bi_2Se_3. *Figure 5.8* shows the O 1*s*, Bi 5*d* and C 1*s* core level XPS spectra of air exposed Bi_2Se_3 and the same sample after mechanical cleaving attempts with Kapton and Scotch tapes. The Bi 5*d* spectra shows chemical signatures of both Bi_2Se_3 and Bi_2O_3 in the starting material. Cleaving attempts with Kapton and Scotch tapes result in a decrease in the Bi 5*d* spectra; however, the relative intensities of the two Bi chemical states remains unchanged. The O 1*s* feature at ~531 eV shows the same intensity trend as the Bi 5*d* core level, that is, it decreases in intensity after cleaving attempts with both adhesive tapes. A 2^nd^ feature in the O 1*s* at ~533 eV, and the C 1*s*, increases in intensity after cleaving attempts using adhesive tapes. From these data it can be concluded that neither the Kapton nor Scotch tapes were successful in cleaving the MBE-grown Bi_2Se_3 sample. To the contrary, the data shows evidence that the tapes are leaving behind a residue. Evidence for residues left behind by the adhesive tapes are the increasing high binding energy component of the O 1*s* spectra and increased intensity of the C 1*s* spectra. Lastly, the decrease in intensities from the Bi_2O_3 and Bi_2Se_3 signals after cleaving attempts is consistent with the presence of an attenuating overlayer.

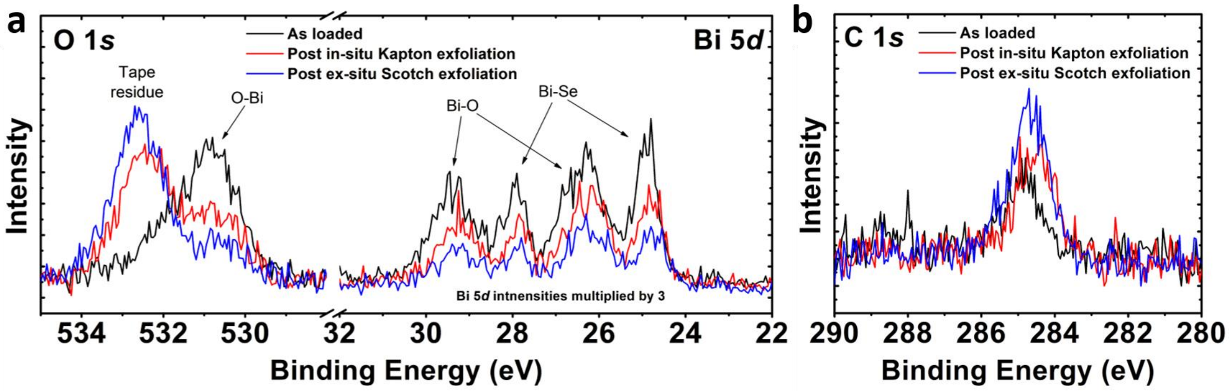

Figure 5.8: XPS spectra of the a) O 1*s*, Bi 5*d*, and b) C 1*s* core levels of air exposed Bi_2Se_3 in the starting state and post cleaving attempts using Kapton and Scotch adhesive tapes.

The data presented here marks a stark contrast in the cleaving tendencies of bulk van der Waals compounds and thin films produced by MBE. For example, bulk, CVT-grown $NbSe_2$ is routinely cleaved using Kapton tape and was employed in the previous chapter. The reasons for the differences in cleaving tendencies are not fully understood. However, they are likely related to the effect the growth processes have on the underlying microstructure. Bulk van der Waals crystals are often single crystals and thus have large areas of undisturbed van der Waals bonding connecting adjacent layers. Van der Waals crystals grown by MBE, such as Bi_2Se_3, consist of many coalesced nuclei and often grow normal to the substrate surface through the propagation of screw dislocations. The presence of screw dislocation in 2D materials ensure continuous covalent bonding normal to the sample surface and thus was investigated as an explanation for the resistance of the material to cleave along the vdW gap. However, this theory can be ruled out by calculating the additional forces required to cleave a 2D material in the presence of screw dislocations; the estimated force required to cleave the material would only increase by <1%. This estimate was made using the calculated interlayer binding force and measure tensile strength of MoS_2; MoS_2 was used for this estimation due to better availability of measured mechanical properties compared to Bi_2Se_3 [166, 167]. This estimate also used the areal density of screw dislocations inferred from AFM images of the Bi_2Se_3 surface in this work. The lack of a significant change in interlayer binding forces in the presence of screw dislocations implies other microstructural characteristics play a more significant role in the cleaving characteristics of MBE-grown Bi_2Se_3.

5.4.3.2. In-Situ Cleave with Torr Seal Epoxy

Mechanical cleaving of MBE-grown Bi_2Se_3 was attempted using Torr Seal as it is a stronger adhesive compared to the previously studied adhesive tapes. Torr Seal is a UHV compatible epoxy often used to repair leaks in UHV equipment. The XPS spectra of Bi_2Se_3 after an in-situ cleave using Torr Seal is presented in *Figure 5.9a*. Present in the figure is the Se 3*d* and Bi 5*d* core levels; the single doublet in each spectrum are consistent with Bi_2Se_3. The fact that no oxides are present in the XPS spectra indicates that the scanned area cleaved completely, and no un-cleaved areas are present. Furthermore, the ARPES spectra in *Figure 5.9b* further confirms a recovered Bi_2Se_3 surface.

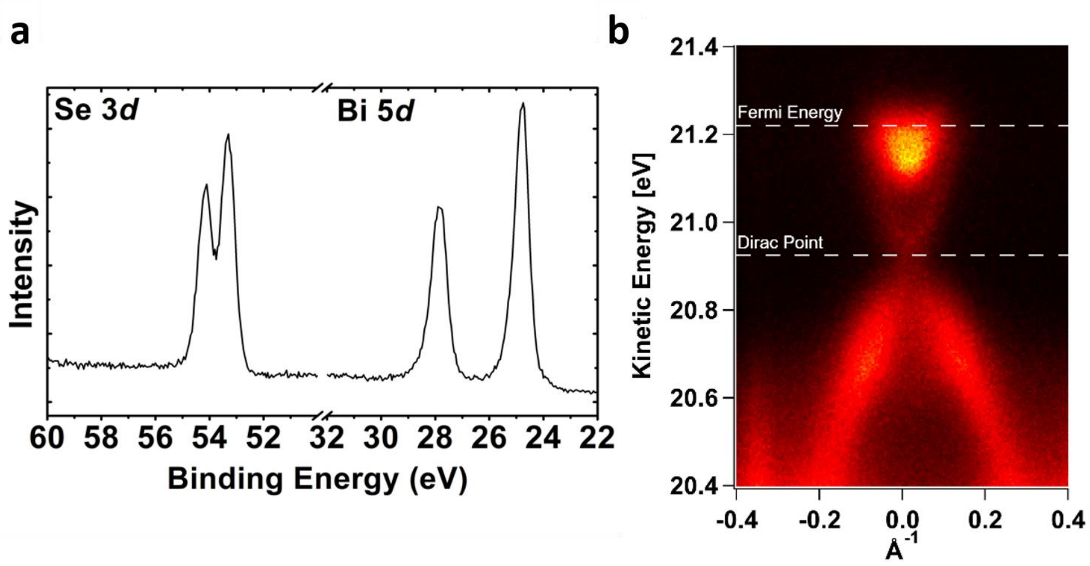

Figure 5.9: The a) XPS and b) ARPES spectra of Bi_2Se_3 cleaved in-situ using Torr Seal epoxy.

Due to the nature of mechanical cleavage, the process is not fully repeatable or predictable. In some instances, the Torr Seal resin will simply break from the sample surface unsuccessfully cleaving the material. Furthermore, in instances where the Bi_2Se_3 sample successfully cleaved, the substrate was often exposed; the degree to which the substrate was exposed was unpredictable and varied sample to sample. *Figure 5.10a* shows XPS data collected of two $Bi_{1.99}Sn_{0.01}Se_3$/GaAs (111) samples after mechanical cleavage. The presence of the As 3*d* and Ga 3*d* core levels of varying intensities between *Cleaved sample 1* and *Cleaved sample 2* shows that different amounts of Bi_2Se_3 were removed after each cleave. *Figure 5.10b* shows superimposed LEED patterns of the Bi_2Se_3

(001) and GaAs (111) surfaces of *Cleaved sample 2* which suggests the GaAs (111) substrate was exposed. Both samples were cleaved from the same wafer suggesting the differences between *Cleaved sample 1* and *Cleaved sample 2* are inherent to the cleaving process, not sample specific factors, i.e., sample thickness, substrate orientation, etc. Intensity analysis of the As 3*d* and Ga 3*d* core levels indicate that the observed Ga to As ratio is ~1.5:1, not 1:1 as would be expected for GaAs. It is likely that during the cleaving process an interfacial $GaSe_x$ compound is also exposed. This is further supported by the high binding energy shoulder in the Se 3*d* spectra for *Cleaved sample 2*. *Figure 5.10c* shows pitting of a $Bi_{1.99}Sn_{0.01}Se_3$/InP (111) sample after mechanical cleavage which shows the macroscopic effect on the surface morphology.

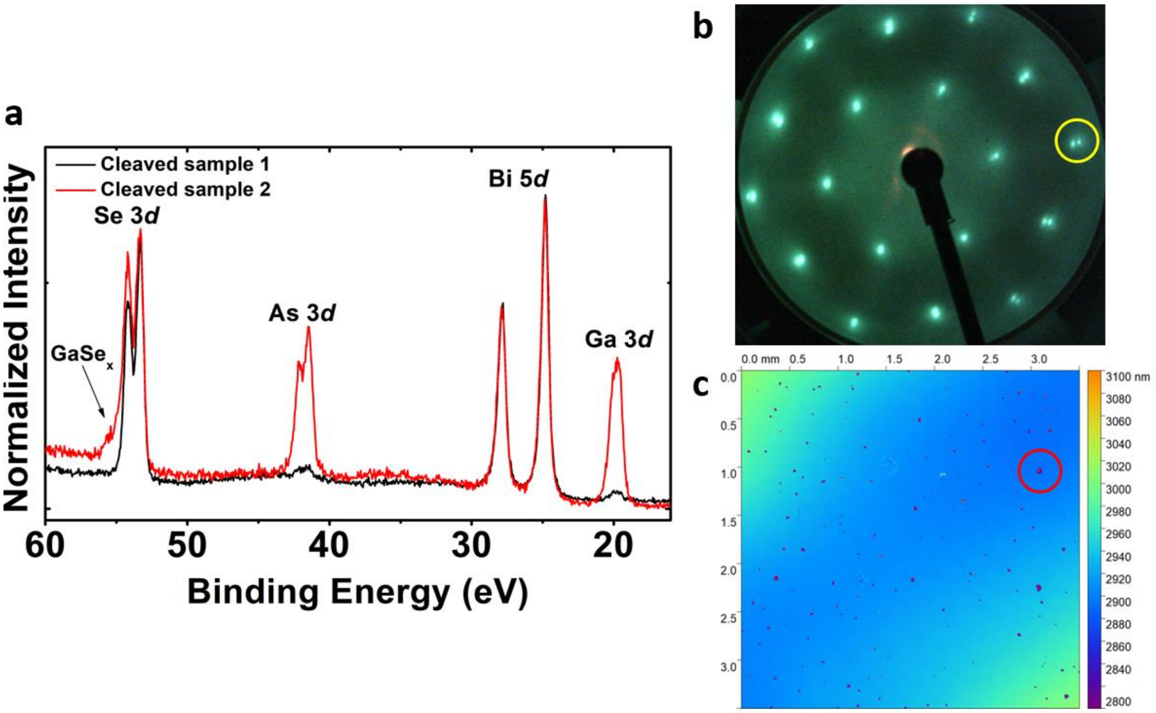

Figure 5.10: a) XPS spectra of the $Bi_{1.99}Sn_{0.01}Se_3$/GaAs (111) spectra after mechanical cleavage. Both samples originated from same wafer suggesting the variability is intrinsic to the method. b) LEED of *Cleave sample 2* revealing patterns of the Bi_2Se_3 (001) and GaAs (111) surfaces. Distinguishable LEED spots highlighted in yellow circle. c) Optical topographic image taken of Bi_2Se_3/InP (111) post in-situ mechanical cleave using Zygo Optical Surface Profilometer. Pitting observed across sample highlighted by red circle.

5.4.4. Establishing the Ideal Method

While the three methods of Bi_2Se_3 preparation were shown to reproduce the expected ARPES spectra, the various methods expectantly had differences between them. Establishing an ideal method, by weighing the advantages and disadvantages of each preparation technique will depend on the goals of an experiment. However, some generalizations can be established based on the results here.

We have shown that the IBA process was effective in recovering both the intended chemistry and surface symmetry as measured by XPS and LEED, respectively. However, through comparison with complementary techniques, such as mechanical cleavage, it is found that an n-type Fermi level shift of the Bi_2Se_3 results uniquely from the IBA process (*Figure 5.11*); in contrast, samples prepared through thermal Se decapping and mechanical cleaving typically result in similar Fermi level positions. The Ar^+ sputter process is a destructive technique. Given the relative atomic weights of Bi and Se, it is reasonable to assume that Se is preferentially sputtered away. Though the chemistry is recovered after annealing the sample in a Se flux, the spectra is further n-type shifted compared to the as-grown material. The n-type shift after the IBA process is potentially a consequence of a higher Se vacancy concentrations when compared to the as-grown material as Se vacancies are known to act as n-type dopants [50-52]. This result is significant in the context of our work as we are specifically studying the effects of doping, which are expected to result in Fermi level shifts. Fermi level shifts due to the IBA process would complicate this analysis. Additionally, the ARPES spectra of the sample which underwent the IBA process is noticeably distorted suggesting that in-situ cleaving is better for observing changes in the band structure due to doping.

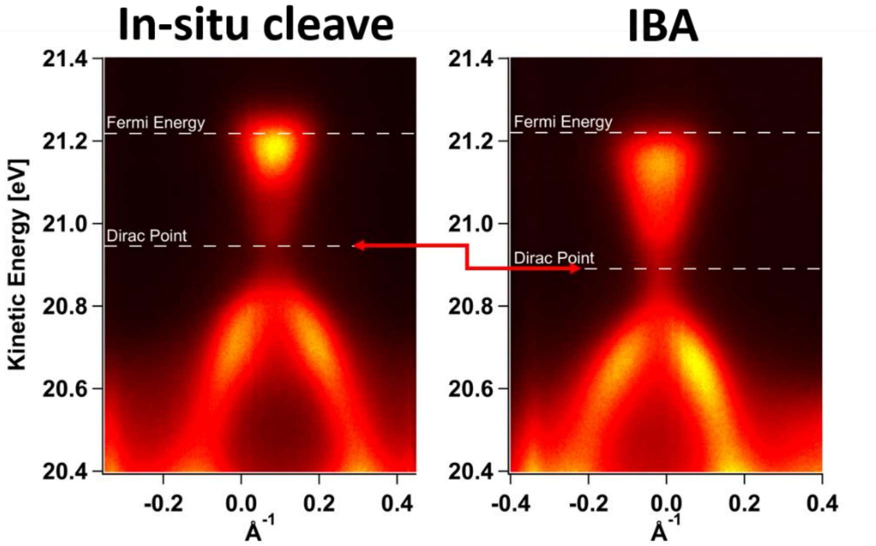

Figure 5.11: Comparison of the ARPES spectra of $Bi_{1.99}Sn_{0.01}Se_3$ after sample preparation utilizing an in-situ cleave and IBA process. Both samples were taken from the same wafer ruling out sample-to-sample variability.

Figure 5.12 shows the change in surface morphology from the as-grown material and after in-situ mechanical cleavage. The AFM image presented in *Figure 5.12a* shows the surface topography after an in-situ thermal Se decap. The surface consists of Bi_2Se_3 islands with triangular like grains. The AFM image in *Figure 5.12b* is of a sample after an in-situ mechanical cleave. Clear from the images is the change in surface morphology. Due to the surface of the material being removed, the island like morphology of the surface is no longer present. Instead, the surface consists of large planar regions and steep cliffs ~100 nm tall. As discussed in *Section 5.4.3.2*, the GaAs substrate is often exposed during mechanical cleavage in a non-predictable manner (see *Figure 5.10*).

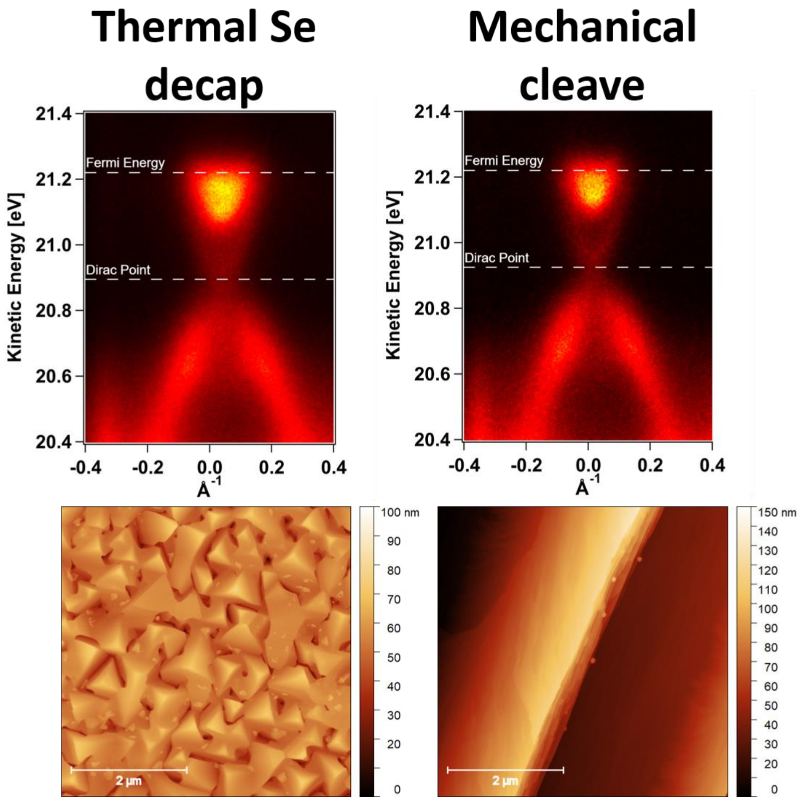
Thermal Se decap

Mechanical cleave

Figure 5.12: ARPES/AFM of Bi_2Se_3/GaAs (100) post in-situ a) thermal Se decap and b) mechanical cleave.

Though thermal Se decapping and mechanical cleaving both result in retaining the material's electronic structure and chemistry, we utilize in-situ mechanical cleaving for the majority of experiments in our follow-up study on Sn-doped Bi_2Se_3. The reasons for this are few-fold. First, qualitative comparison of the ARPES spectra in *Figure 5.12* reveal a sharper ARPES spectra of the mechanically cleaved sample. Additionally, mechanical cleavage requires no heating steps. Given the low thermal stability of Bi_2Se_3 and the fact that the Fermi level is sensitive to degree of Se vacancies, any unnecessary heating should be avoided [51]. Lastly, we discover that Sn-doped Bi_2Se_3 has an artificially Sn-rich surface compared to the bulk of the material; this will be discussed in more detail in the next section. By cleaving the sample, we can rule out contributions from this excess Sn concentration on the material's properties.

5.5. Analysis of Sn-doped $Bi_{2-x}Sn_xSe_3$

The purpose of this section is to report on analysis of Sn doped $Bi_{2-x}Sn_xSe_3$. In the absence of Sn doping, Bi_2Se_3 has an n-type electrical character, i.e., the Fermi level is in the bulk CB. The n-type character is often cited as a consequence of Se vacancies in the synthesized material [50-52]. Proposed devices based on Bi_2Se_3 take advantage of the TSS that cross the bulk band gap [21]. Therefore, to create working devices, control of the Fermi level must be achieved. If the Fermi level is in the bulk CB, the properties of the material will be dominated by the bulk CB states and not the TSS. In this work, we dope Bi_2Se_3 with Sn, which is hypothesized to be a resonant, p-type dopant in Bi_2Se_3 [156]. The goal is to use Sn to counter-dope the native n-type nature of the as-grown Bi_2Se_3. The p-type nature arises from the substitution of Bi with Sn (Sn_{Bi}) as depicted in *Figure 5.13a*. The resonant doping level, which overlaps with the bulk VB, should have the added effect of boosting the Seebeck coefficient through modulation of the bulk density of states around the valence band maximum *Figure 5.13b* [156, 157].

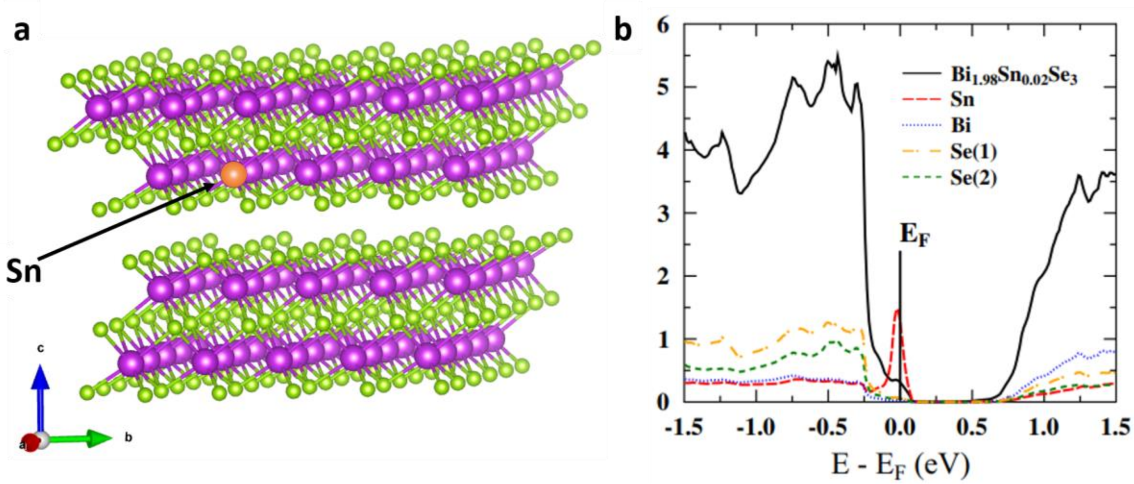

Figure 5.13: a) Ball and stick model of Bi_2Se_3 with Sn substitutionally doped for Bi atom. Bi, Se and Sn atoms depicted in purple, green, and orange, respectively. Model created in VESTA [30]. b) Calculated DOS of $B_{1.98}Sn_{0.02}Se_3$ including Sn resonant doping level. Frame *b* reused from B. Wiendlocha under Creative Commons CC BY license (Copyright © 2016, Springer Nature) [156].

5.5.1. Spectroscopic Analysis of $Bi_{2-x}Sn_xSe_3$

5.5.1.1. ARPES Analysis of $Bi_{2-x}Sn_xSe_3$

ARPES and LEED were carried out on select Sn doped Bi_2Se_3 samples grown on GaAs (100) to explore how the Sn dopant affected the electronic and physical structures of the material. Three different ARPES spectra are presented in *Figure 5.14*: Bi_2Se_3 (*undoped*), $Bi_{1.99}Sn_{0.01}Se_3$ (*low Sn*), and $Bi_{1.90}Sn_{0.10}Se_3$ (*high Sn*). All three spectra were taken at UVA after an in-situ mechanical cleave of the material. The ARPES spectra of undoped Bi_2Se_3 is as expected with both the bulk and surface states clearly resolved. The Dirac point is located ~0.295 eV below the Fermi energy; this value is taken as the minimum in the momentum integrated intensity (*see Section 7.5*). The inset LEED pattern shows a sharp hexagonal pattern consistent with the exposed basal plane of Bi_2Se_3 indicating a high degree of epitaxy exists between the grown Bi_2Se_3 and the GaAs (100) substrate. The ARPES spectra of $Bi_{1.99}Sn_{0.01}Se_3$ shows that the position of the Dirac point, relative to the Fermi level, only results in a subtle shift compared to the undoped sample. The estimated position of the Dirac point in $Bi_{1.99}Sn_{0.01}Se_3$ is ~0.275 eV below the Fermi level. The relative shift of the Dirac point position in $Bi_{1.99}Sn_{0.01}Se_3$ compared to the undoped sample falls within the error of ~0.025 eV for the extrapolation of the Dirac point energy and thus the change in the position of the Dirac point under low doping concentrations is not significant; this error was established through the analysis of multiple samples originating from an individual wafer. However, qualitative analysis of the ARPES spectra indicates that the TSS become less defined in the presence of the Sn dopant. Also apparent is the increased intensity of the bulk VB relative to that of the bulk CB. The LEED pattern observed here is qualitatively similar to that of the undoped Bi_2Se_3. The higher doping level of $Bi_{1.90}Sn_{0.10}Se_3$ blur the TSS of Bi_2Se_3 which are no longer clearly resolved. For this reason, the position of the Dirac point is hard to define in this sample.

Qualitatively, the bulk VB appears to be shifted upward compared to the lower Sn concentration. The observed LEED pattern at high Sn concentration is significantly blurred compared to the undoped and low doped samples.

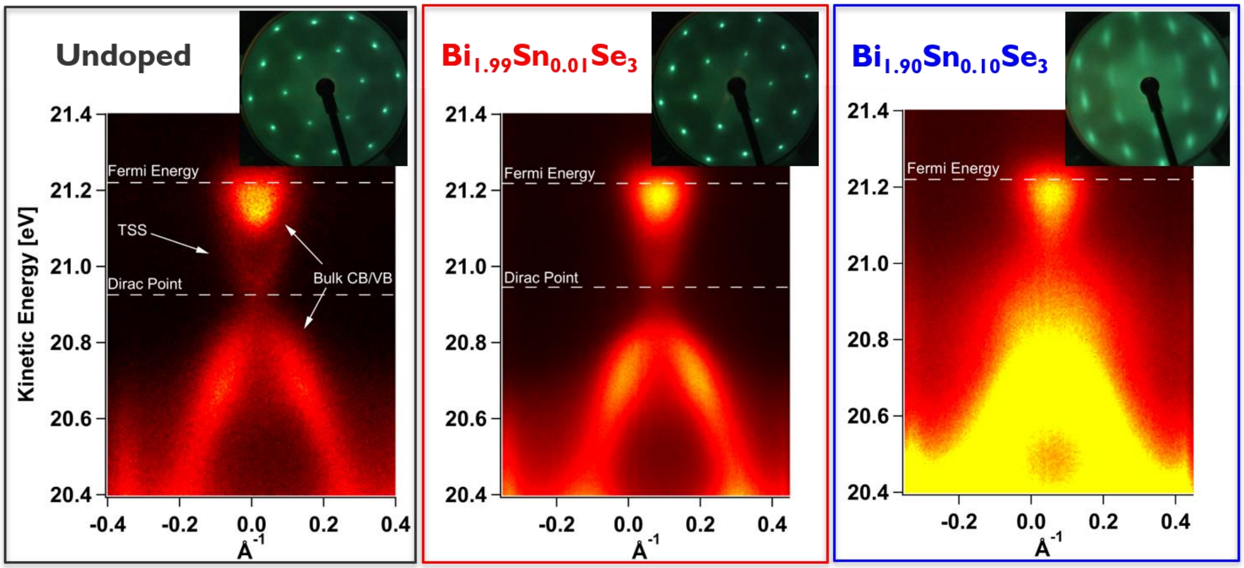

Figure 5.14: ARPES (K-Γ-K) spectra and LEED of $Bi_{2-x}Sn_xSe_3$/GaAs (100) as a function of Sn doping. Sn concentrations inset into image. All spectra taken post in-situ mechanical cleave. TSS and bulk CB/VB states are marked for the undoped sample. Intensities normalized to the maximum intensity of the bulk CB in each plot.

ARPES and LEED of $Bi_{1.99}Sn_{0.01}Se_3$ suggest that the addition of small amounts of Sn do not degrade the crystalline or electronic structures. The increase in intensity of the top of the bulk VB is consistent with the expected resonant state of Sn doped Bi_2Se_3. DFT work has predicted the resonant level of Sn to be a flat band which overlaps with the upper bulk VB [50]. Though we don't see a broad flat band associated with Sn, we do observe a broadening of the top of the bulk VB along with an increase in intensity. LEED suggests that the crystallinity was not significantly affected using this Sn concentration. ARPES of $Bi_{1.90}Sn_{0.10}Se_3$ shows a significantly distorted electronic structure with the intensity of the bulk VB further increasing compared to

$Bi_{1.99}Sn_{0.01}Se_3$. It is unclear whether the TSS are no longer present or obstructed by the diffuse signal originating from the bulk band gap. LEED shows a more diffuse pattern indicating poorer crystallinity compared to the other samples measured.

5.5.1.1.1. Comments on Potential of UV-induced Band Bending

Analysis of the ARPES spectra in this work does not indicate any significant shift of the Fermi level with Sn doping. This brings into question whether Fermi level shifts should be detectable with ARPES. The work by Frantzeskakis et al. revealed an illumination-driven band bending of Bi-based TIs under UV excitation which shifts the position of the Fermi level [168]. Frantzeskakis et al. observed that the onset of UV-illumination resulted in an n-type shift of the Fermi level. Furthermore, this n-type shift was not consistent with time but instead varied. The hypothesized mechanism for this time dependent band bending was the ionization, followed by the desorption, of adsorbed species on the surface of the TI due to the presence of residual gases in UHV. This process, which develops with time, complicates ARPES measurements of Bi_2Se_3 as it suggests the degree of band bending will be continuously changing.

To test whether our samples may be artificially n-type shifted due to UV exposure and whether the degree of band bending changes with time, we collected UPS measurements as a function of UV-exposure time; UPS measurements are employed instead of ARPES because the data acquisition time for UPS is ~10 minutes compared to ~3 hours for ARPES. *Figure 5.15a* shows the UPS spectra of air exposed $Bi_{1.99}Sn_{0.01}Se_3$ upon exposure to the UV source and after 3 hours of constant UV exposure. The data shows that UV-illumination leads to an n-type shift of the spectra, i.e., to lower kinetic energy. *Figure 5.15b* shows the UPS spectra as a function of time for a $Bi_{1.99}Sn_{0.01}Se_3$ sample prepared through in-situ cleaving. All the spectra for the in-situ cleaved sample overlay nearly perfectly. The upper limit of band bending over the course of ~8 hours of

UV-exposure is <0.02 eV which is below the error in our Dirac point energy resolution. From these collected data, it can be concluded that freshly cleaved samples do not undergo continuous UV-exposure induced band bending at time scales relevant to ARPES data acquisition times.

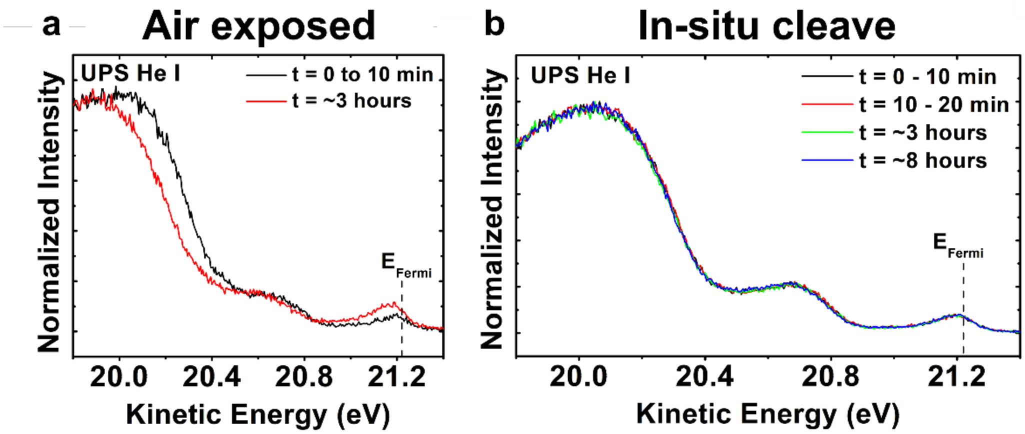

Figure 5.15: UPS spectra of $Bi_{1.99}Sn_{0.01}Se_3$ as a function of UV exposure time. a) Air exposed samples demonstrate UV exposure induced band bending. b) In-situ cleaved samples do not show UV exposure induced band bending.

If the hypothesis of Frantzeskakis et al. is correct, that UV-ionized adsorbates result in band bending, then the data represented in *Figure 5.15* makes sense. The air exposed sample (*Figure 5.15a*) will be decorated in adsorbed species which have the tendency to be ionized upon exposure to the UV source and result in surface band bending. The sample that was cleaved in-situ (*Figure 5.15b*) will have only had a short time (~1 hour) to accumulate adsorbed species in UHV. Therefore, there is significantly fewer adsorbed molecules on the surface which are prone to ionization and thus no UV-illumination induced band bending is observed. What this experiment does not reveal is any potential band bending which occurs over very short timescales. Any spectral shifting that occurs on the order of seconds will be missed in the data in *Figure 5.15*. Frantzeskakis et al. observed band bending occurred over a time scale of ~60 seconds in their work [168]. This observation was made possible due to the larger photon flux available at the synchrotron end station used in their work allowing for quicker measurements to be collected; specifically, the photon fluxes available in their work are ~300x that of the photon fluxes available to us. Given our lower photon flux, any UV-induced band bending is expected to occur over the course of hours rather than minutes or seconds and thus should be detectable in the data presented in *Figure 5.15* [168]. A final difference is that the work by Frantzeskakis et al. was carried out at low temperature, <40 K, which would be expected to enhance the adsorption of molecular species (which have the susceptibility to ionize). Our work was carried out at room temperature which may explain the differences observed between the two works. The data presented in this section, along with consideration for experimental differences from those used by Frantzeskakis et al., suggest that illumination-induced band bending is not the source of the lack of observed Fermi level shifts with ARPES in our work.

Despite the abovementioned reasoning suggesting UV exposure does not result in band bending in our ARPES measurements, the lack of detectable Fermi level shifts with ARPES match results observed elsewhere. Discrepancies between ARPES determined Fermi level positions and those acquired through other characterization techniques, such as STS and Shubnikov–de Haas (SdH) oscillations in magnetotransport measurements, are common [51, 52, 168]. For that reason, estimating Fermi level shifts with ARPES needs to be carried out with caution and, therefore, no major claims regarding Fermi level shifts are made here. What can be stated more concretely is the effect Sn has on the acquired spectral shape. First, low Sn concentrations resulted in a relative increase in the intensity of the bulk VB relative to that of the bulk CB. This relative increase of the bulk VB compared to that of the bulk CB is an expected consequence of the resonant Sn state. Lastly, high levels of Sn result in a further increase of the bulk VB intensity and a distortion of the electronic structure which eliminate or obstruct the TSS.

5.5.1.2. XPS Analysis of $Bi_{2-x}Sn_xSe_3$

XPS of the same three $Bi_{2-x}Sn_xSe_3$ samples have been carried out to better understand the chemical nature of the films. The Sn 3*d* core level and a wide energy window of the Se 3*d*, As 3*d*, Bi 5*d*, and Ga 3*d* are presented in *Figure 5.16a* and *b*, respectively. As discussed previously, the substrate can be exposed during the mechanical cleaving process which explains observed As and Ga core levels. The Sn 3*d* shows the expected increase in intensity with increased doping levels, roughly a 10-fold increase in intensity. The Se 3*d* and Bi 5*d* core levels of all the presented spectra share the expected features of Bi_2Se_3. In the sample with a high Sn concentration ($Bi_{1.90}Sn_{0.10}Se_3$) we see the emergence of additional features, including an increased intensity in the valley of the Bi 5*d* and to the high binding energy side of the Se 3*d* core levels. The increase in intensity of the high binding energy side of the Bi $5d_{5/2}$ feature is consistent with the expected intensity the Sn 4*d* core level which is located ~25 eV; this intensity estimate is made utilizing the known photoionization cross sections of the Sn 3*d* and 4*d* core levels. The high binding energy shoulder in the Se 3*d* core level is similar to that previously explained in *Section 5.4.3.2*, where an interfacial $GaSe_x$ layer was detected after mechanical cleavage.

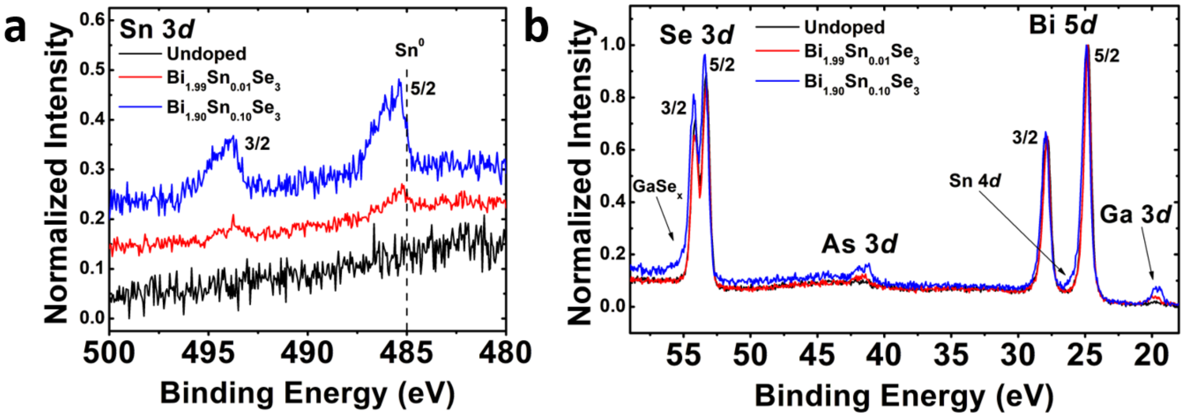

Figure 5.16: XPS of Sn-doped Bi_2Se_3 at different Sn concentrations. All core levels normalized to Bi 5*d* core level of respective sample. Sn 3*d* spectra vertically offset for clarity.

A more careful analysis of the Sn 3*d* core level in *Figure 5.16a* reveals that Sn exists in multiple chemical states; this is most apparent for $Bi_{1.90}Sn_{0.10}Se_3$. The low binding energy component is clearly present at both dopant concentrations and is assumed to be Sn substitutionally replacing Bi. The identity of the high binding energy Sn 3*d* component is not immediately obvious, though a few candidates exist, such as the binary compounds SnSe or $SnSe_2$ and ternary $Bi_xSn_ySe_z$ compounds. The nature of the Sn chemistry of $Bi_{2-x}Sn_xSe_3$ will be further explored in the following section.

5.5.1.3. Identifying a Sn-rich Surface in $Bi_{2-x}Sn_xSe_3$

XPS revealed that the chemistry of the surface and the bulk of $Bi_{1.99}Sn_{0.01}Se_3$ varied with respect to each other. *Figure 5.17* shows the XPS of two $Bi_{2-x}Sn_xSe_3$ samples at nominally identical Sn concentrations. *Sample A* was grown and shipped to UVA without a Se capping layer while *Sample B* was sent to UVA with a Se capping layer which was thermally removed in-situ prior to analysis. XPS of both samples were taken before and after cleaving which allowed the chemistry of the surface and bulk of the films to be compared. The samples were observed to have an enrichment of Sn at the surface compared to the bulk of the films. In addition to the increased Sn content at the sample surfaces, the intensity ratio of the two states differs at the surface and in the bulk. At the surface, the high binding energy component, labeled *Sn-2*, is the stronger of the two features while the lower binding energy component, labeled *Sn-1*, is the stronger signal in the bulk. Two samples were compared here for two reasons: 1) to show the Sn richness at the surface was a repeatable occurrence (and therefore not due to an error in the growth process) and 2) to rule out the possibility that the thermal treatment associated with the Se decap process was in some way changing the surface chemistry.

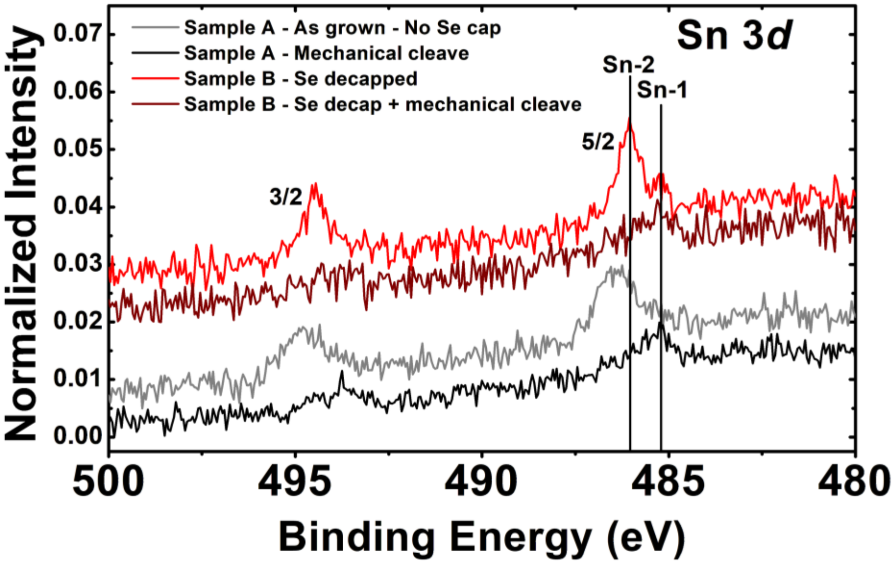

Figure 5.17: Sn 3*d* core level spectra of $Bi_{1.99}Sn_{0.01}Se_3$ grown under similar conditions but analyzed after unique sample preparation methods.

Due to the Sn-enriched nature of the $Bi_{2-x}Sn_xSe_3$ sample surface, the surfaces of $Bi_{1.90}Sn_{0.10}Se_3$ were prepared through an in-situ thermal Se decap, instead of a mechanical cleave, to preserve the high Sn content of the surface and better understand the chemistry. *Figure 5.18* shows four overlapping XPS spectra and are all normalized to the maximum intensity of the Bi 4*f* core level. The samples in black/grey represent undoped samples. The sample in dark red/red represent the spectra of $Bi_{1.90}Sn_{0.10}Se_3$ (*high Sn*); this sample was subsequently heated a 2nd time to ensure complete removal of the Se cap. The greater Se intensity in the spectra of the Sn doped samples tell us that there is a greater Se to Bi ratio in the presence of Sn. Despite the difference in total Se signal there is no clear evidence of a chemical shift in the Se spectra to differentiate the additional Se signal from that of $Bi_{1.90}Sn_{0.10}Se_3$.

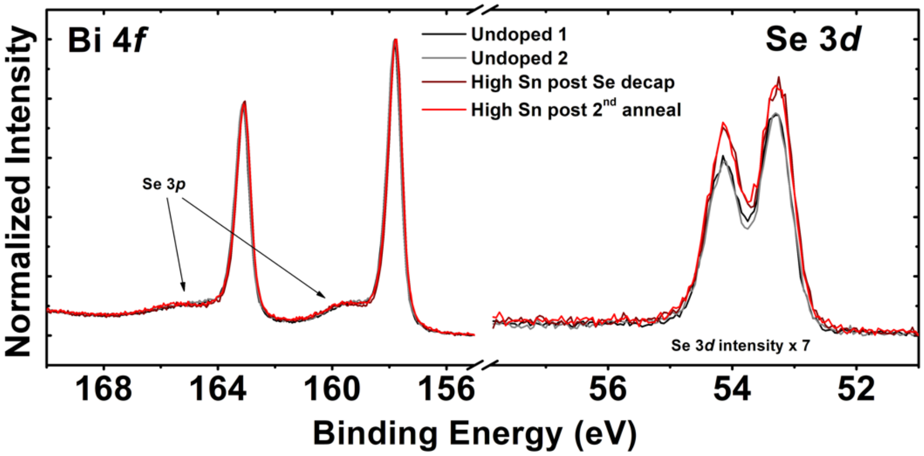

Figure 5.18: A comparison between undoped Bi_2Se_3 and $Bi_{1.90}Sn_{0.10}Se_3$. An increase in the Se intensity in the presence of Sn suggests an additional $SnSe_x$ compound forms during synthesis. Se 3*d* spectra normalized to Bi 4*f* spectra for each respective sample.

The greater Se signal in the presence of Sn doping, along with the presence of two Sn chemical states, are strong evidence for an additional $SnSe_x$ or $Bi_xSn_ySe_z$ compound in the synthesized thin film. Though a ternary $Bi_xSn_ySe_z$ compound can't be ruled out, we suspect a $SnSe_x$ compound to be the origin of the increased Se 3*d* core level; this assumption is due to the sharp Bi 4*f* core level which suggests Bi exists in a single chemical state. The lack of a clear second doublet in the Se 3*d* core level associated with the presence of $SnSe_x$ is due to the low intensity and small chemical shift of the $SnSe_x$ signal compared to that of the $Bi_{2-x}Sn_xSe_3$ component. An estimate of the amount of excess Se can be determined through a known Bi to Se signal ratio (taken from the undoped Bi_2Se_3 film) and the photo-ionization cross-sections (PICS) of the Sn 3*d* and Bi 4*f* core levels. Knowledge of these PICS allows for the substitution of Bi with Sn to be accounted for in our analysis.

To investigate the chemical nature of the 2nd Sn-Se compound (in addition to $Bi_{1.90}Sn_{0.10}Se_3$), we deconvolute the XPS spectra (as presented in *Figure 5.19*). Here we use two chemical states for the Se 3*d* core level, an intense peak for $Bi(Sn)_2Se_3$ (blue), i.e., Se in a QL of $Bi_{2-x}Sn_xSe_3$, and a 2nd chemical feature for $SnSe_x$ (green); the intensity and position of the former is fixed based on the Bi 4*f* and *Sn-1* features while the latter is free in its intensity and position. This allows for the comparison of the *Sn-2* peak to the excess Se 3*d* peak associated with $SnSe_x$. From this fit the estimated stoichiometry of the additional Sn-Se compound is $SnSe_{1.1}$ and the Sn $3d_{5/2}$ – Se $3d_{5/2}$ peaks separation is 432.29 eV.

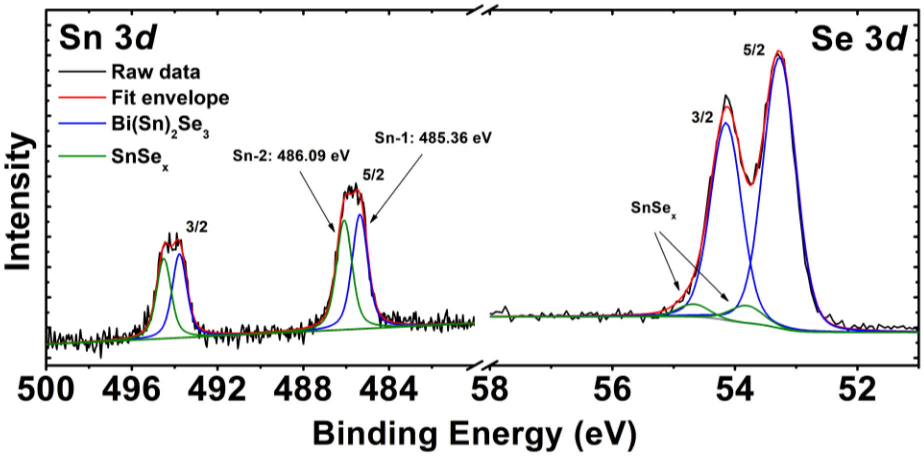

Figure 5.19: Spectral deconvolution of the Sn 3*d* and Se 3*d* core levels in $Bi_{1.90}Sn_{0.10}Se_3$. XPS taken post the thermal desorption of a protective Se capping layer.

The deconvoluted XPS spectra in *Figure 5.19* provide evidence for SnSe (tin monoselenide). The stoichiometry of $SnSe_{1.1}$ is close to SnSe. Furthermore, the Sn $3d_{5/2}$ – Se $3d_{5/2}$ peak separation of 432.29 eV is consistent with the literature values of SnSe at 432.2 - 432.3 eV [169, 170].

5.5.2. X-ray Diffraction of $Bi_{2-x}Sn_xSe_3$

XRD was carried out as a function of doping concentration of the $Bi_{2-x}Sn_xSe_3$ samples; the XRD data in the vicinity of the $Bi_{2-x}Sn_xSe_3$ (00 30) and GaAs (006) is presented in *Figure 5.20*. As the Sn concentration is increased, it is found that the out-of-plane lattice constant decreases which is observed as a shift of the $Bi_{2-x}Sn_xSe_3$ (00 30) to greater 2θ angles. The shift in the 2θ angle does appear to be a real consequence of Sn doping as the GaAs (006) peak does not change in position. The estimated out-of-plane lattice constants range from 2.858 nm to 2.856 nm. This is the expected trend with Sn_{Bi} substitutional doping as Sn is a smaller atom than Bi. This decrease in out-of-plane lattice constant also implies that the intercalation of excess Sn atoms is highly unlikely. Intercalated atoms would be likely to increase the out-of-plane lattice constant (as observed for $Nb_{1+x}Se_2$). Regardless of the Sn concentration used, only the signatures from $Bi_{2-x}Sn_xSe_3$ and the GaAs substrate are observed.

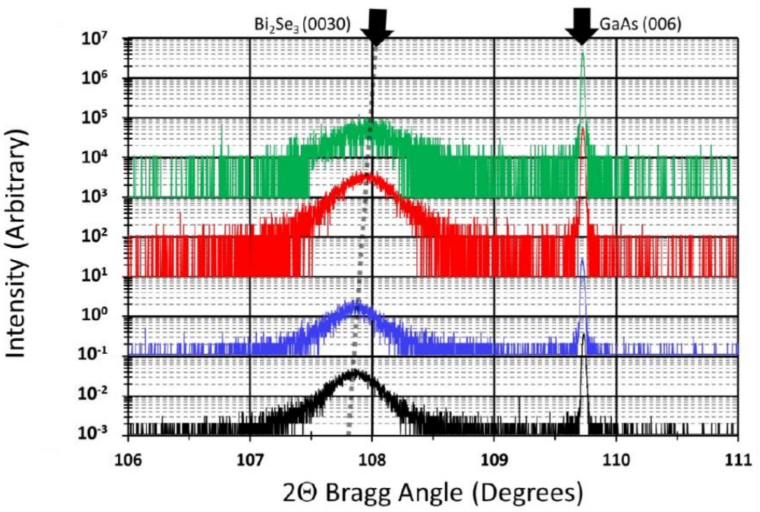

Figure 5.20: XRD patterns for $Bi_{2-x}Sn_xSe_3$ of various Sn concentrations. Data reveals a shift of the Bi_2Se_3 (00 30) reflection to higher *2θ* angles with increased Sn content. Reprinted with permission from G. M. Stephen *et al.*, "Effect of Sn Doping on Surface States of Bi_2Se_3 Thin Films," *The Journal of Physical Chemistry C*, vol. 124, no. 49, pp. 27082-27088, 2020/12/10 2020. Copyright 2023 American Chemical Society [50].

5.5.3. Transport Measurements of $Bi_{2-x}Sn_xSe_3$

The concentration of charge carriers in Bi_2Se_3 is related to the position of the Fermi level. Naturally, the carrier concentration is expected to reach a minimum when the Fermi level resides in the bulk band gap; this is due to the large decrease in bulk charge carriers. Therefore, as the Fermi level moves into the bulk CB, the carrier concentration is expected to increase. Furthermore, the carrier concentration is expected to continuously increase as the Fermi level moves higher into the bulk CB due to the increasing size of the Fermi surface. *Figure 5.21* reveals that the carrier concentration increases with greater levels of Sn doping. Undoped Bi_2Se_3 has a carrier concentration of ~1 x 10^{19} cm^{-3}. The carrier concentration plateaus with increasing Sn to a value of ~4 x 10^{19} cm^{-3}. The data here shows that the carrier concentration does not fall below that of the intrinsic (absence of Sn doping) Bi_2Se_3 at any of the investigated doping concentrations. The carrier mobility is observed to drop in the presence of Sn from ~900 cm^2/Vs in the undoped sample at room temperature to ~150 cm^2/Vs under the highest doping concentrations. Lastly, the resistivity is found to decrease for low Sn concentrations but returns to roughly the same values of the undoped sample (~9 x 10^{-5} Ω-m) in the highly doped samples.

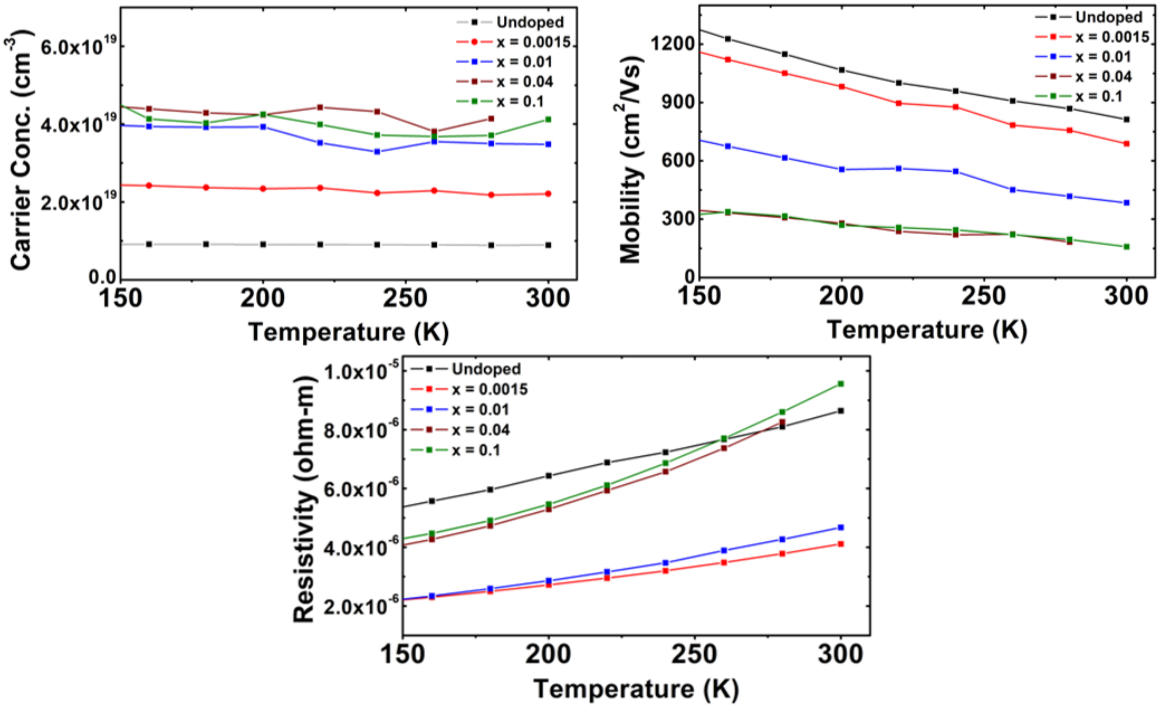

Figure 5.21: Carrier concentration, mobility, and electrical resistivity as a function of Sn doping levels. Plots reveals that Sn doping of Bi_2Se_3 increases the measured carrier concentration and decreases carrier mobility.

The electrical transport data presented here is self-consistent. Initially, doping the sample with low amounts of Sn results in a large increase in the carrier concentration with only a subtle decrease in the carrier mobility and thus the resistivity of the material drops. However, as more Sn is added, the sample-to-sample change in the resistivity is dominated by a large drop in the carrier mobility and thus the electrical resistivity increases. The increase in the carrier concentration implies (in the absence of significant changes to the electronic structure) that Sn acts as an n-type dopant rather than its predicted p-type nature. If the carrier concentration does decrease under any

Sn concentration, it is outside the dopant concentration range explored here. The increased resistivity with increasing temperature follows the expected behavior of a metal suggesting that at all doping concentrations that the Fermi level remains in the bulk CB. The decrease in mobility with increasing Sn concentration is likely a consequence of impurity scattering. Since charge carriers originating from the TSS are in theory immune to such scattering, the electrical conduction in these samples is likely dominated by bulk CB states that would not be protected from impurity scattering. Previous work on Bi_2Se_3 suggests that significant bulk conduction remains at carrier concentrations as low as 1 x 10^{17} cm^{-3} [52, 53]. The measured carrier concentration of $Bi_{2-x}Sn_xSe_3$ of >1 x 10^{19} cm^{-3} suggests that in our work the Fermi level resides in the bulk CB under all doping concentrations.

Due to the resonant nature of the Sn doping level, it is expected that Sn-doped Bi_2Se_3 will have an enhanced Seebeck coefficient [157]. The effect of Sn doping on the negative thermopower of Bi_2Se_3 is presented in *Figure 5.22*; the negative thermopower values are consistent with the n-type nature of the films. From these data, it is observed that the addition of Sn to Bi_2Se_3 decreases the measured thermopower of the material. This result contrasts with the hypothesis that Sn resonant doping would boost the measured thermopower. However, the drop in thermopower is an expected consequence of the increase in carrier concentration observed in the electrical transport data [171]. Together, the electrical and thermal transport data both suggest the grown $Bi_{2-x}Sn_xSe_3$ becomes more metallic with Sn added.

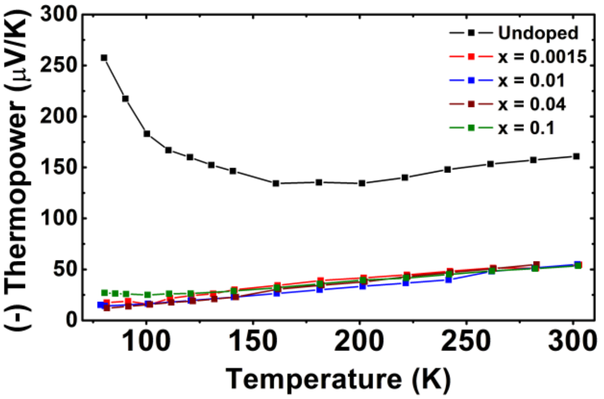

Figure 5.22: Negative thermopower vs temperature as a function of Sn-doping concentration.

5.5.4. Sn-doped Bi_2Se_3 Discussion

In this work, we investigated the use of Sn as a p-type dopant to shift the Fermi level into the bulk band gap and enhance the thermopower of Bi_2Se_3. The analysis in this section highlights that many of these predictions did not match experiment. ARPES measurements revealed no significant change in the position of the Fermi level with increased Sn doping. Increasing the concentration of Sn to higher levels (~5%) were detrimental to the physical and electronic structures. The carrier concentration unexpectantly increased, suggesting enhanced n-type character, and the measured thermopower fell in the presence of Sn. These results are in direct contrast to the expected results of the Sn doping of Bi_2Se_3 where a decrease in the carrier concentration was expected along with an increase in the measured thermopower due to the resonant doping state.

The reasons for the deviations between theoretical and experimental effects of Sn doping of Bi_2Se_3 are not fully understood. Here we discuss two possible explanations for the discrepancy between the hypothesis and experimental results: 1) the effect of the Sn oxidation state in Bi_{2-}

$_x$Sn$_x$Se$_3$ and 2) the presence of SnSe in the grown thin films. Bi is in the 3+ oxidation state in Bi_2Se_3. However, Sn is commonly found in the 2+ and 4+ oxidation states. The binding energy position of the *Sn-1* state is closer to the expected position of Sn^{2+} than that of Sn^{4+} as reported for SnSe and $SnSe_2$, respectively [169, 170, 172, 173]. Substitutional Sn^{2+} would be expected to p-type dope Bi_2Se_3 as it has one less electron participating in bonding compared to that of Bi^{3+}. Sn^{4+} donates an additional electron compared to Bi^{3+} and thus could be expected to n-type dope the Bi_2Se_3 samples as observed here. However, the binding energy position of the *Sn-1* state is below the expected Sn^{4+} energy. Thus, while the presence of Sn^{4+} substitutionally replacing Bi^{3+} is a possible origin of the enhanced n-type nature of the films, this is not supported by XPS analysis.

XPS identified the presence of SnSe in the grown material. However, the presence of SnSe alongside $Bi_{2-x}Sn_xSe_3$ does not offer a simple explanation to the unexpected nature of the transport properties of the grown material. SnSe is a semiconductor with a band gap >1 eV and is most often observed to have p-type character [174]. Therefore, we do not expect the presence of SnSe to result in an increase in carrier concentration. To the contrary, the presence of SnSe would be expected to decrease the carrier concentration in the grown material. The physical distribution of SnSe in the film is not fully understood, but it is speculated to exist at grain boundaries and step edges on the surface. The presence of SnSe terminated step edges is compatible with the observed surface structure changes upon mechanical cleavage. The surface of $Bi_{2-x}Sn_xSe_3$ in the as-grown state shows pyramidal structures which naturally contain a high density of step edges. Upon mechanical cleavage, most edge sites are removed which is consistent with the large decrease in the *Sn-2* state associated with SnSe (*Figure 5.17*), this change in morphology was presented in *Figure 5.12*.

It was observed that highly Sn-doped Bi_2Se_3 ($Bi_{1.90}Sn_{0.10}Se_3$) resulted in an increase in the measured carrier concentration of ~3 x 10^{19} cm^{-3} over undoped Bi_2Se_3. The expected density of Sn in this film (based on stoichiometry estimates) is ~1 x 10^{20} atoms.cm^{-3}. If Sn substitutionally doped for Bi behaves as an n-type dopant as observed (and in contrast to the hypothesized p-type nature), this would suggest that roughly a 3rd of the Sn in the film is actively doping the film. However, based on the XPS data of the $Bi_{1.90}Sn_{0.10}Se_3$ film presented in *Figure 5.16a* and *Figure 5.19*, up to a half of the Sn in the films is in the form of SnSe. This suggests that the change in carrier concentration (~3 x 10^{19} cm^{-3}) is on par with the concentration of Sn substitutionally doped into Bi_2Se_3 (>5 x 10^{19} cm^{-3}).

In summary, the results in this section highlight two unexpected engineering challenges with respect to the doping of Bi_2Se_3 with Sn. First, Sn exists in multiple chemical states with an enriched concentration at the material's surface. Second, the electronic and thermal properties directly contrast the expected results. Given the presented data, the reasons for these results can only be speculated. The results reported here motivate the study of additional dopants which will be further discussed in the *Future work* section.

5.6.Future Work

This section reports on the current state of investigations into MBE-grown TIs and discusses potential future work.

5.6.1. Analysis of EuS-doped Bi_2Se_3

The difficulty in achieving the intended results with Sn motivate the investigation of alternative dopants in Bi_2Se_3. In this section, we show preliminary results of EuS doping of Bi_2Se_3. Eu is hypothesized to be a p-type dopant in Bi_2Se_3. EuS is evaporated congruently from a EuS source during Bi_2Se_3 deposition. Experimentally, EuS (opposed to elemental Eu) was used as a doping source as it was already present in the MBE chamber for the deposition of EuS films. The added effect of S in the film is expected to be minimal due to its 2+ oxidation state, which is the same as Se^{2+} inherent to Bi_2Se_3. EuS has the added effect of being magnetic, with a Curie temperature of ~16 K.

To study the effect of EuS doping on Bi_2Se_3, the carrier concentration and the mobility were measured and are presented in *Figure 5.23*. The EuS flux used during growth was below the sensitivity of the beam flux monitor, therefore the results are presented as a function of EuS flux measured with an integrated flux monitor on the EuS cell. Intrinsic Bi_2Se_3 has a carrier concentration of ~2 x 10^{19} cm^{-3} and drops to 2.1 x 10^{18} cm^{-3} with increased EuS doping. Simultaneously, an increase in the carrier mobility is observed with increasing EuS flux.

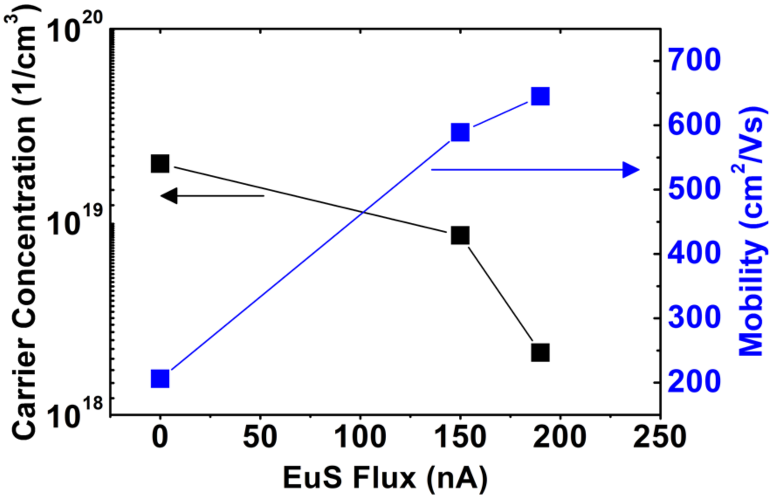

Figure 5.23: Carrier concentration and mobility as a function of EuS flux used during Bi_2Se_3 growth.

The decrease in carrier concentration with increased EuS doping is consistent with the expected p-type Fermi level shift. However, based on a carrier concentration of 2.1 x 10^{18} cm^{-3}, the Fermi level position is suspected to still be in the bulk CB. Previous reports in the literature suggest a Fermi level in the bulk band gap would result in carrier concentrations below 1 x 10^{17}

cm^{-3} [52]. The inverse relationship between carrier concentration and mobility matches that previously observed for $Bi_{2-x}Sn_xSe_3$, albeit, the trends with doping concentration are reversed.

The growth of $Bi_{2-x}Eu_xSe_3$ by MBE has previous been carried out by Aronzon et al. [158]. In contrast to the work here, the authors reported a decrease in carrier mobility with increased Eu content. This decrease in carrier mobility was understood through the formation of Eu-rich, platelets which reduced the crystallinity of the Bi_2Se_3 matrix. The $Bi_{2-x}Eu_xSe_{3-x}S_x$ synthesized here utilized a EuS dopant source in which a flux of EuS molecules is directed towards the sample. HRTEM of the sample produced with a 190 nA EuS flux is presented in *Figure 5.24*. The platelets observed by Aronzon et al. were not observed in the present work. There are two explanations for the differences in microstructure and mobility trend. First, the EuS doping concentration in this work is less than that of Aronzon et al. and therefore no precipitation of Eu clusters is observed. Alternatively, the use of a EuS source may prevent the formation of Eu clusters as pure Eu is never directed towards the sample. Additional investigations into the growth of $Bi_{2-x}Eu_xSe_{3-x}S_x$ is the focus of current research.

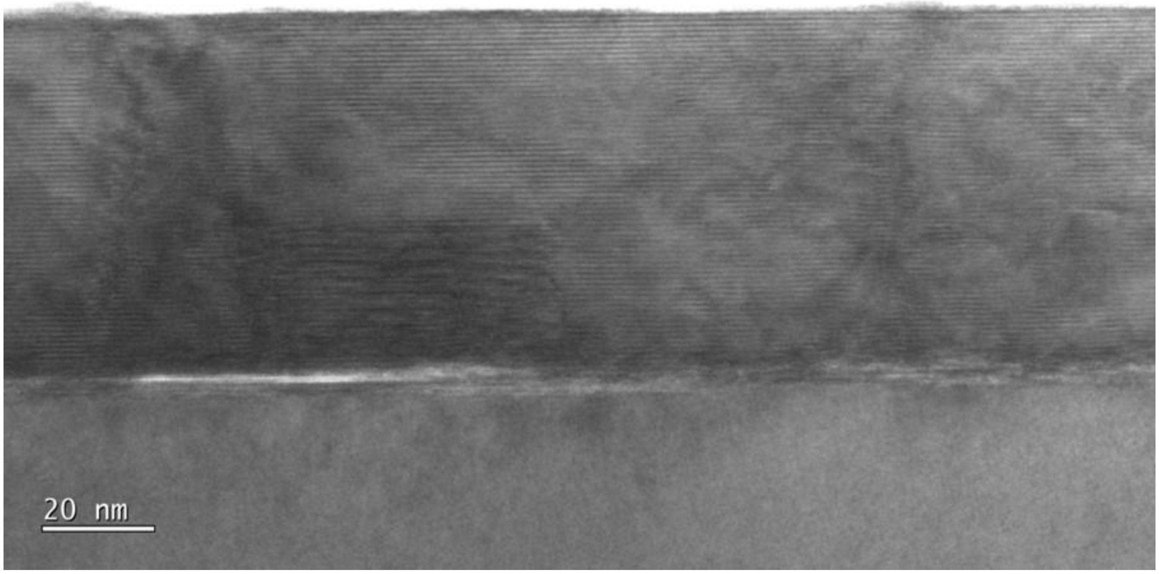

Figure 5.24: HRTEM of $Bi_{2-x}Eu_xSe_{3-x}S_x$ produced with a EuS flux of 190 nA.

5.6.2. Methods of Sample Transfer: Concluding Experiments

In *Section 5.4* we reported on investigations into *Methods of Sample Transfer* for ex-situ grown Bi_2Se_3. While these results facilitated the study of ex-situ grown Bi_2Se_3 in this work, some additional experiments are would result in a more complete study.

In the context of Se capping layers for sample preservation, we only discussed the use of amorphous layers of Se (a-Se). However, it has been shown that crystalline capping layers (c-Se) are more resistant to thinning over time and therefore do a better job at protecting the Bi_2Se_3 surface [165]. Adding the study of c-Se, specifically how it compares to other methods for long term sample storage would make for a more complete study.

Lastly, the study of *Methods of Sample Transfer* used a combination of undoped and Sn doped samples and various substrates (GaAs (100), GaAs (111), and InP (111)); these experimental variations were specified in the relevant text where applicable. Though these differences are thought to have negligible effects on the results of the work, control of these variables will make for a more reliable study.

6. Thesis Conclusions

This thesis reports on studies of the growth of a variety of two-dimensional (2D), van der Waals crystals by molecular beam epitaxy (MBE). The growth of each material was found to present unique engineering challenges that will be recapped in the following paragraphs.

Chapter 3 reported on investigations into the growth of semiconducting WSe_2. For the growth of WSe_2, a processing window for chemically homogenous 2H-WSe_2 was established. Low temperature growth was found to result in the formation of the metastable 1T'-WSe_2 while high temperature growth resulted in the formation of W^0 and WSe_{2-x}. It was found that under moderate growth temperatures that W^0 and WSe_{2-x} could be subdued beyond a critical Se to W BEPR of ~1000:1. The results here expanded on those previously reported in the literature by investigating a wider range of growth temperatures and BEPRs. This work served the additional purpose of establishing general methods of 2D material growth in the McDonnell Lab as it represents the first such investigations into the growth of layered, van der Waals compounds.

In the Chapter 4, we investigate the growth of metallic $NbSe_2$. The growth of $NbSe_2$ was found to host self-intercalation of Nb atoms in the van der Waals gap of adjacent layers. This Nb-rich material, written $Nb_{1+x}Se_2$, was found to exist across a large processing window for both temperature and BEPR. While it was determined that the BEPR could be used to alter the content of Nb self-intercalation, it could not be completely removed, regardless of the Se to Nb BEPR employed. We further identified the Nb intercalant to be detrimental to the in-plane electrical conductivity of the films which was hypothesized to be a consequence of increased charge scattering in the thin films due to the intercalants.

In Chapter 5, we studied the effect of Sn resonant doping on the electronic structure, chemistry, and electrical/thermal transport of Bi_2Se_3. It was hypothesized that adding Sn to Bi_2Se_3

would result in a p-type shift of the Fermi level, a decrease in the measured carrier concentration, and an enhancement of the measured thermopower. All three of these hypotheses were disproven by experiment. ARPES revealed that no measurable shift of the Fermi level was observed at any Sn concentration. The carrier concentration was found to increase upon Sn doping which implied n-type doping of the system. The quenching of the measured thermopower was believed to be a consequence of the increase in carrier concentration. It was observed that low Sn levels resulted in expected changes to the band structure. XPS revealed the presence of SnSe in the $Bi_{2-x}Sn_xSe_3$ films. However, the existence of SnSe in the films does not serve as a straightforward explanation to the results observed here.

7. Appendix

7.1.XPS Characterization of $NbSe_2$ Samples

7.1.1. XPS Fitting of CVT- and MBE-Grown $NbSe_2$

To estimate the stoichiometry of the MBE-grown $NbSe_2$ thin films, the XPS spectra were fit such that the total Nb 3*d* and Se 3*d* peak areas could be determined. The total peak areas were then compared to those of a CVT reference samples which was assumed to be a 2:1 stoichiometry. Example fits of for CVT- and MBE-grown $NbSe_2$ samples are presented in *Figure 7.1*. The purpose of these fits is to extract relative amounts of Nb and Se in each sample and thus we only aim to capture the total areas of the respective peaks. A broad feature due to the Nb 4*s* is also fit in each spectrum; the position, intensity, and width of this feature is linked to that of the Nb 3*d*.

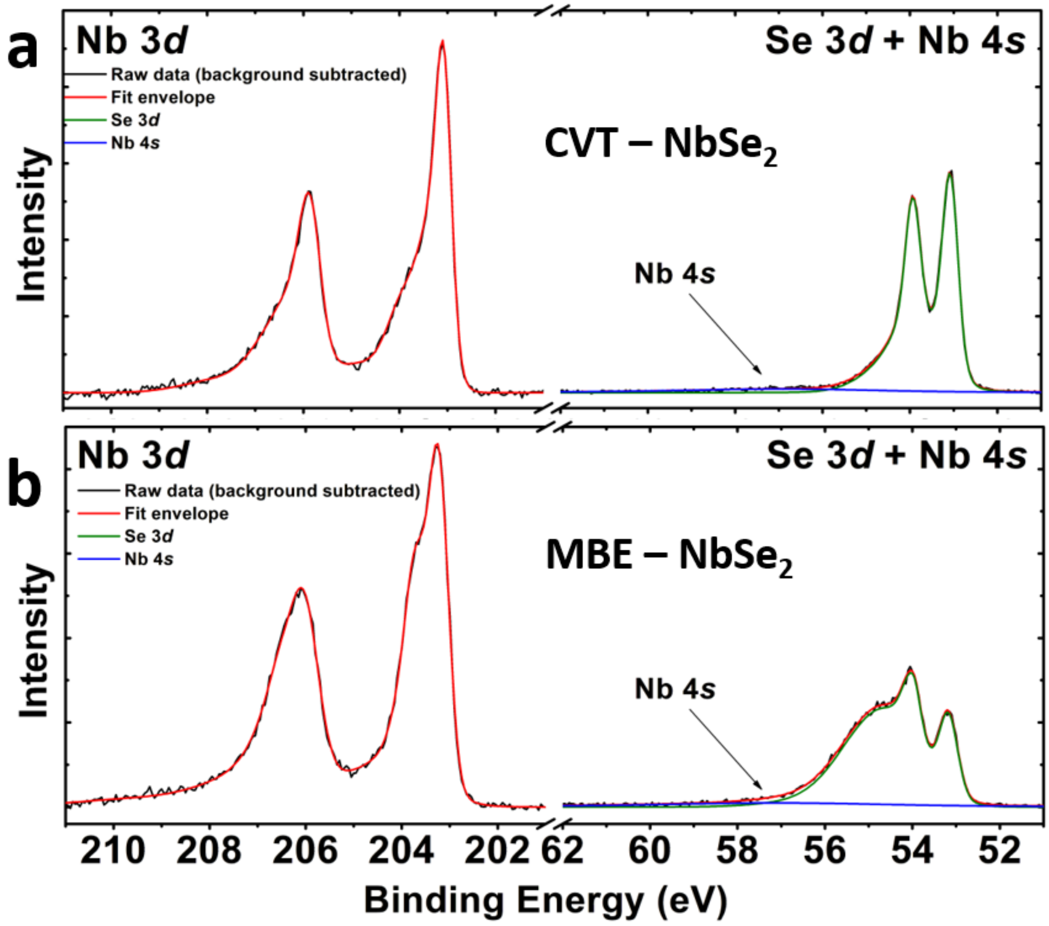

Figure 7.1: Nb 3*d* and Se 3*d* core levels of a) CVT- and b) MBE-grown NbSe$_2$ thin films fit for total area. MBE film grown with a Se to Nb BEPR of 45,000:1. Backgrounds of each spectrum are subtracted.

7.1.2. Identifying Limits of XPS Stoichiometry Estimates

In this section, we test the precision of XPS stoichiometry estimates using the tool in the McDonnell Lab. To do this, we looked at multiple measurements of CVT-grown NbSe$_2$ samples to check for variability in the measured Se/Nb ratio. *Figure 7.2* shows six overlaid XPS spectra of CVT-grown NbSe$_2$ (details of each sample are inset into figure caption). All samples are assumed to be a 2:1 stoichiometry. Clear in the graph is a reproducible Nb 3*d* line shape. However, the intensity of the Se 3*d* spectra (normalized to maximum intensity of Nb 3*d* for each sample) varies from sample to sample. All samples were measured after an in-situ mechanical cleave using Kapton tape and showed no signs of surface contamination.

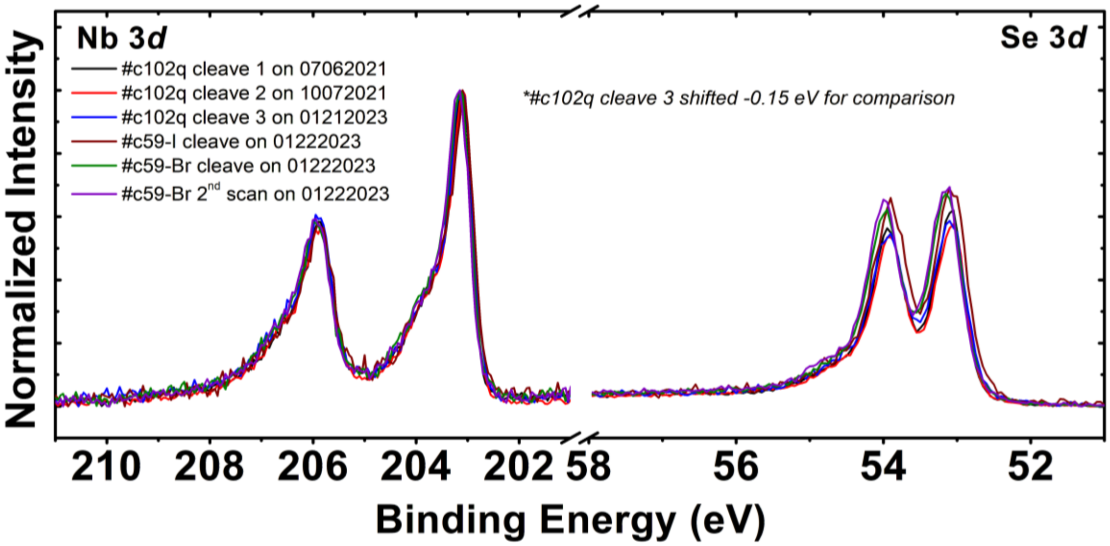

Figure 7.2: XPS of CVT refence samples produced by NIST. Sample ID and data of sample cleavage in figure caption. All samples produced through in-situ mechanical cleavage in UHV using Kapton tape and therefore represent atomically clean surfaces.

Table 7.1 lists the extracted Nb 3*d* / Se 3*d* area ratios from each sample. To observe changes in measured stoichiometry, we establish a relative sensitivity factor (RSF) value for the Nb 3*d* core level of the first listed sample (which results a 2:1 stoichiometry) and apply the same RSF value to the rest of the measured samples. The data here indicates a variance in the stoichiometries of the CVT-grown samples from $Nb_{0.85}Se_2$ to $Nb_{1.06}Se_2$.

Table 7.1: Data from XPS fit of CVT-grown $NbSe_2$ samples after in-situ cleave. RSF value developed from *#c102q cleave 1 on 07062021* used to compare stoichiometries of other five data sets.

Sample	**Nb 3*d*/Se3*d* area ratio**	**RSF (Nb)**	**Se/Nb ratio**	***1+x* in $Nb_{1+x}Se_2$**
#c102q cleave 1 on 07062021	2.004	4.01	2	1
#c102q cleave 2 on 10072021	2.131		1.88	1.06
#c102q cleave 3 on 01212023	2.027		1.98	1.01
#c59-I cleave on 01222023	1.712		2.34	0.85
#c59-Br cleave on 01222023	1.795		2.23	0.90
#c59-Br 2nd scan on 01222023	1.743		2.30	0.87

The stoichiometric data of CVT-grown $NbSe_2$ suggests a large error in the estimated stoichiometries calculated with XPS in the McDonnell Lab. Interestingly, the data suggests a bimodal distribution of estimated stoichiometries with samples labeled *#c102q* ranging from $x = 1$ to *1.06* and samples labeled *#C59* ranging from $x = 0.85$ to *0.90*. From these data it can be hypothesized that the error in x is ~0.05 and that the two batches of $NbSe_2$ show an unintentional variability in stoichiometry. This error in x of ~0.5 is consistent with variability observed in MBE-grown WSe_2 samples. *Figure 7.3* shows the XPS spectra of three nominally identical MBE-grown WSe_2 samples whose measured stoichiometry ranged from $W_{1.00}Se_2$ to $W_{1.04}Se_2$. Note that WSe_2 does not host SI, we write the stoichiometry in the form $W_{1+x}Se_2$ here simply to keep consistent with the above discussed $NbSe_2$ samples.

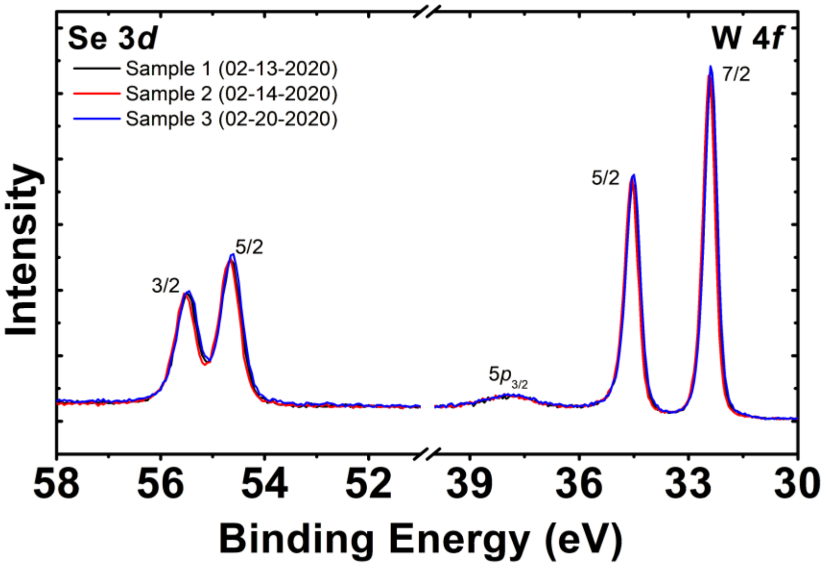

Figure 7.3: XPS of three nominally identical bilayer WSe_2 samples. Stoichiometry estimates ranged from $W_{1.00}Se_2$ to $W_{1.04}Se_2$.

7.2. XRR Thickness Measurements and Resistivity Calculations of $NbSe_2$ Thin Films

XRR was used to measure the thickness of $NbSe_2$ thin films. Thickness values were determined from fitting the XRR data of each sample. Details of the equipment used to collect the data and fitting procedure are provided in *Section 2.2.3*. The collected XRR data and overlaid fits are presented in *Figure 7.4* for Se to Nb BEPRs from 5:1 to 45,000:1.

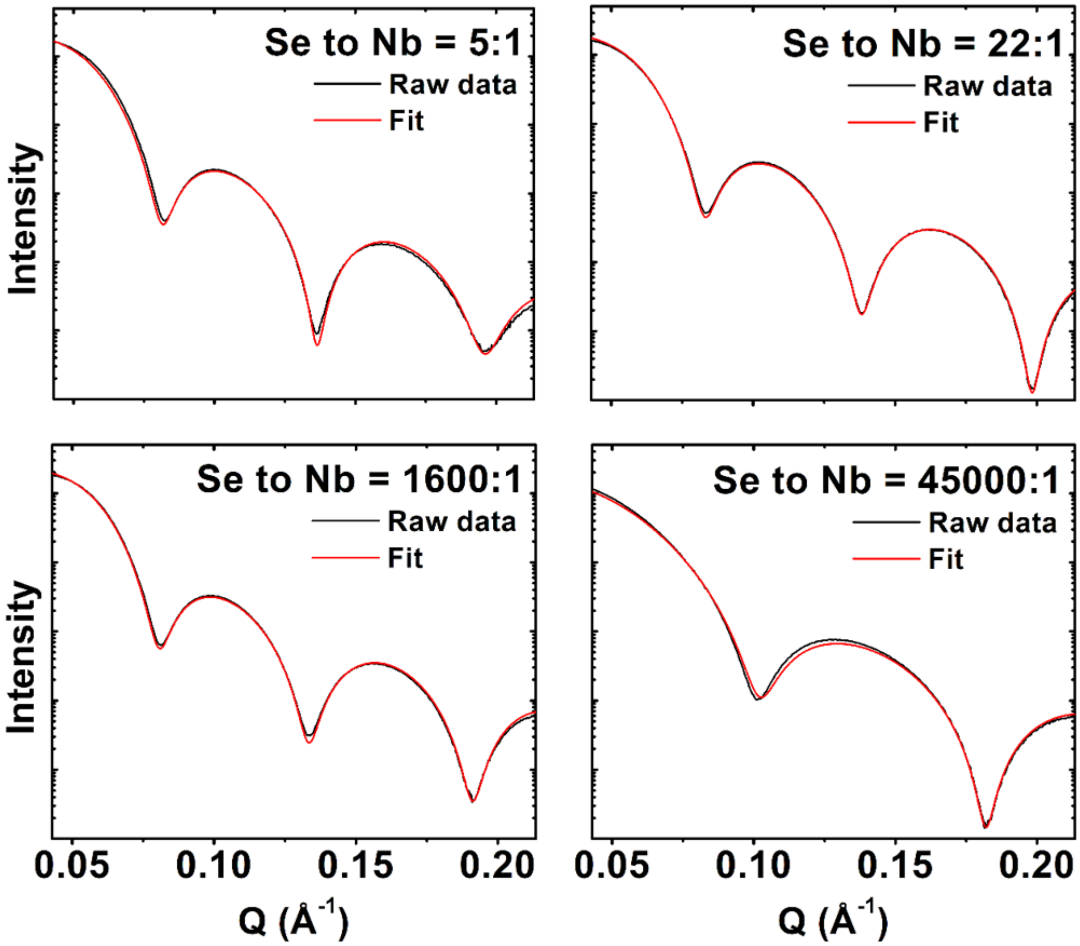

Figure 7.4: XRR data (black) and fit (red) $NbSe_2$ thin films grown with BEPRs from 5:1 to 45,000:1.

To calculate the resistivity of each thin film, the sheet resistance was first collected in Ω/square. The sheet resistance was then divided by the sample thickness determined by XRR to calculate the electrical resistivity of each film. A correction factor was used to account for the effect of sample dimensions on the measured resistivity values; all samples were of the same size/shape in this work and thus the correction factor used was the same for all samples [175].

Table 7.2: Data collected of MBE-grown $NbSe_2$ in order to calculate electrical resistivity. Correction factor used to account for sample dimensions.

BEPR	Sheet Resistance (Ω/Sq)	XRR thickness (cm)	Resistivity (Ω-cm)	Correction factor	Corrected Resistivity (Ω-cm)
5	799.8	1.00E-06	8.00E-04	0.925	7.40E-04
22	734.0	9.90E-07	7.27E-04	0.925	6.72E-04
1600	411.3	1.03E-06	4.24E-04	0.925	3.92E-04
45000	381.2	7.22E-07	2.75E-04	0.925	2.55E-04

7.3.Effective Mass Derived from ARPES Measurements

Due to electrons and holes being particles in a crystal, they exist inside a periodic energy potential landscape and therefore behave differently than a *free* electron in the presence of an external force. The effective mass (m*) of an electron or hole is the *apparent* mass due to the periodic energy potential imposed on it by the crystal lattice. Assuming a parabolic band, the energy, *E*, of the particle is proportional to the square of the particle's wave vector, *k*. This relationship is often written as

$$E(k) = E_0 + \frac{\hbar^2}{2m^*}k^2,$$

where $\hbar$ is reduced Plank's constant. Therefore, the effective mass of the particle is inversely proportional to the curvature of the band through the following expression,

$$m^* = \frac{\hbar^2}{{d^2E}/{dk^2}}.$$

The electronic structure of a material can be directly measured using ARPES. *Figure 7.5 (left)* is the ARPES spectra of MBE-grown monolayer WSe_2 which was previously presented in *section 3.3*. The image represents the raw data of the K-point in WSe_2; the K-point represents the valence band maximum (VBM) in monolayer WSe_2. To improve the clarity of the measured electronic structure, the 2nd derivative of the data was collected along the energy axis; this method was adopted from Zhang et al. [176]. The top of the valence band approximates a parabola and therefore can be fit with a 2nd order polynomial. This allows the curvature of the electronic structure in the vicinity of the VBM to be calculated. From this fitted data, and taking the 2nd derivative of the curve fit to the data, the effective mass can be calculated. Here the effective mass was calculated to be -5.5 x 10^{-31} kg, or -0.6 m_e. The negative value of m* is indicative of the negative curvature characteristic of a hole-like band.

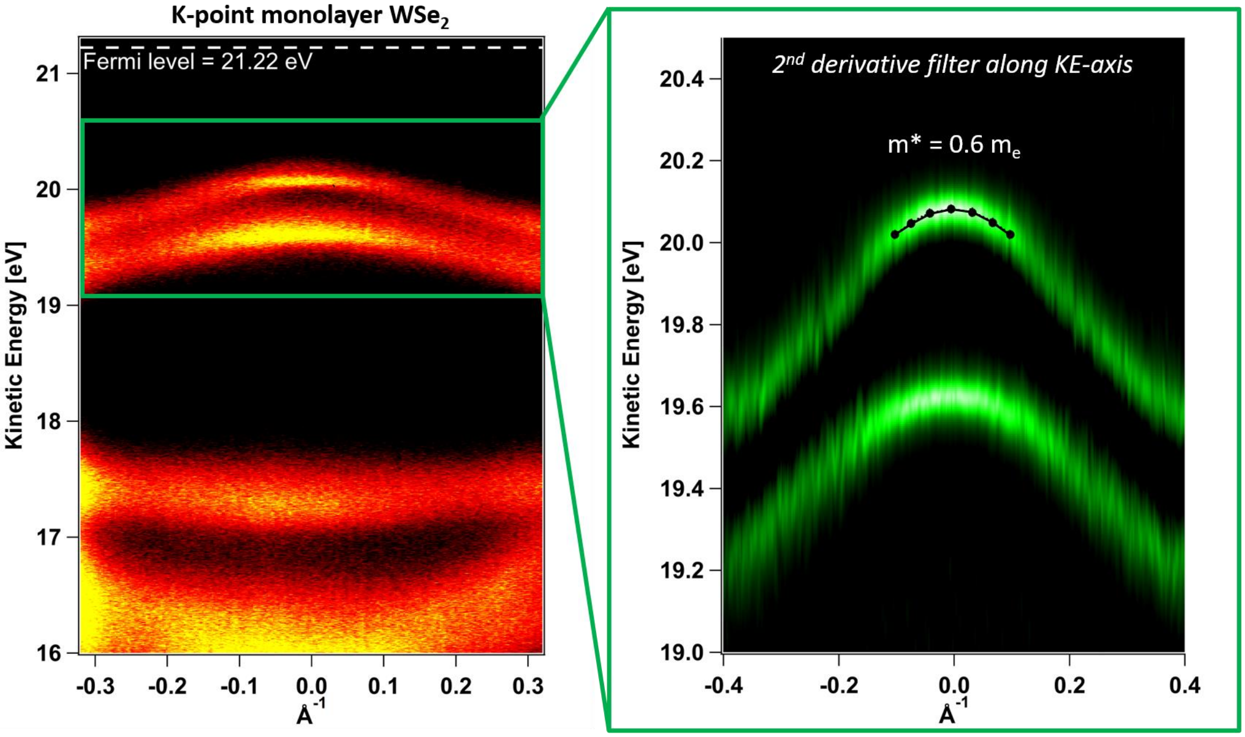

Figure 7.5: Left) ARPES of the K-point in MBE-grown monolayer WSe_2. Right) 2nd derivative filter for better visualization of the electronic structure. The extracted hole effective mas was m* = 0.6 m_e.

7.4.Determining Atomic Fluxes from Measured BEPs

In this work, we use measured beam equivalence pressures (BEPs) to adjust the atomic/molecular fluxes directed towards the sample prior to each growth. The BEP is the pressure read by an ion gauge in the path of an atomic or molecular flux (after subtracting the background pressure reading). This method provides precise control over elemental fluxes and allows for the synthesis recipes developed in this work to be easily repeated and compared to relevant literature. Despite the precision in this measurement, the BEP does not measure an actual flux, but instead an ion current from which an atomic or molecular pressure is assumed. To determine the actual atomic flux hitting the sample in number of atoms/area/time, the flux can be calculated using the known BEP or physically measured using calibration samples; the latter is the simpler route as will be discussed below.

The sensitivity of the ion gauge differs from species to species. Generally, it has been found that the sensitivity of this gauge (or equivalently the probability of atomic/molecular ionization within the gauge) varies linearly with the number of electrons per atom/molecule [177]. Despite this knowledge, it is difficult to accurately estimate what the atomic or molecular flux for a measured a BEP will be. An example which highlights this challenge is the Se flux produced from a standard effusion cell (as used in this work). The Se flux is known to consist of Se_x molecules (x=1-8) [103]. Each of these molecular species differ in the number of electrons and thus are all expected to have different measurement sensitivities which are not well established. Furthermore, the ratio of the varying concentrations of Se_x composing the molecular flux is never known precisely and varies with source temperature.

Using calibration samples to convert a BEP to an atomic flux is more straight forward. The process involves the deposition of the element of interest at a given BEP onto a cool substrate for a set amount of time. The thickness of the sample can be measured post deposition using a profilometer. With a known density of the atomic species deposited, the atomic flux during growth can be determined. There are some challenges with this method which can affect the results. For example, amorphous and crystalline materials have different densities and thus the structural nature of the deposited films should be known to carry out an accurate calculation.

7.5. Determining Dirac Point Energy from Momentum Integrated Intensity

The position of the Dirac Point energy in this work was determined through analysis of the momentum integrated intensity of ARPES spectra in the vicinity of the Dirac Point. *Figure 7.6a* shows the ARPES spectra of Bi_2Se_3 after an in-situ mechanical cleave. *Figure 7.6b* shows the momentum integrated intensity of the spectra presented in *Figure 7.6a*. The *momentum integrated intensity* is the total intensity of each energy step summed over the measured momenta.

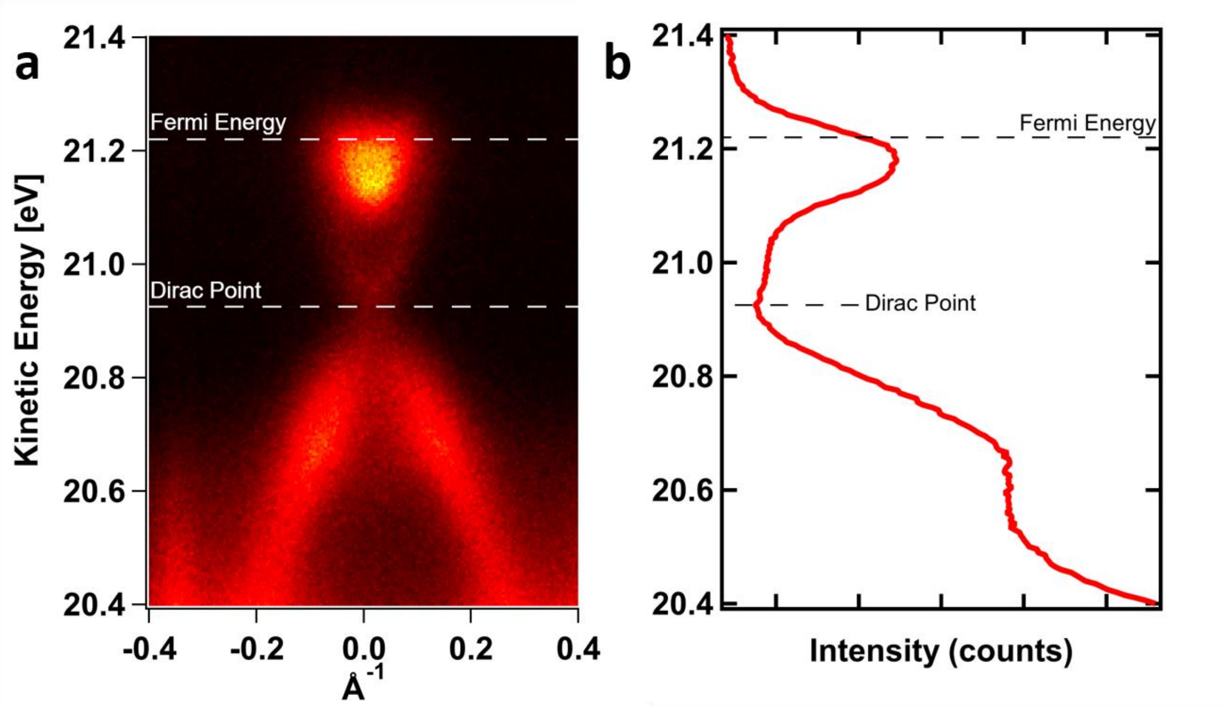

Figure 7.6: a) ARPES of the Γ-point in MBE-grown Bi_2Se_3 post an in-situ mechanical cleave. b) Momentum integrated intensity plotted as a function of kinetic energy. The Dirac point is identified as the minimum in the momentum integrated intensity.

8. List of Acronyms

2D – two-dimensional

3D – three-dimensional

AFM – atomic force microscopy

ARL – Army Research Laboratory

ARPES – angle-resolved photoelectron spectroscopy

BEOL - back-end-of-line

BEP – beam equivalence pressure

BEPR – beam equivalence pressure ratio

BF – bright field

CB – conduction band

CDW – charge density wave

CVD – chemical vapor deposition

CVT – chemical vapor transport

DFT – density functional theory

EAL – effective attenuation length

E_p – pass energy

ESCA – electron spectroscopy for chemical analysis

FET – field-effect transistor

HAADF – high angle annular dark field

HOPG – highly-ordered pyrolytic graphite

HRTEM – high-resolution transmission electron microscopy

IBA – ion-bombardment + anneal

IMFP – inelastic mean free path

LEED – low energy electron diffraction

MBE – molecular beam epitaxy

ML – monolayer

MOCVD – metal-organic chemical vapor deposition

NIST – National Institute of Standards and Technology

PES – photoelectron spectroscopy

PFT – PeakForce tapping

PVD – physical vapor deposition

QL – quintuple layer

RHEED – reflection high-energy diffraction

RMS – root mean square

RSF – relative sensitivity factor

SdH – Shubnikov–de Haas

SOC – spin-orbit coupling

SI – self intercalation

STEM – scanning transmission electron microscopy

STM/STS – scanning tunneling microscopy/spectroscopy

TFET – tunneling field-effect transistor

TI – topological insulator

TMD/TMDC – transition metal dichalcogenide

TSS – topological surface state

UHV – ultra-high vacuum

UPS – ultraviolet photoelectron spectroscopy

UV – ultraviolet

UVA – University of Virginia

VB – valence band

VBM – valence band maximum

VDWE – van der Waals epitaxy

XPS – x-ray photoelectron spectroscopy

XRD – x-ray diffraction

XRR – x-ray reflectivity

9. References

[1] E. Gerstner, "Nobel Prize 2010: Andre Geim & Konstantin Novoselov," *Nature Physics,* vol. 6, no. 11, pp. 836-836, 2010/11/01 2010, doi: 10.1038/nphys1836.

[2] N. Barrial. "Graphene, the coveted future material." https://www.makery.info/en/2017/05/02/graphene-le-materiau-du-futur-qui-se-fait-desirer/ (accessed February 4th, 2023).

[3] M. Ashton, J. Paul, S. B. Sinnott, and R. G. Hennig, "Topology-Scaling Identification of Layered Solids and Stable Exfoliated 2D Materials," *Physical Review Letters,* vol. 118, no. 10, p. 106101, 03/07/ 2017, doi: 10.1103/PhysRevLett.118.106101.

[4] K. Jiahao, C. Wei, X. Xuejun, S. Deblina, L. Wei, and B. Kaustav, "Graphene and beyond-graphene 2D crystals for next-generation green electronics," in *Proc.SPIE*, 2014, vol. 9083, p. 908305, doi: 10.1117/12.2051198. [Online]. Available: https://doi.org/10.1117/12.2051198

[5] G. Fiori *et al.*, "Electronics based on two-dimensional materials," *Nature Nanotechnology,* Review Article vol. 9, p. 768, 10/06/online 2014, doi: 10.1038/nnano.2014.207.

[6] D. Jena, "Tunneling Transistors Based on Graphene and 2-D Crystals," *Proceedings of the IEEE,* vol. 101, no. 7, pp. 1585-1602, 2013, doi: 10.1109/JPROC.2013.2253435.

[7] S. Das, D. Pandey, J. Thomas, and T. Roy, "The Role of Graphene and Other 2D Materials in Solar Photovoltaics," *Advanced Materials,* vol. 31, no. 1, p. 1802722, 2019/01/01 2019, doi: 10.1002/adma.201802722.

[8] N. Xu, Y. Xu, and J. Zhu, "Topological insulators for thermoelectrics," *npj Quantum Materials,* vol. 2, no. 1, p. 51, 2017/09/07 2017, doi: 10.1038/s41535-017-0054-3.

[9] D. Akinwande, N. Petrone, and J. Hone, "Two-dimensional flexible nanoelectronics," *Nature Communications,* Review Article vol. 5, p. 5678, 12/17/online 2014, doi: 10.1038/ncomms6678.

[10] R. Bel, K. Behnia, and H. Berger, "Ambipolar Nernst Effect in ${\mathrm{N}\mathrm{b}\mathrm{S}\mathrm{e}}_{2}$," *Physical Review Letters,* vol. 91, no. 6, p. 066602, 08/05/ 2003, doi: 10.1103/PhysRevLett.91.066602.

[11] G. E. Moore, "Cramming more components onto integrated circuits," ed: McGraw-Hill New York, 1965.

[12] R. K. Ratnesh *et al.*, "Advancement and challenges in MOSFET scaling," *Materials Science in Semiconductor Processing,* vol. 134, p. 106002, 2021/11/01/ 2021, doi: https://doi.org/10.1016/j.mssp.2021.106002.

[13] M. V. Fischetti, B. Fu, and W. G. Vandenberghe, "Theoretical Study of the Gate Leakage Current in Sub-10-nm Field-Effect Transistors," *IEEE Transactions on Electron Devices,* vol. 60, no. 11, pp. 3862-3869, 2013, doi: 10.1109/TED.2013.2280844.

[14] Y. Hu, P. Conlin, Y. Lee, D. Kim, and K. Cho, "van der Waals 2D metallic materials for low-resistivity interconnects," *Journal of Materials Chemistry C,* 10.1039/D1TC05872J vol. 10, no. 14, pp. 5627-5635, 2022, doi: 10.1039/D1TC05872J.

[15] K. Nakamura, N. Nagamura, K. Ueno, T. Taniguchi, K. Watanabe, and K. Nagashio, "All 2D Heterostructure Tunnel Field-Effect Transistors: Impact of Band Alignment and Heterointerface Quality," *ACS Applied Materials & Interfaces,* vol. 12, no. 46, pp. 51598-51606, 2020/11/18 2020, doi: 10.1021/acsami.0c13233.

[16] S. Kanungo, G. Ahmad, P. Sahatiya, A. Mukhopadhyay, and S. Chattopadhyay, "2D materials-based nanoscale tunneling field effect transistors: current developments and future prospects," *npj 2D Materials and Applications,* vol. 6, no. 1, p. 83, 2022/11/16 2022, doi: 10.1038/s41699-022-00352-2.

[17] C. Gong, H. Zhang, W. Wang, L. Colombo, R. M. Wallace, and K. Cho, "Band alignment of two-dimensional transition metal dichalcogenides: Application in tunnel field effect transistors," Text 2013/08/01 2013, doi: doi:10.1063/1.4817409.

[18] E. C. Ahn, "2D materials for spintronic devices," *npj 2D Materials and Applications,* vol. 4, no. 1, p. 17, 2020/06/18 2020, doi: 10.1038/s41699-020-0152-0.

[19] H. Vakili, S. Ganguly, G. J. de Coster, M. R. Neupane, and A. W. Ghosh, "Low Power In-Memory Computation with Reciprocal Ferromagnet/Topological Insulator Heterostructures," *ACS Nano,* vol. 16, no. 12, pp. 20222-20228, 2022/12/27 2022, doi: 10.1021/acsnano.2c05645.

[20] H. Wu *et al.*, "Magnetic memory driven by topological insulators," *Nature Communications,* vol. 12, no. 1, p. 6251, 2021/10/29 2021, doi: 10.1038/s41467-021-26478-3.

[21] X. Duan, Y. G. Semenov, and K. W. Kim, "Spin Logic via Controlled Correlation in Nanomagnet--Dirac-Fermion Heterostructures," *Physical Review Applied,* vol. 2, no. 4, p. 044003, 10/09/ 2014, doi: 10.1103/PhysRevApplied.2.044003.

[22] M. H. Lee and W. Wu, "2D Materials for Wearable Energy Harvesting," *Advanced Materials Technologies,* https://doi.org/10.1002/admt.202101623 vol. 7, no. 9, p. 2101623, 2022/09/01 2022, doi: https://doi.org/10.1002/admt.202101623.

[23] F. R. Fan and W. Wu, "Emerging Devices Based on Two-Dimensional Monolayer Materials for Energy Harvesting," *Research,* vol. 2019, doi: 10.34133/2019/7367828.

[24] C. Androulidakis, K. Zhang, M. Robertson, and S. Tawfick, "Tailoring the mechanical properties of 2D materials and heterostructures," *2D Materials,* vol. 5, no. 3, p. 032005, 2018/06/13 2018, doi: 10.1088/2053-1583/aac764.

[25] J. A. Wilson and A. D. Yoffe, "The transition metal dichalcogenides discussion and interpretation of the observed optical, electrical and structural properties," *Advances in Physics,* vol. 18, no. 73, pp. 193-335, 1969/05/01 1969, doi: 10.1080/00018736900101307.

[26] S. J. McDonnell and R. M. Wallace, "Atomically-thin layered films for device applications based upon 2D TMDC materials," *Thin Solid Films,* vol. 616, pp. 482-501, 10/1/ 2016, doi: http://dx.doi.org/10.1016/j.tsf.2016.08.068.

[27] W. Choi, N. Choudhary, G. H. Han, J. Park, D. Akinwande, and Y. H. Lee, "Recent development of two-dimensional transition metal dichalcogenides and their applications," *Materials Today,* vol. 20, no. 3, pp. 116-130, 2017/04/01/ 2017, doi: https://doi.org/10.1016/j.mattod.2016.10.002.

[28] R. Dong and I. Kuljanishvili, "Review Article: Progress in fabrication of transition metal dichalcogenides heterostructure systems," *Journal of Vacuum Science & Technology B,* vol. 35, no. 3, p. 030803, 2017/05/01 2017, doi: 10.1116/1.4982736.

[29] D. Voiry, A. Mohite, and M. Chhowalla, "Phase engineering of transition metal dichalcogenides," *Chemical Society Reviews,* 10.1039/C5CS00151J vol. 44, no. 9, pp. 2702-2712, 2015, doi: 10.1039/C5CS00151J.

[30] *VESTA 3 for three-dimensional visualization of crystal, volumetric and morphology data*. (2011). Journal of Applied Crystallography. [Online]. Available: https://doi.org/10.1107/S0021889811038970

[31] S. Gautam *et al.*, "Structural, Electronic and Thermoelectric Properties of Bi2Se3 Thin Films Deposited by RF Magnetron Sputtering," *Journal of Electronic Materials,* vol. 51, no. 5, pp. 2500-2509, 2022/05/01 2022, doi: 10.1007/s11664-022-09498-7.

[32] G. Sun *et al.*, "Enhanced thermoelectric performance of n-type Bi2Se3 doped with Cu," *Journal of Alloys and Compounds,* vol. 639, pp. 9-14, 2015/08/05/ 2015, doi: https://doi.org/10.1016/j.jallcom.2015.03.124.

[33] C. B. Satterthwaite and R. W. Ure, "Electrical and Thermal Properties of ${\mathrm{Bi}}_{2}$ ${\mathrm{Te}}_{3}$," *Physical Review,* vol. 108, no. 5, pp. 1164-1170, 12/01/ 1957, doi: 10.1103/PhysRev.108.1164.

[34] H. Zhang, C.-X. Liu, X.-L. Qi, X. Dai, Z. Fang, and S.-C. Zhang, "Topological insulators in Bi2Se3, Bi2Te3 and Sb2Te3 with a single Dirac cone on the surface," *Nature Physics,* Article vol. 5, p. 438, 05/10/online 2009, doi: 10.1038/nphys1270.

[35] P. Roushan *et al.*, "Topological surface states protected from backscattering by chiral spin texture," *Nature,* vol. 460, no. 7259, pp. 1106-1109, 2009/08/01 2009, doi: 10.1038/nature08308.

[36] M. Autore *et al.*, "Terahertz plasmonic excitations in Bi2Se3topological insulator," *Journal of Physics: Condensed Matter,* vol. 29, no. 18, p. 183002, 2017/03/31 2017, doi: 10.1088/1361-648x/aa63ac.

[37] Y.-H. Lee *et al.*, "Synthesis of Large-Area MoS2 Atomic Layers with Chemical Vapor Deposition," *Advanced Materials,* vol. 24, no. 17, pp. 2320-2325, 2012/05/02 2012, doi: 10.1002/adma.201104798.

[38] J.-K. Huang *et al.*, "Large-Area Synthesis of Highly Crystalline WSe2 Monolayers and Device Applications," *ACS Nano,* vol. 8, no. 1, pp. 923-930, 2014/01/28 2014, doi: 10.1021/nn405719x.

[39] Y.-H. Chang *et al.*, "Monolayer MoSe2 Grown by Chemical Vapor Deposition for Fast Photodetection," *ACS Nano,* vol. 8, no. 8, pp. 8582-8590, 2014/08/26 2014, doi: 10.1021/nn503287m.

[40] A. L. Elías *et al.*, "Controlled Synthesis and Transfer of Large-Area WS2 Sheets: From Single Layer to Few Layers," *ACS Nano,* vol. 7, no. 6, pp. 5235-5242, 2013/06/25 2013, doi: 10.1021/nn400971k.

[41] S. M. Eichfeld *et al.*, "Highly Scalable, Atomically Thin WSe2 Grown via Metal–Organic Chemical Vapor Deposition," *ACS Nano,* vol. 9, no. 2, pp. 2080-2087, 2015/02/24 2015, doi: 10.1021/nn5073286.

[42] H. Kim, D. Ovchinnikov, D. Deiana, D. Unuchek, and A. Kis, "Suppressing Nucleation in Metal–Organic Chemical Vapor Deposition of MoS2 Monolayers by Alkali Metal Halides," *Nano Letters,* vol. 17, no. 8, pp. 5056-5063, 2017/08/09 2017, doi: 10.1021/acs.nanolett.7b02311.

[43] S. Nasir, W. J. Smith, T. E. Beechem, and S. Law, "Growth of ultrathin Bi2Se3 films by molecular beam epitaxy," *Journal of Vacuum Science & Technology A,* vol. 41, no. 1, p. 012202, 2023/01/01 2022, doi: 10.1116/6.0002299.

[44] L. A. Walsh and C. L. Hinkle, "van der Waals epitaxy: 2D materials and topological insulators," *Applied Materials Today,* vol. 9, pp. 504-515, 2017/12/01/ 2017, doi: https://doi.org/10.1016/j.apmt.2017.09.010.

[45] P. Batude *et al.*, "3D Sequential Integration: Application-driven technological achievements and guidelines," in *2017 IEEE International Electron Devices Meeting (IEDM)*, 2-6 Dec. 2017 2017, pp. 3.1.1-3.1.4, doi: 10.1109/IEDM.2017.8268316.

[46] D. Neumaier, S. Pindl, and M. C. Lemme, "Integrating graphene into semiconductor fabrication lines," *Nature materials,* vol. 18, no. 6, p. 525, 2019.

[47] H. Ago *et al.*, "Visualization of Grain Structure and Boundaries of Polycrystalline Graphene and Two-Dimensional Materials by Epitaxial Growth of Transition Metal Dichalcogenides," *ACS Nano,* vol. 10, no. 3, pp. 3233-3240, 2016/03/22 2016, doi: 10.1021/acsnano.5b05879.

[48] V. K. Sangwan *et al.*, "Gate-tunable memristive phenomena mediated by grain boundaries in single-layer MoS2," *Nature Nanotechnology,* vol. 10, no. 5, pp. 403-406, 2015/05/01 2015, doi: 10.1038/nnano.2015.56.

[49] T. F. Jaramillo, K. P. Jørgensen, J. Bonde, J. H. Nielsen, S. Horch, and I. Chorkendorff, "Identification of Active Edge Sites for Electrochemical H₂ Evolution from MoS₂ Nanocatalysts," *Science,* vol. 317, no. 5834, p. 100, 2007, doi: 10.1126/science.1141483.

[50] G. M. Stephen *et al.*, "Effect of Sn Doping on Surface States of Bi2Se3 Thin Films," *The Journal of Physical Chemistry C,* vol. 124, no. 49, pp. 27082-27088, 2020/12/10 2020, doi: 10.1021/acs.jpcc.0c07176.

[51] L. A. Walsh *et al.*, "Fermi Level Manipulation through Native Doping in the Topological Insulator Bi2Se3," *ACS Nano,* vol. 12, no. 6, pp. 6310-6318, 2018/06/26 2018, doi: 10.1021/acsnano.8b03414.

[52] J. G. Analytis *et al.*, "Bulk Fermi surface coexistence with Dirac surface state in ${\text{Bi}}_{2}{\text{Se}}_{3}$: A comparison of photoemission and Shubnikov--de Haas measurements," *Physical Review B,* vol. 81, no. 20, p. 205407, 05/05/ 2010, doi: 10.1103/PhysRevB.81.205407.

[53] N. P. Butch *et al.*, "Strong surface scattering in ultrahigh-mobility ${\text{Bi}}_{2}{\text{Se}}_{3}$ topological insulator crystals," *Physical Review B,* vol. 81, no. 24, p. 241301, 06/01/ 2010, doi: 10.1103/PhysRevB.81.241301.

[54] J. Moon, N. Koirala, M. Salehi, W. Zhang, W. Wu, and S. Oh, "Solution to the Hole-Doping Problem and Tunable Quantum Hall Effect in Bi2Se3 Thin Films," *Nano Letters,* vol. 18, no. 2, pp. 820-826, 2018/02/14 2018, doi: 10.1021/acs.nanolett.7b04033.

[55] J. R. Arthur, "Molecular beam epitaxy," *Surface Science,* vol. 500, no. 1, pp. 189-217, 2002/03/10/ 2002, doi: https://doi.org/10.1016/S0039-6028(01)01525-4.

[56] V. Savchuk, B. Kotlyarchuk, and R. Lesyuk, "New Progress in Laser Technologies for Designing Semiconductor Nanostructures," *PHYSICS AND CHEMISTRY OF SOLID STATE,* vol. 9, no. 2, pp. 368-374, 2008.

[57] A. Koma, K. Sunouchi, and T. Miyajima, "Fabrication and characterization of heterostructures with subnanometer thickness," *Microelectronic Engineering,* vol. 2, no. 1, pp. 129-136, 1984/10/01/ 1984, doi: https://doi.org/10.1016/0167-9317(84)90057-1.

[58] D. Tsoutsou *et al.*, "Epitaxial 2D MoSe2 (HfSe2) Semiconductor/2D TaSe2 Metal van der Waals Heterostructures," *ACS Applied Materials & Interfaces,* vol. 8, no. 3, pp. 1836-1841, 2016/01/27 2016, doi: 10.1021/acsami.5b09743.

[59] L. A. Walsh *et al.*, "W Te 2 thin films grown by beam-interrupted molecular beam epitaxy," *2D Materials,* vol. 4, no. 2, p. 025044, 2017/03/08 2017, doi: 10.1088/2053-1583/aa61e1.

[60] K. Ueno, T. Shimada, K. Saiki, and A. Koma, "Heteroepitaxial growth of layered transition metal dichalcogenides on sulfur-terminated GaAs{111} surfaces," *Applied Physics Letters,* vol. 56, no. 4, pp. 327-329, 1990/01/22 1990, doi: 10.1063/1.102817.

[61] A. Ohtake and Y. Sakuma, "Heteroepitaxy of MoSe2 on Si(111) substrates: Role of surface passivation," *Applied Physics Letters,* vol. 114, no. 5, p. 053106, 2019/02/04 2019, doi: 10.1063/1.5083974.

[62] A. Koma, K. Saiki, and Y. Sato, "Heteroepitaxy of a two-dimensional material on a three-dimensional material," *Applied Surface Science,* vol. 41-42, pp. 451-456, 1990/01/01/ 1990, doi: https://doi.org/10.1016/0169-4332(89)90102-5.

[63] K. Onomitsu, A. Krajewska, R. A. E. Neufeld, F. Maeda, K. Kumakura, and H. Yamamoto, "Epitaxial growth of monolayer MoSe2on GaAs," *Applied Physics Express,* vol. 9, no. 11, p. 115501, 2016/10/21 2016, doi: 10.7567/apex.9.115501.

[64] K. Ueno. "Welcome to Van Der Waals Epitaxy!" http://van-der-waals-epitaxy.info/?page_id=11 (accessed March 28th, 2023).

[65] Y. Cheng *et al.*, "Van der Waals epitaxial growth of MoS2 on SiO2/Si by chemical vapor deposition," *RSC Advances,* 10.1039/C3RA42171F vol. 3, no. 38, pp. 17287-17293, 2013, doi: 10.1039/C3RA42171F.

[66] K. M. Freedy, P. M. Litwin, and S. J. McDonnell, "(Invited) In-Vacuo Studies of Transition Metal Dichalcogenide Synthesis and Layered Material Integration," *ECS Transactions,* vol. 77, no. 8, pp. 11-25, 2017.

[67] H. Hertz, "Ueber einen Einfluss des ultravioletten Lichtes auf die electrische Entladung," *Annalen der Physik,* vol. 267, no. 8, pp. 983-1000, 1887.

[68] A. Einstein, "Über einem die Erzeugung und Verwandlung des Lichtes betreffenden heuristischen Gesichtspunkt," *Annalen der physik,* vol. 4, 1905.

[69] J. C. Vickerman and I. Gilmore, *Surface Analysis: The Principal Techniques*. Wiley, 2009.

[70] J. F. Watts, "X-ray photoelectron spectroscopy," *Vacuum,* vol. 45, no. 6, pp. 653-671, 1994/06/01/ 1994, doi: https://doi.org/10.1016/0042-207X(94)90107-4.

[71] S. Hagström, C. Nordling, and K. Siegbahn, "Electron spectroscopy for chemical analyses," *Physics Letters,* vol. 9, no. 3, pp. 235-236, 1964/04/15/ 1964, doi: https://doi.org/10.1016/0031-9163(64)90062-9.

[72] E. Astm, "Standard Practice for Calibration of the Electron Binding-Energy Scale of an X-Ray Photoelectron Spectrometer," ed: ASTM International West Conshohocken, 2015.

[73] S. Doniach and M. Sunjic, "Many-electron singularity in X-ray photoemission and X-ray line spectra from metals," *Journal of Physics C: Solid State Physics,* vol. 3, no. 2, pp. 285-291, 1970/02/01 1970, doi: 10.1088/0022-3719/3/2/010.

[74] A. Damascelli, Z. Hussain, and Z.-X. Shen, "Angle-resolved photoemission studies of the cuprate superconductors," *Reviews of Modern Physics,* vol. 75, no. 2, pp. 473-541, 04/17/ 2003, doi: 10.1103/RevModPhys.75.473.

[75] S. Suga and C. Tusche, "Photoelectron spectroscopy in a wide hv region from 6eV to 8keV with full momentum and spin resolution," *Journal of Electron Spectroscopy and Related Phenomena,* vol. 200, pp. 119-142, 2015/04/01/ 2015, doi: https://doi.org/10.1016/j.elspec.2015.04.019.

[76] Y. Leng, *Materials characterization: introduction to microscopic and spectroscopic methods*. John Wiley & Sons, 2009.

[77] S. Kobayashi, "X-ray thin-film measurement techniques," *The Rigaku Journal,* vol. 26, no. 1, pp. 3-11, 2010.

[78] M. Chubarov, T. H. Choudhury, X. Zhang, and J. M. Redwing, "In-plane x-ray diffraction for characterization of monolayer and few-layer transition metal dichalcogenide films," *Nanotechnology,* vol. 29, no. 5, p. 055706, 2018/01/05 2018, doi: 10.1088/1361-6528/aaa1bd.

[79] M. Yasaka, "X-ray thin-film measurement techniques," *The Rigaku Journal,* vol. 26, no. 2, pp. 1-9, 2010.

[80] H. Kiessig, "Untersuchungen zur Totalreflexion von Röntgenstrahlen," *Annalen der Physik,* https://doi.org/10.1002/andp.19314020607 vol. 402, no. 6, pp. 715-768, 1931/01/01 1931, doi: https://doi.org/10.1002/andp.19314020607.

[81] C. K. Saw, W. K. Grant, J. Stanford, and L. N. Dinh, "An Investigation on X-ray Reflectivity technique at LLNL," Lawrence Livermore National Lab.(LLNL), Livermore, CA (United States), 2016.

[82] B. H. Toby and R. B. Von Dreele, "GSAS-II: the genesis of a modern open-source all purpose crystallography software package," *Journal of Applied Crystallography,* vol. 46, no. 2, pp. 544-549, 2013.

[83] C. Davisson and L. H. Germer, "Diffraction of Electrons by a Crystal of Nickel," *Physical Review,* vol. 30, no. 6, pp. 705-740, 12/01/ 1927, doi: 10.1103/PhysRev.30.705.

[84] C. Davisson and L. H. Germer, "The Scattering of Electrons by a Single Crystal of Nickel," *Nature,* vol. 119, no. 2998, pp. 558-560, 1927/04/01 1927, doi: 10.1038/119558a0.

[85] S. Hasegawa, "Reflection high-energy electron diffraction," *Characterization of Materials,* vol. 97, pp. 1925-1938, 2012.

[86] H. Zhang *et al.*, "Atomic force microscopy for two-dimensional materials: A tutorial review," *Optics Communications,* vol. 406, pp. 3-17, 2018/01/01/ 2018, doi: https://doi.org/10.1016/j.optcom.2017.05.015.

[87] D. Nečas and P. Klapetek, "Gwyddion: an open-source software for SPM data analysis," vol. 10, no. 1, pp. 181-188, 2012, doi: doi:10.2478/s11534-011-0096-2.

[88] V. Podzorov, M. E. Gershenson, C. Kloc, R. Zeis, and E. Bucher, "High-mobility field-effect transistors based on transition metal dichalcogenides," *Applied Physics Letters,* vol. 84, no. 17, pp. 3301-3303, 2004/04/26 2004, doi: 10.1063/1.1723695.

[89] B. Radisavljevic, A. Radenovic, J. Brivio, V. Giacometti, and A. Kis, "Single-layer MoS2 transistors," *Nature Nanotechnology,* vol. 6, p. 147, 01/30/online 2011, doi: 10.1038/nnano.2010.279

https://www.nature.com/articles/nnano.2010.279#supplementary-information.

[90] Y. Ma *et al.*, "Metallic Twin Grain Boundaries Embedded in MoSe2 Monolayers Grown by Molecular Beam Epitaxy," *ACS Nano,* vol. 11, no. 5, pp. 5130-5139, 2017/05/23 2017, doi: 10.1021/acsnano.7b02172.

[91] L. Jiao *et al.*, "Molecular-beam epitaxy of monolayer MoSe2: growth characteristics and domain boundary formation," *New Journal of Physics,* vol. 17, no. 5, p. 053023, 2015/05/15 2015, doi: 10.1088/1367-2630/17/5/053023.

[92] E. Xenogiannopoulou *et al.*, "High-quality, large-area MoSe2 and MoSe2/Bi2Se3 heterostructures on AlN(0001)/Si(111) substrates by molecular beam epitaxy," *Nanoscale,* 10.1039/C4NR06874B vol. 7, no. 17, pp. 7896-7905, 2015, doi: 10.1039/C4NR06874B.

[93] H. J. Liu *et al.*, "Molecular-beam epitaxy of monolayer and bilayer WSe2: a scanning tunneling microscopy/spectroscopy study and deduction of exciton binding energy," *2D Materials,* vol. 2, no. 3, p. 034004, 2015/06/25 2015, doi: 10.1088/2053-1583/2/3/034004.

[94] A. Khosravi *et al.*, "Covalent nitrogen doping in molecular beam epitaxy-grown and bulk WSe2," *APL Materials,* vol. 6, no. 2, p. 026603, 2018/02/01 2018, doi: 10.1063/1.5002132.

[95] R. Yue *et al.*, "Nucleation and growth of WSe2: enabling large grain transition metal dichalcogenides," *2D Materials,* vol. 4, no. 4, p. 045019, 2017/09/22 2017, doi: 10.1088/2053-1583/aa8ab5.

[96] C. M. Smyth, R. Addou, S. McDonnell, C. L. Hinkle, and R. M. Wallace, "WSe2-contact metal interface chemistry and band alignment under high vacuum and ultra high vacuum deposition conditions," *2D Materials,* vol. 4, no. 2, p. 025084, 2017/04/28 2017, doi: 10.1088/2053-1583/aa6bea.

[97] H. Fang, S. Chuang, T. C. Chang, K. Takei, T. Takahashi, and A. Javey, "High-Performance Single Layered WSe2 p-FETs with Chemically Doped Contacts," *Nano Letters,* vol. 12, no. 7, pp. 3788-3792, 2012/07/11 2012, doi: 10.1021/nl301702r.

[98] W. S. Yun, S. W. Han, S. C. Hong, I. G. Kim, and J. D. Lee, "Thickness and strain effects on electronic structures of transition metal dichalcogenides: 2H-$M{X}_{2}$ semiconductors (M $=$ Mo, W; X $=$ S, Se, Te)," *Physical Review B,* vol. 85, no. 3, p. 033305, 01/17/ 2012, doi: 10.1103/PhysRevB.85.033305.

[99] W. H. Blades, N. J. Frady, P. M. Litwin, S. J. McDonnell, and P. Reinke, "Thermally Induced Defects on WSe2," *The Journal of Physical Chemistry C,* vol. 124, no. 28, pp. 15337-15346, 2020/07/16 2020, doi: 10.1021/acs.jpcc.0c04440.

[100] H. Liu, P. Lazzaroni, and C. Di Valentin, "Nature of Excitons in Bidimensional WSe2 by Hybrid Density Functional Theory Calculations," *Nanomaterials,* vol. 8, no. 7, p. 481, 2018.

[101] P. M. Litwin, M. G. Sales, V. Nilsson, P. V. Balachandran, C. Constantin, and S. McDonnell, "The effect of growth temperature and metal-to-chalcogen on the growth of WSe2 by molecular beam epitaxy," in *Low-Dimensional Materials and Devices 2019*, 2019, vol. 11085: International Society for Optics and Photonics, p. 110850U, doi: 10.1117/12.2530454. [Online]. Available: https://www.spiedigitallibrary.org/conference-proceedings-of-spie/11085/110850U/The-effect-of-growth-temperature-and-metal-to-chalcogen-on/10.1117/12.2530454.full[Online]. Available: https://www.spiedigitallibrary.org/conference-proceedings-of-spie/11085/110850U/The-effect-

of-growth-temperature-and-metal-to-chalcogen-on/10.1117/12.2530454.short[Online]. Available: https://www.spiedigitallibrary.org/conference-proceedings-of-spie/11085/110850U/The-effect-of-growth-temperature-and-metal-to-chalcogen-on/10.1117/12.2530454.pdf

[102] Y. Nie *et al.*, "First principles kinetic Monte Carlo study on the growth patterns of WSe2monolayer," *2D Materials,* vol. 3, no. 2, p. 025029, 2016/05/19 2016, doi: 10.1088/2053-1583/3/2/025029.

[103] H. Cheng, J. M. DePuydt, M. A. Haase, and J. E. Potts, "Molecular-beam epitaxy growth of ZnSe using a cracked selenium source," *Journal of Vacuum Science & Technology B: Microelectronics Processing and Phenomena,* vol. 8, no. 2, pp. 181-186, 1990/03/01 1990, doi: 10.1116/1.584850.

[104] J. Berkowitz and W. A. Chupka, "Equilibrium Composition of Selenium Vapor; the Thermodynamics of the Vaporization of HgSe, CdSe, and SrSe," *The Journal of Chemical Physics,* vol. 45, no. 11, pp. 4289-4302, 1966/12/01 1966, doi: 10.1063/1.1727488.

[105] A. Rajan, K. Underwood, F. Mazzola, and P. D. C. King, "Morphology control of epitaxial monolayer transition metal dichalcogenides," *Physical Review Materials,* vol. 4, no. 1, p. 014003, 01/15/ 2020, doi: 10.1103/PhysRevMaterials.4.014003.

[106] M. M. Ugeda *et al.*, "Observation of topologically protected states at crystalline phase boundaries in single-layer WSe2," *Nature Communications,* vol. 9, no. 1, p. 3401, 2018/08/24 2018, doi: 10.1038/s41467-018-05672-w.

[107] P. Chen *et al.*, "Large quantum-spin-Hall gap in single-layer 1T′ WSe2," *Nature Communications,* vol. 9, no. 1, p. 2003, 2018/05/21 2018, doi: 10.1038/s41467-018-04395-2.

[108] M. S. Sokolikova, P. C. Sherrell, P. Palczynski, V. L. Bemmer, and C. Mattevi, "Direct solution-phase synthesis of 1T′ WSe2 nanosheets," *Nature Communications,* vol. 10, no. 1, p. 712, 2019/02/12 2019, doi: 10.1038/s41467-019-08594-3.

[109] W. Chen *et al.*, "Growth and Thermo-driven Crystalline Phase Transition of Metastable Monolayer 1T′-WSe2 Thin Film," *Scientific Reports,* vol. 9, no. 1, p. 2685, 2019/02/25 2019, doi: 10.1038/s41598-019-39238-7.

[110] W. Chen *et al.*, "Epitaxial Growth of Single-Phase 1T'-WSe2 Monolayer with Assistance of Enhanced Interface Interaction," *Advanced Materials,* https://doi.org/10.1002/adma.202004930 vol. 33, no. 7, p. 2004930, 2021/02/01 2021, doi: https://doi.org/10.1002/adma.202004930.

[111] J. M. Vandenberg-Voorhoeve, "Structural and magnetic properties of layered chalcogenides of the transition elements," in *Optical and Electrical Properties*: Springer, 1976, pp. 423-457.

[112] D. Fu *et al.*, "Molecular Beam Epitaxy of Highly Crystalline Monolayer Molybdenum Disulfide on Hexagonal Boron Nitride," *Journal of the American Chemical Society,* vol. 139, no. 27, pp. 9392-9400, 2017/07/12 2017, doi: 10.1021/jacs.7b05131.

[113] K. W. Nebesny *et al.*, "Organic/inorganic-molecular beam epitaxy: formation of an ordered phthalocyanine/tin(IV) sulfide heterojunction," *Chemistry of Materials,* vol. 3, no. 5, pp. 829-838, 1991/09/01 1991, doi: 10.1021/cm00017a018.

[114] C. Kreis, M. Traving, R. Adelung, L. Kipp, and M. Skibowski, "Tracing the valence band maximum during epitaxial growth of HfS2 on WSe2," *Applied Surface Science,* vol. 166, no. 1, pp. 17-22, 2000/10/09/ 2000, doi: https://doi.org/10.1016/S0169-4332(00)00433-5.

[115] K. K. Kam and B. A. Parkinson, "Detailed photocurrent spectroscopy of the semiconducting group VIB transition metal dichalcogenides," *The Journal of Physical Chemistry,* vol. 86, no. 4, pp. 463-467, 1982.

[116] D.-Y. Lin, J.-J. Jheng, T.-S. Ko, H.-P. Hsu, and C.-F. Lin, "Doping with Nb enhances the photoresponsivity of WSe2 thin sheets," *AIP Advances,* vol. 8, no. 5, p. 055011, 2018/05/01 2018, doi: 10.1063/1.5024570.

[117] E. Revolinsky, B. E. Brown, D. J. Beerntsen, and C. H. Armitage, "The selenide and telluride systems of niobium and tantalum," *Journal of the Less Common Metals,* vol. 8, no. 1, pp. 63-72, 1965/01/01/ 1965, doi: https://doi.org/10.1016/0022-5088(65)90058-5.

[118] H. Okamoto and T. B. Massalski, "Binary alloy phase diagrams," *ASM International, Materials Park, OH, USA,* 1990.

[119] H. Yamamoto, K. Yoshii, K. Saiki, and A. Koma, "Improved heteroepitaxial growth of layered NbSe2 on GaAs (111)B," *Journal of Vacuum Science & Technology A,* vol. 12, no. 1, pp. 125-129, 1994/01/01 1994, doi: 10.1116/1.578906.

[120] I. Naik and A. K. Rastogi, "Charge density wave and superconductivity in 2H- and 4H-NbSe2: A revisit," *Pramana,* vol. 76, no. 6, pp. 957-963, 2011/06/01 2011, doi: 10.1007/s12043-011-0028-0.

[121] K. Selte and A. Kjekshus, "On the structural properties of the Nb1+ Se2 phase," *Acta chem. scand.,* vol. 18, pp. 697-706, 1964.

[122] J. B. Nelson and D. P. Riley, "An experimental investigation of extrapolation methods in the derivation of accurate unit-cell dimensions of crystals," *Proceedings of the Physical Society,* vol. 57, no. 3, p. 160, 1945/05/01 1945, doi: 10.1088/0959-5309/57/3/302.

[123] F. Kadijk, R. Huisman, and F. Jellinek, "Niobium and tantalum diselenides," *Recueil des Travaux Chimiques des Pays-Bas,* vol. 83, no. 7, pp. 768-775, 1964.

[124] R. Huisman, F. Kadijk, and F. Jellinek, "The non-stoichiometric phases Nb1+ xSe2 and Ta1+ xSe2," *Journal of the Less Common Metals,* vol. 21, no. 2, pp. 187-193, 1970.

[125] M. Sidoumou, S. Merazka, A. Gómez-Herrero, M. Kars, and R. Thierry, "X-ray diffraction and theoretical study of the transition 2H-3R polytypes in Nb1 (0< x< 0.1)."

[126] M. Bonilla *et al.*, "Compositional Phase Change of Early Transition Metal Diselenide (VSe2 and TiSe2) Ultrathin Films by Postgrowth Annealing," *Advanced Materials Interfaces,* https://doi.org/10.1002/admi.202000497 vol. 7, no. 15, p. 2000497, 2020/08/01 2020, doi: https://doi.org/10.1002/admi.202000497.

[127] O. Khyzhun, "XPS Study of the Electronic Structure of Nb1.27Se2," *Metallofizika i Noveishie Tekhnologii,* vol. 24, pp. 141-149, 02/01 2002.

[128] M. H. van Maaren and H. B. Harland, "An energy band model of Nb - and Ta -dichalcogenide superconductors," *Physics Letters A,* vol. 29, no. 9, pp. 571-573, 1969/07/28/ 1969, doi: https://doi.org/10.1016/0375-9601(69)90446-0.

[129] L. H. Brixner, "Preparation and properties of the single crystalline AB2-type selenides and tellurides of niobium, tantalum, molybdenum and tungsten," *Journal of Inorganic and Nuclear Chemistry,* vol. 24, no. 3, pp. 257-263, 1962/03/01/ 1962, doi: https://doi.org/10.1016/0022-1902(62)80178-X.

[130] Y. Nakata *et al.*, "Monolayer 1T-NbSe2 as a Mott insulator," *NPG Asia Materials,* vol. 8, no. 11, pp. e321-e321, 2016/11/01 2016, doi: 10.1038/am.2016.157.

[131] Y. Nakata *et al.*, "Robust charge-density wave strengthened by electron correlations in monolayer 1T-TaSe2 and 1T-NbSe2," *Nature Communications,* vol. 12, no. 1, p. 5873, 2021/10/07 2021, doi: 10.1038/s41467-021-26105-1.

[132] F. Kadijk and F. Jellinek, "On the polymorphism of niobium diselenide," *Journal of the Less Common Metals,* vol. 23, no. 4, pp. 437-441, 1971/04/01/ 1971, doi: https://doi.org/10.1016/0022-5088(71)90053-1.

[133] H. P. Hughes and J. A. Scarfe, "Site Specific Photohole Screening in a Charge Density Wave," *Physical Review Letters,* vol. 74, no. 15, pp. 3069-3072, 04/10/ 1995, doi: 10.1103/PhysRevLett.74.3069.

[134] R. Zhao, B. Grisafe, R. K. Ghosh, K. Wang, S. Datta, and J. Robinson, "Stabilizing the commensurate charge-density wave in 1T-tantalum disulfide at higher temperatures via

potassium intercalation," *Nanoscale,* 10.1039/C8NR09732A vol. 11, no. 13, pp. 6016-6022, 2019, doi: 10.1039/C8NR09732A.

[135] Z. Wang *et al.*, "Surface-Limited Superconducting Phase Transition on 1T-TaS2," *ACS Nano,* vol. 12, no. 12, pp. 12619-12628, 2018/12/26 2018, doi: 10.1021/acsnano.8b07379.

[136] H. P. Hughes and R. A. Pollak, "Charge density waves in layered metals observed by X-ray photoemission," *The Philosophical Magazine: A Journal of Theoretical Experimental and Applied Physics,* vol. 34, no. 6, pp. 1025-1046, 1976/12/01 1976, doi: 10.1080/00318087608227726.

[137] L. Liu *et al.*, "Direct identification of Mott Hubbard band pattern beyond charge density wave superlattice in monolayer 1T-NbSe2," *Nature Communications,* vol. 12, no. 1, p. 1978, 2021/03/30 2021, doi: 10.1038/s41467-021-22233-w.

[138] X. Xi *et al.*, "Strongly enhanced charge-density-wave order in monolayer NbSe2," *Nature Nanotechnology,* vol. 10, no. 9, pp. 765-769, 2015/09/01 2015, doi: 10.1038/nnano.2015.143.

[139] E. Revolinsky, E. P. Lautenschlager, and C. H. Armitage, "Layer structure superconductor," *Solid State Communications (England-US),* vol. 1, no. 3, pp. 59-61, 1963.

[140] K. Selte and A. Kjekshus, "The crystal structures of Nb3Se4 and Nb3Te4," *Acta Crystallographica,* vol. 17, no. 12, pp. 1568-1572, 1964.

[141] E. Revolinsky, G. A. Spiering, and D. J. Beerntsen, "Superconductivity in the niobium-selenium system," *Journal of Physics and Chemistry of Solids,* vol. 26, no. 6, pp. 1029-1034, 1965.

[142] K. Selte and A. Kjekshus, "On the magnetic properties of niobium selenides and tellurides," *Acta Chem. Scand,* vol. 19, no. 1, 1965.

[143] K. Igaki and S. Nishine, "Thermodynamic Properties and Crystal Structures of Nonstoichiometric Niobium Selenides NbSex for x= 1.48− 2.00," *Transactions of the Japan Institute of Metals,* vol. 20, no. 5, pp. 219-226, 1979.

[144] T. Shimada *et al.*, "Structure determination of ultrathin nbse2 films by grazing incidence x-ray diffraction," *Solid state communications,* vol. 89, no. 7, pp. 583-586, 1994.

[145] X. Zhao *et al.*, "Engineering covalently bonded 2D layered materials by self-intercalation," *Nature,* vol. 581, no. 7807, pp. 171-177, 2020/05/01 2020, doi: 10.1038/s41586-020-2241-9.

[146] J. Yang *et al.*, "Ultrahigh-current-density niobium disulfide catalysts for hydrogen evolution," *Nature Materials,* vol. 18, no. 12, pp. 1309-1314, 2019/12/01 2019, doi: 10.1038/s41563-019-0463-8.

[147] Z.-Y. Liu *et al.*, "Charge Transfer Gap Tuning via Structural Distortion in Monolayer 1T-NbSe2," *Nano Letters,* vol. 21, no. 16, pp. 7005-7011, 2021/08/25 2021, doi: 10.1021/acs.nanolett.1c02348.

[148] H. Yang *et al.*, "Visualization of Charge-Density-Wave Reconstruction and Electronic Superstructure at the Edge of Correlated Insulator 1T-NbSe2," *ACS Nano,* vol. 16, no. 1, pp. 1332-1338, 2022/01/25 2022, doi: 10.1021/acsnano.1c09249.

[149] M. Liu *et al.*, "Monolayer 1T-NbSe2 as a 2D-correlated magnetic insulator," *Science Advances,* vol. 7, no. 47, p. eabi6339, doi: 10.1126/sciadv.abi6339.

[150] F. Calavalle *et al.*, "Tailoring Superconductivity in Large-Area Single-Layer NbSe2 via Self-Assembled Molecular Adlayers," *Nano Letters,* vol. 21, no. 1, pp. 136-143, 2021/01/13 2021, doi: 10.1021/acs.nanolett.0c03386.

[151] C. Chen *et al.*, "Strain-Controlled Superconductivity in Few-Layer NbSe2," *ACS Applied Materials & Interfaces,* vol. 12, no. 34, pp. 38744-38750, 2020/08/26 2020, doi: 10.1021/acsami.0c08804.

[152] F. Cheng *et al.*, "Epitaxial Growth of Single-Layer Niobium Selenides with Controlled Stoichiometric Phases," *Advanced Materials Interfaces,* vol. 5, no. 15, p. 1800429, 2018/08/01 2018, doi: 10.1002/admi.201800429.

[153] Y. Xia *et al.*, "Observation of a large-gap topological-insulator class with a single Dirac cone on the surface," *Nature Physics,* vol. 5, no. 6, pp. 398-402, 2009/06/01 2009, doi: 10.1038/nphys1274.

[154] H. Zhang, C.-X. Liu, X.-L. Qi, X. Dai, Z. Fang, and S.-C. Zhang, "Topological insulators in Bi2Se3, Bi2Te3 and Sb2Te3 with a single Dirac cone on the surface," *Nature Physics,* vol. 5, no. 6, pp. 438-442, 2009/06/01 2009, doi: 10.1038/nphys1270.

[155] M. Zhang, X. Wang, F. Song, and R. Zhang, "Layered Topological Insulators and Semimetals for Magnetoresistance Type Sensors," *Advanced Quantum Technologies,* https://doi.org/10.1002/qute.201800039 vol. 2, no. 1-2, p. 1800039, 2019/02/01 2019, doi: https://doi.org/10.1002/qute.201800039.

[156] B. Wiendlocha, "Resonant Levels, Vacancies, and Doping in Bi2Te3, Bi2Te2Se, and Bi2Se3 Tetradymites," *Journal of Electronic Materials,* vol. 45, no. 7, pp. 3515-3531, 2016/07/01 2016, doi: 10.1007/s11664-016-4502-9.

[157] J. P. Heremans *et al.*, "Enhancement of Thermoelectric Efficiency in PbTe by Distortion of the Electronic Density of States," *Science,* vol. 321, no. 5888, p. 554, 2008, doi: 10.1126/science.1159725.

[158] B. A. Aronzon *et al.*, "Magnetic and magnetotransport properties of Bi2Se3 thin films doped by Eu," *Journal of Magnetism and Magnetic Materials,* vol. 459, pp. 331-334, 2018/08/01/ 2018, doi: https://doi.org/10.1016/j.jmmm.2017.09.058.

[159] R. Yu, W. Zhang, H.-J. Zhang, S.-C. Zhang, X. Dai, and Z. Fang, "Quantized Anomalous Hall Effect in Magnetic Topological Insulators," *Science,* vol. 329, no. 5987, pp. 61-64, 2010/07/02 2010, doi: 10.1126/science.1187485.

[160] H. Li *et al.*, "Carrier density dependence of the magnetic properties in iron-doped Bi2Se3 topological insulator," *Journal of Applied Physics,* vol. 113, no. 4, p. 043926, 2013, doi: 10.1063/1.4788834.

[161] Y. Tung *et al.*, "Tuning the transport and magnetism in a Cr–Bi2Se3 topological insulator by Sb doping," *RSC Advances,* 10.1039/C7RA08201K vol. 7, no. 75, pp. 47789-47795, 2017, doi: 10.1039/C7RA08201K.

[162] A. Li *et al.*, "Demonstration of valley anisotropy utilized to enhance the thermoelectric power factor," *Nature Communications,* vol. 12, no. 1, p. 5408, 2021/09/17 2021, doi: 10.1038/s41467-021-25722-0.

[163] W. Zhou, H. Zhu, C. M. Valles, and J. A. Yarmoff, "Preparation of clean surfaces and Se vacancy formation in Bi2Se3 by ion bombardment and annealing," *Surface Science,* vol. 662, pp. 67-73, 2017/08/01/ 2017, doi: https://doi.org/10.1016/j.susc.2017.04.004.

[164] K. Virwani *et al.*, "Controlled removal of amorphous Se capping layer from a topological insulator," *Applied Physics Letters,* vol. 105, no. 24, p. 241605, 2014/12/15 2014, doi: 10.1063/1.4904803.

[165] H. Y. Lin *et al.*, "A new stable, crystalline capping material for topological insulators," *APL Materials,* vol. 6, no. 6, p. 066108, 2018/06/01 2018, doi: 10.1063/1.5029706.

[166] K. Tang, W. Qi, Y. Wei, G. Ru, and W. Liu, "High-Throughput Calculation of Interlayer van der Waals Forces Validated with Experimental Measurements," *Research,* vol. 2022, doi: 10.34133/2022/9765121.

[167] S. Bertolazzi, J. Brivio, and A. Kis, "Stretching and Breaking of Ultrathin MoS2," *ACS Nano,* vol. 5, no. 12, pp. 9703-9709, 2011/12/27 2011, doi: 10.1021/nn203879f.

[168] E. Frantzeskakis *et al.*, "Trigger of the Ubiquitous Surface Band Bending in 3D Topological Insulators," *Physical Review X,* vol. 7, no. 4, p. 041041, 11/20/ 2017, doi: 10.1103/PhysRevX.7.041041.

[169] T. Van Duong *et al.*, "A facile way to optimize thermoelectric properties of SnSe thin films via sonication-assisted liquid-phase exfoliation," *Journal of Materials Science: Materials in Electronics,* vol. 33, no. 19, pp. 15385-15392, 2022/07/01 2022, doi: 10.1007/s10854-022-08446-9.

[170] N. D. Boscher, C. J. Carmalt, R. G. Palgrave, and I. P. Parkin, "Atmospheric pressure chemical vapour deposition of SnSe and SnSe2 thin films on glass," *Thin Solid Films,* vol. 516, no. 15, pp. 4750-4757, 2008/06/02/ 2008, doi: https://doi.org/10.1016/j.tsf.2007.08.100.

[171] T. Zhu, Y. Liu, C. Fu, J. P. Heremans, J. G. Snyder, and X. Zhao, "Compromise and Synergy in High-Efficiency Thermoelectric Materials," *Advanced Materials,* https://doi.org/10.1002/adma.201605884 vol. 29, no. 14, p. 1605884, 2017/04/01 2017, doi: https://doi.org/10.1002/adma.201605884.

[172] G. D'Olimpio *et al.*, "Charge Redistribution Mechanisms in SnSe2 Surfaces Exposed to Oxidative and Humid Environments and Their Related Influence on Chemical Sensing," *The Journal of Physical Chemistry Letters,* vol. 11, no. 21, pp. 9003-9011, 2020/11/05 2020, doi: 10.1021/acs.jpclett.0c02616.

[173] G. Olimpio *et al.*, "Tin Diselenide (SnSe2) Van der Waals Semiconductor: Surface Chemical Reactivity, Ambient Stability, Chemical and Optical Sensors," *Materials*, vol. 15, no. 3*,* doi: 10.3390/ma15031154.

[174] W. Shi *et al.*, "Tin Selenide (SnSe): Growth, Properties, and Applications," *Advanced Science,* https://doi.org/10.1002/advs.201700602 vol. 5, no. 4, p. 1700602, 2018/04/01 2018, doi: https://doi.org/10.1002/advs.201700602.

[175] H. Topsoe, "Geometric factors in four point resistivity measurement," *Bulletin,* vol. 472, no. 13, p. 63, 1968.

[176] P. Zhang, P. Richard, T. Qian, Y. M. Xu, X. Dai, and H. Ding, "A precise method for visualizing dispersive features in image plots," *Review of Scientific Instruments,* vol. 82, no. 4, p. 043712, 2011/04/01 2011, doi: 10.1063/1.3585113.

[177] T. A. Flaim and P. D. Ownby, "Observations on Bayard–Alpert Ion Gauge Sensitivities to Various Gases," *Journal of Vacuum Science and Technology,* vol. 8, no. 5, pp. 661-662, 1971/09/01 1971, doi: 10.1116/1.1316382.